ABSTRACT

Title of Dissertation:	COLLISION DYNAMICS OF HIGHLY ORIENTED SUPER ROTOR MOLECULES FROM AN OPTICAL CENTRIFUGE
	Matthew J. Murray, Doctor of Philosophy, 2017
Dissertation directed by:	Professor Amy S. Mullin, Department of Chemistry and Biochemistry

Sophisticated optical methods provide some of the most promising tools for complete control of a molecule's energy and orientation, which enables a more complete understanding of chemical reactivity and structure. This dissertation investigates the collision dynamics of molecular super rotors with oriented angular momentum prepared in an optical centrifuge. Molecules with anisotropic polarizabilities are trapped in the electric field of linearly polarized light and then angularly accelerated from 0 to 35 THz over the duration of the optical pulse. This process drives molecules to extreme rotational states and the ensemble of molecules has a unidirectional sense of rotation determined by the propagation of the optical field. High resolution transient IR absorption spectroscopy of the super rotor molecules reveals the dynamics of collisional energy transfer.

These studies show that high energy CO_2 and CO rotors release large amounts of translational energy through impulsive collisions. Time-evolution of the

translational energy distribution of the CO_2 J=0-100 state shows that depletion from low J states involves molecules with sub-thermal velocities. Polarization-dependent Doppler profiles of CO rotors show anisotropic kinetic energy release and reveal a majority population of molecular rotors in the initial plane of rotation. Experimental modifications improved signal to noise levels by a factor of 10, enabling new transient studies in the low-pressure, single-collision regime. Polarization-dependent studies show that CO_2 rotors in the J=54-100 states retain their initial angular momentum orientation, and that this effect increases as a function of rotational angular momentum. These studies show that rotating molecules behave like classical gyroscopes. Polarization-dependent measurements of CO_2 rotors in the presence of He and Ar buffer gases show that CO_2 super rotors are more strongly relaxed by He collisions, demonstrating the importance of rotational adiabaticity in the relaxation process. Quantum scattering calculations of the He-CO_2 and Ar-CO_2 collision systems were performed to interpret the qualitative features of the experimental results. This work provides a detailed mechanistic understanding of the unique collisional dynamics of super rotor molecules.

COLLISION DYNAMICS OF HIGHLY ORIENTED SUPER ROTOR
MOLECULES FROM AN OPTICAL CENTRIFUGE

by

Matthew J. Murray

Dissertation submitted to the Faculty of the Graduate School of the
University of Maryland, College Park, in partial fulfillment
of the requirements for the degree of
Doctor of Philosophy
2017

Advisory Committee:
 Professor Amy S. Mullin, Chair
 Professor Millard H. Alexander
 Professor John T. Fourkas
 Professor Charles W. Clark
 Professor Steven L. Rolston

Dedication

I dedicate this thesis to my dad, Joseph Murray, who could not see me complete this

thesis, but fostered my initial interest in science.

Acknowledgements

There are many people that have made the work I present in this thesis possible. First, I would like to thank my advisor, Dr. Amy S. Mullin. Amy's dedication to teaching her students to become better scientists is unmatched. She has continually supported my work and ambitions as a scientist and professional. In addition, her work with the optical centrifuge is certainly the most interesting experiment I have encountered and is one of the primary reasons I came to the University of Maryland. I could not have been happier with the group I chose for my research.

I would like to thank Professor Millard Alexander who was like a second advisor to me. I thoroughly enjoyed his class on quantum chemistry where I could really see many ideas I have learned in chemistry and physics come together. He provided the tools and taught me the skills necessary to complete much of the computational work and continued to advise me throughout my career at Maryland.

I would also like to thank my committee members Prof. John T. Fourkas, Prof. Charles W. Clark, and Prof. Steve Rolston for taking the time to read and provide comments on this thesis.

The members of the Mullin group have been indispensable to my work. Dr. Carlos Toro and Dr. Qingnan Liu taught me many of the experimental techniques I have used throughout my career. In addition, both became close friends. I would also thank Hannah Ogden who helped me complete many of the experiments presented here. Her help was invaluable with many of inevitable instrumental challenges that occur in this type of work. I have no doubt that she will continue to be one of the most valued

Table of Contents

List of Tables

List of Figures

fits used to extrapolate the rates for each value of Δj are shown in red in each plot.

List of Abbreviations

BBO $\qquad$ BaB_2O_4

CPA $\qquad$ chirped pulse amplification

CW $\qquad$ continuous wave

FSR $\qquad$ free spectral range

FWHM $\qquad$ full-width-at-half-maximum

IR $\qquad$ infrared

MPA $\qquad$ multipass amplifier

Nd:YAG $\qquad$ neodymium: yttrium aluminium garnet

OC $\qquad$ optical centrifuge

OPO $\qquad$ optical parametric oscillator

PBC $\qquad$ polarizing beam cube

PC $\qquad$ Pockels cells

QCL $\qquad$ quantum cascade laser

REMPI $\qquad$ resonance enhance multi-photon ionization

rms $\qquad$ root-mean-square

R$\rightarrow$T $\qquad$ rotation-to-translation

SFG $\qquad$ sum frequency generation

TTL $\qquad$ transistor-to-transistor logic

Chapter 1: Introduction

In molecular physics, the Born-Oppenheimer approximation assumes that the electronic, vibrational, and rotational components of a molecule's energy can be treated separately. Within this approximation, the electronic energy is determined with the nuclei stationary and the vibrational and rotational motion of the molecule is described with canonical quantum models: the harmonic oscillator and the rigid rotor. For molecules at 300 K, the gaps between vibrational energy levels are often much larger than the gaps between rotational levels and the separate treatment of the vibrational and rotational motion provides a reasonably exact description of the molecular motion. However, this approach may not be valid for molecules in extreme rotational states. As rotational energy increases, the gap between adjacent rotational levels increases based on rigid rotor states. As vibrational energy increases, the gap between adjacent vibrational levels decreases due to anharmonicity. In the high-energy regime where energy gaps between rotational and vibrational states can be comparable, the traditional separable treatment of rotational and vibrational motion may break down. Studying molecules that do not fall within a region where their behavior is well-described by the canonical quantum models provides the opportunity to learn about molecular structure and energy transfer mechanisms at a fundamental level. New information about a molecule's energy and energy transfer mechanisms have important consequences for the study of reactive and non-reactive collisions that occur far from 300 K environments.

One goal in chemical physics is to selectively control chemical reactions and molecular collisions. Preparing all initial conditions of a molecular collision, including the internal energy and orientation of both collision partners, could lead to reaction efficiencies that approach unity[1]. Significant enhancements in chemical reaction rates have been obtained if molecules have added energy in motions that overlap with the reactive coordinate[2-5]. With the development of new laser-based techniques, molecular control has blossomed into a sophisticated and rapidly advancing field[6-8]. The complete control over all the degrees of freedom in a molecule has significant applications to the study of chemical reactivity[9], molecular structure[10], nonlinear optics[11], nanoscale design[12], and photoelectron spectroscopy[13]. While a number of approaches have been developed to control electronic, vibrational, and translational degrees of freedom, control of rotational motion remains challenging. Such challenges include strict optical selection rules and the fact that molecules exhibit a wide range of isotropic rotational motion determined by the thermal distribution and molecular symmetry. Structural and collisional information is often smeared out by the isotropic nature of molecular rotation under most conditions. As such, it is desirable to not only have control over the rotational energy, but also over the orientation of angular momentum.

Over the past 20 years, a suite of creative optical techniques has been developed that prepare molecules with well-defined rotational energies and orientations[14-19]. One of the most powerful techniques, the optical centrifuge, drives molecules into "super rotor" states with large amounts of oriented angular momenta. The work described in this thesis uses an optical centrifuge in conjunction with a high resolution transient IR absorption

spectrometer to investigate the collision dynamics and spectroscopic properties of highly oriented molecular super rotors.

1.1 Controlling Angular Momentum Magnitude and Orientation

Optical methods provide some of the most promising prospects for controlling a molecule's orientation and rotation[19]. The optical methods described here involve either resonant or non-resonant molecular transitions. The methods can be classified as either adiabatic or nonadiabatic. An adiabatic rotational control method involves light that interacts with the molecule on the order of or longer than the rotational period of the molecule (typically a few to tens of picoseconds). A non-adiabatic technique rapidly changes the state of the molecule through an interaction much faster than the rotational period of the molecule. Below, adiabatic and non-adiabatic methods are described for manipulating a molecule's angular momentum magnitude and orientation.

Li *et al.* proposed a resonant scheme for rotationally exciting molecules into extreme quasi-bound rotational states they termed "super rotors"[15]. In this theoretical work, sequential chirped pulses of light excited Li_2 molecules into states with a rotational quantum number, J, near 115 via sequential rovibronic transitions. In principal, this method is capable of producing molecules with oriented angular momentum. However, this technique was never demonstrated, probably, in part, because the scheme requires a very specific energy level structure and transition lifetimes such that enough population is excited into the high energy states.

In another resonant optical technique, stimulated Raman pumping with circularly polarized light successfully oriented the angular momentum of molecules such as

nitrogen[20] and acetylene[17]. However, due to strict selection rules, the rotational states excited were not above thermally populated states (for nitrogen J ≈ 6 and for acetylene J ≈ 19). An important result from these studies was that the molecules were found to maintain their initial angular momentum orientation despite inelastic and elastic collisions[17, 20]. In addition, the orientation decay was about four times slower than the depopulation of the excited state[21]. The projection of the angular momentum onto the z-axis is quantized in numbers, M_J, that range in value from −J to +J. This prior work showed that M_J populations decay more slowly than J state populations. This finding is consistent with the previously hypothesized prediction that M_J is nearly conserved during collisions[22]; however, since the orientation does eventually decay through collisions, this idea cannot be strictly true.

A non-resonant technique has achieved angular momentum orientation with a pair of orthogonally polarized femtosecond pulses of light separated by a time delay. This non-adiabatic scheme excited translationally cooled benzene molecules to a broad range of J states (J = 1 − 4) on an ultrafast timescale[16]. A significant result from this work is the degree to which angular momentum orientation ($|M_J|/J = 0.6$) is created in a nonadiabatic regime. In addition, the non-resonant nature of this optical scheme permits this approach to be applied to any polarizable molecule[16].

This cross-polarized technique has been used by two other groups to create angular momentum orientation in diatomic molecules such as D_2 and N_2[18, 23]. Lavorel, Faucher, and coworkers have slightly modified the cross-polarized method such that the fs pulses with orthogonal polarization are partially overlapped in time to generate an electric field polarization that continuously rotates over the duration of the two pulses[18]. They

nonadiabatically rotated N_2 molecules with a unidirectional sense of rotation. Both groups observed clear evidence of angular momentum orientation via the rotational Doppler effect, but the probe technique used did not resolve specific rotational states. Other recent optical methods for creating super rotor molecules include variations on a sequence or train of intense pulses of light to stimulate sequential rotational excitation[24, 25]. The development of new methods to manipulate molecular rotation is an ongoing focus in current research.

Ivanov, Corkum and coworkers were the first to propose[14] and demonstrate[26] the "optical centrifuge for molecules." This non-resonant method adiabatically excites molecules to super rotor states with oriented angular momentum. In an optical centrifuge a pair of oppositely chirped pulses of light, each with opposite circular polarization, are overlapped in time and space to generate an electric field which angularly accelerates in time. Polarizable molecules align with this field and the optical centrifuge generates an ensemble of coherently spinning rotors. With this pioneering work, the group could non-resonantly spin molecules to extreme, previously inaccessible, rotational states. They showed with mass spectrometry that Cl_2 rotors were spun beyond the energy of dissociation, corresponding to a rotational state of J ~420[26]. Corkum and coworkers described the action of the optical centrifuge in a purely classical sense. However, a full quantum mechanical analysis of the optical centrifuge excitation, which describes the excitation by a series of sequential Raman transitions, was completed by Vitanov and Girard in 2004. They showed that centrifugation is most effective when all of the sample population starts completely in the J = 0 state, although extreme rotation occurs regardless the distribution of states[27]. Interestingly, linearly polarized, oppositely chirped pulses can

also lead to extreme rotational excitation, but the induced Raman transitions in the linearly polarized case are 4 times weaker[27]. More recent theoretical work has developed a model to predict the fraction of molecules trapped and excited by the optical centrifuge[28]. Since its development, the optical centrifuge method has garnered increased interest from both experimental[29-32] and theoretical[28, 33-37] groups as a way to study the collision dynamics and optical properties of highly oriented super rotor molecules.

1.2 Super Rotor and Optical Centrifuge Studies

The rotational energy transfer and collision dynamics of rotating molecules has proven to be a complex and challenging subject to study[38, 39]. Many studies have saught to describe rotational relaxation with a matrix of state-to-state rate constants. Evidence suggests that there is a propensity for small changes in J caused by collisions and that state changes that return the system to thermal equilibrium are favored[40]. As such, it is common to describe the rate constants with an exponential gap law or power gap law based on changes in J state or energy[22, 41-48]. However, no real consensus has been reached as far as whether the energy gap or angular momentum gap description is best. Studies that investigated collisions with inert buffer gases led to the conclusion that collisions with less massive particles are more effective at removing rotational quanta[41, 49]. Experiments were primarily constrained to inelastic collisions in the low J regime, in which adjacent rotational states are separated by tens of wavenumbers—an order of magnitude less than thermal energy.

In one of the first super rotor studies, BrCN molecules were photo-dissociated and resulted in some CN fragments in the highly-excited J = 80 state[50]. The highly rotationally

excited CN molecules exhibited a collisional meta-stability that persisted for thousands of collisions with Ar and Kr[50]. The collision dynamics of super rotor molecules, in which energy gaps are on the order of the thermal energy, has not been extensively studied; however, theoretical predictions and the observation of several unique properties in early experiments offer some insights into rotational energy transfer dynamics of super rotors. The optical centrifuge provides an opportunity to study the collision dynamics of super rotor molecules.

The Mullin lab at the University of Maryland has built a high power optical centrifuge combined with a high resolution transient IR absorption spectrometer. An ensemble of super rotors is prepared and time dependent changes in translational energy and population of specific rotational states are measured following the optical centrifuge pulse. Early experiments detected high-J rovibrational transitions of N_2O molecules that had not been seen previously [51]. In addition, the study of the collision dynamics of CO_2 $J = 60-80$ rotors in the optical centrifuge showed that large amounts of translational energy ($T_{trans} \approx 1100$ K) result from collisions of the rotating molecules[29]. Polarization-dependent measurements on CO_2 J=76 probed the oriented nature of the rotors and showed that J=76 rotors maintain the initial angular momentum orientation through many J-changing collisions[30]. This experiment was the first to analyze super rotors in terms of classical gyroscopes as a way to describe the inhibited randomization of the angular momentum orientation[30]. This high-resolution experimental technique allows the study of time dependent, state-specific, energy evolution of molecular super rotors generated in an optical centrifuge.

7

Recently, Milner and coworkers have built an optical centrifuge and have used coherent Raman spectroscopy to study super rotor molecules[31]. Their technique probes a broad range of rotational states with ps time resolution. They quantified the loss of coherence in N_2 and O_2 super rotors and showed that higher angular momentum states are more stable against collisions[52, 53]. Other experiments used a resonance enhance multi-photon ionization (REMPI) technique to test higher-order rotational constants of O_2 super rotors[54]. Experiments have looked at the super rotors in an external magnetic field[55, 56], the non-linear SO_2 molecule in the optical centrifuge[57], and the production of sound waves from super rotor molecules[58].

Super rotor dynamics are in an energy regime far from equilibrium, and numerical studies of super rotor molecules are necessary to help understand some of the complex collisional behavior. Forrey has completed numerical calculations in which super rotor diatomic molecules are translationally cooled near 0 K to generate an ensemble of energetic super rotors that are stable against energy-loss collisions[34, 59]. Detailed calculations of J = 80 oxygen molecules show that collisions with helium can remove rotational energy three orders of magnitude faster than the rate at which energy can be removed from hydrogen rotors[60]. In addition, scattering calculations of cold collisions of He with CO_2 J = 200 super rotors show that the elastic cross sections are five times larger than inelastic cross sections—i.e., CO_2 super rotors are stable against collisions[61]. These calculations suggest that super rotor behavior is not universal. Other studies show that quasi-resonant rotation-to-vibration transfer may play an important role in super rotor relaxation[36], demonstrating the complexity of super rotor dynamics.

8

Recent molecular dynamics simulations of N_2 and CO_2 super rotors corroborate the large translational energy gains seen by the Mullin group[37, 62]. These studies show that super rotor dynamics can be described by two regimes. At early times, super rotors are in a gyroscopic stage in which spinning molecules release little energy and maintain their initial angular momentum orientation[37]. This stage is followed by an explosive release of translational energy as the rotational distribution relaxes[37]. The simulations also predict anisotropic diffusion away from the excited region[62] and the production of macroscopic gas vortices[35]. These predictions pose interesting questions about the behavior of molecular super rotors. Such questions can guide experiments to elucidate the super rotor properties and dynamics.

1.3 Outline

The main objective of this thesis is to study the collision dynamics of highly oriented molecular super rotors generated in an optical centrifuge. This introduction has provided the context in which this work resides and provides some of the ongoing challenges and potentially interesting avenues of research in super rotor studies. The research presented here provides new information on the dynamics of CO_2 and CO super rotors. Various experimental conditions and detection schemes have been employed to reveal how the super rotor molecules relax from states that are far removed from equilibrium by the optical centrifuge pulse. The outline of the rest of the thesis is as follows:

- Chapter 2: A description of how the optical centrifuge works and details on the ultra-fast laser system that generates the optical centrifuge are given.

High resolution transient IR absorption spectroscopy is described and the details on the spectrometer are given. Information on gas kinetics relevant to the rest of the thesis is also presented here.

- Chapter 3: This chapter is a survey of the rotational and translation energy dynamics of a broad range of CO_2 rotational states ($J = 0 - 100$) after optical centrifuge excitation. Comparisons are made to quantum scattering calculations of the Ar-CO_2 collision system (described more fully in Chapter 7). Experimental and computational results reveal a propensity for small changes in J at high rotational states.

- Chapter 4: Polarization-dependent IR measurements of CO rotors reveal anisotropic kinetic energy release in the probe volume, indicating that super rotor relaxation involves anisotropic transport. Results are compared with previous polarization-dependent CO_2 studies, showing that CO angular momentum orientation is randomized in fewer collisions than that of CO_2.

- Chapter 5: Instrumental modifications are described that enable polarization-dependent measurements on the CO_2 $J = 0 - 100$ rotational states. With the improved signal-to-noise, early-time measurements show that molecules oriented perpendicular to the plane of rotation have more translational energy than those molecules parallel to the rotation plane. In addition, polarization-dependent population ratios reveal the that both the magnitude and duration of the orientational anisotropy is larger for higher J molecules. High-J molecules act more like molecular gyroscopes.

- Chapter 6: Polarization-dependent experiments of CO_2 super rotors with Ar and He buffer gases are explored. Measurements show that He is more effective at removing rotational energy.

- Chapter 7: Quantum scattering calculations of the Ar-CO_2 and He-CO_2 collision systems were performed in collaboration with Professor Millard Alexander. Trends in the state-to-state inelastic scattering cross sections of the two collision systems are explored. The cross sections are averaged over all energies to obtain state-to-state rate constants and used as part of a master equation to compare the rotational relaxation with that observed in experiments.

- Chapter 8: Conclusions and future work

Chapter 2: Experimental Apparatus and Methods

This chapter describes the optical centrifuge spectrometer and gives an overview of the experimental principles and apparatus necessary for the completion of this work. A detailed description of the theoretical principles that govern the optical centrifuge is given. Information about the laser system that generates the optical centrifuge is also provided. The high resolution transient IR absorption spectrometer is described and relevant ideas from gas kinetics are explained.

2.1 Generating an Optical Centrifuge

2.1.1 Theory

In the research reported here, a high power optical centrifuge is used to study rotational energy transfer of molecules in high rotational states. The theoretical principles fundamental to the operation of the optical centrifuge are outlined in this section. Much of this description is based on the paper by Paul Corkum and coworkers in which the optical centrifuge technique was first described[14].

Fundamental to the operation of the optical centrifuge is the means by which a molecule interacts with an electric field. An optical field induces a dipole in a polarizable molecule. Optical centrifuge rotation is successfully achieved only for molecules that have an anisotropic polarizability. The induced dipole experiences an interaction potential with

the optical field and causes the molecule to align with the polarization of the field. We begin by writing the Hamiltonian of a molecule in an optical field:

$$H = H_0 + H_E(t) \tag{2.1}$$

where H_0 is the internal energy of the molecule and is time-independent and $H_E(t)$ is its interaction with the optical field, which is necessarily time-dependent. We take each component of the Hamiltonian individually. Within the rigid rotor model, H_0 is the rotational energy of the molecule:

$$H_0 = B\hat{J}^2, \tag{2.2}$$

where B is the rotational constant and $\hat{J}^2$ is the angular momentum operator. The Schrodinger equation becomes:

$$H_0 |J\, M_J\rangle = E |J\, M_J\rangle, \tag{2.3}$$

where $|J\, M_J\rangle$ are the eigenvectors of the Hamiltonian and correspond to the spherical harmonics $Y_{J,M}(\theta, \phi)$. J is the rotational quantum number and M_J is the projection of the rotational quantum number onto the molecular axis. The eigenvalues of $\hat{J}^2$, which correspond to the rotational energy levels, are[63]

$$E_{rot} = BJ(J + 1). \tag{2.4}$$

The interaction of a molecule in an electric field is

$$H_E(t) = -\vec{p} \cdot \vec{E}(t). \tag{2.5}$$

Here, $\vec{p}$ is the dipole moment and $\vec{E}$ is the optical field vector. For an induced dipole, the dipole moment is $\vec{p} = \boldsymbol{\alpha} \cdot \vec{E}$, where $\boldsymbol{\alpha}$ is the molecular polarizability tensor[64]. Using this definition and rewriting equation 2.5 in terms of the individual components of the electric field and polarizability yields

13

$$H_E = -\boldsymbol{\alpha} \cdot \vec{E} \cdot \vec{E} = -\frac{1}{2}[\alpha_\| E_\|^2 + \alpha_\perp E_\perp^2], \tag{2.6}$$

where the explicit time-dependence of the optical field has been dropped for simplicity.

In equation 2.6, $E_\| = E \cos\theta$ and $E_\perp = E \sin\theta$, where θ is the angle between the optical field and the most polarizable axis of the molecule[64]. Recalling that $\sin^2\theta + \cos^2\theta = 1$, equation 2.6 becomes

$$H_E = -\frac{1}{2}E^2[\alpha_\perp + (\alpha_\| - \alpha_\perp)\cos^2\theta]. \tag{2.7}$$

We are mainly concerned with the angular dependence of this term. Therefore, the potential in terms of the angle dependent terms is

$$H_E \propto -\frac{1}{2}E^2\Delta\alpha\cos^2\theta. \tag{2.8}$$

The interaction energy is at a minimum when the angle between the molecular axis and the polarization vector of the optical field is $\theta = 0$. In this situation, the molecule is aligned.

From equation 2.8 we see that if the optical field rotates in time, the molecule will follow the optical field and also rotate. As the optical field angularly accelerates, the aligned molecule gains rotational energy. The well depth of the interaction potential is defined by the value of $U_0 = -(1/2)E^2\Delta\alpha$, where we have represented $\alpha_\| - \alpha_\perp$ by $\Delta\alpha$, the anisotropic polarizability. For a molecule with greater anisotropic polarizability, the well depth of the interaction potential is deeper, making it easier to trap such a molecule in the optical centrifuge. In addition, the value of E^2 is proportional to the intensity of the optical field and therefore a larger optical field intensity results in a greater interaction energy between the molecules and the field.

14
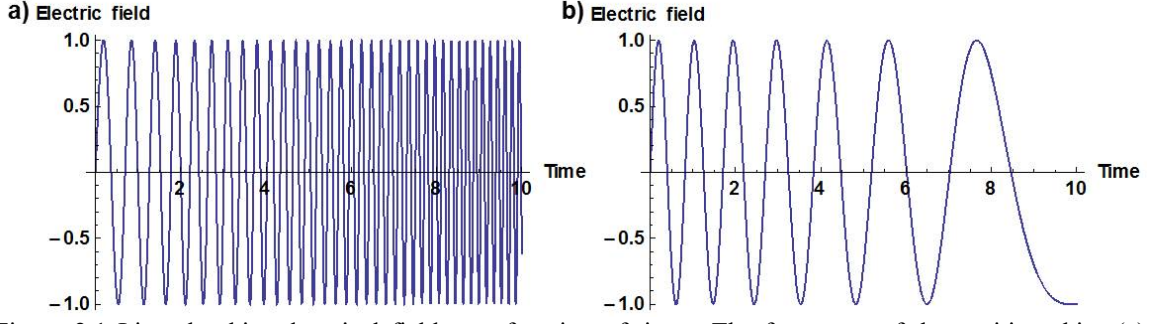
Figure 2.1 Linearly-chirped optical field as a function of time. The frequency of the positive chirp (a) increases while the frequency of the negative chirp (b) decreases.

We now describe in detail the time-evolving optical field responsible for angularly accelerating molecules in the optical centrifuge. The angularly accelerating optical field in the optical centrifuge is generated by combining two oppositely-chirped pulses of light, each with counter-rotating circular polarization of the electric field. A chirped pulse of light has a frequency that changes over the duration of the pulse. In the optical centrifuge we define the chirps, $\omega_+(t)$ and $\omega_-(t)$:

$$\omega_+(t) = \omega_0 + \frac{1}{2}\beta t$$

$$\omega_-(t) = \omega_0 - \frac{1}{2}\beta t, \tag{2.9}$$

where ω_0 is the common starting frequency and β is the rate at which the frequency is changing. Figure 2.1 shows the waveform of a positive (a) and negative (b) chirped optical field. The factor of one half in equation 2.9 makes the convenient definition of the time-dependent frequency difference,

$$\Delta\omega(t) = \omega_+(t) - \omega_-(t) = \beta t. \tag{2.10}$$

The optical field of the positively-chirped pulse is represented by

$$\vec{E} = \frac{E_0}{2}[\hat{x}\cos(\omega_+ t) + \hat{y}\sin(\omega_+ t)], \tag{2.11}$$

15

where $E_0/2$ is the amplitude on the field and the explicit time-dependence of the field frequency has been removed. Equation 2.11 represents an optical field rotating in the counter-clockwise direction. Likewise, the equation of an negatively-chirped electric field rotating in the clockwise direction:

$$\vec{E} = \frac{E_0}{2}[\hat{x}\cos(\omega_- t) - \hat{y}\sin(\omega_- t)]. \tag{2.12}$$

The sum of equations 2.11 and 2.12 yields

$$\vec{E} = E_0 \begin{bmatrix} \cos\left(\frac{\omega_+ + \omega_-}{2}t\right)\cos\left(\frac{\omega_- - \omega_+}{2}t\right)\hat{x} \\ -\cos\left(\frac{\omega_+ + \omega_-}{2}t\right)\sin\left(\frac{\omega_- - \omega_+}{2}t\right)\hat{y} \end{bmatrix}. \tag{2.13}$$

Simplifying the above expression by noting that $\omega_+ + \omega_- = 2\omega_0$ and that $\omega_- - \omega_+ = -\Delta\omega$ yields:

$$\vec{E} = E_0\cos(\omega_0 t)\left[\cos\left(\frac{\Delta\omega}{2}t\right)\hat{x} + \sin\left(\frac{\Delta\omega}{2}t\right)\hat{y}\right], \tag{2.14}$$

where we have used the fact that cosine is an even function, while sine is an odd function. Equation 2.14 represents a linearly polarized electric field propagating in the z-direction which angularly accelerates in time. Note that the rotation of the optical field is a direct result of the time-dependent frequency difference, $\Delta\omega(t)$, between the two pulses. As the optical frequency difference increases, so does the rotational frequency of the optical field. From equation 2.14 we see that the instantaneous rotational frequency, $\Omega(t)$, of the optical field polarization is

$$\Omega(t) = \frac{\Delta\omega}{2}. \tag{2.15}$$

It is this rotational frequency, along with the molecule's moment of inertia I, which defines the amount of rotational energy imparted onto the molecule. The amount of classical rotational energy given to the molecule is

$$E_{rot} = \frac{1}{2} I \Omega^2. \qquad (2.16)$$

The optical field most effectively traps molecules which have their molecular axis aligned parallel to the polarization of the optical field. A significant portion of randomly oriented molecules is trapped if the field maps an angle of at least π as it turns on. In other words, the time-dependent angle, $\Omega(t)\,t$, which defines the optical field polarization direction, must be greater than π. By noting that $\Omega(t) = \beta t/2$ the following relation can be written:

$$\frac{\beta t_{on}^2}{2} > \pi, \qquad (2.17)$$

In addition, the kinetic energy gained by the molecules should not exceed the depth of the potential trap ($K < U_0$). The kinetic energy gained by the molecules is

$$K \sim \frac{U_0}{2} + \frac{1}{2} I(\beta t_{on}/2)^2, \qquad (2.18)$$

where the factor of 2 in the first term comes from the Virial Theorem[14]. The second term is the rotational energy gained during the turn on period. By requiring $K < U_0$,

$$(\beta t_{on}/2)^2 < \frac{U_0}{I}. \qquad (2.19)$$

Using the minimum value of t_{on} from equation 2.17 and the expression for U_0, we determine the criterion for efficient centrifugation.

$$\frac{\pi \beta}{E^2} < \frac{\Delta \alpha}{I}. \qquad (2.20)$$

17

To summarize, there are two important molecular parameters that must be considered when choosing a molecular candidate for the optical centrifuge. The first parameter is the polarizability anisotropy, $\Delta\alpha$, which determines the depth of the trap; a larger anisotropy means a more effective trap. The second is the ratio, $\frac{\Delta\alpha}{I}$, which must be large enough so that the molecule remains trapped throughout the pulse. Table 2.1 gives the values for $\Delta\alpha$ and $\frac{\Delta\alpha}{I}$ for several linear molecules. In addition, two important experimental parameters are the field intensity, which along with $\Delta\alpha$ determines the interaction potential well depth, and the value of β, which defines the angular acceleration of the rotating optical field.

An estimate of the J-state for a molecule excited in the optical centrifuge is determined by equating the classical rotational energy (equation 2.16) to the quantum energy (equation 2.4). The results are shown in Table 2.1 for this set of candidate molecules. The estimate was calculated using $E_{rot} \approx BJ^2$. The optical centrifuge angular frequency used for this estimate was $\Omega \approx 35$ THz. These calculations show that the optical centrifuge can excite molecules to rotational states that far exceed those that are thermally

Table 2.1 Molecular candidates for the optical centrifuge. a[65] b[66] c[67]

Molecule	$\Delta\alpha$ (au)	I (10^{-46} kg m^2)	$\Delta\alpha$/I (10^{15} m/kg)	E_{rot} (cm^{-1})	$J_{excited}$
CO	3.59[a]	1.46	3.6	4480	50
HCN	8.43[b]	1.89	6.6	5810	60
HCCH	12.55[a]	2.38	7.8	7300	80
CO_2	14.25[a]	7.17	2.9	22000	220
N_2O	19.81[a]	6.68	4.4	20500	210
OCS	27.5[a]	13.8	3.0	42300	450
CS_2	63.9[a]	25.7	3.7	78700	850
CSe_2	83.53[c]	76.1	1.6	233000	2500

populated at 300 K. While extremely high J states can theoretically be accessed by the optical centrifuge, some molecules may fall out of the trap before reaching the estimated state due to small $\frac{\Delta\alpha}{I}$ values.

Molecules that are not randomly oriented in space are said to be *polarized*[8]. Polarization of a distribution of vectors is divided into two categories: *alignment* and *orientation*[8]. Alignment occurs when the vectors lie along a single axis, but have no preferred direction. Orientation occurs when the vectors lie along a single axis and have a preferred direction.   In this work, the vector of interest is the angular momentum vector $\vec{J}$. The direction of $\vec{J}$ is defined by the projection quantum number M_J. Figure 2.2 shows the distributions of the angular momentum vectors with J = 100 in an (a) isotropic, (b) aligned, and (c) oriented sample. The isotropic sample has all values of M_J equally populated. The aligned sample has only $M_J = \pm\, 100$ and the oriented sample has only $M_J = +\, 100$. The lower panels in Figure 2.2 show the ideal distribution of M_J values in each case. In many experiments, there are a distribution of M_J values. For an aligned sample, there is an anisotropic distribution of $|M_J|$, but for an oriented sample, there is an anisotropic distribution of M_J.

The molecules trapped by the optical centrifuge spin in the same direction and have a coherent phase. In the classical limit, the angular momentum vectors of the trapped molecules point in the same direction and the angular momentum vectors are oriented. Figure 2.3a illustrates the configuration of the propagation vector $\vec{k}_{OC}$ and optical field vector $\vec{E}_{OC}$ of the optical centrifuge beam denoted as OC. The optical centrifuge (OC) beam propagates along the z-axis and prepares molecules with an angular momentum
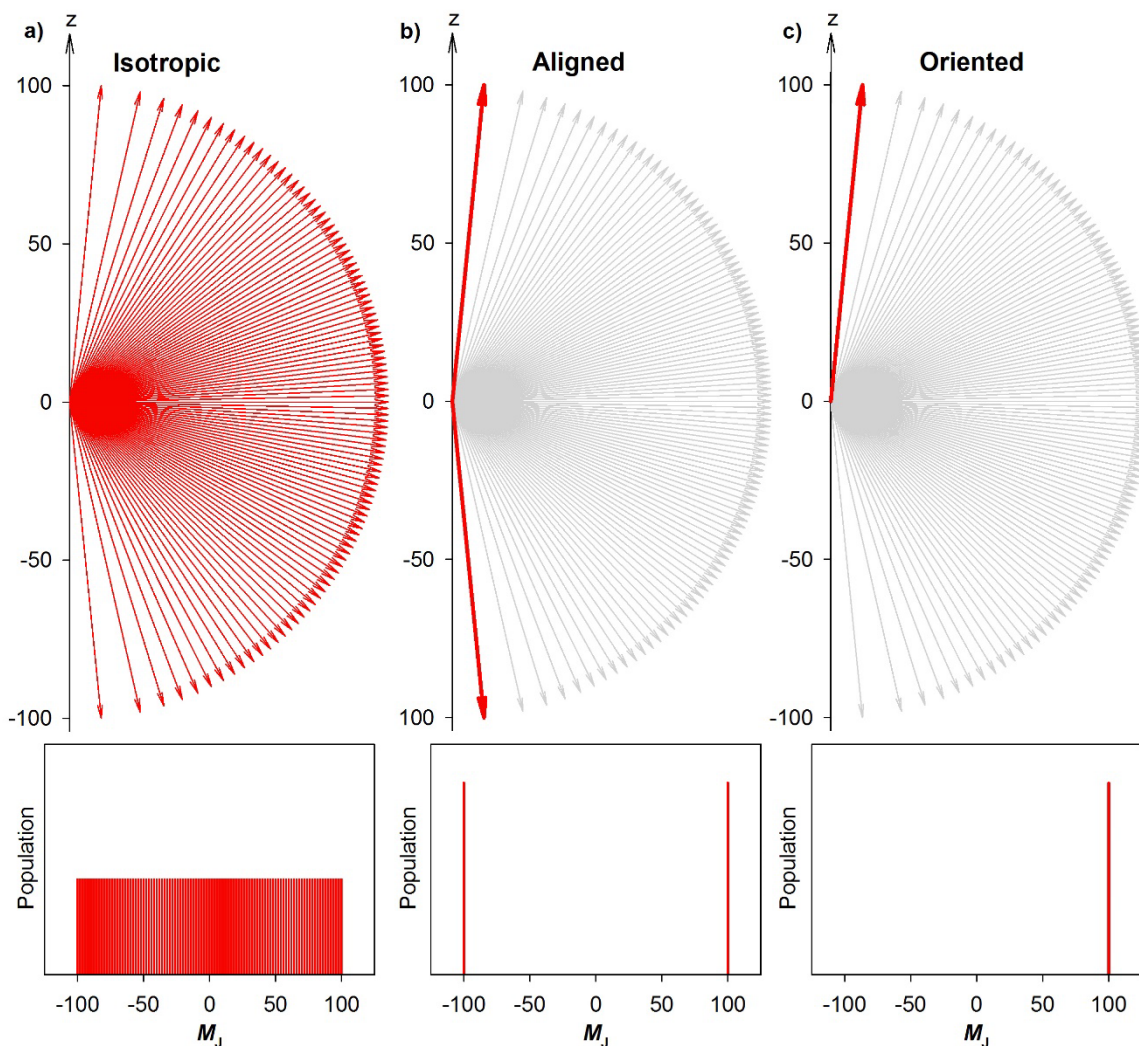
Figure 2.2 Distribution of angular momentum vectors in a sample that is (a) isotropic, (b) aligned, and (c) oriented. The lower panels show the ideal distributions of M_J values.

vector $\vec{J}_{OC}$ that is nearly parallel to the optical centrifuge propagation vector $\vec{k}_{OC}$ and the z-axis. Each molecule that is optically centrifuged rotates with the electric field of the OC in the xy-plane. Figure 2.3b shows an ensemble of CO_2 molecules with oriented angular momenta. In the limit of perfectly trapped molecules, each rotor has the same angular momentum projection quantum number M_J. In this way, the optical centrifuge generates
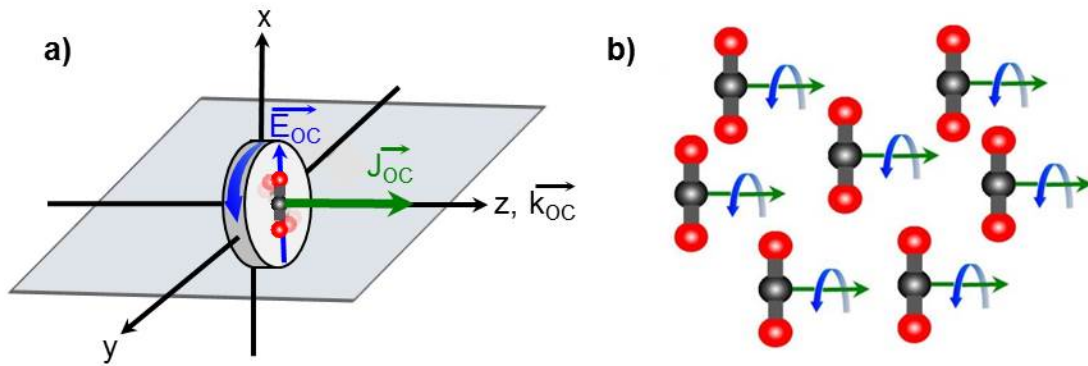
Figure 2.3 a) Geometry of optical centrifuge electric field ($\vec{E}_{OC}$) and propagation vector ($\vec{k}_{OC}$) along with the angular momentum ($\vec{J}_{OC}$) of the spinning molecule. b) Ensemble of spinning molecules in the optical centrifuge with oriented angular momenta.

an ensemble of molecules with oriented angular momentum and large amounts of rotational energy.

2.1.2 Construction of an Optical Centrifuge

The optical centrifuge pulse is generated from a custom-built, ultrafast Ti:sapphire laser system. The laser system has four main components: a Ti:sapphire oscillator, a regenerative amplifier, a custom pulse shaper, and a multipass amplifier.

The Ti:sapphire oscillator generates modelocked pulses of light centered around $\lambda_0 = 805$ nm. The gain medium of the oscillator is a Ti:sapphire crystal, which is pumped by 532 nm light generated from a frequency-doubled Nd:YVO$_4$ laser[68]. The Ti^{3+} ion is responsible for the laser action of the Ti:sapphire crystal. The ion absorbs in the 400-600 nm range and fluoresces at wavelengths above 600 nm[64]. Lasing is achieved when an integral number of half wavelengths fit between the cavity mirrors of the oscillator[68]. Many wavelengths can satisfy this condition simultaneously and these wavelengths constitute the longitudinal modes of the cavity. The simultaneously lasing modes

constructively and destructively interfere with one another. Mode-locking is achieved when the phase of the each of the modes is matched and held constant, generating narrow, high intensity pulses[68]. These pulses have a pulse width of less than 100 femtoseconds (fs) and an average power of several hundred mW[68].

The oscillator pulses are sent to a regenerative amplifier, where they are amplified via chirped pulse amplification (CPA). In this technique, the fs pulses are stretched in time by three orders of magnitude. Stretching is achieved by the use of reflection gratings. A reflection grating is a mirror with a repeating surface structure. As with a diffraction grating, the repeating structure affects the amplitude and phase of the incoming optical wave, causing interference in the outgoing wave. Light is reflected off the grating at discrete orders. The interference pattern depends upon the frequency of the incoming light and therefore the light is spread out spatially according to frequency. In the stretcher, the optics can be arranged such that the blue wavelengths travel a longer distance than the red wavelengths, thereby stretching the pulse width and inducing a positive chirp, wherein the wavelength of light shifts blue over the time of the pulse[69]. The distance between the grating and the retroreflector defines the amount of stretching. The chirped light serves as the seed for the regenerative amplifier. The regenerative amplifier consists of an optical cavity which contains a Ti:sapphire rod[69]. The rod is pumped by 527 nm light from a frequency-doubled Nd:YLF laser[69]. The optical alignment of the amplifier allows the pulse to complete many round trips of the optical cavity, resulting in an amplification of around 10^6 [69]. Typically in the CPA technique, the light would then be compressed with another grating pair; however, our experiment requires the longer (picosecond) chirped
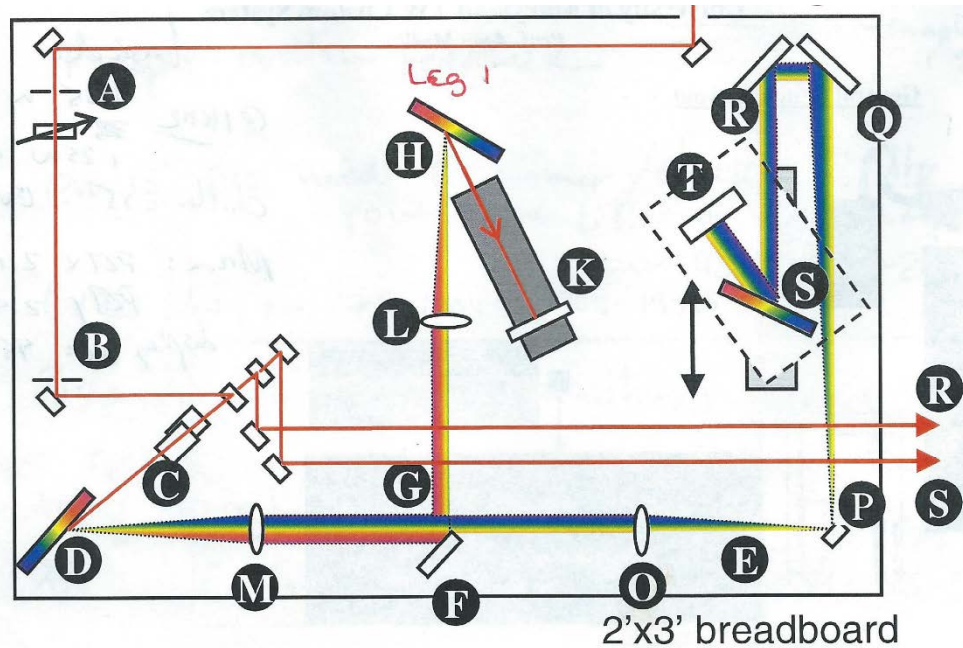
Figure 2.4 Optical layout of reverse chirp box used to generate the two oppositely chirped pulses of light.

pulses and so the compressor is by-passed. The regenerative amplifier is run at a repetition rate of 1 kHz and pulse picked to 10 Hz so that it can be further amplified by a frequency-doubled 10 Hz Nd:YAG laser.

The positively chirped picosecond amplified pulses from the regenerative amplifier are sent to a custom-built reverse chirp box to generate a pair of oppositely chirped pulses. A diagram of the optical layout of the reverse chirp box is shown in Figure 2.4. The positively chirped pulse of light is sent to reflection grating D and a mirror F is placed in the Fourier plane of the beam such that beam is split in half spectrally. One leg maintains the positive chirp created by the regenerative amplifier, while the other leg reverses the chirp of the second pulse. The distance between grating S of the reverse chirp leg and the focusing lens O (with focal length f) must be equal to $1f + 4$ times the distance used in the stretcher to achieve the positive chirp. This criterion ensures the positive chirp is exactly

23
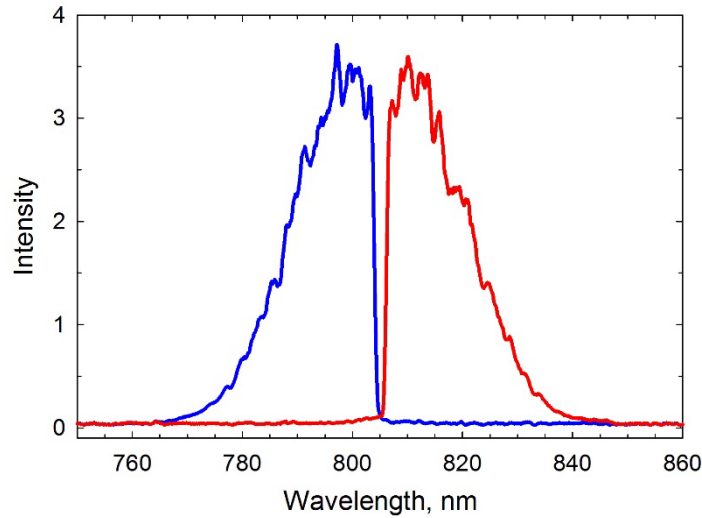
Figure 2.5 Spectra of the positive (blue) and negative (red) chirps from the optical centrifuge.

reversed. Retroreflectors in each leg pass the beam through the gratings so that the spatial distortion of the beam is reversed, while the temporal chirp is maintained. The gratings of each leg of the pulse shaper must be exactly parallel to one another to have no spatial chirp.

As stated in section 2.1.1, the time-dependent frequency difference between the two pulses defines the angular acceleration of the optical field. Figure 2.5 shows the spectra of the two oppositely chirped pulses of light. The full-width-at-half-maximum (FWHM) of the combined spectrum corresponds to a wavelength separation of 16 nm ($\Delta\omega = 7\times10^{13}$ Hz) between the two chirps. At this point the rotational frequency of the optical centrifuge is $\Omega = \Delta\omega/2 = 35$ THz. The rotational numbers given in Table 2.1 reflect this frequency and the spectral chirps shown in Figure 2.5.

The intensity of each chirped pulse is amplified by two orders of magnitude with a multipass amplifier (MPA). The MPA contains two Ti:sapphire rods that are 0.5" in diameter, which are pumped at 10 Hz by ~3 W of 532 nm light from a frequency-doubled

24

Nd:YAG laser. Both the positive and negative chirped pulses pass through a Ti:sapphire rod four times, resulting in a final energy of about 30 mJ per pulse in each leg.

Figure 2.6 is a diagram of the optical components of the optical centrifuge experiment. After exiting the MPA each chirped pulse has the same linear polarization. The negatively chirped pulse is sent to a delay line. The positively chirped pulse passes through a $\lambda/2$ waveplate, which rotates the pulse's polarization by 90°. The orthogonal polarizations of the two pulses permit the pair of beams to be overlapped spatially into a single beam with a polarizing beam cube (PBC). The beam containing the two pulses passes through a $\lambda/4$ waveplate and since the pulses have orthogonal polarizations, the $\lambda/4$ imparts opposite circular polarization to each pulse. Figure 2.7 shows a schematic of the polarization at each step after exiting the MPA. The combined pulse is sent to the sample cell with an energy of about 50 mJ per pulse.

For the optical fields of the two pulses to interfere in a manner producing the optical field described by equation 2.14, the two beams must be precisely overlapped in time and space. Cross-correlation is used to provide this precise overlap within a few picoseconds.
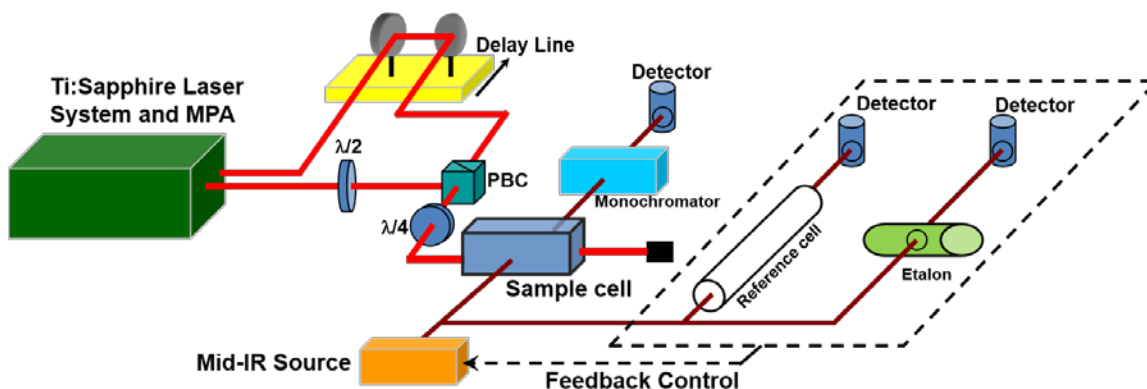
Figure 2.6 Experimental set-up of the optical centrifuge with a high resolution transient IR absorption spectrometer for detection. The labels refer to the multipass amplifier (MPA), polarizing beam cube (PBC), and the $\lambda/2$ and $\lambda/4$ waveplates.

Creating an Optical Centrifuge: Evolution of Optical Field Polarization
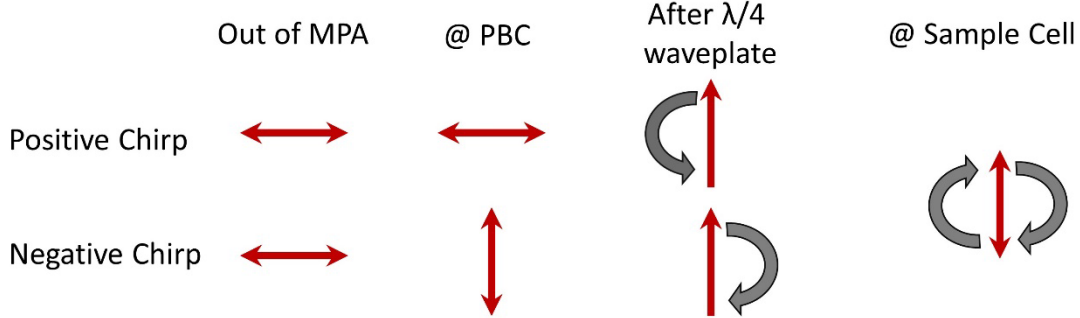
Figure 2.7 Evolution of the electric field polarization at each step used to generate an optical centrifuge. The headings refer to the multipass amplifier (MPA), polarizing beam cube (PBC), λ/4 waveplate and sample cell shown in Figure 2.6.

The technique is similar to the intensity autocorrelation used to measure pulse widths[70]. In this technique, a non-linear crystal is placed in the beam path to generate the sum frequency. Sum frequency generation (SFG) is a second order non-linear process in which high intensity light of frequencies ω_1 and ω_2 are combined to give light of frequency $\omega_1 + \omega_2$[71]. A spectrometer placed behind the crystal collects the SFG signal[64]. In our set-up, a BaB_2O_4 (BBO) crystal is placed in the optical centrifuge beam path to generate 400 nm light[64]. The 400 nm light is collected on an Ocean Optics USB 2000 spectrometer. The mechanical delay stage shown in Figure 2.6 is used to adjust the time delay between the two 800 nm pulses. The SFG signal is maximized when a pulse from each leg arrives at the crystal at the same time.

The combined optical centrifuge pulse is focused into a sample cell containing the gas under investigation. Two different lenses have been used in the optical centrifuge studies in this thesis. A 50 cm focal length lens focuses the beam to a beam waist $\omega_0 = 26$ µm with an intensity of 4.2×10^{13} W/cm^2. The beam waist corresponds to the radius of the beam at the focal point. A 100 cm focal length lens focuses the beam to a beam waist $\omega_0 =$

51 μm with an intensity of 1.1×10^{13} W/cm^2. The high intensities increase the magnitude of the interaction energy between the optical field and the molecules as described by equation 2.8.

2.1.3 A Note on Timing

Crucial to the operation of the optical centrifuge laser system is a system of precisely controlled fast electronics, which controls the timing of the various components. This system ensures that the proper pulse is selected and maximum amplification is achieved at each step. Figure 2.8 shows the electronic scheme of the various timing components for the optical centrifuge laser system. The master clock is a 1 kHz transistor-to-transistor logic (TTL) radio frequency signal from the regenerative amplifier Nd:YLF pump laser (Evolution 20)[72]. A synchronization and delay generator (SDG) serves as a hub to synchronize the timing of various electrical components[72]. The Ti:sapphire oscillator (Micra 5, Coherent) produces ultrashort pulses at a repetition rate of 80 MHz. The 80 MHz signal is sent to the SDG and synchronized with the 1 kHz signal from the pump laser.

The SDG has 4 outputs. One output is fixed in time, while the other three outputs have adjustable delays[72]. The SDG also has an adjustable circuit that allows the outputs to be operated at a repetition rate below the master input[72]. In this case, the circuit is set
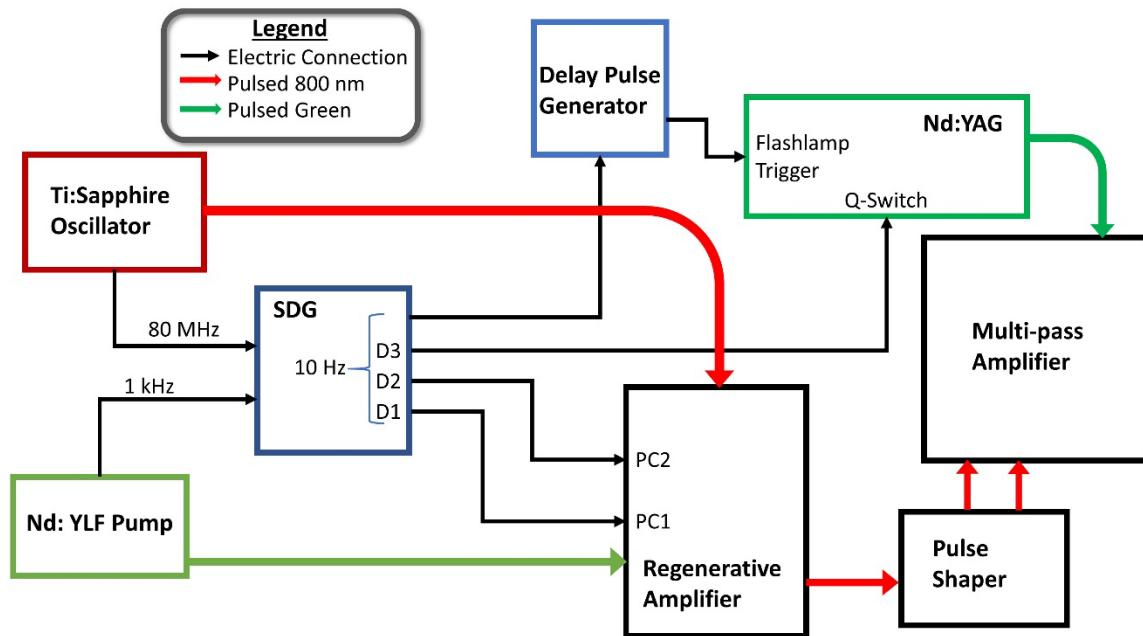
Figure 2.8 Electric connection diagram of system controlling the timing of the optical centrifuge pulsed laser system.

such that the 1 kHz input is divided by 100 to enable operation at 10 Hz. Outputs for delay 1 (D1) and 2 (D2) trigger Pockels cells (PC1 and PC2) in the regenerative amplifier[72]. Pockels cells are electro-optic devices that act as quarter waveplates when a large electric field is applied[64]. These devices use polarization to act as an optical gate, permitting a selected pulse of 800 nm light from the stretcher into the amplification cavity (PC1). The amplified is then released from the cavity by PC2[72]. Delay 3 (D3) triggers the Q-switch of the Nd:YAG. This delay is set such that the YAG pulse arrives at the MPA Ti:sapphire crystals 20 ns before the 800 nm pulse in order to achieve maximum amplification. The fixed output of the SDG is sent to an external delay generator which triggers the flashlamps for the *next* YAG pulse. This pulse is set at a time such that maximum power out of the YAG is achieved. This control scheme produces the 10 Hz optical centrifuge pulse train.

2.2 High Resolution Transient IR Absorption Spectroscopy

2.2.1 Principles of Transient IR Spectroscopy

The studies presented here used high resolution transient IR absorption spectroscopy to investigate the collision dynamics of molecules after a gas sample was excited by the optical centrifuge. Individual rotational states of molecules was probed by tuning high resolution light to specific rovibrational transitions. Detailed information about rovibrational transitions of many atmospherically relevant molecules is given in the HITRAN database[73]. The rovibrational spectral lines of carbon dioxide and carbon monoxide that are studied in this thesis are shown in Figure 2.9.

The basic energy scheme for studying centrifuged molecules is shown in Figure 2.10. Molecules in the sample cell initially start in the ground vibrationless state with a
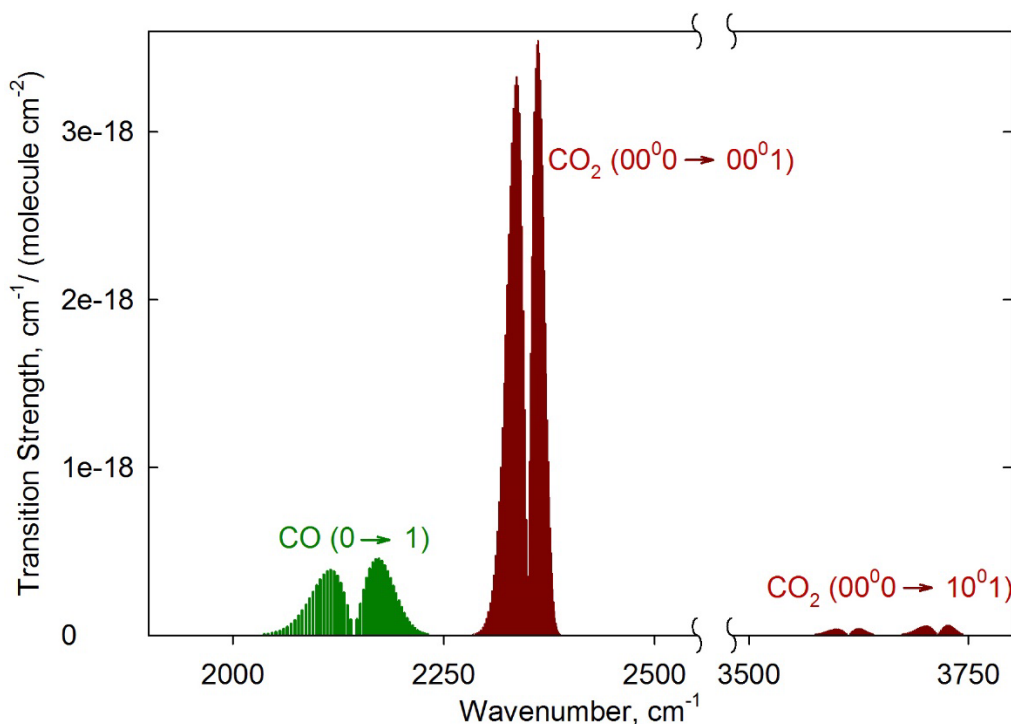
Figure 2.9 IR transitions for CO and CO_2 obtained from the HITRAN database.
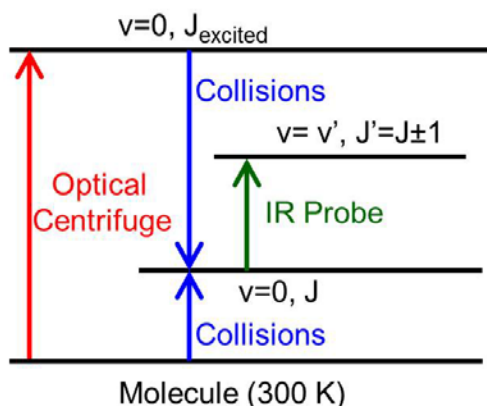
Figure 2.10 Energy scheme of molecules being investigated in the optical centrifuge.

300 K Boltzmann distribution of rotational states. The optical centrifuge excites a portion of the molecules to a narrow distribution of high rotational states. A high resolution, continuous wave (CW) IR light source is used to probe individual rotational states by inducing a rovibrational transition. Time-resolved changes in the populations of individual quantum states reveal how energy is transferred in the excited sample.

Linear absorption of IR light from a specific state is directly related to the population in that state as described by the Beer-Lambert law[74]. The absorption coefficient of the molecule corresponds to a disk of area σ and represents the effective area seen by a photon of frequency υ. The cross section $\sigma(\upsilon)$ is frequency dependent. Light with intensity $I(z)$ is incident upon a sample that contains absorbing particles with density N in an infinitesimal volume with area Q and length dz. The light intensity before interacting with the sample is I_0. The light absorbed by infinitesimal volume is dI and the intensity of light transmitted through the sample of length L is I_t. The total absorbing cross section is equal to $\sigma N Q dz$. The fraction of light absorbed, dI/I, is equal to the ratio of the total absorbing cross section to the area Q:

$$\frac{dI}{I} = -\frac{\sigma NQ dz}{Q}. \tag{2.21}$$

Simplifying and integrating both sides from $z = 0$ to $z = L$:

$$\int_{I(0)}^{I(L)} \frac{dI}{I(z)} = -\int_{0}^{L} \sigma N dz$$

$$\ln\frac{I_t}{I_0} = -\sigma NL$$

$$\frac{I_t}{I_0} = e^{-\sigma NL}. \tag{2.22}$$

Equation 2.22 is the Beer-Lambert law and shows how absorption is related to the population of absorbing molecules[74]. In the gas phase, this law is also commonly written in terms of pressure p and the total absorption strength α:

$$\frac{I_t}{I_0} = e^{-\alpha pL}. \tag{2.23}$$

The absorption coefficient α has units of cm^{-1} Torr^{-1} and is defined as

$$\alpha = Sf(0)N. \tag{2.24}$$

The absorption strength S is the cross section integrated over all frequencies:

$$S = \int_{0}^{\infty} \sigma(v) dv. \tag{2.25}$$

$f(0)$ is a line-shape factor and that describes the broadening of the transition

$$f(0) = \frac{2}{\Delta v}\sqrt{\frac{\ln 2}{\pi}}. \tag{2.26}$$

In the above expression Δv is the full-width-at-half-max (FWHM) of the transition.

The HITRAN database lists the S value of each rovibrational transition, which includes contributions from the oscillator strength S_0, the fraction of population f_J in rotational state J, and the fraction of population f_v in vibrational state v:

$$S = S_0 \, f_J \, f_v. \tag{2.27}$$

The fractional populations are determined by the Boltzmann distribution at temperature T for a degree of freedom with quantum number n and energy E_n:

$$f_n = \frac{1}{Z} g_n e^{-\left(\frac{E_n}{k_B T}\right)}. \tag{2.28}$$

In equation 2.28 Z is the partition function, g_n is a degeneracy factor, and k_B is Boltzmann's constant. The values of S_0 are used along with a line shape to relate transient IR absorption intensities to number densities of molecules.

2.2.2 Components of the IR Spectrometer

The components of the high resolution transient IR absorption spectrometer are shown in Figure 2.6. In this section, a description of the four major components of the spectrometer are described: the IR sources, the IR detectors, the frequency stabilization via active feedback, and the sample cell.

IR Sources

Three different IR light sources were used to study the dynamics of molecules excited by the optical centrifuge. Each IR source provides high-resolution, tunable, single-mode light. A lead salt diode laser from Laser Components operates at $\lambda = 4.3$ μm and has a tuning range of 200 cm^{-1}. The diode laser has a spectral resolution of $\Delta v_{IR} < 3 \times 10^{-4}$ cm^{-1} and an output power of 100—200 μW. A quantum cascade laser (QCL) from

Table 2.2 Properties of the IR sources used in the high resolution spectrometer.

IR Source	λ range	Resolution (cm^{-1})	Power
Pb-Salt Diode	4.3 µm	0.0003	100 µW
QCL	4.2 - 4.5 µm	0.0003	60 mW
OPO	2.5 - 3.2 µm	0.00003	1 W

Daylight Solutions operates between $\lambda = 4.2$ and 4.5 µm. The QCL has a spectral resolution of $\Delta v_{IR} < 3 \times 10^{-4}$ cm^{-1} and an output power of ~ 60 mW. The third source is a mid-IR optical parametric oscillator (OPO) by Lockheed Martin Aculight Corp. that provides IR light between $\lambda = 2.5$ and 3.2 µm. The IR light from the OPO has a resolution of $\Delta v_{IR} < 3 \times 10^{-5}$ cm^{-1} and output power of approximately 1 W. The high quality, linearly polarized light provided by the QCL and OPO makes these two IR sources ideal tools to use in polarization-dependent studies. The light from the diode is also linearly polarized, but the poorer beam quality introduces some error in polarization-dependent measurements. Table 2.2 provides a summary of the important properties of the IR sources.

Detectors

Transient changes in IR absorption were detected using liquid-nitrogen-cooled, low noise, solid-state photodiodes. These photovoltaic devices generate a current proportional to the number of photons absorbed by the active area of the detector. Like most solid-state detectors, these devices contain a junction between a p-type semiconductor material and an n-type semiconductor material. At this p-n junction holes diffuse toward the n region and electrons diffuse toward the p region. This transfer of charge creates an electric field

between the two regions, which halts any further diffusion and leaves a space without mobile charge carriers. The resulting electric field creates a potential difference across the region, which is called the depletion region. Therefore, if a charge is liberated in the depletion region by an incoming source of radiation, the charge will be swept away by the electric field and create a current. The energy required to liberate an electron depends on the material. Some common IR semiconductor materials are HgCdTe, which has a band gap energy of about 0.48 eV (2.55 μm), and InSb, which has a band gap energy of about 0.23 eV (5.4 μm)[75]. In general, both IR radiation and thermal energy can excite electrons in these types of detectors. Therefore, to avoid interference from thermal excitation, the detectors must be cooled to temperatures well below room temperature. In the studies reported here the detectors were cooled with liquid nitrogen to 77 K[76].

Indium antimonide (InSb) detectors from Judson Technologies, which have an active area of 0.2 mm^2 and a field of view of 60° were used for data collection. Detectors with smaller active areas have lower noise[76]. The 10-90 response time of the detector is defined as the time it takes for the detector to go from 10% to 90% of the final signal intensity. The response time of the detector and the gain are inversely proportional[76]. Measurements were obtained with detectors that have a response time better than 100 ns and a gain of 60,000. Voltage response transients were averaged for about 400 shots and collected using a digital oscilloscope.

Active Feedback

The IR light used for transient detection was stabilized by active feedback using a lock-in amplifier, which "locks" to a desired signal at a specific modulation frequency.

Frequency stabilization was achieved in two ways: locking to a rovibrational peak in a reference cell or locking to a fringe generated in a tunable etalon. In the first case, the reference cell contained a sample of the gas under investigation. The cell length (~3 m) and gas pressure were adjusted so that rovibrational transitions of interest could be detected. Transient absorption at line center of the IR transition was measured by locking the IR frequency to a known spectral peak in a reference gas cell.

For the second type of frequency stabilization, a Fabry-Perot etalon was used for controlling the IR frequency during Doppler profile scans. An etalon is an optical cavity composed of two parallel, partially transmissive mirrors. Light enters the cavity and interferes with itself, producing an output signal of evenly spaced maxima. The maxima are separated by a frequency defined by the free spectral range (FSR) of the etalon, which is given by

$$\text{FSR} = \frac{c}{2L},\tag{2.29}$$

where c is the speed of light and L is distance between the etalon mirrors[64]. One of the mirrors in the etalon is mounted on a piezoelectric base. A high-voltage amplifier that is controlled via LabVIEW applies a voltage to the piezoelectric base, which changes the length of the cavity. In this way, the fringe can be tuned across a rovibrational line in small frequency steps. By locking the IR source to an etalon fringe, the frequency of the light can be precisely stepped across the transition in steps as small as 5×10^{-4} cm^{-1}. In comparison, the FWHM of CO and CO_2 line profiles at 300 K are about 4×10^{-3} cm^{-1}.

Two sample cell configurations were used in this work. All sample cells were made of Pyrex glass with fused silica antireflective coated windows to the allow the optical centrifuge light to pass into the cell with minimal reflective losses. A pair of calcium fluoride windows allowed the IR to pass through the cell, crossing the OC beam and probing the optical centrifuge dynamics. The IR beam propagated at 90° with respect to the OC beam. Figure 2.11 shows the single pass configuration. In the single pass configuration, the IR light was focused onto the OC beam waist with a 10 cm focal length lens. The IR beam waist at the focal point was $\omega_0 = 52$ μm. A tunable waveplate before the sample cell was used to flip the IR polarization from horizontal to vertical. The waveplate in combination with the 90° crossing angle enabled the IR light to probe the spatial orientation of the optically centrifuged molecules.

To improve signal-to-noise levels, a second cell with a multipass IR configuration was constructed. This sample cell used a 50 cm focal length lens ($\omega_0 = 230$ μm) to focus
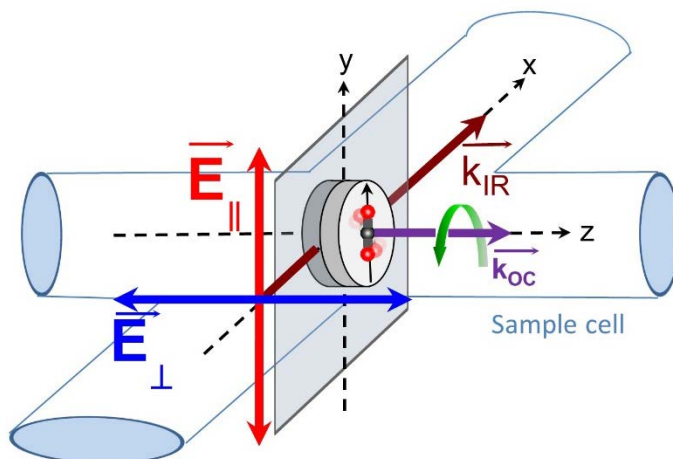
Figure 2.11 Single pass configuration or IR probe beam, highlighting how changing the polarization probes molecular orientation.
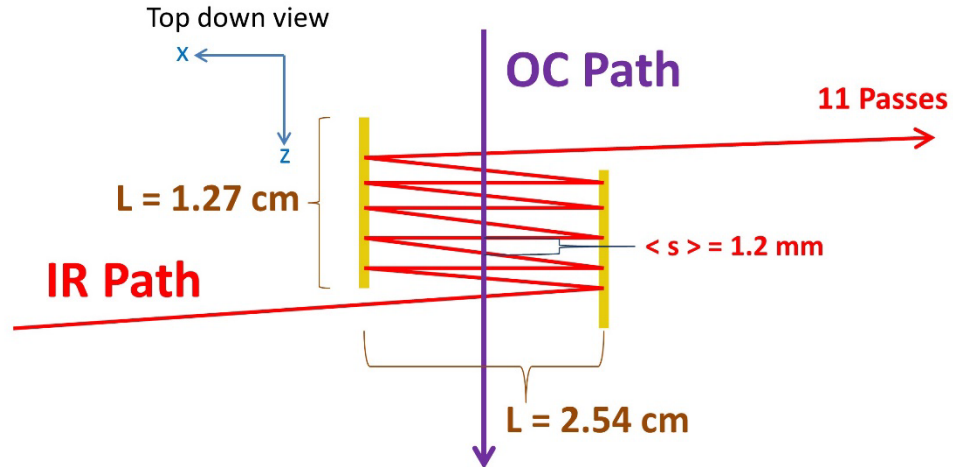
Figure 2.12 Top-down view of the multi-pass IR configuration.

the IR beam between a pair of parallel gold mirrors, crossing the OC beam 11 times. A top-down schematic of this sample cell configuration is shown in Figure 2.12. The angle of the IR beam propagation was nearly orthogonal to the propagation of the OC beam. The distance between each point the IR beam crosses the OC was $< s >= 1.2$ mm.

Figure 2.13 shows a side view of the single and multipass configurations and highlights the difference in overlap of the OC beam in the two configurations. In the single pass configuration, the path length that IR and OC overlap was 50 μm and the overlap volume was about 2×10^5 μm^3. In the multipass configuration, the path length of IR and OC overlap was about 520 μm and the overlap volume was increased to 970×10^5 μm^3.
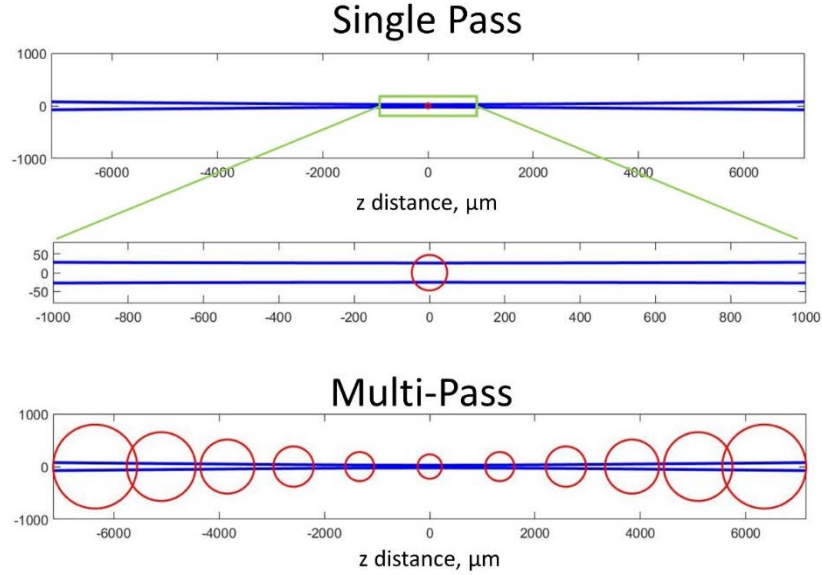
Figure 2.13 A side view of the single and multipass IR configurations. The OC beam is shown in blue and the IR beam is shown in red.

2.2.3 Transient Absorption

Transient changes in absorption were measured with a digital oscilloscope (Tektronix) and collected with a computer via a LabVIEW interface. The oscilloscope was triggered with a photodiode that detected the optical centrifuge pulse and defined $t = 0$ on the oscilloscope. The signal on the IR detector was collected on the oscilloscope with an AC coupled channel and a DC-coupled channel. The AC channel represented ΔI, the change in IR intensity, while the DC channel represented the transmitted intensity I_t. The initial, pre-trigger intensity on the DC channel was I_0. Using these definitions, the fractional change in absorption, $\Delta I / I_0$, was

$$\frac{\Delta I}{I_0}(t) = \frac{AC/DC}{1 + AC/DC}.$$

(2.30)

The fractional changes in absorption were used to measure state-specific translational energy distributions and populations of molecules following the optical centrifuge pulse.

38

2.2.4 Doppler-Broadened Line Profiles

Information on the translational energy of molecules in individual rotational states was obtained by measuring Doppler-broadened line profiles. In these measurements, the transient fractional changes in absorption are collected in evenly spaced frequency steps across an individual IR transition. The Doppler-broadened profiles are Gaussian shaped. The Gaussian shape and translational energy information come from a Maxwell-Boltzmann velocity distribution. The derivation is described here.

The general form of the Boltzmann probability distribution is

$$P = Ae^{-\left(\frac{E}{k_B T}\right)}, \tag{2.31}$$

where A is a normalization constant, E is energy, k_B is Boltzmann's constant, and T is temperature. Molecules of mass m travelling in the x direction with a velocity v_x have kinetic energy $E = \frac{1}{2}mv_x^2$. The Maxwell-Boltzmann velocity distribution in one direction with the proper normalization is

$$P(v_x)dv_x = \left(\frac{m}{2\pi k_B T}\right)^{\frac{1}{2}} e^{-\left(\frac{mv_x^2}{2k_B T}\right)}dv_x. \tag{2.32}$$

For an isotropic sample, the probability distribution in all directions is just the product of the distribution in the x, y, and z directions;

$$P(v_x)dv_x P(v_y)dv_y P(v_z)dv_z = \left(\frac{m}{2\pi k_B T}\right)^{\frac{3}{2}} e^{-\left(\frac{mv^2}{2k_B T}\right)}dv_x dv_y dv_z, \tag{2.33}$$

where we have used $v^2 = v_x^2 + v_y^2 + v_z^2$. By changing to spherical coordinates and integrating over all angles, the Maxwell-Boltzmann distribution becomes

$$P(\mathrm{v})d\mathrm{v} = 4\pi \left(\frac{m}{2\pi k_B T}\right)^{\frac{3}{2}} \mathrm{v}^2 e^{-\left(\frac{m\mathrm{v}^2}{2k_B T}\right)} d\mathrm{v}. \tag{2.34}$$

A moving molecule causes a shift in absorption frequency based on the Doppler effect. The frequency v of light propogating along x that is "observed" by the particle is related to the velocity v of the particle:

$$v = v_0 \left(1 \pm \frac{\mathrm{v}_x}{c}\right). \tag{2.35}$$

Rearranging the above expression:

$$\pm \mathrm{v}_x = \frac{c}{v_0}(v - v_0). \tag{2.36}$$

Using equation 2.36 to change variables in equation 2.34 yields a Doppler-broadened line profile

$$P(v)dv = \left(\frac{m}{2\pi k_B T}\right)^{\frac{1}{2}} \left(\frac{c}{v_0}\right) e^{-\frac{mc^2(v-v_0)^2}{2k_B T v_0^2}} dv. \tag{2.37}$$

The intensity is proportional to $P(v)$ and the line shape is a Gaussian function centered at v_0. The FWHM Δv of this function is

$$\Delta v = \sqrt{\frac{8\ln 2\, k_B T}{mc^2}}\, v_0. \tag{2.38}$$

The translational temperature of the molecules determines the width of the Gaussian profile. By fitting the measured transient IR line profiles to Gaussian functions, one can determine the translational temperature of the molecules in that state by the following expression:

$$T = \frac{mc^2}{8\ln(2)\, k_B} \left(\frac{\Delta v}{v_0}\right)^2. \tag{2.39}$$

Transient IR absorption line profile data were fit to Gaussian functions of the form:

$$y = ae^{-0.5\left(\frac{x-x_0}{b}\right)^2}, \tag{2.40}$$

where a and b are adjustable fitting parameters. The FWHM Δx of the Gaussian function is $\Delta x = b\sqrt{8\ln 2}$, and is used in equation 2.39 to determine the translational temperature. The total change in population of molecules in an individual state is determined by the area under the Doppler-broadened line profile. The area of a Gaussian function is equal to

$$\int_{-\infty}^{\infty} ae^{-0.5\left(\frac{x-x_0}{b}\right)^2} dx = ab\sqrt{2\pi}. \tag{2.41}$$

This expression is a measure of a profile's intensity and broadened line shape. Using the integrated area under the Gaussian profile and the oscillator strength S_0 defined in Section 2.2.1, we determine the relative population in the individual rotational states.

2.3 Gas Kinetics

2.3.1 Gas Kinetic Collisions

This thesis describes research on gas-phase collisions. The gas kinetic model provides a useful description of gas-phase collisions and a framework from which to discuss the results. The time between collisions is an important issue to consider when studying gas-phase collisions and the gas kinetic model provides a reasonable estimation of this parameter. Here, some key concepts are presented[77].

The gas kinetic model assumes that a gas consists of molecules of mass m undergoing random motion, that the size of the molecules is much smaller than the average distance between molecules, and that molecules interact through brief, elastic collisions[77].

One key result of the theory is the Maxwell-Boltzmann speed distribution given by equation 2.34. From this distribution, we can calculate the average velocity $\bar{v}$ of molecules in a sample by integrating over all speeds:

$$\bar{v} = \int_0^\infty vP(v)dv = 4\pi \left(\frac{m}{2\pi k_B T}\right)^{\frac{3}{2}} \int_0^\infty v^3 e^{-\left(\frac{mv^2}{2k_B T}\right)} dv \tag{2.42}$$

$$\bar{v} = \left(\frac{8k_B T}{\pi m}\right)^{\frac{1}{2}}. \tag{2.43}$$

If we are concerned with the relative speed of the molecules then we replace the mass by the reduced mass, μ;

$$\bar{v}_{rel} = \left(\frac{8k_B T}{\pi \mu}\right)^{\frac{1}{2}}. \tag{2.44}$$

The average time between collisions in a pure sample is determined as follows. When an idealized spherical molecule travels through a sample, it maps out a collisional cylinder with a cross sectional area, $\sigma = \pi d^2$, where d is the diameter of the molecule[77]. The length of the cylinder is equal to the distance between collisions, which is known as the mean free path λ;

$$\lambda = \bar{v}_{rel}\Delta t, \tag{2.45}$$

where Δt is the time between collisions[77]. One molecule is in this cylinder and therefore the number density is $1/\sigma\lambda$. The number density in the collision cylinder is equal to the bulk number density from the ideal gas law $N/V = p/k_B T$, where p is pressure. Equating these two number densities and solving for Δt yields

$$\Delta t = \frac{k_B T}{\sigma \bar{v}_{rel} p}. \tag{2.46}$$

42

Note that Δt and p are inversely proportional. Table 2.3 lists the average time between collisions for 10 Torr samples of CO and CO_2 at 300 K.

Table 2.3 Time between collisions for CO and CO_2 at 300 K and 10 Torr.

Molecule	Mass (g/mol)	σ (nm^2)	$\bar{v}_{rel}$ (m/s)	Δt (ns) @ 300 K & 10 Torr
CO	28	0.44	674	10.4
CO_2	44	0.52	537	11.1

2.3.2 Diffusion

Another important property of gas-phase molecules is diffusion. Diffusion may play a significant role in the relaxation of molecules excited by the optical centrifuge and can impact transient absorption measurements as molecules can diffuse into and out of the excitation and probe volumes. The 1-D diffusion equation relates the time rate of change in concentration to the spatial change in concentration;

$$\frac{\partial c}{\partial t} = D \frac{\partial^2 c}{\partial x^2}, \tag{2.47}$$

where D is the diffusion coefficient[77]. The solution to this equation, assuming, the concentration is isotropic in the y-z plane is

$$c(x,t) = \frac{N_0}{A\sqrt{\pi D t}} e^{-x^2/4Dt}, \tag{2.48}$$

where N_0 is the total number of particles present and A is the area in the y-z plane. It is possible to develop a probability density function by dividing the number of particles in a slice of area A and thickness dx by the total number of particles;

$$\frac{cA dx}{N_0} = \frac{1}{\sqrt{\pi D t}} e^{-x^2/4Dt} dx. \tag{2.49}$$

43

To calculate the spread of particles from a central origin we calculate the root-mean-square displacement, $\langle x^2 \rangle^{1/2}$, using the probability density in equation 2.49:

$$\langle x^2 \rangle = \frac{1}{\sqrt{\pi D t}} \int_{-\infty}^{\infty} x^2 e^{-x^2/4Dt} dx. \tag{2.50}$$

The solution to this integral is

$$\langle x^2 \rangle = 2Dt. \tag{2.51}$$

Taking the square root of both sides

$$\langle x^2 \rangle^{1/2} = (2Dt)^{1/2}. \tag{2.52}$$

This equation describes how far molecules spread out spatially in a time t given their diffusion constant D. The diffusion constant can be estimated from the gas kinetic model as

$$D = \frac{1}{3} \lambda \bar{v}. \tag{2.53}$$

Table 2.4 shows the diffusion constants, mean free path, and root-mean-square displacement in 1 µs at 300 K for 10 Torr samples of CO and CO_2. As the single pass IR configuration has a beam waist of 48 µm, diffusion can play a role in the dynamics observed in the single pass configuration. In the multipass configuration, the beam waist is increased to 230 µm, thereby reducing the role of diffusion in measurements at 1 µs.

Table 2.4 Mean free path, λ, diffusion constant, D, and root-mean-square displacement in 1 µs at 300 K and 10 Torr of CO and CO_2.

Molecule	λ (µm)	D (m² s⁻¹)	$\langle x^2 \rangle^{1/2}$ (µm)
CO	4.9	7.85E-04	40
CO_2	4.2	5.35E-04	33

Chapter 3: State-Specific Collision Dynamics of Molecular Super Rotors with Oriented Angular Momentum

Adapted from: M. J. Murray, H. M. Ogden, C. Toro, Q. N. Liu, D. A. Burns, M. H. Alexander, A. S. Mullin, State-Specific Collision Dynamics of Molecular Super Rotors with Oriented Angular Momentum. *J. Phys. Chem. A* **2015**, *119*, 12471-12479.

3.1 Introduction

The dynamics of non-reactive collisions are affected by the translational, vibrational, and rotational degrees of freedom, leading to a rich variety of observed behaviors[38, 44, 78-82]. Because rotational energy states are relatively closely spaced (compared to vibrational and electronic energy states), J-changing collisions are common in molecular samples, with many collision systems exhibiting a propensity for small changes in rotational quantum numbers[41, 43, 83, 84]. Most studies have focused on J-changing collisions within a thermal distribution of states. Here, we investigate the rotationally inelastic collisions of molecules in ultra-high rotational states that are initially prepared with a well-defined plane of rotation and a uniform direction of rotation using an optical centrifuge.

With the advancement of non-resonant laser schemes, new tools are available for controlling the orientation of rotational motion in the lab frame[14, 16, 26, 29, 31, 51]. Kitano *et. al.* used a pair of cross-polarized pulses of light to achieve non-adiabatic angular momentum orientation of benzene molecules in the $J_K = 0_0$, 1_0, 1_1, 2_2, and 3_3 states[16]. In another approach, oppositely-chirped pulses of light were used by Ivanov, Corkum, and

5

45

coworkers to create an optical centrifuge, in which molecules in extreme rotational states, termed super rotors[15], were prepared by an angularly accelerating optical field[14, 26]. They used the optical centrifuge to excite Cl_2 molecules adiabatically to states near J~420, from which dissociation was detected. A key feature of both of these approaches is that the molecules have a unidirectional sense of rotation, so that the ensemble of rotors has oriented angular momenta.

Molecular super rotors exhibit a number of interesting collisional properties. There is evidence that super rotor angular momentum orientation is meta-stable with respect to collisions[50, 52]. It has also been suggested that macroscopic gas vortices may result from the super rotors' extreme angular momenta[35].

In the work reported here, we have used a high power optical centrifuge in conjunction with a high resolution transient IR absorption spectrometer to investigate the time-evolution of the translational and rotational energy profiles of CO_2 super rotors. Previous work from our group has focused on CO_2 molecules in the range from J=60 to J=80 and has shown that transient absorption signals are a result of collision-induced relaxation of the centrifuge–excited molecules[29]. Recent studies have shown that the spatially oriented nature of the molecules prepared by the optical centrifuge is preserved after the molecules have gone through many J-changing collisions[30]. This chapter presents a set of experiments studying the transient populations and translational energies of CO_2 in a number of rotational states ranging from J=0 to 100 in order to provide a broader picture of the collisional energy transfer dynamics of super rotors.

3.2 Experimental Details

The setup of the optical centrifuge high resolution transient IR absorption spectrometer has been described in Chapter 2. These experiments were performed using the single pass IR detection. Based on the spectral chirp shown in Figure 2.5, the optical centrifuge has a maximum rotational frequency of 32-35 THz. For CO_2 this rotational frequency corresponds to rotational energy $E_{rot} = 18,200$ cm^{-1} and an angular momentum quantum number of J~220.

Population changes for individual rotational states were measured following the centrifuge pulse using high resolution transient IR absorption. The CO_2 samples had a pressure of 5 -10 Torr (99.99%, Matheson Tri-gas). Two IR probe sources were used depending on the rotational state under investigation. A quantum cascade laser (QCL) from Daylight Solutions operating between λ=4.2 and 4.5 μm was used to probe the J=76 and 100 states with the fundamental CO_2 ($00^00 \rightarrow 00^01$) transition. The second IR source is a mid-IR optical parametric oscillator (OPO) by Lockheed Martin Aculight Corp. with output between λ=2.5 and 3.2 μm. The J=0, 36, and 54 states of CO_2 were probed using combination band ($00^00 \rightarrow 10^01$) transitions. The absorption strength of the combination band is ~60 times weaker than the fundamental, thereby minimizing interference from background CO_2 absorption[73]. In each case, only a small fraction of the IR power was used to avoid saturating the probe transitions.

The experiments described here were performed with the IR and optical centrifuge (OC) beams crossing at 90º, as shown in Figure 2.11. The optical centrifuge beam propagates along the z-axis and prepares molecules with an angular momentum vector $\vec{J}_{OC}$

that is nearly parallel to the optical centrifuge propagation vector $\vec{k}_{OC}$ and the z-axis. Individual CO_2 molecules that are optically centrifuged map out a rotating disk that spins with the electric field of the centrifuge pulse, $\vec{E}_{OC}$. The ensemble of molecules has a unidirectional sense of rotation, corresponding to oriented angular momentum vectors. For the measurements reported here, the IR beam was polarized along the z-axis, i.e. perpendicular to plane defined by the rotating disk of centrifuged molecules.

Five CO_2 states were investigated in this study: J=0, 36, 54, 76, and 100. Experimental conditions were adjusted based on signal levels of each state. The optical centrifuge was focused down to a beam waist ω_0= 25 μm in all sets of experiments, except for the J=100 state experiments, in which the beam waist was ω_0= 51 μm. Measurements of the J=0, 36, and 54 states used the OPO and R branch transitions ($\Delta J = + 1$) of the combination band ($00^00 \rightarrow 10^01$). The J=76 and J=100 states were measured using the QCL with P branch transitions ($\Delta J = - 1$) of the fundamental ($00^00 \rightarrow 00^01$) band. Light from the OPO and QCL was focused with a 10 cm lens to a beam waist ω_0= 50 μm. For the J=0, 54, and 76 states, the pressure was maintained at 10 Torr. For J=100, the pressure was 7.5 Torr. For J=36, the pressure was lowered to 5 Torr to reduce background absorption. The average time between collisions for these studies was 10 ns for 10 Torr, 15 ns for 7.5 Torr and 20 ns for 5 Torr, based on gas-kinetic collision frequencies. In order to compare transient signals for different measurements on a common scale, time t is converted to average number of collisions N using the relationship $N = t \cdot k$, where k is the gas-kinetic collision frequency. For CO_2 at 300 K: $k = 1.0 \times 10^8$ s^{-1} at 10 Torr; $k = 6.7 \times 10^7$ s^{-1} at 7.5 Torr; and $k = 5.0 \times 10^7$ s^{-1} at 5 Torr. Transient absorption changes were

detected with a liquid-nitrogen-cooled InSb photodiode. Wavelength modulation was used to lock the IR frequency to the fringe of a scanning confocal etalon, thereby stabilizing the IR frequency during transient measurements. Transient line profiles were measured by collecting transient absorption at a series of closely spaced, discrete IR frequency steps (~ 0.001 cm^{-1}) across individual ro-vibrational transitions. Most of the line width is due to Doppler broadening; contributions from pressure broadening are assessed in the data fitting.

3.3 Results and Discussion

The trapping efficiency of the optical centrifuge depends on the intensity of the optical pulse and the chirp rate. As discussed above, the rotational frequency of the optical centrifuge corresponds to a CO_2 rotational state near J=220 state. If the intensity profile of the pulse were uniform, one would expect the rotors to have a narrow distribution of J states. However, because the intensity profile drops off as the wavelength detunes from λ_0, it is likely that super rotors are prepared in a distribution of states with J < 220. Milner and coworkers have shown that cutting the spectral extent of the chirp can lead to greater rotational coherences in the excited molecules and a narrower distribution of excited states[52].

3.3.1 Dynamical Studies

Line-center transient IR absorption signals for CO_2 rotational states J=100, 76, 54, 36, and 0 are shown in Figure 3.1. The detector response time is shown as a green dashed line in Figure 3.1a and 3.1e. The transient signals show a range of behavior and timescales. Appearance of population is observed for the J=100, 76, and 54 states (Figure 3.1a-3.1c). Depletion of population is seen for the J=36 and 0 states (Figure 3.1d, 3.1e). The transient population in J=100 has come and gone by ~100 gas-kinetic collisions, whereas population in J=76 and 54 persists past 400 collisions. Similarly, the depletion of population in J=36 and 0 lasts beyond 400 collisions. These data show that substantial energy has been
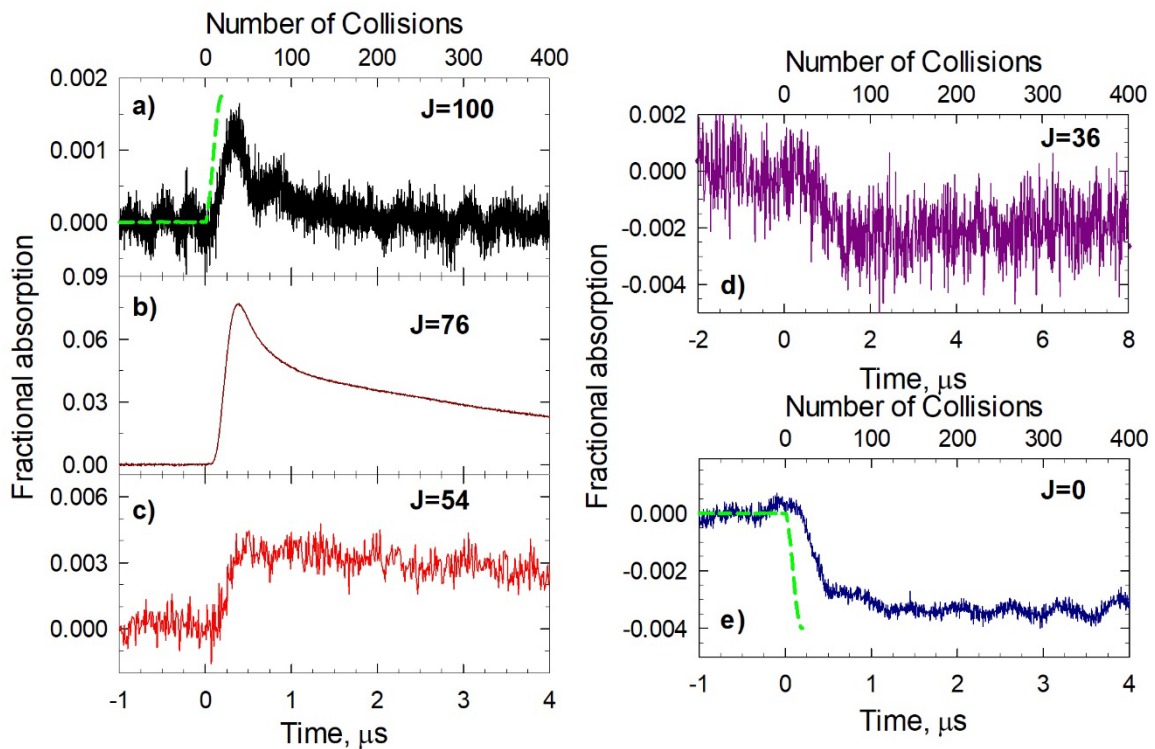
Figure 3.1 Line center transient absorption measurements of CO_2 J = 100 (a), 76 (b), 54 (c), 36 (d), and 0 (e) after excitation by the optical centrifuge. The detector response is shown as a dashed green line in Figure 3.1a and 3.1e. Note that the signals are slower than the detector response in all cases.

imparted to the system by excitation of the super rotors and that the redistribution of that energy requires many collisions before equilibrium is reached.

Figure 3.2 shows transient line profiles of the J=100, 76, 54, and 0 states measured at a series of times corresponding to 25, 50, 75, and 100 gas-kinetic collisions after the optical centrifuge excitation. At each time step in Figure 3.2, fractional absorption data are fit to a Gaussian function to determine the Doppler broadening. Translational temperatures are determined from the full width at half maximum (FWHM) of the Gaussian fitting results, as listed in Table 3.1. To check for possible pressure-broadening contributions, we
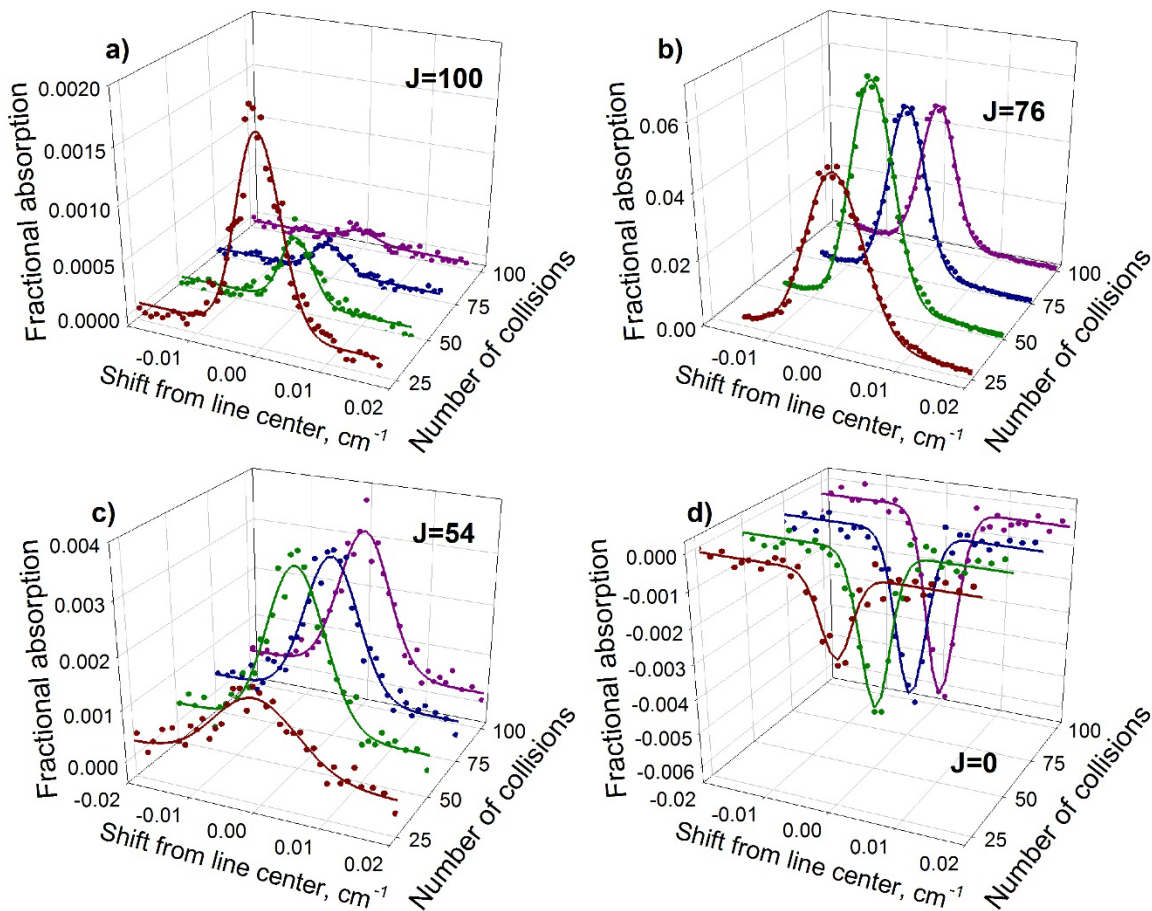
Figure 3.2 Time-dependent Doppler-broadened line profiles for J= 100 (a), 76 (b), 54 (c), 0 (d) are shown at 25, 50, 75, and 100 gas-kinetic collisions after optical centrifuge excitation.

have also fit the data using a Voight profile (a combined Lorentzian and Gaussian profile) with known pressure-broadening coefficients for CO_2 from the HITRAN Database. Translational temperatures resulting from the Voigt fitting are within 10% of the results from Gaussian fitting, which is within our experimental uncertainty.

Table 3.1 J-Dependent Linewidths and Translational Temperatures

CO_2 J	v (cm^{-1})	N [a]	FWHM (cm^{-1})	T_{trans}, K (Gaussian)
100	2241.196	25	7.84E-03	1040 ± 80
		50	5.93E-03	600 ± 80
76	2272.533	25	1.02E-02	1700 ± 50
		50	7.94E-03	1040 ± 30
		75	7.17E-03	850 ± 20
		100	6.81E-03	760 ± 20
54	3748.084	25	1.50E-02	1360 ± 180
		50	1.07E-02	700 ± 50
		75	1.04E-02	650 ± 50
		100	9.76E-03	580 ± 50
0	3715.556	25	4.54E-03	130 ± 30
		50	5.52E-03	190 ± 20
		75	5.30E-03	170 ± 20
		100	5.82E-03	210 ± 20

[a] N is the average number of collisions as described in the text.

The state-specific translational energies are determined by the measured line widths and the rotational state populations are determined from the integrated area under each curve. The population changes in each rotational state describe the evolution of rotational energy in the system. The time dependence of transient line profile intensities varies substantially among states, indicating the presence of a wide range of energy transfer dynamics and cross sections. Line profile results are only reported for times at which signal

levels are sufficient for a reliable Gaussian fit, in which case the rms (root-mean-square) residuals are less than 15% of the line-center intensity.

Of the states investigated here, the J=36 state is unique because depletion is detected at line center and appearance is detected in the wings of the Doppler profile, as shown in Figure 3.3. When depletion and appearance rates are comparable, signal levels for absorption become small; low signal-to-noise levels for the line-center transient of J=36 are evident in Figure 3.1d. To analyze the line profiles, the transients for J=36 were smoothed using a running average, as shown in Figure 3.3a. The smoothed data were then fit to a sum of two Gaussian functions with opposite amplitudes, one corresponding to appearance and the other corresponding to depletion. The double Gaussian behavior indicates that molecules are appearing in J=36 with more translational energy than those molecules being removed from the state.

Figure 3.4 shows the evolution of translational temperatures based on the transient Doppler profiles for J=100, 76, 54, 36, and 0 (Figure 3.4a-Figure 3.4e). Molecules
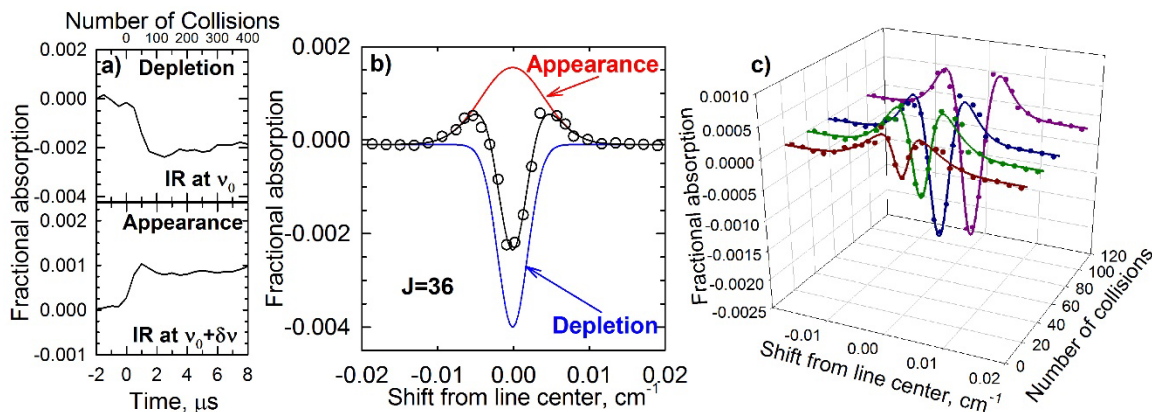
Figure 3.3 a) Smoothed transient absorption signals show depletion at line center and appearance in the wings. b) Doppler-broadened line profiles for J=36 are fit to double Gaussian functions since appearance and depletion are simultaneously detected in this state. The fit at 50 collisions (1 μs) is displayed here. c) Doppler-broadened line profiles at 20, 40, 60, and 100 collisions after the optical centrifuge excitation.

scattered into the J=100, 76, 54, and 36 states all have translational temperatures above 300 K, showing that super rotor relaxation occurs by rotation-to-rotation/translation (R-to-RT) energy transfer. The extent and time-dependence of translational energy profiles vary significantly as a function of J. Under the conditions of these measurements, the earliest data for J=100 (Figure 3.4a) show an initial product translational temperature near 400 K (after 10 collisions), indicating that relatively small amounts of translational energy have been imparted after 10 collisions. In contrast, the J=76 state has a translational temperature of almost 3000 K after 10 collisions, showing that much larger amounts of translational energy are released for states that are further away in energy and J quantum number from the initial super rotors. As discussed next, these findings show that near-resonant rotational transitions are occurring and that super rotor energy transfer can involve ΔJ values well beyond the minimum value of $\Delta J=2$ for CO_2.

The mismatch between the rotational energy loss and gain in collisions is the amount of energy available for translation. First we consider the relaxation of a CO_2 super rotor in a series of 10 collisions with thermal CO_2 molecules (initially in J=16) that lead to the production of J=100 with 400 K in translational energy. A J=120 super rotor that is relaxed by rotationally resonant transitions by the minimum step of $\Delta J_{SR} = -2$ leads to energy gains in the acceptors with ΔJ_{acc}=10 to 8. The energy mismatch between donor and acceptor states leaves a translational energy of 170 cm^{-1} in the J=100 molecules. If super rotor relaxation occurs by larger ΔJ steps, there is more translational energy available to J=100 molecules. For example, a J=220 super rotor ends up in J=100 after 10 collisions
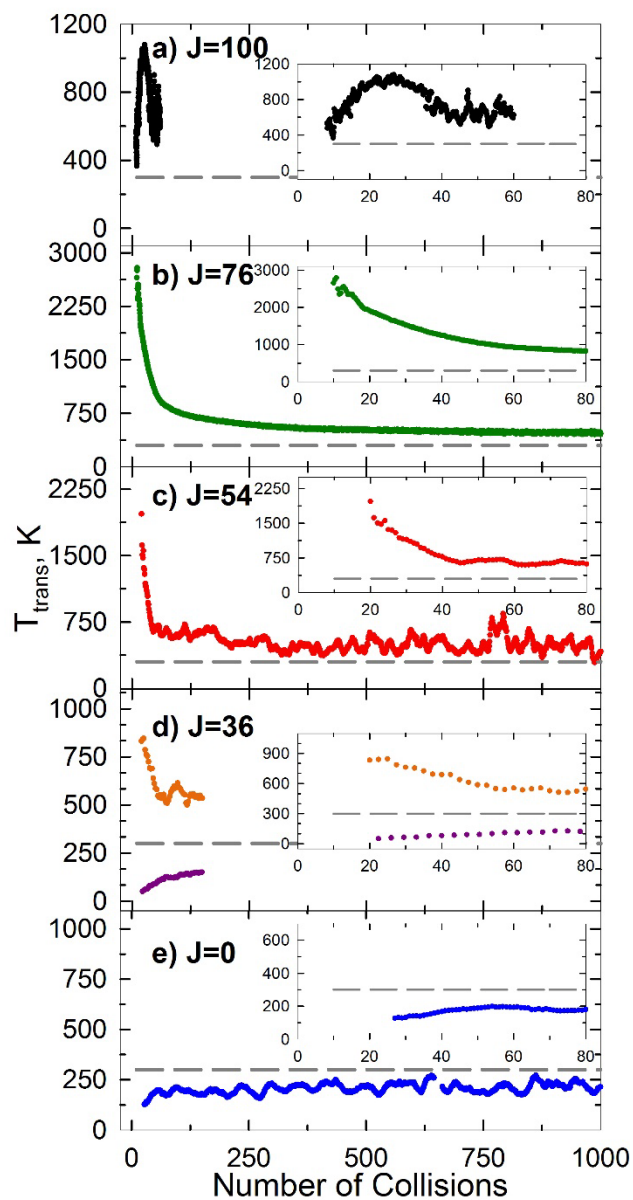
Figure 3.4 Time-resolved translational temperatures of CO_2 J = 100 (a), 76 (b), 54 (c), 36 (d), and 0 (e) are shown as a function of number of collisions after optical centrifuge excitation. The inset in each graph shows a zoomed view of the data from 0 to 80 collisions. The grey dashed line in each figure is the 300 K initial ambient temperature.

with $\Delta J_{SR} = -12$ for each collision, corresponding to energy gains in the acceptors with

ΔJ_{acc}=56 to 36. In this case, the energy mismatch between donor and acceptor states leaves

400 cm^{-1} of translational energy in the J=100 molecules. The second scenario is resembles our experimental results for J=100.

The presence of high translational energy (3000 K) in the J=76 collision products after 10 collisions shows that non-resonant rotational energy transfer is also taking place, with the excess energy going into recoil between collision partners. Super rotors starting in J=220 can end up in J=76 after 10 sequential down-collisions with $\Delta J_{SR}= -14$. A maximum of 3400 cm^{-1} is available in translational energy for J=76 if ΔJ_{acc}=56 to 26.

It is also possible, and indeed likely, that at least some of the population in J=76 results from collisional excitation of thermal molecules. A J=16 molecule undergoing 10 sequential up-collisions with super rotors ends up in J=76 when $\Delta J_{acc}= 6$. If a J=220 super rotor is the collision partner and $\Delta J_{SR}= -2$, the J=76 molecule ultimately has a translational energy of 1260 cm^{-1}. If $\Delta J_{SR}= -4$ super rotor transitions occur, the maximum translational energy increases to 4690 cm^{-1}. It is clear from this analysis that the translational energy from non-resonant super rotor collisions is extremely sensitive to the ΔJ values involved in the relaxation process.

Currently we cannot distinguish the J-specific dynamics of super rotors that are coming down the rotational ladder from the dynamics of thermal molecules that are going up the ladder through collisions with super rotors. In addition, there is uncertainty in the initial distribution of super rotors. Nevertheless, it is clear from these results and the simple energy gap analysis that super rotor collisions occur by rotationally resonant and non-resonant processes and that ΔJ values in these processes are not limited to the minimum allowed values.

The data in Figure 3.4 give additional insights into the collision dynamics. The energy profiles for J=76 and J=54 show that the translational energy from super rotor collisions is rapidly dissipated and has reached a quasi-equilibrium temperature by 60 collisions that is well above the initial 300 K value. The long-time behavior for these states is a signature of the large amounts of rotational energy and the number of super rotors initially created in the optical centrifuge.

Another interesting result from Figure 3.4 is that the translational energy profiles along the x-axis for J=0 and 36 depletion are consistently below 300 K, indicating that inelastic collisions of super rotors, or partially relaxed super rotors, preferentially remove a slower subset of molecules from thermally populated states. The low translational temperatures measured for depletion of J=0 and J=36 imply that the total inelastic scattering cross section, represented by $\sigma_{0 \to j}$ for J=0, decreases with increasing collision energy. It is perhaps not surprising that super rotor relaxation preferentially involves a subset of slower velocity collisions within the plane of super rotor rotation, given the impulsive nature of rotational energy transfer. Effective rotational relaxation requires impulsive collisions that occur at short range. High-velocity collisions can be ineffective if the time scale for relative translation is much faster than the angular frequency; in this case, it is unlikely that the collision partners have the most effective relative orientation with which to transfer energy. On the other hand, in the limit of low-velocity collisions, the energy-accepting molecule can be considered as essentially stationary as the rotor spins.
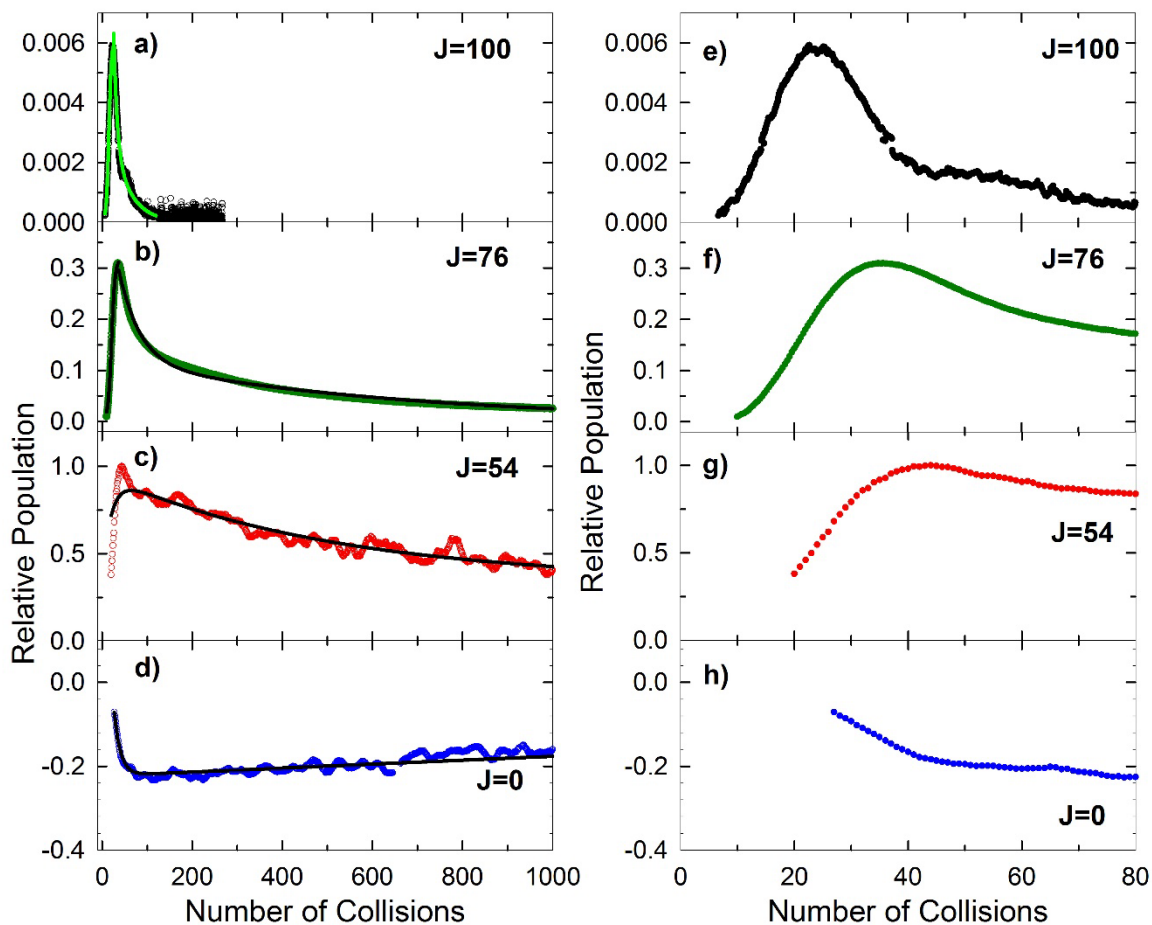
Figure 3.5 The long-time (a-d) and early-time (e-h) behavior of the relative populations of the J=100, 76, 54, and 0 states.

Figure 3.5 shows the evolution of the relative populations in the J=100, 76, 54, and

0 states of CO_2 out to 1000 collisions (Figure 3.5a—3.5d) and a zoomed-in view to 80

collisions (Figure 3.5e—3.5h). The relative populations are scaled to the maximum value

of the population of J=54. The population of J=36 is not included here since this state has

essentially no net population change. The population data are fit to a sum of exponential

functions in order to get qualitative timescales for which population is entering or leaving

an individual state. The fits are shown in Figure 3.5a—3.5e. A summary of the individual

timescales and the associated collision numbers is shown in Table 3.2. The first column

gives the timescale τ_A for molecules appearing into the state, or in the case of J=0, the timescale for which molecules are depleted from the state. τ_B represents the first timescale for which population recovers back toward equilibrium. In the case of J=100 and 76, a second recovery timescale τ_C was included to describe the long-time return to quasi-equilibrium. The slow return to equilibrium of J=0 and J=54 is evidence of the extreme amount of energy imparted to the system by the optical centrifuge. Changes in population for these states are detected as far out as 1000 collisions after the optical centrifuge excitation. In contrast, population passes through the J=100 window within 200 collisions, indicating that high rotational states relax more quickly than the lower states, which are closer to states thermally populated at 300 K.

Table 3.2 Timescales and Collision Numbers for J-specific Populations

J	τ_A	N_A	τ_B	N_B	τ_C	N_C
0 [a]	140 ns	14	210 μs	21000	—	—
54 [a]	188 ns	19	5.1 μs	510	—	—
76 [a, b]	39 ns	3.9	460 ns	46	6.3 μs	630
100 [a, b]	41 ns	2.7	110 ns	7	590 ns	39

[a] The timescale for population appearance (or depletion for J=0) is τ_A; the timescale for recovery to quasi-equilibrium is τ_B.
[b] For J=76 and 100, a second recovery timescale τ_C was included to describe the long-time dynamics.
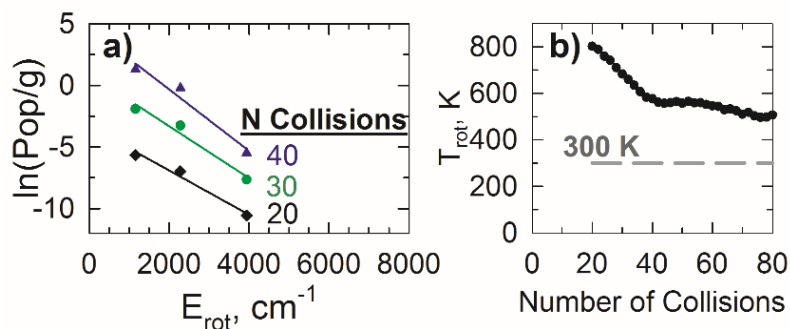
Figure 3.6 a) Semi-log plot of the degeneracy-weighted relative population for the J=54, 76 and 100 states measured at various times following the optical centrifuge pulse corresponding to 20, 30, and 40 collisions. b) Time evolution from 20 to 80 collisions of the rotational temperature.

From the relative populations of the J=100, 76, and 54 states, we can estimate the evolution of rotational energy as the super rotors undergo collisional relaxation. Figure 3.6a shows a semi-log plot of the relative population data weighted by the degeneracy g for these states, along with the rotational distribution fitting results at 20, 30, and 40 collisions. Based on a Boltzmann distribution, the rotational temperatures are determined from the slopes of the fitting results as a function of collision number. Figure 3.6b shows the rotational temperatures between 20 and 80 collisions. After 20 collisions, the rotational temperature for these states is T_{rot} ~800 K. A relatively rapid rotational cooling is observed, followed by a second, slower relaxation to T_{rot} ~500 K. This result is consistent with previous measurements from our group on the long-time behavior of the J=60-78 rotational distribution for super rotor relaxation[29].

3.3.2 Effects of Field Intensity and Cell Pressure

We performed additional measurements on the J=76 state to test for effects of varying the field strength and the pressure. Figure 3.7a and Figure 3.7b show the time
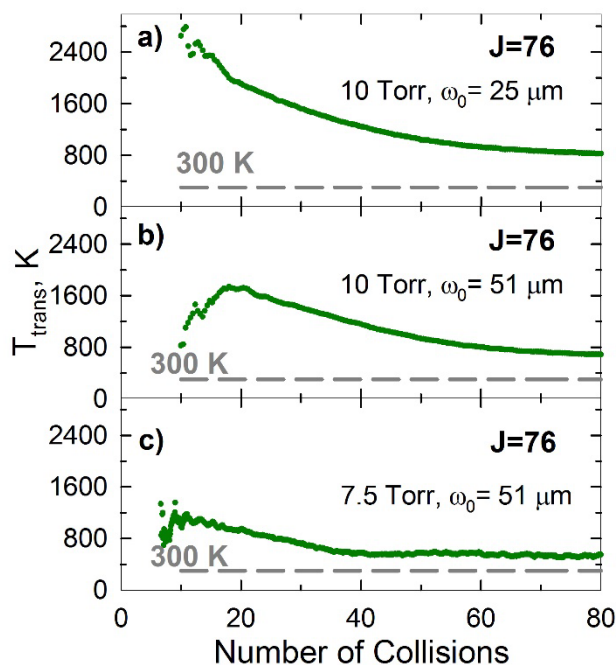
Figure 3.7 Translational temperatures of J=76 at 10 Torr and focusing the OC down to ω_0= 25 μm (a), at 10 Torr and focusing the OC down to ω_0= 51 μm (b), and at 7.5 Torr and focusing the OC down to ω_0= 51 μm (c).

evolution of the translational temperature measured at 10 Torr with the optical centrifuge focused to a beam waist of ω_0= 25 μm and with a less focused beam waist of ω_0= 51 μm, respectively. The overall power is the same for both sets of measurements but the beam intensity is decreased by a factor of 4 when the beam waist is doubled. Figure 3.7b shows that the translational temperatures are cooler overall for the less focused beam. In addition, the field intensity affects the time-dependent behavior, showing that the collision dynamics are affected by the number density of the centrifuged molecules. Rather than a monotonic decrease in translational temperature starting from T=2800 K (as in Figure 3.7a), the looser focus results in a lower initial translational temperature of T=800 K, followed by a temperature increase to T=1800 K and subsequent slower overall relaxation. The weaker focus effectively reduces the number density of super rotors since the depth of the potential

61

well experienced by the molecules in the optical centrifuge is proportional to the intensity of the beam[14]. In a less intense beam, more molecules can fall out of the trap before the end of the pulse. The early-time data shown in Figure 3.7b supports this picture as there are fewer super rotors from which to gain translational energy.

The density of super rotors was further reduced by decreasing the pressure to 7.5 Torr. Figure 3.7c shows the translational temperatures for $J = 76$ at 7.5 Torr with the optical centrifuge focused to a beam waist $\omega_0 = 51$ μm. At this pressure, the translational temperature is initially $T = 600$ K, then rises to $T = 1200$ K, followed by slower relaxation to quasi-equilibrium. At both pressures, the initial temperatures are similar, indicating that with fixed optical centrifuge intensity, a comparable fraction of molecules is excited by the optical field. The data in Figure 3.7b and c show that pressure influences the overall energy cascade.

At 80 collisions, translational temperatures remain above 300 K, indicating that the system continues to approach equilibrium. A comparison of the three data sets in Figure 3.7 shows that the long-time energy content decreases as the field intensity and the pressure are reduced. Losses from transport of molecules out of the probe volume may contribute to the differences in the translational temperatures at long times.

3.3.3 Comparison with Quantum Scattering Calculations

In order to gain insight into the inelastic collision dynamics of super rotors, quantum scattering calculations were performed on the Ar-CO_2 (j) system. As an atom-triatom collision system, Ar-CO_2 (j) scattering is a starting place from which to consider the state-to-state dynamics of CO_2 super rotor collisions. A more detailed analysis and

explanation of these quantum scattering calculations is given in Chapter 7. Here some of the key results are presented.

Inelastic scattering cross sections for collisions of Ar with $CO_2(j)$, based on an *ab initio* potential energy surface from Klos[85], were calculated using the Hibridon[86] scattering package which solves the close-coupled equations for molecular collisions. The matrix of inelastic scattering cross sections was calculated for transitions involving all CO_2 states with $j = 0$ to 72 at five collision energies: 150, 200, 310, 525, and 1000 cm^{-1}. A contour plot of the inelastic scattering cross sections at a collision energy of 200 cm^{-1} is shown in Figure 3.8. The elastic cross sections have been removed so that features of the inelastic collisions are highlighted.

The variation of state-to-state cross section with Δj gives insight into the distribution of rotational energy transfer. The inset in Figure 3.8 shows the inelastic cross sections for molecules starting in an initial state $j'' = 20$ and 54, each ending in a range of final states denoted by j', at a collision energy of 200 cm^{-1}. In both cases, the down-collision Δj values range from -2 to $-j''$. The range of up-collision Δj values is smaller and is limited by the available collision energy. The up-collision cross sections for $j'' = 20$ extend to larger Δj values than those for $j'' = 54$ because of the increasing energy gap with rotational quantum number. As j'' increases, the down-collision cross sections have a steeper j' dependence, which localizes the probabilities to smaller Δj values.

Extrapolating out to the high j'' values of super rotors, we expect that the down-collisions will have the full range of Δj values, but that the majority of inelastic collisions will occur for a fairly narrow range of Δj values. Our rigid-rotor energy gap analysis
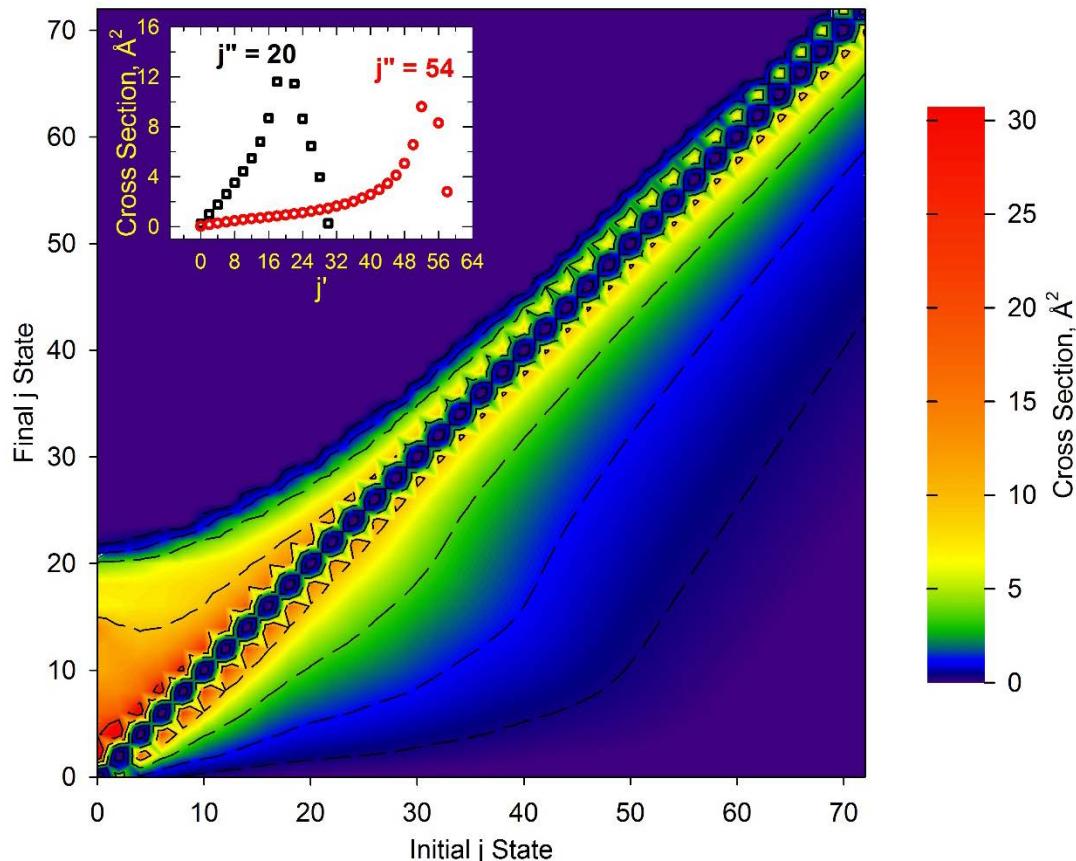
Figure 3.8 State-to-state inelastic scattering cross sections calculated for the Ar-CO_2 system at a collision energy of 200 cm^{-1}. Redder colors represent higher cross sections. The elastic cross sections are not included in this plot.

invoked down-collisions of super rotors ΔJ values that are less than 10% of the initial J value. It is reasonable that these types of collisions have appreciable cross sections, given the results of the quantum scattering calculations.

The cross section for removal from a particular state is determined by summing the cross sections over all possible final states:

$$\sigma_{j''} = \sum_{j' \neq j''} \sigma_{j'' \to j'}$$

where j'' is the initial state and j' is the final state. Figure 3.9 shows the removal scattering cross sections for $j'' = 0$, 36, and 54 as a function of collision energy. For these states, the

64
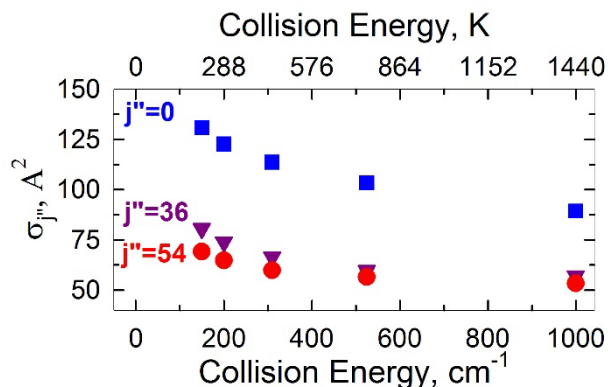
Figure 3.9 Total removal scattering cross section for CO_2 $j'' = 0$, 36, and 54 as a function of collision energy.

depletion cross sections increase with decreasing collision energy. This result is consistent with our experimental observation that the initial depletion profiles for J=0 and 36 have cooler translational energies that the ambient cell temperature.

3.4 Conclusions

We have investigated the collision dynamics of CO_2 super rotors created in an optical centrifuge and measured the time evolution of translational and rotational energy over a broad range of rotational states with J=0 to 100. Transient, J-specific, Doppler-broadened line profiles reveal that molecules appearing in J=100, 76, 54, and 36 have translational temperatures significantly above 300 K, indicating that large translational energy gains are possible from super rotor collisions. The time evolution of the translational energy varies significantly with J state and reveals detailed information about the collision dynamics. An energy gap analysis identifies both rotationally resonant and non-resonant pathways for super rotor relaxation. Super rotor down-collisions with $\Delta J = -12$ can be used to explain the observed translational energy content. Quantum scattering calculations on Ar-$CO_2(j)$ indicate that this type of transition is reasonable, based on

65

estimates for super rotors with initial J values near 220. In addition, the data indicate that low-lying J states with sub-thermal velocity distributions are predominantly depleted in the super rotor collisional cascade. This finding is supported by the results of quantum scattering calculations and provides limiting time scales for efficient energy transfer that can guide future theoretical models.

The J-specific scattering results presented here lay the framework upon which to build a more in-depth understanding of super rotor dynamics. The rich variety of J-dependent behavior reported here identifies many new directions for research. On the experimental side, the new multipass cell design described in Chapter 2 gives earlier-time detection of optically centrifuged super rotors and their collision dynamics. Enhancements in signal-to-noise from this cell design are reported in Chapter 5 of this thesis. The current results guide future studies to investigate the meta-stability of high-J rotors using polarization-sensitive detection. We have results from polarization-sensitive measurements that CO_2 molecules in J=76 act like molecular gyroscopes, wherein the initial orientation of the super rotors is preferred for as many as 2000 collisions[30]. Chapters 4 and 5 report new investigations into this behavior for a broad range of J states. Theoretically, the current quantum scattering calculations could be extended to higher *j* states. Chapter 7 reports a more detailed look into the calculated scattering cross sections and their effect on the collision dynamics. Moving forward on both experimental and theoretical fronts will lead to progress towards a better understanding of this interesting class of high energy molecules.

Chapter 4: Impulsive Collision Dynamics of CO Super Rotors from an Optical Centrifuge

4.1 Introduction

Rotational energy transfer between gas-phase molecules is a primary means by which energy redistribution occurs under non-equilibrium conditions. This process is important for chemistry and heat flow in combustion and photochemical processes in the atmosphere. One challenge in studying the dynamics of rotational energy transfer is that thermal samples have isotropic rotational motion. The development of new laser-based techniques has expanded opportunities in this area and led to the ability to produce molecules in extreme rotational states with a well-defined connection between the lab and molecular frames[14, 15, 19, 87, 88].

The optical centrifuge uses chirped pulses of light to trap gas-phase molecules and induce unidirectional molecular rotation with large amounts of orientated angular momentum[26]. Spectroscopic evidence for long-lived populations of super rotors with oriented angular momenta was first reported in 2013 for CO_2 in the J=76 rotational state[30]. Polarization-sensitive IR measurements showed that following the optical centrifuge pulse, CO_2 J=76 molecules maintain their initial orientation through thousands of J-changing collisions[30]. The propensity of collisions to conserve angular momentum orientation

while changing J has also been predicted[62, 89] and experimentally observed in an ensemble of molecules aligned with linearly polarized femtosecond pulses[18, 90]. Other experiments showed that loss of birefringence in an O_2 sample prepared with an optical centrifuge occurs in ~20 collisions; this observation was attributed to the loss of oriented angular momentum[32]. This behavior is in contrast to collisions involving lower J states, for which spatial randomization typically occurs after a small number of collisions[38]. In transient IR measurements of CO_2 super rotor collisions show that large amounts of translational energy are observed for molecules probed in the initial plane of rotation[30, 37]. Molecular dynamics simulations agree with the experiments, indicating that super rotors initially have a gyroscopic stage, followed by an explosive translational energy release[37]. In the current study, we use polarization-sensitive transient IR absorption probing to investigate the collision dynamics of CO super rotors made in an optical centrifuge. These experiments are designed to test how oriented angular momentum in molecules other than CO_2 is relaxed by collisions.

Rotational energy transfer is often characterized by energy gaps between rotational states. Rotational energy transfer is seen to occur readily, on the order of every gas kinetic collision, because the energy gap ΔE between rotational states is relatively small[38, 91]. It is generally observed that smaller ΔE values lead to greater probabilities of rotational energy transfer[38]. In addition, there is a propensity for small changes in rotational angular momentum. Studies on low-lying, thermally-populated states of Na_2, HCN, HF, HCCH, and CO reveal that processes with small ΔJ are favored, but that transitions are not limited

to small ΔJ values[22, 41-46, 48]. In the case of acetylene, transitions with $\Delta J = 20$ have been reported. Distributions of ΔJ broaden as J increases.

Studies have revealed interesting collisional properties for molecules in high J states. Rotational energy gaps increase as J increases, which impacts rotational relaxation rates. Collisional metastability has been observed for CN molecules with J=80 that are formed by photodissociation of BrCN[50]. The CN $J = 80$ molecules persist for more than 1000 collisions with Ar and Kr buffer gases. It is also possible to produce collisional metastability by translationally cooling the rotating molecules while maintaining high angular momentum states[34, 59]. The optical centrifuge provides controlled excitation of molecules into high angular momentum states where the energy gaps between adjacent rotational levels are on the order of the average collision energy at 300 K.

This chapter reports results on the collision dynamics of CO molecules that have been optically centrifuged to $J \approx 50$. Polarization-sensitive, time-resolved IR detection of the translational energy distributions and population of CO in the $J = 29$ directly yields information about the collision-induced spatial reorientation of the CO rotors. The results are compared to previous measurements of inhibited rotational quenching in CO_2 $J = 76$[30]. In addition, information about J-dependent collisional relaxation is obtained from transient IR measurements for a number of CO rotational states with $J = 29$ to 39.

4.2 Experimental Details

4.2.1 The Optical Centrifuge Spectrometer

The details of the optical centrifuge laser system are described in Chapter 2. Differences in the spectral chirp impact the extent of rotational excitation. Figure 4.1a shows the spectra of the two opposite chirps used in this set of experiments. The full-width at half maximum (FWHM) of the two chirped pulses corresponds to a rotational frequency of $\omega \sim 35$ THz. A CO molecule rotating at 35 THz has a classical rotational energy of ~ 5000 cm^{-1}, corresponding to a rotational quantum number near $J = 50$.

Collision-induced population changes of individual CO rotational states were measured following the optical centrifuge pulse using high resolution transient IR absorption spectroscopy. A quantum cascade laser (QCL) (Daylight Solutions) operating between λ=4.2 and 4.5 μm was used to probe individual R-branch transitions of the CO fundamental $(0 \rightarrow 1)$ band. The QCL provides linearly polarized, high resolution light with $\Delta\nu_{IR} < 3 \times 10^{-4}$ cm^{-1} and a power of ~ 60 mW. A small fraction of the IR light was used
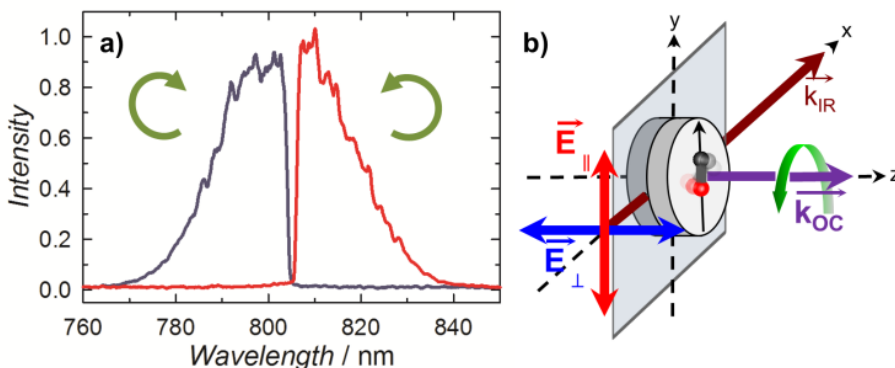
Figure 4.1 a) The spectra of the pair of oppositely-chirped pulses. The pulses are superimposed in time to generate the optical centrifuge. The rotational frequency at FWHM of the spectra corresponds to a rotational frequency of $\omega \sim 35$ THz. b) The IR probe beam is linearly polarized either parallel (red) or perpendicular (blue) to the x-y plane.

for transient detection of individual CO rotational states. The IR probe beam was propagated at 90° with respect to the optical centrifuge beam (Figure 4.1b) and focused to a beam waist of $\omega_0 = 48$ μm in a Pyrex cell containing 5 or 10 Torr CO gas. The optical centrifuge beam was propagated along the z-axis, focused to $\omega_0 = 26$ μm and used to prepare molecules with angular momentum vectors $\vec{J}_{OC}$ that are nearly parallel to the optical centrifuge propagation vector $\vec{k}_{OC}$ and the *z*-axis. The motion of individual CO molecules map out a rotating disk that spins with the optical field of the centrifuge pulse $\vec{E}_{OC}$. As described in Chapter 2, the ensemble of trapped molecules has a unidirectional sense of rotation, corresponding to oriented angular momentum vectors. The IR probe light was polarized either parallel or perpendicular to the plane of molecular rotation, as shown in Figure 4.1b.

Line-center transient IR measurements were collected for a number of CO states with J=29-39 after optical centrifuge excitation. These measurements were made with the polarization of the IR light parallel to the plane of molecular rotation, the optical centrifuge power at ~26 mJ/pulse and the pressure at 10 Torr.

Polarization-dependent, Doppler-broadened line profiles were collected for the J=29 state of CO. For these measurements, the power of the optical centrifuge pulse was increased to 46 mJ/pulse and the CO pressure was reduced to 5 Torr. The pulse energy in each measurement was below the threshold for emission, as discussed in section 4.2.3. We use the gas kinetic collision frequency at 300 K to convert time to number of collisions. This step provides a common timescale to compare different experiments. The average time between collisions at 300 K is 10.4 ns at 10 Torr and is 20.8 ns at 5 Torr. However,

in our experiments we observe translational temperatures that are greater than 300 K. As a result, the actual collision rates are larger and the number of 300 K gas kinetic collisions represents a lower limit.

Transient IR absorption was detected with a liquid-nitrogen-cooled InSb photodiode. Wavelength modulation was used to lock the IR frequency to either a CO reference transition or the fringe of a scanning confocal etalon, thereby stabilizing the IR frequency during transient measurements. Transient Doppler-broadened line profiles were measured by collecting transient absorption signals at a series of closely-spaced IR frequency steps (~0.001 cm^{-1}) across individual ro-vibrational transitions. Transient absorption signals were typically averaged for ~400 centrifuge pulses.

4.2.2 Role of Diffusion

The impact of diffusion on the transient signals is based on the detection geometry, detection time, sample pressure, and CO translational energy. The diameter of the IR probe beam at the focal point was $d_{IR} = 2\omega_0 = 96$ μm. This length is nearly a factor of 2 larger than the focused optical centrifuge beam diameter of $d_{OC} = 2\omega_0 = 52$ μm. The Rayleigh length for the optical centrifuge beam was 0.25 cm. The IR path length (along the x-direction) in Figure 4.1b is 15 cm and signal loss from diffusion resulted only from diffusive motion along the y- and z-directions. From equation 2.52, diffusion for CO at 300 K and 5 Torr in 1 μs corresponds to a 1-D root mean square (rms) displacement of $x_{rms} = 56$ μm, based on a diffusion coefficient of $D(300\,K) = 1.57x10^{-3}$ m^2/s. Diffusion at 300 K gives a lower limit to the average displacement. At 1000 K, the 1-D

rms displacement increases to $x_{rms} = 138$ μm, based on $D(1000\ K) = 9.56x10^{-3}$ m^2/s.

Diffusion is slower at 10 Torr: $D(300\ K) = 0.785x10^{-3}$ m^2/s and $x_{rms} = 80$ μm at 4 μs.

4.2.3 Strong Field Effects

Successful optical centrifuge experiments require a balance of optical field strengths to generate sufficient number densities of super rotors while avoiding strong field effects. Above a CO pressure of 10 Torr, visible emission was detected, indicating the presence of strong field effects. Strong fields should be avoided in studies of super rotor collisions and so power dependent studies were performed to identify the threshold for emission. The emission was detected by focusing the emitted light into an Ocean Optics UV-VIS 2000+ spectrometer. The dispersed emission had a spectrum that corresponds to the C$_2$ Swan bands and not the CO Angstrom bands, indicating that intense laser fields can initiate reactions to form C$_2$ from CO[92, 93]. Threshold energies for C$_2$ emission increase as the CO pressure is decreased, as shown in Figure 4.2a. This behavior is consistent with a collision-induced mechanism for the formation of C$_2$. No emission was detected at
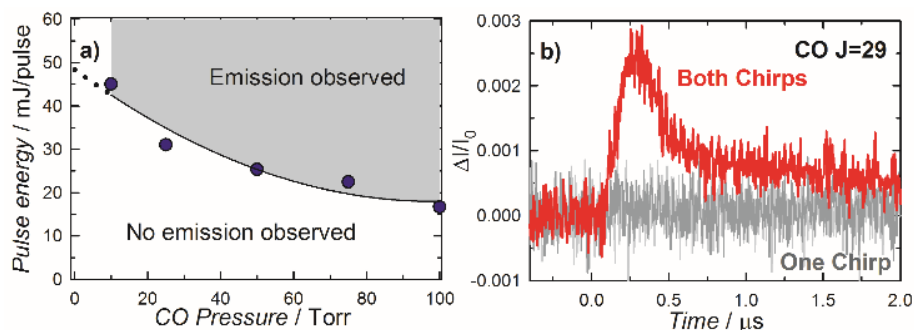
Figure 4.2 a) Energy threshold for emission in a CO gas measured at pressures of 10-100 Torr. No emission was detected below 10 Torr at the maximum laser power. b) Line-center transient IR absorption signal for CO J=29 (with total energy of 26 mJ/pulse and pressure of 10 Torr) with both oppositely chirped pulses (red) and with only one of the chirped pulses (grey). Transient signals were observed only when both chirped pulses were present.

pressures below 10 Torr. In the limit of zero CO pressure, no C_2 will be formed and the corresponding emission threshold energy will be infinite. The dotted line in Figure 4.2a is an extrapolation to zero pressure based on the threshold energy having an exponential pressure dependence. The extrapolation represents a worst case scenario for the presence of strong field effects at low pressures. The measurements reported here were performed at pressure/power combinations that are below the emission threshold.

As an additional check of strong field effects, two transient absorption measurements for CO J = 29 were made with a CO pressure of 10 Torr. The first measurement was collected using the pair of oppositely chirped pulses with a total power of ~26 mJ/pulse. The second measurement used only one chirped pulse with a power of ~26 mJ/pulse. Figure 4.2b shows that transient signals for J = 29 were observed only with both chirped pulses present, indicating that transient IR signals result from super rotor collisions and not from strong field effects.

4.3 Results and Discussion

Here we report the time-resolved translational energy and populations for CO molecules in J=29 following the optical centrifuge pulse based on polarization-sensitive, transient, Doppler-broadened, line profile measurements. These data show how the orientational anisotropy of the CO rotors is relaxed by impulsive collisions. Transient IR data for CO states with J = 29 to 39 provide additional information about the J-dependent relaxation of CO super rotors.

4.3.1 Polarization-dependent Doppler profiles of CO J=29

Doppler-broadened IR line profiles were collected for CO J = 29 as a function of time following the optical centrifuge pulse and of IR probe polarization. The pressure was 5 Torr. Data were collected using the R29 transition at λ=4.4 μm. Figure 4.3 shows polarization-dependent transient absorption signals at the transition line center along with an exponential decay fit. Signal decay can result from collision-induced changes in rotational state and/or velocity vector and from transport in or out of the probe volume. The initial intensities at line center are similar for parallel vs. perpendicular probing, but the decay constant for parallel probing ($\tau_{par} = (540 \pm 100)$ ns) is a factor of 3 faster than that for perpendicular probing ($\tau_{per} = (1700 \pm 700)$ ns). Differences are also seen in the Doppler-broadened line widths.

Figure 4.4 shows Doppler profiles (based on transients such as in Figure 4.3) with the IR probe polarization parallel and perpendicular to the initial plane of rotation at 200 ns (~10 collisions) and 500 ns (~24 collisions) after the optical centrifuge pulse. The J =
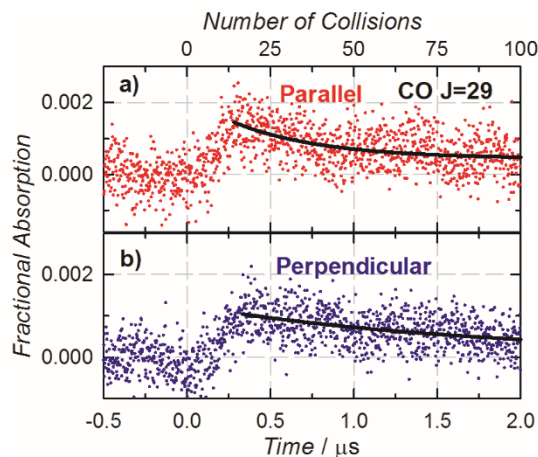
Figure 4.3 Line-center transient absorption signals of CO J=29 at 5 Torr, measured with the IR polarization a) parallel and b) perpendicular to the plane of initial rotation.
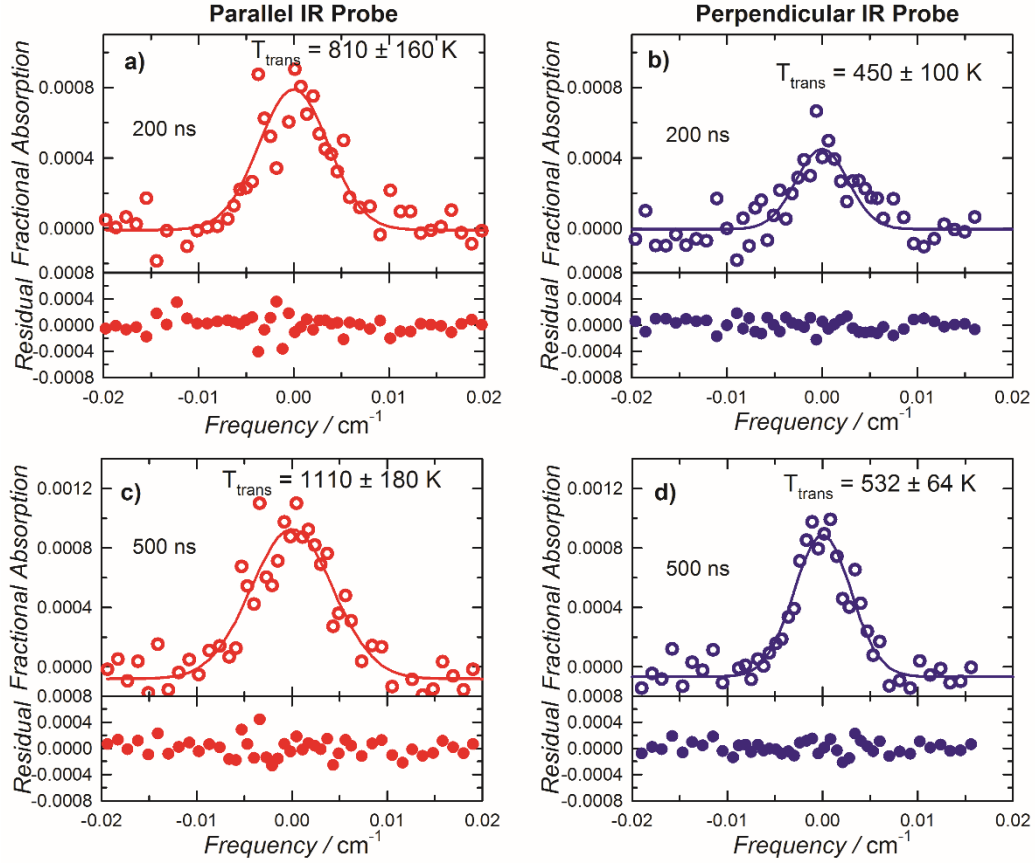
Figure 4.4 Doppler-broadened line profiles of CO J=29 with a) parallel and b) perpendicular IR probe polarizations at 200 ns (~10 collisions), along with Gaussian fitting results and residuals. Line profiles at 500 ns (~24 collisions) with c) parallel and d) perpendicular IR probe polarizations.

29 data were fit to Gaussian functions as described in section 2.2.4 and the translational temperatures were determined from width of the Gaussian profile. At 200 ns (~10 collisions), the Doppler profile with the parallel IR probing had a FWHM line width of $\Delta\nu$ = $(8.6 \pm 1.7) \times 10^{-3}$ cm^{-1}, which corresponds to a translational temperature of T_{trans} = 810 ± 160 K. For perpendicular IR probing, the linewidth was $\Delta\nu$ = $(6.4 \pm 1.4) \times 10^{-3}$ cm^{-1} and the translational temperature was T_{trans} = 450 ± 100 K. At 500 ns (~24 collisions), parallel probing yields $\Delta\nu$ = $(10.1 \pm 1.6) \times 10^{-3}$ cm^{-1} and T_{trans} = 1110 ± 180 K, while perpendicular probing yields $\Delta\nu$ = $(7.0 \pm 0.7) \times 10^{-3}$ cm^{-1} and T_{trans} = 532 ± 64 K. These data show that

molecules rotating in the original xy-plane have more translational energy than those rotating in orthogonal planes.

The polarization-dependent Doppler-profiles show that an anisotropic translational energy distribution exists in the CO sample after collisions with centrifuged molecules. This phenomenon has also been observed in previous studies of CO_2 rotors[30]. This finding means that transport of the translationally hot molecules away from the probe volume is also anisotropic. Transport of molecules out of the probe volume can affect the decay times (as in Figure 4.3) and time-dependent translational energy distributions. At 500 ns after the optical centrifuge pulse, the parallel translational temperature is T = 1000 K and the perpendicular translational temperature is T = 500 K. The transport of molecules away from the excitation volume is ballistic in nature as compared to 300 K Brownian motion associated with thermal diffusion. Calculations in the diffusive limit provide estimates for the timescales with which the thermal diffusion evolves. In the diffusive limit, 1000 K molecules diffuse out of the probe volume in ~500 ns, whereas 500 K molecules diffuse from the probe volume in ~1.3 μs. Anisotropic diffusion is also seen in molecular dynamics simulations of nitrogen super rotors, in which 40% greater diffusion is seen parallel to the plane of rotation than that seen in the perpendicular orientation[62]. Such anisotropic motion is a characteristic feature of oriented super rotor relaxation.

At all times observed, CO molecules aligned in the plane of initial rotation have more translational energy than those aligned perpendicularly. The time-dependent translational temperatures for parallel (red) and perpendicular (blue) IR probing are shown
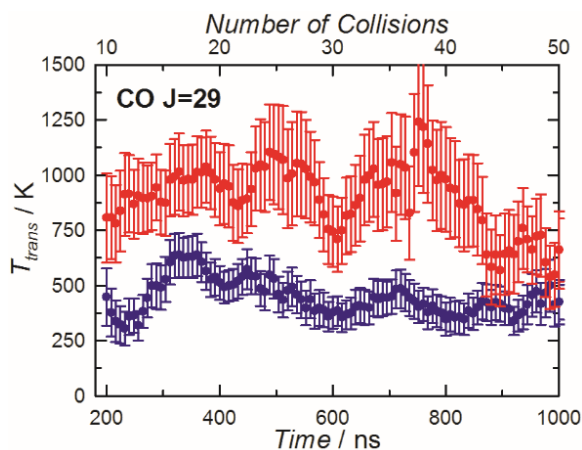
Figure 4.5 Translational temperatures of CO J=29 with parallel (red) and perpendicular (blue) IR probing as a function of time following the optical centrifuge pulse at a cell pressure of 5 Torr.

in Figure 4.5 for times out to 1000 ns. Fluctuations in the translational temperature reflect uncertainty in the Gaussian fitting results, stemming from limiting signal-to-noise levels in the transient signals. Relative to the initial translational energy at 300 K, CO molecules detected with parallel probing gain three times as much translational energy than do those with perpendicular detection. These findings are clear evidence that collisions of super rotors have a preferred spatial outcome as part of the relaxation mechanism. The data show that impulsive collisions are responsible for prompt rotation-to-translation energy transfer with recoil velocities that preferentially lie in the initial plane of rotation.

The presence of large translational energies also shows that the collisions are not rotationally resonant. Rotationally resonant energy transfer occurs when down-collisions have rotational energy loss that nearly matches the rotation energy gain in up-collisions of the collision partner, thereby leaving little remaining energy for translation. Our results show that a propensity rule that favors small ΔJ for low-J molecules are also important in relatively high-J molecules.

4.3.2 Polarization-Dependent Populations of CO J=29

Time-dependent relative populations of CO molecules in J=29 were determined by integrating the area of the Gaussian fits to the Doppler-broadened line profiles, as shown in Figure 4.4. Immediately following the centrifuge pulse, the population of CO molecules probed with parallel IR light (with spatial orientation aligned with the initial rotational plane) is greater than that probed in the orthogonal direction. Figure 4.6a shows the relative populations detected with parallel and perpendicular IR probing. The ratio of parallel-to-perpendicular populations is shown in Figure 4.6b. At 200 ns (~10 collisions) after the centrifuge pulse, the parallel to perpendicular ratio is 2.3. The ratio decays to unity with an exponential lifetime $\tau = 0.3 \pm 0.1$ μs, corresponding to ~15 collisions.

The orientational anisotropy of CO decays more quickly than does the population in J=29, which has a decay constant corresponding to ~60 collisions. The population ratio in Figure 4.6b is a lower limit to the actual ratio because of the transport anisotropy of the
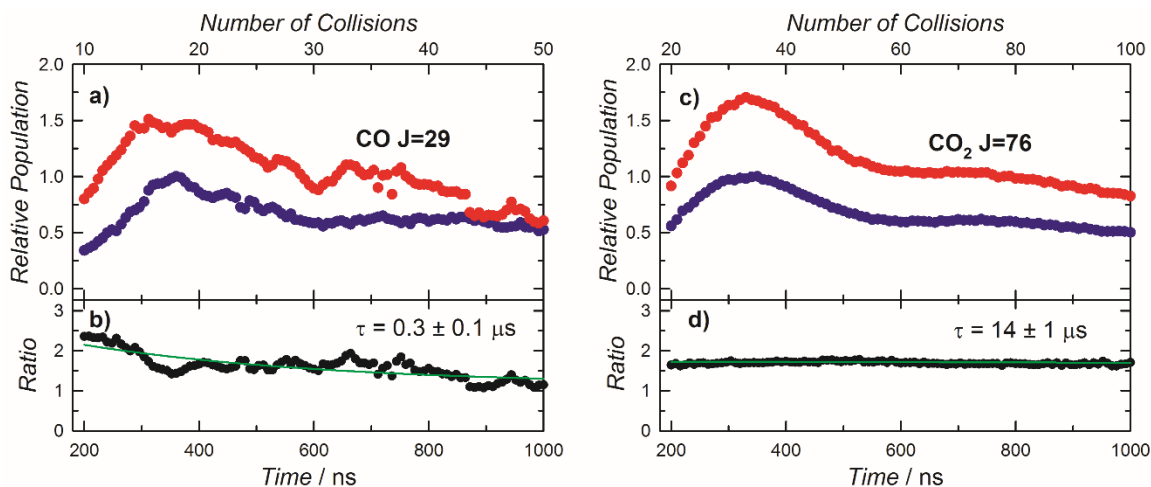
Figure 4.6 a) Relative populations of CO J=29 at 5 Torr with parallel (red) and perpendicular (blue) IR probing. b) The time-dependent ratio of parallel to perpendicular populations fits to a single exponential decay with $\tau = 0.3 \pm 0.1$ μs. c) Relative populations of CO_2 J=76 at 10 Torr with parallel (red) and perpendicular (blue) IR probing. d) The time-dependent ratio of parallel to perpendicular populations fits to a single exponential decay with $\tau = 14 \pm 1$ μs.

two population subsets: CO molecules probed with parallel light have larger translational energies and hence transport out of the probe volume is expected to play a larger role for this subset of molecules. The decay time of the population ratio is a lower limit because losses from transport of molecules out of the probe volume affect the hot population more.

Other optical centrifuge studies of O_2 have observed an exponential decay of an optical birefringence signal in about 20 collisions, which was attributed to the overall decay of oriented molecular rotation[32]. The O_2 relaxation rate is comparable to the time that we observe for the spatial randomization of CO J=29. Thus, we find that collisional reorientation rates for these two molecules are of the same order of magnitude. Although rotational relaxation is a complex process, to first order it is reasonable that molecules with similar moments of inertia would have comparable relaxation rates.

Absolute number densities can be determined from state-resolved transient IR absorption when the effective path length and ambient temperature of the ensemble are known. For the crossed beam detection in our experiments, the path length could be as small as the optical centrifuge diameter of 52 μm or as big as the cell distance of 15 cm and the distribution of states is not known. However, we can make a rough estimate based on the translational temperature and population data in Figure 4.5 and Figure 4.6. At 1 μs following the optical centrifuge pulse, CO molecules in J=29 appear to have reached a quasi-equilibrium translational temperature near 500 K which could, with caution, be taken to describe the rotational distribution. For the minimum path length of 52 μm, the resulting CO number density is $[CO] = 6 \times 10^{16}$ cm^{-3} corresponding to 40% of the 5 Torr sample. For the maximum path length of 15 cm, the resulting CO number density is $[CO] = 5 \times 10^{13}$

cm^{-3} corresponding to 0.03% of the 5 Torr sample. Estimates based on CO_2 data for which the distributions were known yielded a fractional excitation of 1-2%[29].

4.3.3 Comparison of CO and CO₂ Super Rotor Relaxation

Previously we investigated the dynamics of CO_2 super rotors in the optical centrifuge[30]. A comparison of CO and CO_2 illustrates interesting differences in super rotor collision dynamics. Here we have chosen to compare the CO J = 29 data with that for CO_2 J=76 because of several similarities in their collision properties. These states have similar rotational energy gaps (~110 cm^{-1}) and the ratio of the classical rotational period to collision duration at 300 K for both states is close to unity.

Figure 4.6c shows the polarization-dependent populations from earlier measurements of CO_2 in J = 76 following the optical centrifuge pulse and detected at a 45° IR crossing angle with respect to the centrifuge beam. The CO_2 pressure was 10 Torr, whereas that for CO was 5 Torr, leading to a factor of 2 difference in the number of collisions for Figure 6. Doppler profiles for CO_2 show that the super rotors have large amounts of translational energy, with transient translational temperatures of T >2000 K and more translational energy in the parallel population[30]. After 20 collisions, there is ~70% more population in the initial plane of rotation[30]. The population ratio for CO_2 (Figure 4.6d) persists for more than 2200 collisions with a decay constant of $\tau = 14 \pm 1$ μs or ~1400 collisions. This value is a lower limit because for the molecules with higher translational energy transport out of the probe volume is greater. The long-time decay of the population ratio shows that CO_2 rotors in high J-states act like molecular gyroscopes and maintain a preference for their initial orientation through thousands of J-changing

81

collisions. The results for CO J=29 are considerably different. The CO population ratio shows that CO undergoes spatial randomization with a decay constant near 15 collisions. Although there is a preference for the CO molecules to remain oriented in the xy-plane, the orientational anisotropy is lost nearly two orders of magnitude faster than for CO_2 rotors.

Several factors contribute to the observed differences in the dynamics of CO and CO_2 spatial reorientation. One difference is that the CO_2 super rotors have much more angular momentum than do the CO super rotors. In both sets of experiments, the molecules were first spun to frequencies near $\omega = 35$ THz based on the spectral chirp, but the molecules' rotational energy and angular momentum are determined by the rotational frequency and moment of inertia. At 35 THz, CO has a rotational energy of ~5000 cm^{-1} with J~50 while CO_2 has ~19,000 cm^{-1} and J ~220.

Molecules with larger angular momenta undergo smaller collision-induced angle shifts. CO_2 super rotor relaxation was discussed previously in terms of a simple gyroscope model to describe collisions that reorient the super rotors[30]. Collisions that are the most effective at removing orientational anisotropy in molecules with oriented angular momentum involve collision velocities that are orthogonal to the initial plane of rotation. Consider a centrifuged molecule that is spinning about its center of mass with angular velocity ω and classical angular momentum of $L = I\omega$, where I is the moment of inertia. A torque K that is applied for an instant dt at a right angle to the plane of rotation induces a change in angular momentum of magnitude Kdt. The angle change $d\varphi$ in the rotor is

$$d\varphi = \frac{Kdt}{I\omega}. \tag{4.1}$$

The torque imparted is $K = r \times dp/dt$, where r is the distance from the center of the rotor and dp is the change in momentum. Therefore, equation 4.1 becomes

$$d\varphi = \frac{r\mu dv}{I\omega},\qquad(4.2)$$

where μ is the reduced mass and dv is the change in relative velocity. Consider a 300 K collision between a non-rotating CO_2 molecule and a J = 220 CO_2 molecule. In this limiting type of collision, a tilt of 6° is induced in the rotating CO_2 molecule. A similar analysis for collisions of J=50 CO with J=0 CO yields a tilt angle of 11°. Thus, as rotational energy is dissipated through collisions, CO is predicted to undergo spatial reorientation in fewer collisions. Interestingly, the gyroscope model shows that collisions of CO_2 (J=76) and CO_2 (J=0) have the same tilt angle (16°) as collisions between CO (J=29) and CO (J=0). The angular momentum values that are initially prepared in the optical centrifuge dictate how rapidly spatial reorientation takes place.

A second important difference is that CO_2 in the optical centrifuge initially has more energy and a higher rotational state density than does CO. The J=76 state of CO_2 is further down in the energy cascade from the initial J=220 rotors than is the J=29 state of CO from the initial J=50 state. The propensity for small-ΔJ collisions means that the pathways to generate CO_2 J=76 and CO J=29 involve very different cascades. The cascades for both CO and CO_2 involve the release of large amounts of translational energy, but the amount of energy released depends on the J-state and the molecule. Large translational energy releases are seen in CO_2 J=76 following collisions of CO_2 super rotors, with the J=76 state having a translational temperature as high as 4000 K[30]. Higher J-states of CO_2 (such as J=100) probed with perpendicular IR light have smaller translational

83

energy releases, with initial temperatures near 400 K that increase through collisions to 800 K.[94] These observations show that more translational energy is found for states further down the cascade. CO prepared by the optical centrifuge initially has much less rotational energy than CO_2 and collisions lead to CO J=29 with translational temperatures near 1000 K. The extent of translational energy released depends on the initial rotational energy and the number of states in the cascade. Assuming CO_2 starts in J=220, transient population in J=76 may result from as many as 72 collisions, each with $\Delta J = -2$ whereas CO J=29 may result from 21 $\Delta J = -1$ collisions if it starts in J=50. The greater initial CO_2 rotational energy and the greater number of collisions required to reach the observed states combine so that the CO_2 signals persist for much greater times.

A practical issue to consider when comparing results for CO and CO_2 is the intensity of the transient absorption signals. The signals for CO are smaller by a factor of 20 than those for CO_2. Transient IR signal intensities depend on the number density of centrifuged molecules and the strength of the IR transition used for detection. The number density of centrifuged molecules is affected by the field strength, pressure, and the anisotropic polarizability ($\Delta\alpha$) of the molecule. Comparable field strengths were used in the two experiments but the CO pressure was half that used in CO_2 studies. The value of $\Delta\alpha$ for CO is one-fourth that of CO_2, but the ratio of $\Delta\alpha$ to moment of inertia is similar for CO and CO_2. The IR transition strength for CO J=29 is about one-eighth that for CO_2 J=76. Pressure and transition strength differences account for a factor of 16 in signal levels. Including $\Delta\alpha$ in a linear dependence increases the expected CO_2 signal enhancement to a factor of 64, which is much larger than observed.

4.3.4 J-Dependent Dynamics of CO Super Rotors

To explore higher J states of CO in the optical centrifuge, we measured transient IR absorption profiles at line center for a number of states between J=29 and 39. Transient signals were detected for J=40 and 41, but were too small for analysis. For these data, the pressure was 10 Torr and the total pulse energy was 26 mJ/pulse. Figure 4.7 shows transient absorption measurements for the CO J = 29, 35, 37, and 39 states. Each state exhibits prompt appearance, followed by slower decay. The signals approach the detector-limited response as J increases, indicating that the J=35-39 states are populated in about 20 collisions.
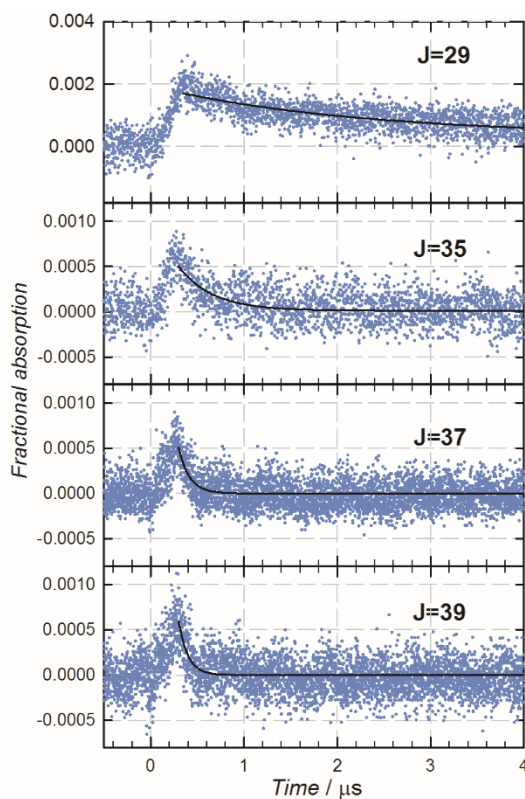
Figure 4.7 Transient absorption measurements at a pressure of 10 Torr of the CO J=29 (a), 35 (b), 37 (c), and 39 (d) states. Transient signals are fit to single exponential decays shown in black.
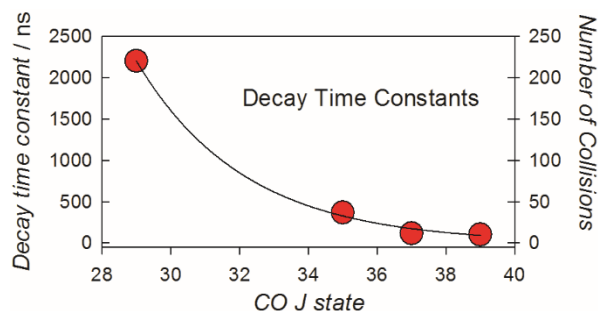
Figure 4.8 Exponential decay lifetimes of transient IR absorption signals for CO (J) based on data in Figure 4.7.

Figure 4.7 shows that population in the higher J states (J=35-39) is short-lived, as is consistent with a rotational cascade from J≈50. The transient decays were fit using single exponential functions, as shown in black in Figure 4.7. The resulting lifetimes decrease exponentially with increasing J, as plotted in Figure 4.8. The J=37 and 39 states decay with lifetimes of about 10 collisions. For CO initially prepared in J≈50, this rate indicates that rotational relaxation occurs on essentially every collision. This result is also consistent with previous double resonance studies on J-specific rotational relaxation in CO-CO collisions that find thermalization is complete for CO J=14 in 7 hard sphere collisions[47].

Recent molecular dynamics simulations by Steinitz *et. al.* provide an estimate for what the initial distribution might look like for N_2 and CO_2 in an optical centrifuge and how that distribution evolves[62]. Initially a relatively narrow asymmetric distribution of super rotor states is prepared with the optical field on. As the system relaxes back to equilibrium, the distribution of rotational states broadens substantially, with a maximum intensity at mid-J states that are lower than the initially excited molecules, but higher than the states with the greatest population at 300 K[62]. J-dependent optical centrifuge studies from our lab are consistent with the simulation results. CO_2 population in the mid-J states

86

take longer to return to equilibrium than the higher J states due to the broad distribution of population in surrounding mid-J states[94].

The lifetimes presented in Figure 4.8 show that the decay of population in the CO J = 29 state is much slower than that for J = 35 to 39. In our experiments, CO J = 29 falls in the mid-J region and has population that persists for longer times than the higher J states. Rotational relaxation for ensembles of molecules is best described by a matrix of state-to-state rate constants. The solution of the coupled differential equations describes the time evolution of the population in each state. Collision studies show that the rate constants are slightly asymmetric about the initial J state, indicating a preference to return to equilibrium[41, 94]. This asymmetry increases for the higher J states, with high J molecules being more likely to lose rotational energy than gain it. For CO, this process will move population into J = 29 from higher J states. In addition, the large translational energy that is released by super rotor collisions can also move population into the mid-J states by collision-induced excitation of thermal molecules. The longer lived population in J=29 is consistent with population coming from both higher and lower J states, as a result of the asymmetry in the rate constants. Anisotropic transport is expected to play a limited role for the higher J states since their population is gone at times shorter than the diffusion time for the IR probe volume.

4.4 Conclusions

The results presented yield a clear picture for the evolution of CO molecules after being excited to J≈50 with oriented angular momentum in an optical centrifuge. Collisions cause the rotors to lose both rotational energy and angular momentum orientation as the

system moves toward equilibrium. Polarization-dependent transient measurements show that the CO rotors undergo a collisional cascade involving impulsive collisions wherein the rotors are rotationally relaxed but preferentially maintain their original angular momentum direction. The anisotropic orientation for J=29 persists for more than 50 collisions following the optical centrifuge pulse, with a natural lifetime for spatial randomization of ~15 collisions. The scattered J=29 molecules that are aligned in the plane of the centrifuge rotation have 3 times more translational energy than those with perpendicular orientation. We observe greater translational energy in molecules that are in the initial plane of the optical centrifuge rotation and this anisotropic kinetic energy release leads to anisotropic transport of molecules away from the optical centrifuge pulse. Preferred translational energy release with CO_2 prepared with the optical centrifuge has been observed previously in our laboratory and has been predicted by theory to induce macroscopic vortices[35].

Our J-dependent measurements show that higher J states of CO (such as J = 37 and above) relax in fewer than 10 collisions, likely through transitions involving small changes in J. The spatial reorientation of CO J=29 is substantially faster compared to CO_2 J=76 rotors; the shorter-lived anisotropy in CO is a direct result of the smaller initial values of angular momentum and rotational energy in the CO molecules prepared by the optical centrifuge.

Early time measurements made at low pressure offer the best opportunity to observe the unique collisional behavior of super rotors. However, limitations of the signal-to-noise reduce the amount of information obtainable from transient data. Increasing detection

88

sensitivity and time response will enable detection of the initially centrifuged ensemble and give us an opportunity to investigate the dynamics for the first set of collisions that relax super rotors. These types of studies will provide important results that can be compared with molecular dynamics simulations and lead to a greater understanding of super rotor collisions and relaxation.

Chapter 5: Anisotropic Kinetic Energy Release and Gyroscopic Action of CO₂ Super Rotors from an Optical Centrifuge.

5.1 Introduction

At equilibrium, the spatial orientation and rotational motion of molecules are isotropic. In contrast, the ensemble of molecules excited by the optical centrifuge have a unidirectional sense of rotation with respect to the lab frame. As such, there exists a orientational anisotropy that is not present in equilibrium systems. The oriented nature of the angular momentum is a characteristic feature of the molecules prepared in the optical centrifuge and is the focus of this chapter. In this work, we interrogate orthogonal subsets of molecules after optical centrifuge excitation to study how the initial orientation of the molecules is manifested in the collision dynamics.

Previous experiments by the Mullin group have shown that angular momentum randomization of CO_2 J = 76 rotors is inhibited[30]. The molecules exhibit gyroscopic behavior—maintaining their initial orientation despite many J-changing collisions. The results in Chapter 4 show that the oriented nature of the super rotors leads to anisotropic kinetic energy in the CO J = 29 rotors[95]. This finding suggests that molecules leave the excitation volume anisotropically. Optical centrifuge experiments provide the ability to

probe the dynamics of spatially-distinct molecular ensembles in non-equilibrium environments.

.

In the experiments described in this chapter, the optical centrifuge (OC) excites an ensemble of CO_2 molecules to $J \approx 220$ with oriented angular momentum. Orthogonal IR polarizations are used to probe how the spatial orientation of the molecules affects the collision dynamics. Here, the polarization-dependent collision dynamics of CO_2 $J = 0-100$ rotors after optical centrifuge excitation are reported. Polarization-dependent, transient IR detection of the state-resolved translational energy distributions and populations of individual CO_2 states reveals information of the J-dependent spatial reorientation dynamics. New information about the spatial dependence on the kinetic energy transferred during collisions of CO_2 rotors is presented. Modifications to the IR detection set up resulted in improved signal-to-noise levels that permitted new dynamics studies in the single-collision regime.

5.2 Experimental Details

The details of the OC spectrometer have been described in Chapter 2. However, an understanding of the spatial geometry of the molecules, OC light, and IR light is crucial to the work in this chapter. The experiments described here were performed with the IR and OC beams crossing at 90°, as shown in Figure 5.1. The optical centrifuge beam propagated along the z-axis and prepared molecules with an angular momentum vector $\vec{J}_{OC}$ that was nearly parallel to the optical centrifuge propagation vector $\vec{k}_{OC}$ and the z-axis. Each CO_2 molecule that is optically centrifuged rotates with the optical field of the OC in
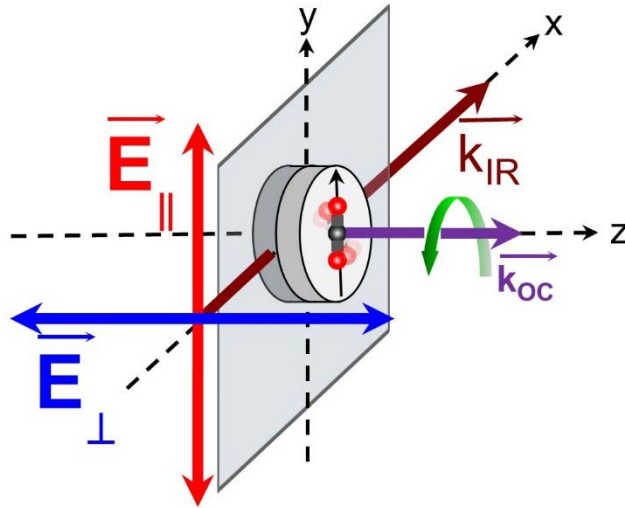
Figure 5.1 Geometry of optical centrifuge beam propagation, IR probe polarization, and initial molecular rotation.

the xy-plane. The ensemble of molecules has a unidirectional sense of rotation, corresponding to oriented angular momentum vectors. The propagation vector $\vec{k}_{IR}$ of the linearly polarized IR probe intersected the optical centrifuge propagation vector $\vec{k}_{OC}$ at 90°. The IR polarization was varied with a $\lambda/2$ waveplate. For the measurements reported here, the IR polarization was either parallel $\vec{E}_{\parallel}$ or perpendicular $\vec{E}_{\perp}$ to the xy-plane.

Molecules can have their angular momentum point along any combination of x-, y-, or z-axes. IR light polarization that is parallel to the xy-plane probes molecules with angular momentum projections along the x- or z-axes. The parallel IR probe measures a population $p_{\parallel}$ that is a sum of the population p_x (rotors with M_J along the x-axis) and population p_z (rotors with M_J along the z-axis):

$$p_{\parallel} = p_x + p_z \tag{5.1}$$

IR light polarization that is perpendicular to the xy-plane probes molecules with angular momentum projections along the x- or y-axes. The perpendicular IR probe measures a population $p_\perp$ that is a sum of populations p_x and p_y:

$$p_\perp = p_x + p_y \tag{5.2}$$

Therefore, measurements made with both probe polarizations detect molecules with all possible orientations.

As shown in Figure 5.1, the OC rotates in the xy-plane. In this work, we use the plane of OC rotation to define two orthogonal subsets of molecular rotors. The population p_z of molecules that have an angular momentum vector along the z-axis are *in-plane rotors.* The population $p_x + p_y$ are *out-of-plane rotors.* By symmetry, the out-of-plane rotors have the same dynamics. Based on equations 5.1 and 5.2, perpendicular IR-polarization probes the dynamics of out-of-plane rotors, whereas parallel IR-polarization probes the dynamics of in-plane rotors and a subset of the out-of-plane rotors.

The work presented in this chapter investigates a broad range of CO_2 rotational states. As such, two different IR sources were used in these experiments. A quantum cascade laser (QCL) probed states with J=76-100 using the ν_3 fundamental ($00^00 \rightarrow 00^01$) transition at $\lambda = 4.3$ µm. A mid-IR optical parametric oscillator (OPO) probed the J = 0 and 54 states of CO_2 using the $\nu_1 + \nu_3$ combination band ($00^00 \rightarrow 10^01$) transitions at $\lambda = 2.9$ µm.

Table 2.2 shows the resolution and power of these IR sources. The absorption strength of the combination band is ~60 times lower than that of the fundamental, thereby

minimizing interference from background CO_2 absorption[73]. In each case, the IR power was reduced significantly to avoid saturating the probe transitions.

The transient absorption measurements were made with two different IR beam path configurations as described in Section 2.2.2. A single pass configuration was used to probe the most intense part of the optical centrifuge pulse and a multipass configuration passed through the optical centrifuge pulse 11 times, as shown in Figure 2.12. In the single pass configuration, the IR light was focused to a beam waist of $\omega_0 = 52$ μm and propagated at 90° with respect to the optical centrifuge propagation. In the multipass configuration, the IR light was focused to a beam waist of $\omega_0 = 230$ μm and propagated at nearly 90° with respect to the optical centrifuge beam. Figure 2.13 shows a side view of the relative overlap between the IR and OC beams for the two detection configurations.

To investigate the role that intensity plays in the collision dynamics of molecular super rotors, two different focusing lenses for the OC beam were used for these studies. A 50 cm lens was used to focus the OC light to a beam waist of $\omega_0 = 26$ μm with a peak field intensity of 42 TW/cm^2. A 100 cm lens was used to focus the OC light to a beam waist of $\omega_0 = 51$μm with a peak field intensity of 11 TW/cm^2. Throughout this chapter, the high intensity (42 TW/cm^2) OC and low intensity (11 TW/cm^2) OC are defined by these conditions.

A range of pressures was used in these experiments as well. The average time between collisions, Δt_C, from gas kinetic theory described in Section 2.3.1, provides a way in which to compare experiments collected at different pressures. Time t is converted to the average number of collisions, $N = t / \Delta t_C$. Because the time between collisions

depends on the translational temperature of the molecules, the 300 K gas kinetic collision number provides a lower limit of the number of collisions. For a 300 K sample, at 10 Torr the time between collisions is approximately 10 ns. At 7.5 Torr, $\Delta t_C \cong 15$ ns and at 5 Torr, $\Delta t_C \cong 20$ ns.

5.3 Results and Discussion

The results presented here are divided into two sections. The first section focuses on single pass measurements, which provide an overview of the J-dependent and polarization-dependent dynamics of CO_2 J=0-100 rotors. These studies identified the best conditions for observing super rotor collision dynamics. The second section reports on multipass measurements, which probed the collisional dynamics and spatial reorientation of super rotor molecules.

5.3.1 Single Pass Measurements

This section provides an overview of the polarization-dependent dynamics from measurements of the line-center absorption for 6 rotational states of CO_2 ranging from J = 0 to 100. Modifications made to the instrument and experimental procedure are described and the new results are compared with previous work. A study of the state and pressure dependent trends is reported. The influence of intensity and pressure on the polarization-dependent Doppler profiles are also investigated. J-dependent trends in the time-resolved translational temperature of the J = 0, 54, and 76 are presented. Population ratios in the J=76 and 100 states give information about the spatial reorientation of super rotors.
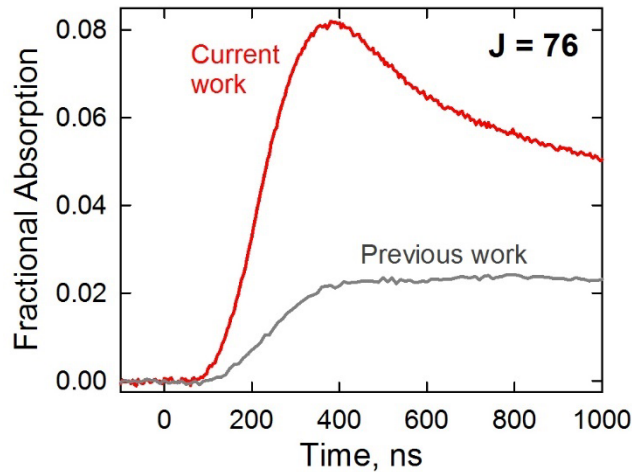
Figure 5.2 Comparison of transient signal collected in previous work[30] with a lead-salt diode crossing the OC at 45° and collected in current work with a quantum cascade laser crossing the OC at 90°. Both measurements probed CO_2 J = 76 with parallel IR polarization and used the high intensity OC.

Comparison with Previous Results

The polarization-dependent studies presented here are compared with previous polarization-dependent studies of CO_2 J=76 [30]. A number of modifications have been made to the instrument and experimental methods to increase the signal level and reproducibility in Doppler-broadened line profiles. The previous work performed a polarization-dependent study for CO_2 J=76 using an IR beam crossed at 45° with respect to the OC beam. A lead-salt diode laser was used and the IR polarization was changed using steering mirrors on a periscope. The new experiment used a quantum cascade laser that has better polarization quality and power stability. Polarization control in the new experiments was achieved by using a $\lambda/2$ waveplate. Other improvements include better methods to overlap the OC and IR probe beams. The more consistent overlap volume leads to increased signal-to-noise levels and reproducibility. Figure 5.2 shows line center transient absorption signals for CO_2 J = 76. The signal-to-noise was improved by a factor of four for this state. The reproducibility of the measured Doppler-broadened line profiles

96
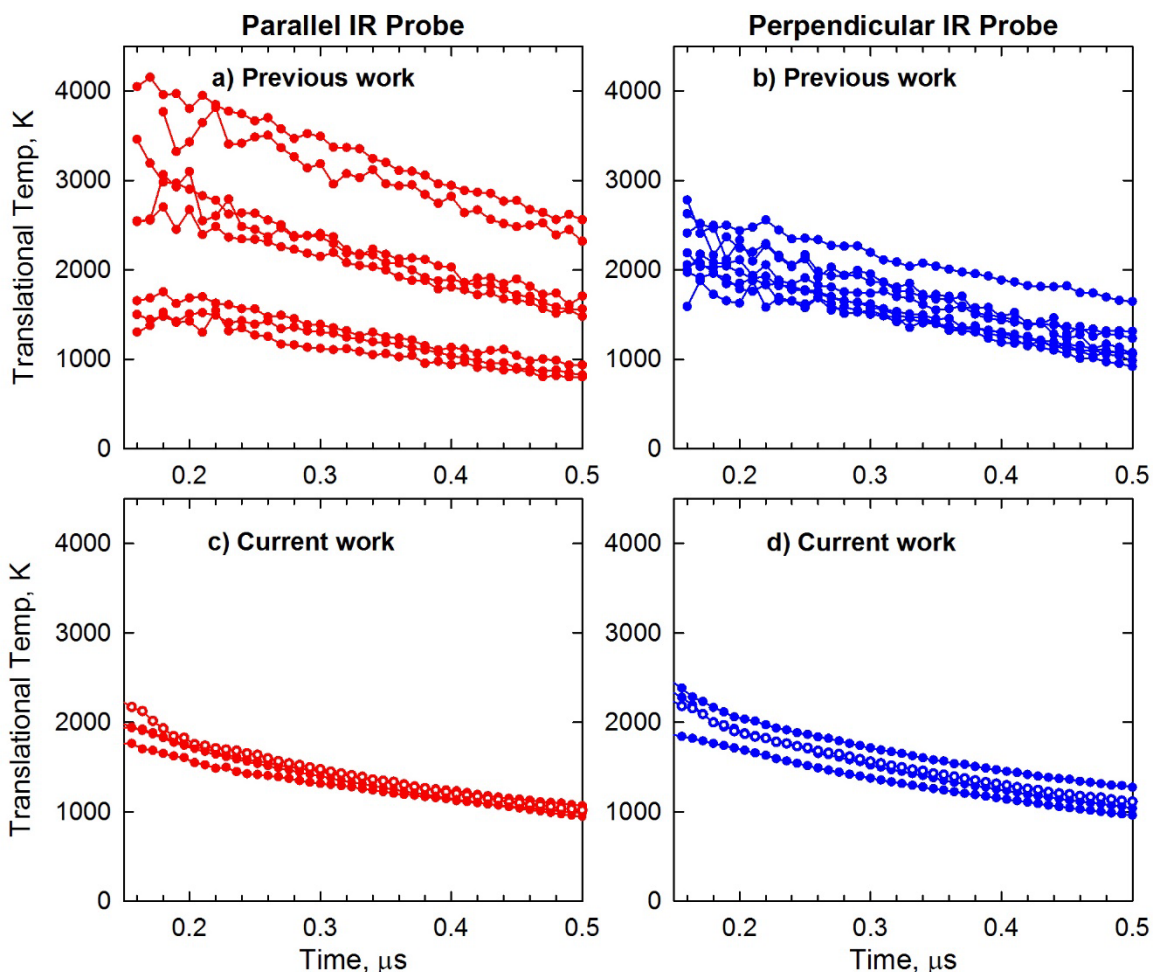
Figure 5.3   Polarization-dependent translational temperatures showing reproducibility of results from previous work collected with parallel (a) and perpendicular (b) probing and current work collected with parallel (c) and perpendicular (d) probing. The graphs show 8 measurements from the previous work[25] which probe at 45° with respect to the OC beam and 4 measurements from the current work, which probe at 90° with respect to the OC beam. Both studies were conducted at 10 Torr with a high intensity OC.

was further improved by smoothing the transient absorption measurements with a Savitsky-Golay filter, thereby reducing noise.

Figure 5.3 shows 8 measurements of the polarization-dependent translational temperatures collected in the previous work (Figure 5.3a and b) and 4 measurements of the temperatures collected in the new study (Figure 5.3c and d). In the previous work, the spread in the temperatures measured with parallel IR probing was about 2000 K, whereas

the spread with perpendicular probing was about 1000 K. In the current work, the spread in the translational temperatures was reduced to less than 300 K for both probe polarizations. The translational temperatures measured with parallel probing in the previous work are on average slightly larger than those measured in the current work. These data show that measurements of the translational temperature are sensitive to the IR polarization set up. Overall, the translational temperatures are consistent with previous results.

J-Dependent Overview of Polarization-Dependent Dynamics

The dynamics of CO_2 in a number of J states were investigated using parallel and perpendicular IR probing, as described in the experimental details section above. These measurements were made using the low intensity OC and a CO_2 pressure of 10 Torr. Figure 5.4 shows line center transient absorption measurements for the J=100, 92, 88, 76, 54, and 0 states. Appearance of population was observed in the J=100, 92, 88, 76, and 54 states, whereas depletion of population was observed in the J=0 state. Of the states shown, molecules in the J = 100 state appear earliest and appearance times become longer as J decreases. The left column of Figure 5.4 shows the early time polarization-dependent signals for the 6 states, with parallel probing in red and perpendicular probing in blue. This color coding will be used throughout this chapter. To check the reproducibility of the transient signals, the measurements were collected at least 3 times for each state and probe polarization. In all states, the parallel probe signal (shown in red) appears before the perpendicular probe signal (shown in blue), i.e. in-plane rotors appear before out-of-plane

rotors. Because the OC initially prepares molecules with angular momentum vectors along the z-axis (see Figure 5.1), in-plane rotors are expected to appear first.
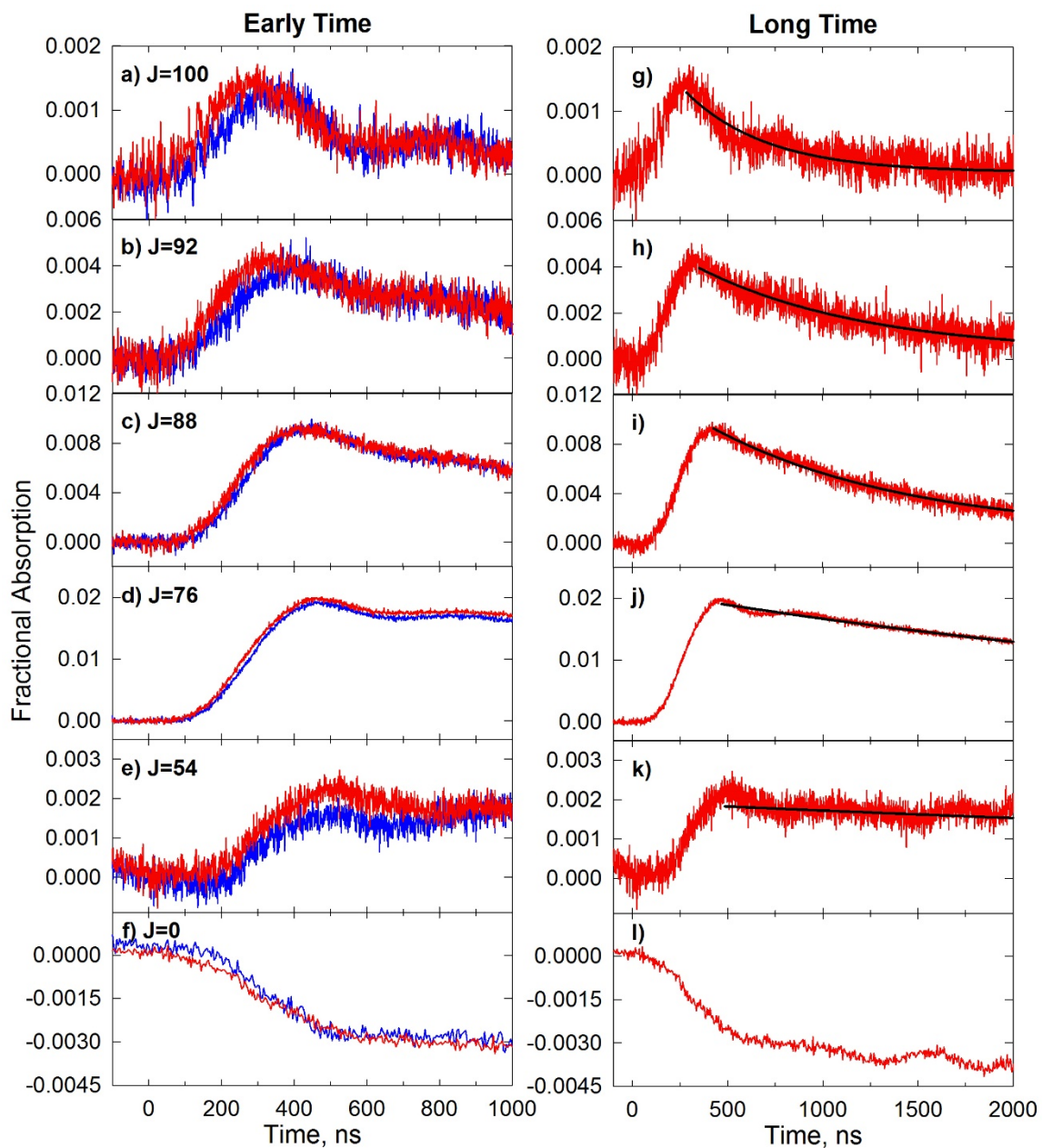
Figure 5.4 Line center transient absorption measurements of CO_2 J= 100 (a, g), 92 (b, h), 88 (c, i), 76 (d, j), 54 (e, k), 0 (f, l). The left column shows polarization-dependent early time behavior with parallel IR polarization probing in red and perpendicular IR probing in blue. All measurements are made with the low intensity OC and a CO_2 pressure of 10 Torr. The right column shows long time behavior of the parallel measurements. Exponential fits to the signal decay are shown in black for the J=100, 92, 88, and 54 states.
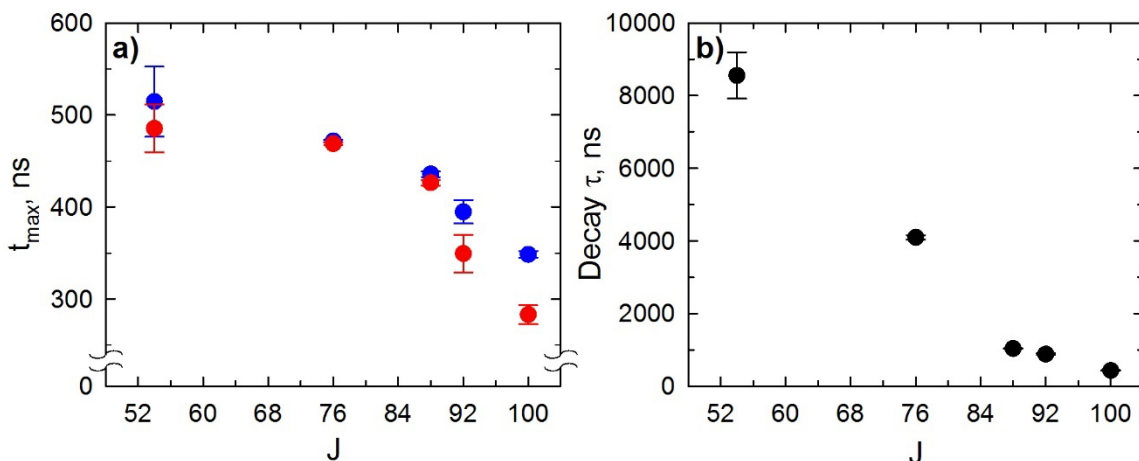
Figure 5.5 a) Average time at which transient signals reach a maximum, t_{max}, for each state and probe polarization. Parallel IR probing is in red and perpendicular probing is in blue. b) Exponential lifetime of signal measured with parallel probing for the J=54, 76, 88, 92, and 100 states.

To quantify this polarization-dependent difference, the time at which the transient signal reaches a maximum, t_{max}, was determined for each measurement. Figure 5.5a shows the average t_{max} for each probe polarization of the five states in which the appearance of population is detected. As J increases, t_{max} decreases and there is a greater difference between t_{max} measured with parallel and perpendicular probing. The larger uncertainty in the J=54 state data is due to increased interference from atmospheric absorption.

The right column of Figure 5.4 shows the long-time behavior of the transient signals measured with parallel IR probing. The signal decays in the J=100, 92, 88, 76, and 54 states are fit to exponential functions. The fits are shown in black in Figure 5.4. Figure 5.5b shows the natural lifetimes τ of the J=100, 92, 88, 76, and 54 states. Population in the J=100 state is the shortest lived of this group. As J decreases, the lifetime of the decay increases. This observation is evidence of a collisional cascade, which relaxes population from the high J states generated in the optical centrifuge down to lower thermally populated states.

Transport of molecules away from the probe volume can impact the decay of the transient signals. The probe IR in these measurements had a beam waist of $\omega_0 = 48$ μm. In the diffusive limit, a CO_2 molecule will diffuse out from the center of the probe volume at 10 Torr and 300 K in about 1700 ns. The 300 K diffusion rate gives an upper limit to the time it takes for molecules to leave the probe volume. Collisions of optically centrifuged molecules result in large translational energies and transport a. At 1000 K, a CO_2 molecule diffuses out of the probe volume in about 300 ns. Therefore, in order to mitigate diffusional effects, results are presented out to 1000 ns for the remainder of this chapter.

Effects of Intensity and Pressure

In this section, the effects of sample cell pressure and optical centrifuge intensity on the polarization-dependent dynamics of CO_2 rotors are reported. Line center transient IR absorption measurements correspond to the dynamics of molecules with zero Doppler shift. Here, line center measurements are reported for the J = 76 and 100 states at each polarization with sample pressures from 2 Torr to 10 Torr. Doppler-broadened line profiles measure the distribution of velocities along the beam direction. The Doppler profiles of the CO_2 J = 76 state are reported at two OC intensities and two pressures. The time evolution of translational temperature as determined from the Doppler profiles is also reported for each IR probe polarization.
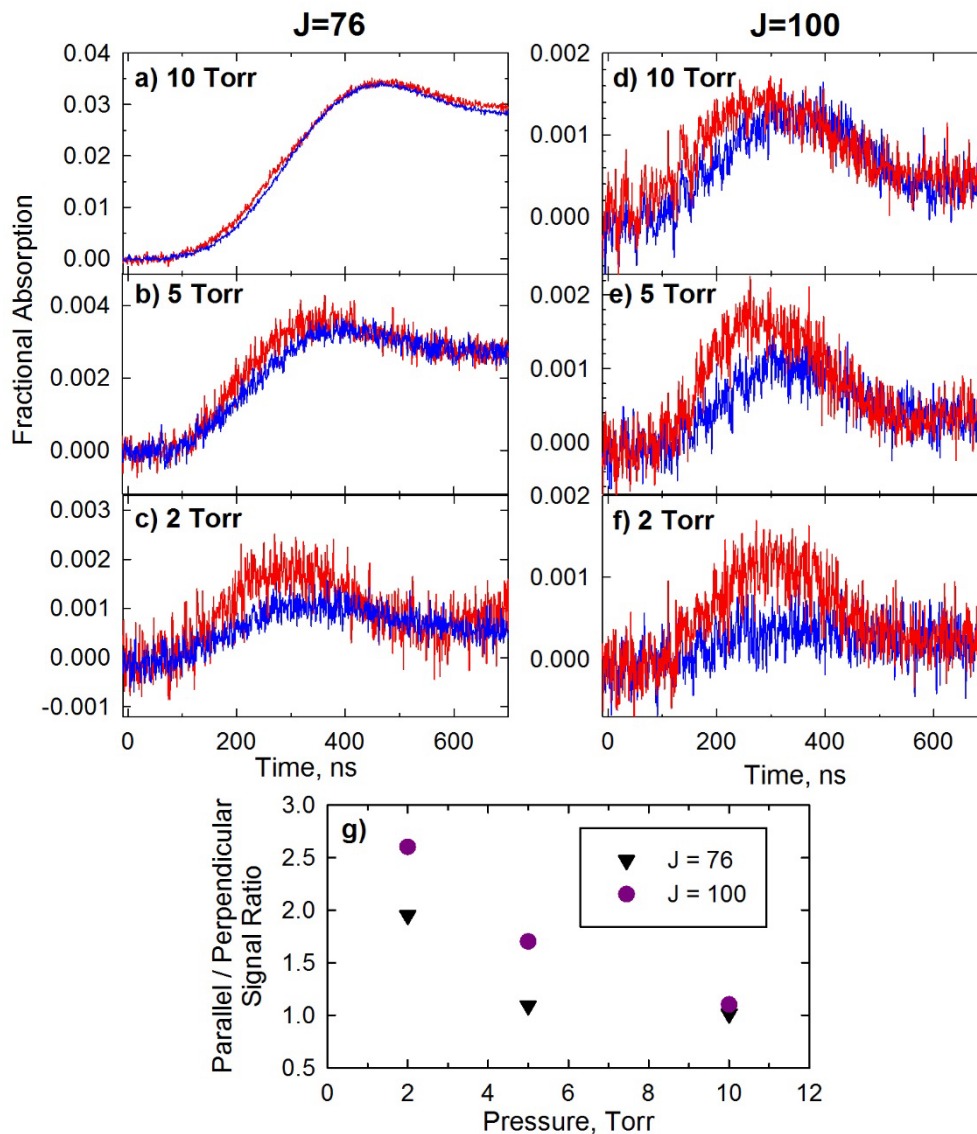
Figure 5.6 Polarization-dependent transient absorption measurements of CO_2 J = 76 (a-c) and J = 100 (d-f) at 10 Torr, 5 Torr, and 2 Torr. Parallel probing is in red, while perpendicular probing is in blue. Measurements are collected with the low intensity OC. g) Ratio of parallel signal at its maximum to perpendicular signal at its maximum as a function of pressure.

Figure 5.6 shows line-center, polarization-dependent absorption measurements of the J = 76 and J = 100 states at 10 Torr, 5 Torr, and 2 Torr collected at low OC intensity (11 TW/cm^2). For the J = 76 state, transient absorption signals with parallel and perpendicular probing are nearly identical at 10 Torr, whereas at 2 Torr differences in

parallel and perpendicular probing provide evidence for more pronounced orientational anisotropy. Evidence for orientational anisotropy is even more pronounced for the $J = 100$ state. Figure 5.6g shows the ratio of the parallel signal (at its maximum) to the perpendicular signal (at its maximum) as a function of pressure for both states. These data show that differences between parallel and perpendicular probing are more pronounced at lower pressures and higher J states.

The line center measurements yield information about a single Doppler slice of the polarization-dependent populations. To investigate the total population change, full Doppler-broadened line profiles were measured by collecting transient absorption measurements in a series of frequency steps as small as 0.001 cm^{-1}. The line profiles were fit to Gaussian functions, as described in Chapter 2. Translational temperatures were determined from the profile widths. Transient Doppler-broadened line profiles were measured for the $J = 76$ state of CO_2 at two OC intensities and two pressures. Figure 5.7 shows the Doppler-broadened line profiles for CO_2 J=76 at 200 ns at 10 Torr and 7.5 Torr, both collected with the low intensity OC. Measurements with parallel and perpendicular IR probing are shown. At 10 Torr and 200 ns after optical centrifuge excitation, the molecules measured with parallel IR probing had a translational temperature of 1800 ± 70 K, whereas the rotors measured with perpendicular IR probing had a translational temperature of 1710 ± 60 K. At a lower pressure of 7.5 Torr, the molecules measured with the parallel probe had a temperature of 960 ± 50 K and the out-of-plane rotors had a temperature of 1080 ± 50 K.
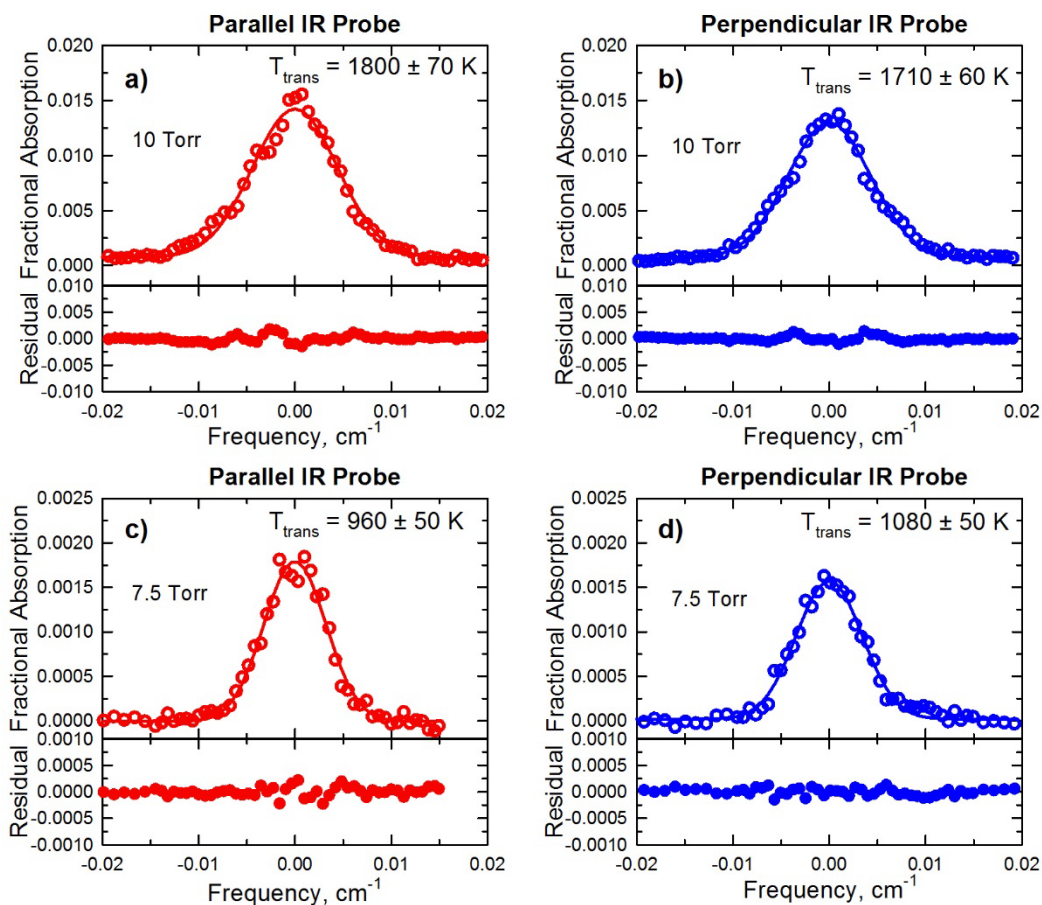
Figure 5.7 Doppler-broadened line profiles of the CO_2 J=76 state at 200 ns collected with the low intensity (11 TW/cm^2) OC. The profiles with 10 Torr of gas for parallel (a) and perpendicular (b) probing are displayed. The profiles with 7.5 Torr of gas collected with parallel (c) and perpendicular (d) probing are also shown.

As discussed in section 5.2, the parallel IR probe detects in-plane rotors as well as a subset of out-of-plane rotors. The Doppler profiles measured with parallel IR probing therefore contain contributions from both sets of molecules. The contribution from the out-of-plane rotors is obtained directly from the Doppler profiles with perpendicular IR probing. It is possible therefore to characterize the in-plane component of the parallel profiles by modeling the parallel profiles as a sum of two Gaussian functions. The parameters for one Gaussian would be determined from the out-of-plane measurements and those for the in-plane component would be fit from the parallel profiles. This process

was performed for the J = 76 state and the resulting translational temperatures of in-plane rotors were found to be about 10-15% lower than those determined from a single Gaussian fit. The extent to which the parallel Doppler profiles describe the in-plane rotors depends on the relative magnitude and broadening of both components. In this case, the differences between the various populations is not too significant and the analysis to extract the in-plane profiles has not been performed. The analysis described here can be used in future studies where there are substantial differences between the in-plane and out of plane populations.

A key result in Figure 5.7 is that lowering the pressure reduces the translational temperature of the molecules. At lower pressures, there are fewer super rotors because there are fewer molecules in the excitation volume. Because the total energy imparted to the sample is proportional to the number of super rotors, the lower translational energy is evidence of the reduced overall energy of the sample. There are no significant differences in the translational temperatures measured with parallel and perpendicular probing. However, at 7.5 Torr the magnitude of the Gaussian profile measured with parallel probing appears larger than that measured with perpendicular probing. This difference suggests that a greater population of in-plane rotors is detected than out-of-plane rotors. Lower pressures, having fewer collisions, appear to increase the retention of the population anisotropy.

Polarization-dependent Doppler-broadened profiles of the J=76 state were also collected with the OC at high intensity (42 TW/cm^2). Figure 5.8 shows the Doppler profiles measured at 200 ns with each probe polarization and with sample pressures of 10
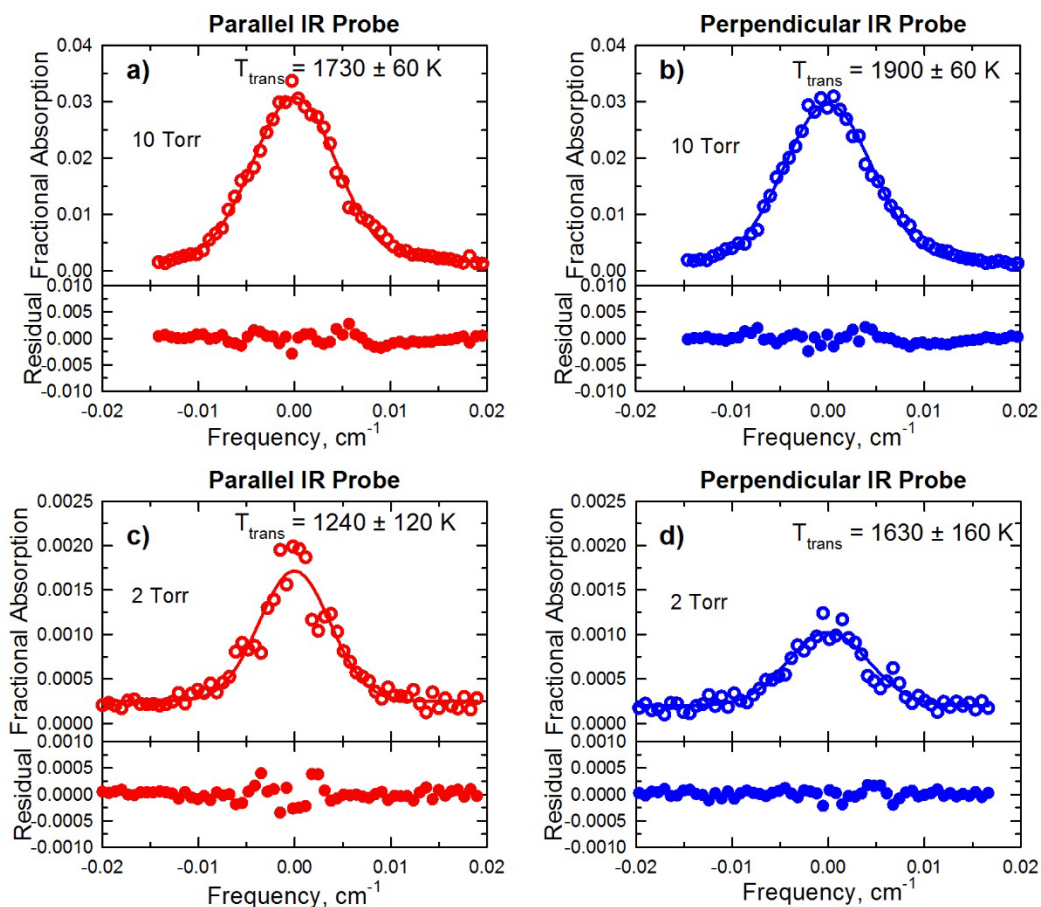
Figure 5.8 Doppler-broadened line profiles of the CO2 J=76 state at 200 ns collected with the high intensity (42 TW/cm²) OC. The profiles with 10 Torr of gas for parallel (a) and perpendicular (b) probing are displayed. The profiles with 2 Torr of gas collected with parallel (c) and perpendicular (d) probing are also shown.

Torr and 2 Torr. At 10 Torr and 200 ns, the in-plane rotors and molecules rotating in the yz plane measured with parallel IR probing have a translational temperature of 1730 ± 60 K, whereas the out-of-plane rotors measured with perpendicular IR probing have a translational temperature of 1900 ± 60 K. At a lower pressure of 2 Torr, the molecules measured with parallel probing have a temperature of 1240 ± 120 K and those measured with perpendicular probing have a temperature of 1630 ± 160 K.

Comparing the translational temperatures measured with parallel and perpendicular probing shows that at 10 Torr the out-of-plane molecules carry marginally more translational energy. At 2 Torr this difference in translational energy is somewhat more pronounced. In addition, the amplitude of the parallel Doppler profile is larger than that of the perpendicular profile, indicating greater population for parallel probing. At 2 Torr, the 300 K gas kinetic collision time is $\Delta t_C \cong 50$ ns. Therefore, at $t = 200$ ns, approximately $t/\Delta t_C = 4$ collisions have taken place. As with the low intensity data, greater retention of the population anisotropy is observed at lower pressures.

At 10 Torr the translational temperatures measured with the OC at high intensity (Figure 5.8) are slightly higher than the translational temperatures measured with the OC at low intensity (Figure 5.7). The higher intensity optical centrifuge traps more molecules due to a deeper interaction potential as described by equation 2.8. As discussed in Section 2.1.1 molecules can fall out of the trap as they are rotationally excited. The higher translational energies observed with the higher intensity OC may be a result of a higher initial super rotor density.

Figure 5.9 shows the time evolution of the polarization-dependent translational temperatures of CO_2 J = 76 using high and low OC intensities and various pressures. Under these conditions, large translational temperatures (≥ 900 K) are seen within the first 200 ns. Reducing the OC intensity reduces the translational energy released by the super rotors. At 10 Torr with the high intensity OC, translational energy gains are largest at the earliest times measured (100 ns). In contrast, with the lower intensity OC, the translational energy increases from 100 to 200 ns. The number density of super rotors is proportional to the
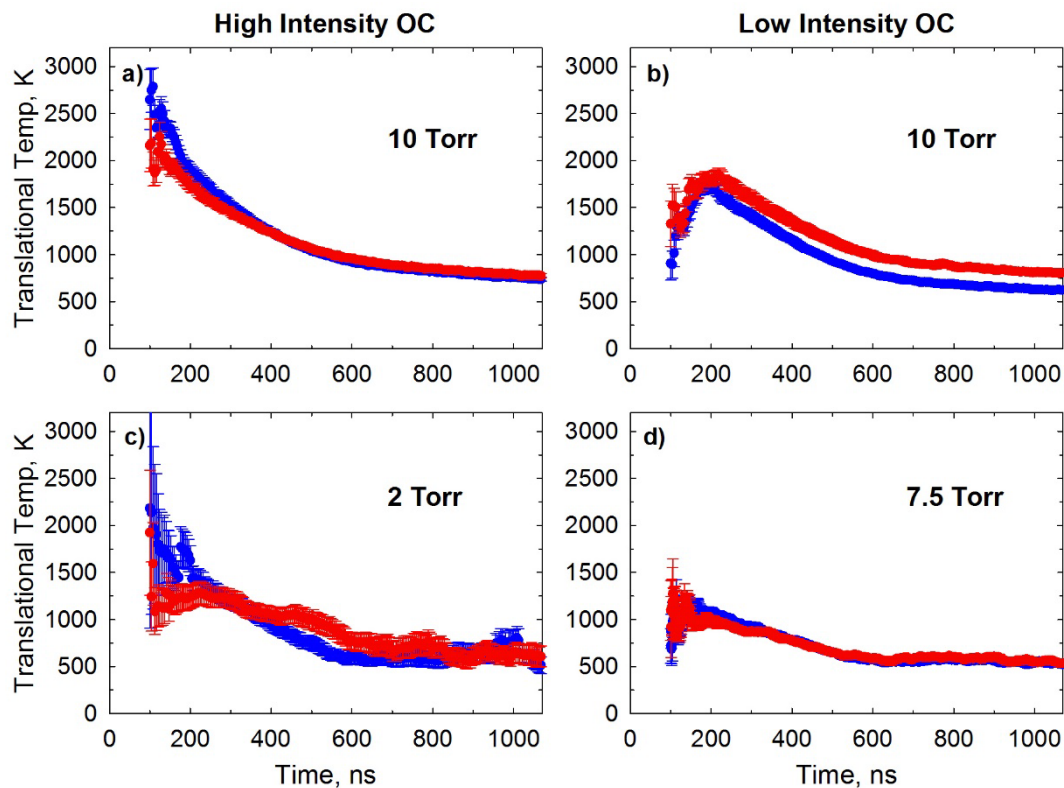
Figure 5.9 Time evolution of translational temperature with parallel (red) and perpendicular (blue) probing of CO_2 J=76 with the high intensity (42 TW/cm^2) OC at 10 Torr (a) and 2 Torr (c) and with the low intensity (11TW/cm^2) OC at 10 Torr (b) and 7.5 Torr (d).

intensity of the OC, so that with lower intensities, there are fewer super rotors. The lower translational temperatures measured from 100 to 200 ns with the low intensity OC support this picture. The lower pressure measurements show how the translational energy evolves in lower density samples. Super rotor orientation is most apparent at higher OC intensities and lower pressures.

J-Dependent Translational Energies and Populations: J = 76, 54, and 0

In this section, the J-dependence on the dynamics of rotational relaxation and spatial reorientation in the OC is described. A set of experiments performed with the OC at high intensity measured the time evolution of the polarization-dependent translational temperatures for the J = 76, 54, and 0 states. The total population change in each individual

state was determined by integrating the area under the Doppler profiles. The data provide information on the J-dependent spatial reorientation of the molecules after OC excitation.

Polarization-dependent Doppler-broadened line profiles were measured for the J=0, 54, and 76 states at 10 Torr with the OC at high intensity. Figure 5.10 shows the time evolution of the polarization-dependent translational temperatures (left column) determined from the Doppler profiles. In the right column, the corresponding polarization-dependent populations are shown. The insets in each of the translational temperature graphs shows the reproducibility of individual temperature measurements. Appearance of population is observed in the J =76 and 54 states, whereas depletion of population is observed in the J = 0 state. Figure 5.10a shows that impulsive collisions impart large amounts of translational energy to the molecules in the J = 76 state. At early times, the translational temperatures of rotors probed with perpendicular polarization are greater than the temperatures of molecules probed with parallel polarization. Figure 5.10c shows that molecules in the J = 54 state have translational temperatures above 300 K, but the temperatures are not as high as those for the J = 76 state. For J = 54, the early time perpendicular probe translational temperatures are greater than the parallel probe translational temperatures. Figure 5.10e shows that molecules with a sub-thermal velocity distribution are removed from the J = 0 state. The data indicate that cross sections for CO_2 J = 0 molecules and rotationally excited molecules increase as the collision energy decreases.

Anisotropic translational energy release is detected at early times for the J = 76 and J = 54 states (Figure 5.10a and Figure 5.10c). This result shows that the out-of-plane rotors

initially have more translational energy than do the molecules probed with parallel IR polarization. The different energy distributions of the different subsets of molecules reveals information about rotation-to-translation (R→T) energy transfer in super rotor collision
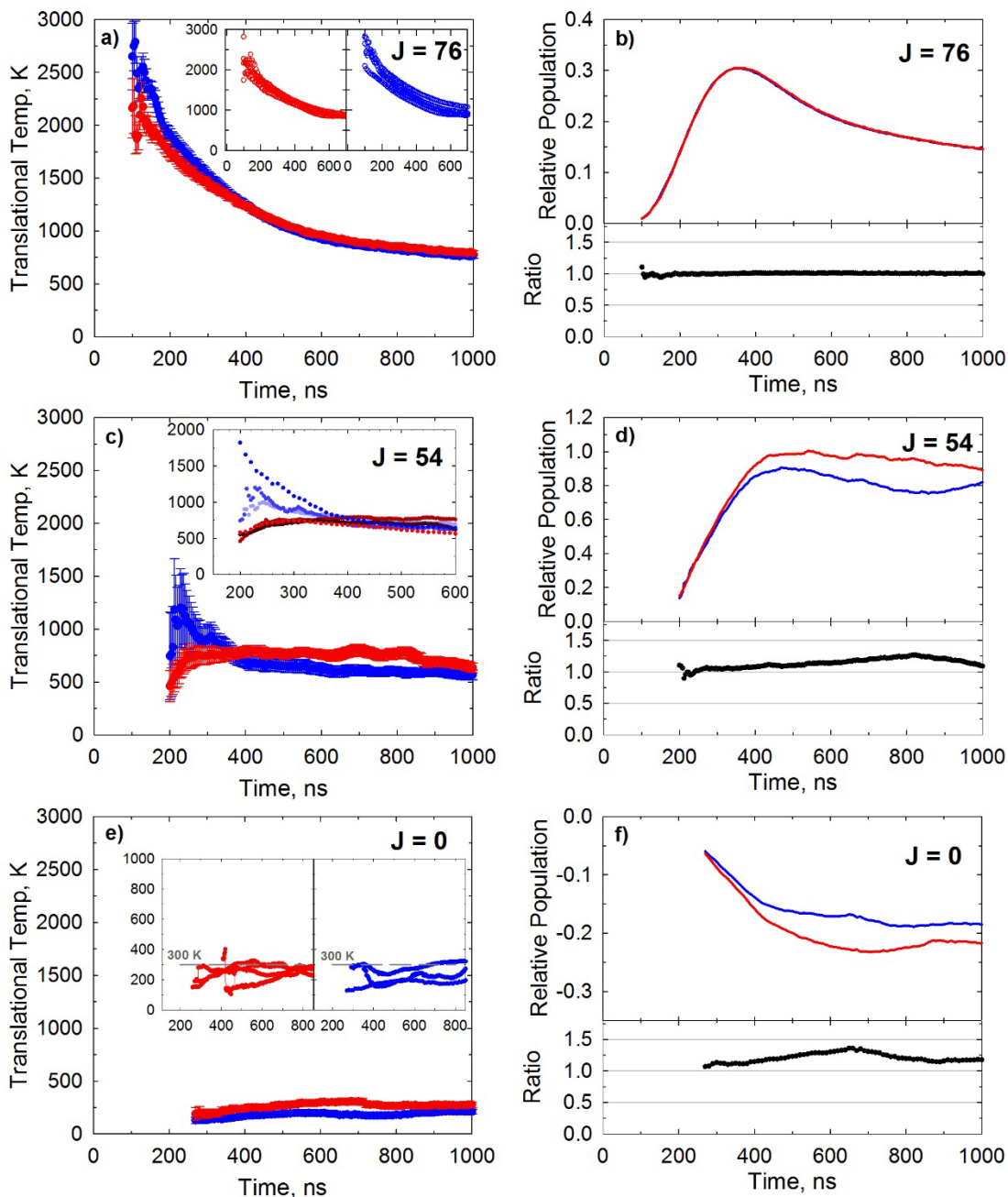
Figure 5.10 Polarization-dependent translational temperatures and populations for the J = 76 (a and b), J = 54 (c and d), and J = 0 (e and f) states. The inset in a, c, and e shows the reproducibility of the translational temperatures. The lower panel of the population plots shows the ratio of in-plane rotors to out-of-plane rotors. All measurements were collected with 10 Torr of gas and the high intensity (42 TW/cm^2) OC.

dynamics. In Chapter 3, results showed that there is a propensity for super rotor molecules to undergo small changes in J during collisions. In a rigid rotor molecule, the energy gap between adjacent rotational levels increases linearly with J. At super rotor states near J = 220 this energy gap is about 300 cm^{-1}. Molecules detected with parallel polarization arise predominantly from collisions between two super rotor molecules. Two super rotor molecules have comparable rotational energy gaps. Collisions between two super rotors that result in resonant rotational energy transfer leave small amounts of energy available to go into translation. In contrast, the out-of-plane rotors detected with perpendicular polarization arise predominantly from collisions between a super rotor and a 300 K bath molecule. The energy gap between adjacent states for the 300 K bath molecule is much smaller than the gap between states for the super rotor. Collisions between a super rotor and bath molecule that result in non-resonant rotational energy transfer leave large amounts of energy to go into translation. Furthermore, the out-of-plane rotors, which are hotter, translate out of the probe volume faster.

There is no detectable difference between the polarization-dependent translational temperatures for the J = 0 state. Collision cross sections to remove molecules from the J = 0 state are independent of the molecules' spatial orientation.

Populations were obtained for the J = 76, 54, and 0 states by integrating the area under the Doppler-broadened line profiles. The populations were normalized for J-specific IR absorption strength and were scaled relative to the maximum population reached in the J = 54 state. The right column of Figure 5.10 shows the polarization-dependent populations. The population ratio for parallel:perpendicular probing is close to 1 for all

three J states. The data for J = 54 and 0 states have larger uncertainties due to larger

background IR absorption (small I_0), which contributes to the fluctuations away from 1.

The J = 76 and 54 states, despite anisotropic translational energy distributions, have

isotropic spatial distributions. The translational energy of J = 0 molecules does not depend

on their orientation and the molecules have an orientationally isotropic spatial distribution.

These observations are to results for J = 100 in the next section

Dynamics and Spatial Reorientation for CO_2 J = 100

Additional experiments were performed with the OC at low intensity to probe the

evolution of the Doppler profiles and polarization-dependent populations in the J = 100

state at 7.5 Torr. These results are compared with those for the J = 76 state. Figure 5.11

shows the polarization-dependent Doppler profiles for J = 100. There is essentially no

difference between the translational temperatures with parallel probing and those with

perpendicular probing. The amplitude of the Doppler profile in Figure 5.11a is greater than

the amplitude of the Gaussian in Figure 5.11b, indicating that the parallel population is
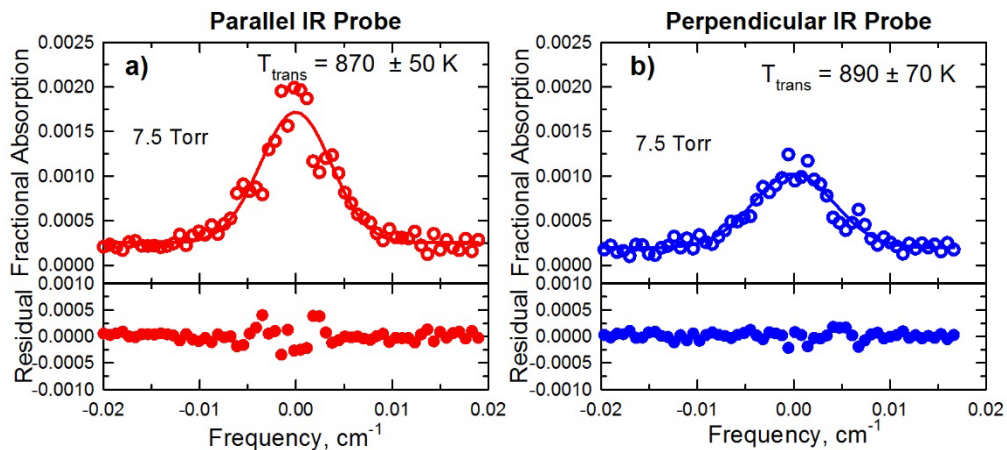
Figure 5.11 Doppler-broadened profiles at 200 ns of J = 100 rotors collected with 7.5 Torr of gas and the low intensity OC. Profiles measured with parallel (a) and perpendicular (b) probing are shown.
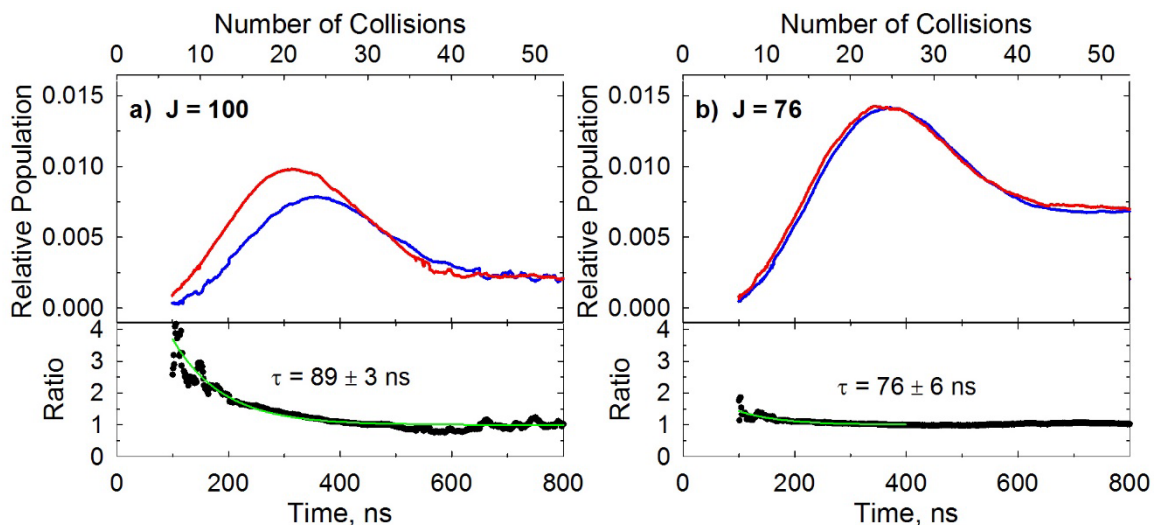
Figure 5.12 Polarization-dependent populations of the J = 100 (a) and J = 76 (b) states collected with 7.5 Torr of gas and the low intensity OC. The lower panel in each graph shows the ratio of in-plane rotors (red) to out-of-plane rotors (blue).

larger than the perpendicular population. Anisotropic motion away from the probe volume has a a comparable effect on both populations because the translational temperatures are approximately equal. Comparing the J = 100 Doppler profiles with the Doppler profiles of J = 76 shown in Figure 5.7c and Figure 5.7d shows that molecules appearing in both states have similar translational temperatures (870 K and 960 K, respectively). The difference in the amplitudes of the polarization-dependent Doppler profiles is more pronounced for the J = 100 state than for the J = 76 state.

Figure 5.12 shows the polarization-dependent relative populations of the (a) J = 100 and (b) J = 76 states. The population is normalized for J-specific IR absorption strength and scaled relative to the maximum population of the J = 54 state. At 100 ns (about 7 collisions) for the J = 100 state, nearly four times as much population is observed with parallel probing compared to perpendicular probing. In contrast, for J = 76 molecular there is less than twice as much population observed with parallel probing. The lower panels in

113

Figure 5.12a and b show the time evolution of the parallel:perpendicular population ratio. The lifetime τ of the population ratio decay was determined by fitting the ratio to an exponential function. For the J =100 rotors the ratio decays with $\tau = 89 \pm 3$ ns (about 6 gas kinetic collisions) and for the J = 76 rotors the ratio decays with $\tau = 76 \pm 6$ ns (about 5 gas kinetic collisions). As described in Section 5.2, the parallel IR probe measures a molecule population, $p_\parallel$, which is a sum of the in-plane rotors p_z and a subset of out-of-plane rotors p_x (equation 5.1). The ratio of $p_\parallel/p_\perp$ is an experimental measure that indicates whether orientational anisotropy is present in the sample. However, to determine the population of only the in-plane rotors, the contribution from p_x rotors in the parallel measurement must be removed. From symmetry, $p_x = p_y$. Equations 5.1 and 5.2 can be rewritten to solve for the population of in-plane rotors (p_z) and the total population $p_{tot} = p_x + p_y + p_z$:

$$p_z = p_\parallel - \frac{1}{2}p_\perp \tag{5.3}$$

$$p_{tot} = p_\parallel + \frac{1}{2}p_\perp \tag{5.4}$$

Equations 5.3 and 5.4 were used to determine the fraction f_z of in-plane rotors:

$$f_z = \frac{p_z}{p_{tot}} = \frac{p_\parallel - \frac{1}{2}p_\perp}{p_\parallel + \frac{1}{2}p_\perp}. \tag{5.5}$$

In an isotropic sample, there is an equal number of rotors with angular momentum along each of the three Cartesian axes and $f_z = 1/3$. Strictly speaking, equation 5.5 assumes that the translational temperatures of the molecules in each plane are the same. Since the
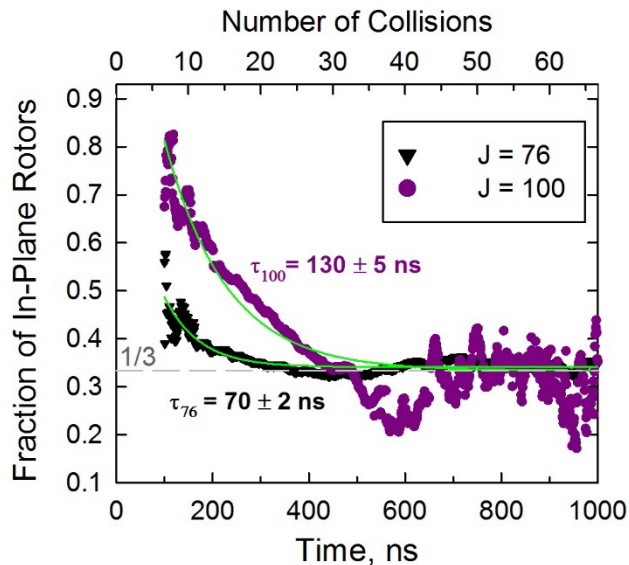
Figure 5.13 Fraction of in-plane rotors in a 7.5 Torr sample using the low intensity OC for the J = 76 and 100 states as a function of time. The data are fit to exponential functions shown in green. The exponential lifetimes the decay for each state are shown in the plot.

translational temperatures detected with the both polarizations are generally close the effect is minor (< 10%).

Figure 5.13 shows the time evolution of the fraction of in-plane rotors for the J = 76 and 100 states using the data in Figure 5.12. At 100 ns (about 7 gas kinetic collisions) approximately 80% of the molecules in the J = 100 state had their angular momentum along the z-axis, which is the angular momentum orientation prepared by the OC. For J = 100, the fraction of in-plane rotors decays with an exponential lifetime $\tau_{100} = 130 \pm 5$ ns (about 9 gas kinetic collisions). At 100 ns approximately 50% of the molecules in the J = 76 state had their angular momentum along the z-axis. For J = 76, the fraction of in-plane rotors decays with an exponential lifetime $\tau_{76} = 70 \pm 2$ ns (about 5 gas kinetic collisions). A significant ($f_z \gg 1/3$) orientational anisotropy is detected in both states at early times. Notably, molecules in the J = 100 state have more orientational anisotropy than the J = 76

molecules. Furthermore, the anisotropy lasts longer for the J = 100 rotors than it does in for J = 76 rotors. At long times the fraction of in-plane rotors approaches 1/3, indicating that the sample has become orientationally isotropic.

The increased lifetime of the orientational anisotropy in the higher J state can be understood in terms of in terms of the simple gyroscope model discussed in Section 4.3. The most effective collisions at removing orientational anisotropy in molecules with oriented angular momentum involves collision velocities that are orthogonal to the initial plane of rotation. Consider such a collision between a J = 76 rotor and a rotationless 300 K molecule. The maximum collision-induced tilt of the J = 76 rotor according to a gyroscope model is about 16°. In a similar collision with a J = 100 rotor, the maximum collision-induced tilt is about 12°. The gyroscope model provides a picture of why the J = 100 rotor's angular momentum orientation is more stable during collisions.

The single-pass polarization-dependent measurements described in this section have revealed new information about the collision dynamics of super rotors from an optical centrifuge. Orientational anisotropy is most apparent in polarization-dependent measurements for J states at low pressures with high OC intensities. Polarization-dependent Doppler profiles show that out-of-plane rotors carry more translational energy than do in-plane rotors. This anisotropic kinetic energy release can be understood by considering super rotor collisions that involve rotationally resonant and non-resonant energy transfers. The observed rates for collision-induced randomization of the orientation is understood in terms of a classical gyroscope picture. Experiments to investigate this

phenomena further are challenging because signal-to-noise is small at low pressures and in high J states. In addition, transport of molecules out of the probe volume can contribute to time-dependent signal loss. A new multipass IR detection scheme was developed to mitigate these effects and to probe even higher states under low pressure conditions. These multipass measurements are described next.

5.3.2 Multipass Measurements

A new multipass configuration (see Section 2.2.2) was employed to investigate the polarization-dependent dynamics of CO_2 rotors in the OC. The signals from the multipass configuration are compared to those from single pass detection. Improvements in the signal-to-noise levels enabled the use of lower pressures so that collision dynamics of super rotors could be investigated in the single collision regime. Doppler-broadened profiles of the J = 76, 84, 92, and 100 states yield information about the anisotropic energy release and spatial orientation characteristic of super rotor relaxation. All measurements reported in this section were performed with the OC at high intensity (42 TW/cm^2).

Comparison of Single and Multi-Pass Transient Absorption Signals

Figure 5.14 shows line center transient absorption signals collected at 10 Torr with the single pass and multipass configurations. The multipass IR configuration crosses the OC beam 11 times and probes a volume that is about 480 times larger than the single pass probe. Signals are shown for the J = 76 and J = 100 states. The multipass configuration results in a five-fold increase in the J = 76 signal and a ten-fold increase in the J = 100 signal. The increase in signal size is not uniform across J states.
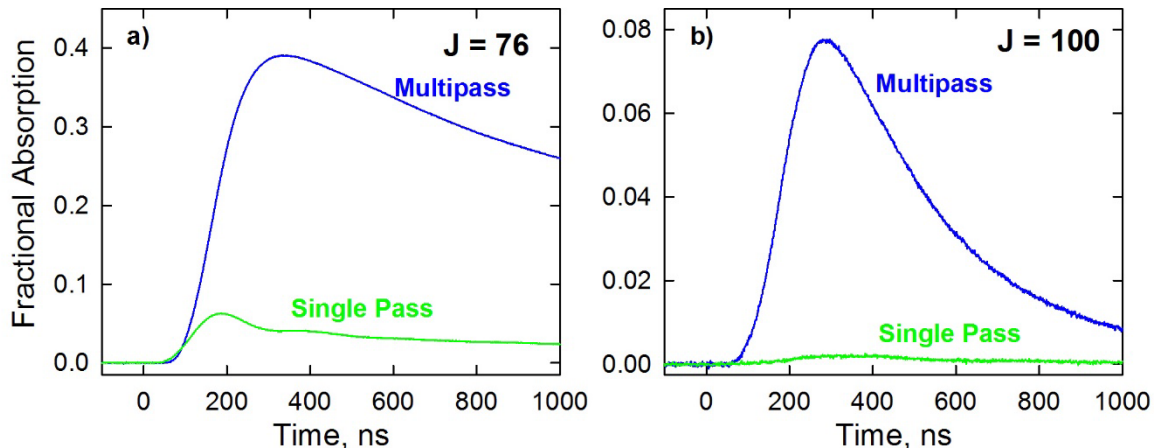
Figure 5.14 Line center transient absorption measurements for the J = 76 (a) and J = 100 (b) states collected at 10 Torr with the single pass (green) and multipass (blue) IR configurations. Measurements were made with the high intensity OC and perpendicular IR probing.

The OC is focused to a beam waist $\omega_0 = 26$ μm and the intensity of the OC beam changes along the z dimension. Figure 2.12 and Figure 2.13 in Section 2.2.2 show that the multipass configuration probes the OC at 11 points along the z-axis. At the furthest point, the IR light probes a volume that is ~6 mm away from the focal point of the OC beam. At this point, the intensity of the OC is about 7 times less than it is at the focal point. As seen in Section 5.3.1, the OC intensity impacts the energy release dynamics because it affects the number density of super rotors. The multipass configuration probes an OC volume that is about 480 times larger than the single pass configuration, but some of this volume is in a lower density OC regime.

The larger probe volume of the multipass configuration reduces signal loss from molecular transport. In the multipass configuration the IR focal length was 50 cm, which focused the IR beam to a beam waist of 230 μm. A calculation shows that in the diffusive limit it would take over $t = 20$ μs for a molecule to diffuse from the center of the IR probe volume at 5 Torr and 300 K. For a translational temperature of T = 1500 K, the diffusion

118

time becomes $t = 2$ μs. In this section, transient measurements are reported for times up to $t = 1$ μs.

Line Center Transient Absorption in the Single Collision Regime

Figure 5.15 shows the line center polarization-dependent transient absorption signals of CO_2 J = 76 and 100 rotors at four pressures from 2 Torr to 250 mTorr. Lowering the pressure reduces the number of super rotors and the number of collisions that can reorient super rotors. At 250 mTorr, the average time between collisions is $\Delta t_C = 440$ ns
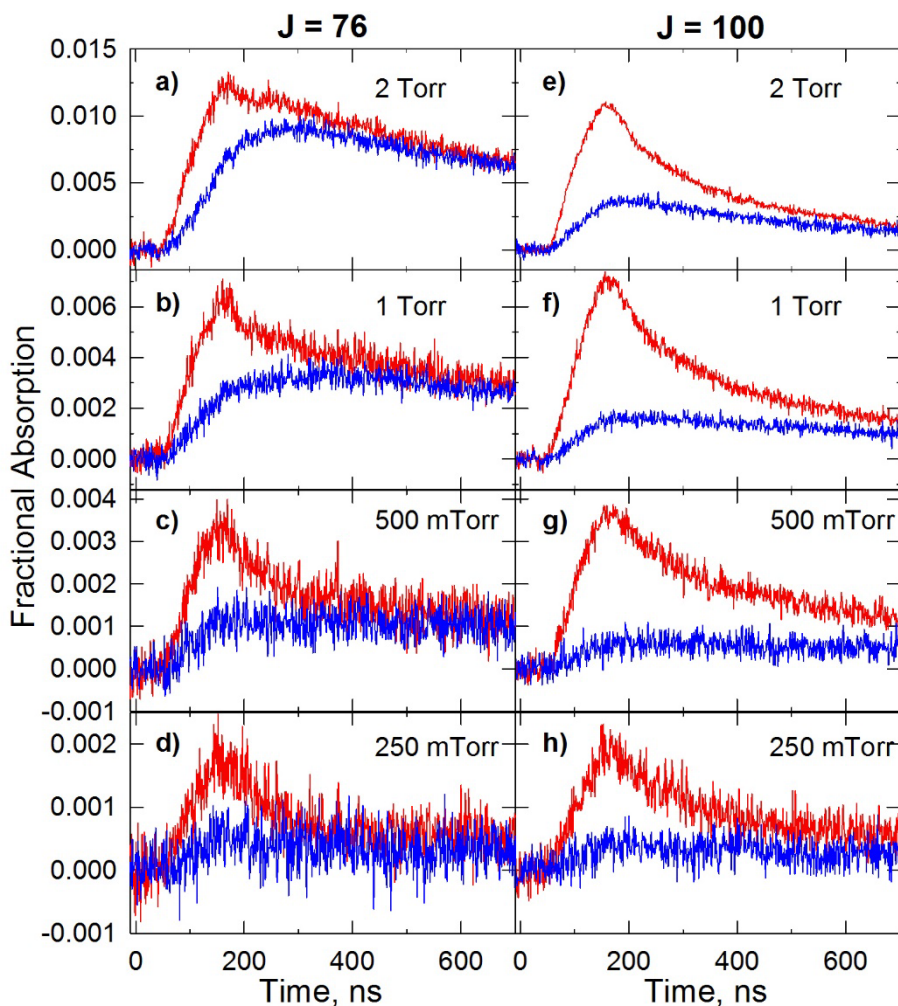
Figure 5.15 Line center polarization-dependent transient absorption measurements of CO_2 J = 76 (a-d) and J = 100 (e-h) rotors at four pressures: 2 Torr, 1 Torr, 500 mTorr, and 250 mTorr. All measurements are made with the multipass IR configuration and the high intensity OC.
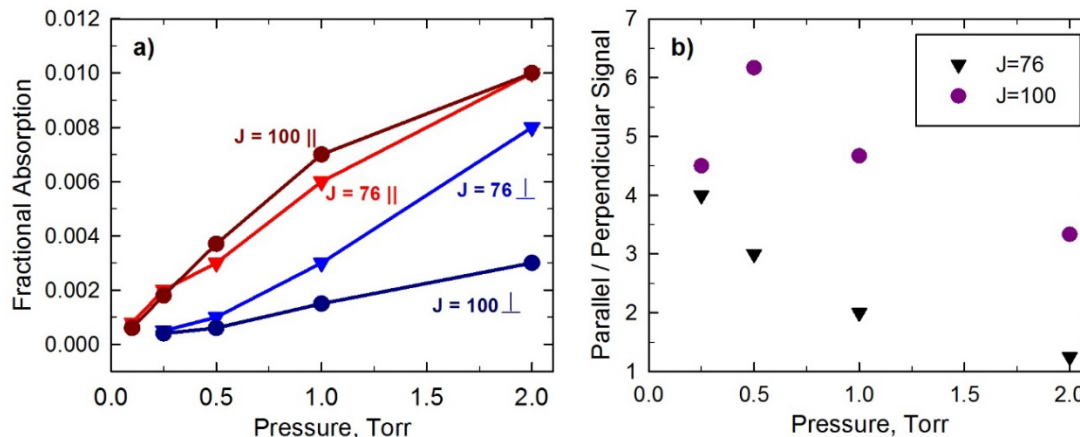
Figure 5.16 a) Maximum fractional change in absorption detected for the $J = 100$ and 76 states with parallel and perpendicular probing. b) Ratio of maximum signal collected with parallel probing to the maximum signal collected with perpendicular probing for the $J = 100$ and 76 states as a function of pressure.

for a 300 K CO_2 sample. Under these conditions, the early time transients correspond to the outcome of single collisions.

Figure 5.15 shows significant differences in transient absorption measurements made with parallel and perpendicular probing. At each pressure the magnitude of the perpendicular signal is less than the magnitude of the parallel signal. Lowering the pressure magnifies these differences. The differences between the parallel and perpendicular probe signals are more pronounced for $J = 100$ than for $J = 76$. Figure 5.16a shows the maximum fractional change in absorption collected with parallel and perpendicular probing for the $J = 100$ and 76 states plotted as a function of pressure. At the pressures reported here with the multipass configuration, absorption signals collected with parallel IR probing for the two states are approximately equal. In contrast, at 10 Torr signals for the $J = 100$ state were about 10 times smaller than those for the $J = 76$ state using the single pass configuration (see Figure 5.6).

Figure 5.16b shows the ratio of the parallel signal to perpendicular signal as a function of pressure for the $J = 100$ and 76 states. In general, lowering the pressure increases this ratio. For example, the $J = 100$ parallel signal is over 6 times larger than the perpendicular signal at 500 mTorr. Such high contrast suggests a high degree of orientational anisotropy. In addition, the ratios for $J = 100$ are larger than those for $J = 76$ at all pressures, suggesting that molecules in higher J states have a higher degree of orientational anisotropy.

The decay times of the parallel signals in Figure 5.15 were analyzed by fitting each to an exponential decay. The resulting fits are shown in Figure 5.17a and b. The pressure-dependence of the natural lifetimes τ for each state is shown in Figure 5.17c. The data show that the $J = 100$ signals are shorter lived than the $J = 76$ signals. However, as pressure is reduced from 2 Torr to 250 mTorr, the lifetimes of the two states get closer. The lifetime of the $J = 100$ state increases, while that for the $J = 76$ state decreases. Because collisions occur less often at lower pressures, the $J = 100$ rotors are quenched more slowly as the pressure is lowered. The lifetime of the $J = 76$ state may decrease because pressure reduces the number of collisions that rotationally excite 300 K molecules into this state.
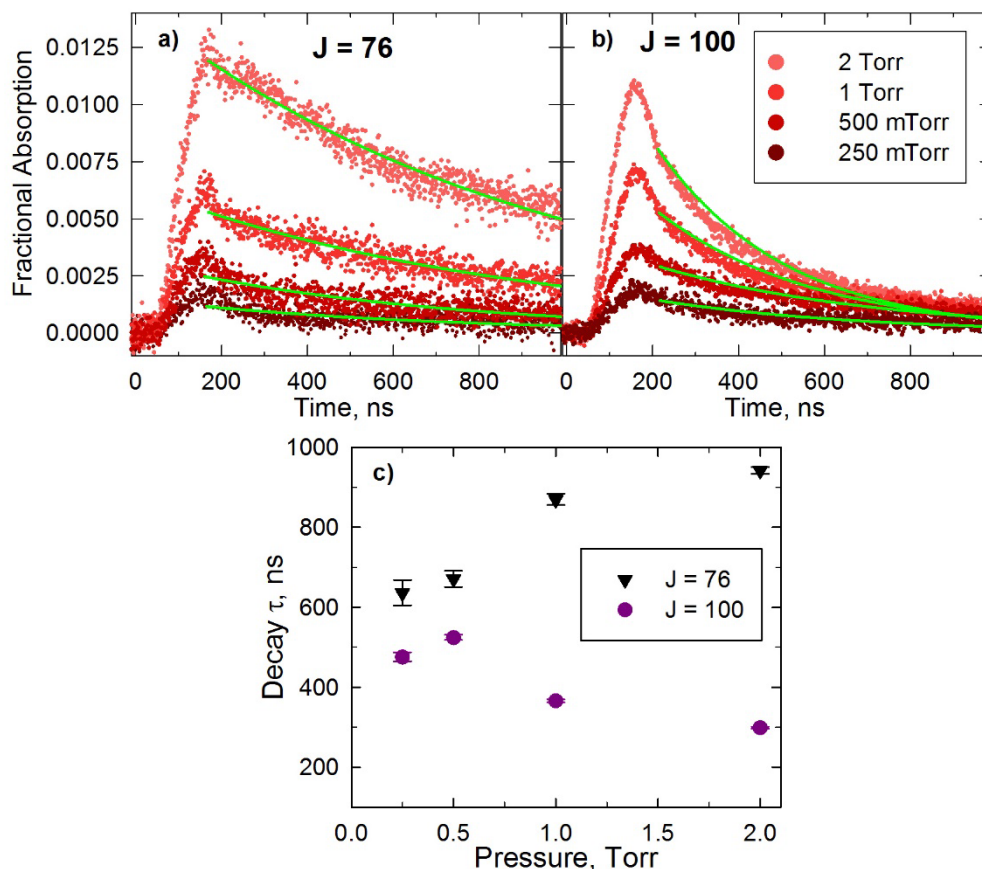
Figure 5.17 Exponential fits to the decay in the absorption signal collected with parallel probing for the J = 76 (a) and 100 (b) states. c) Exponential lifetime of parallel probe absorption signal for the J = 76 and 100 states as a function of pressure.

Collisional Quenching of Molecular Gyroscopes

Polarization-dependent translational energy distributions were measured for a number of CO_2 states using the multipass configuration. Doppler-broadened line profiles were measured at 5 Torr for the J = 100, 92, 84, and 76 states using the OC at high intensity. Each measurement was repeated three times. Figure 5.18 shows the time evolution of the translational temperatures for each state. The 300 K gas kinetic collision number is shown on the upper axis. Each set of data is characterized by an initial increase in temperature followed by a slower decay as the system relaxes to equilibrium. The J = 100, 92, and 84

data sets are also characterized at early times by more translational energy for the

perpendicular probe. Such a difference suggests that the out-of-plane rotors carry more
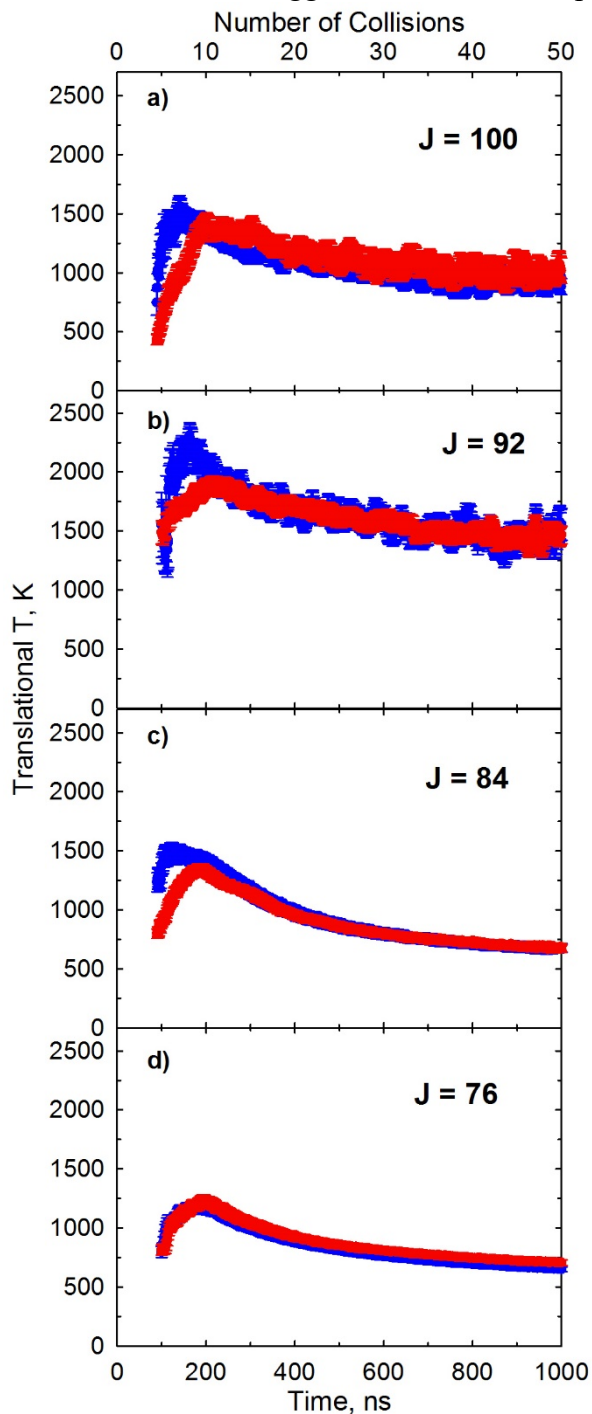
Figure 5.18 Polarization-dependent translational temperatures for the J = 100 (a), 92 (b), 84 (c), and 76 (d) states collected with the multipass configuration.

translational energy than do the in-plane rotors. This result is consistent with the data from the single pass measurements as was described in Section 5.3.1. The effect can be described by considering collisions that have rotationally resonant energy transfer (for parallel probing) and non-resonant energy transfer (for perpendicular probing). Figure 5.18d shows nearly identical translational temperatures for parallel and perpendicular probing. Such behavior is more consistent with the translational temperatures measured using the OC at low intensity (see Figure 5.9b). Since the multipass configuration probes both low and high intensity regions of the OC, the translational temperatures will reflect the dynamics occurring throughout the OC beam. For each state, the polarization-dependent translational temperatures are equal well before 1000 ns. The translational temperatures at 1000 ns for the $J = 100$ and 92 states are greater than those for the $J = 84$ and 76 states. This result shows that R$\rightarrow$T cross sections are J-dependent.

Polarization-dependent Doppler profiles were integrated to yield the time-dependent pairs of populations for the states studied here. Figure 5.19 shows the relative populations for the first 1000 ns. For each state, there is more population measured with the parallel probe compared to the perpendicular probe. The ratios of the population measured with parallel probing to the population measured with perpendicular probing are shown in the lower panels of Figure 5.19. At early times, populations measured with parallel probing are about two times larger than the populations measured with perpendicular probing for all states. The difference is evidence of the oriented nature of
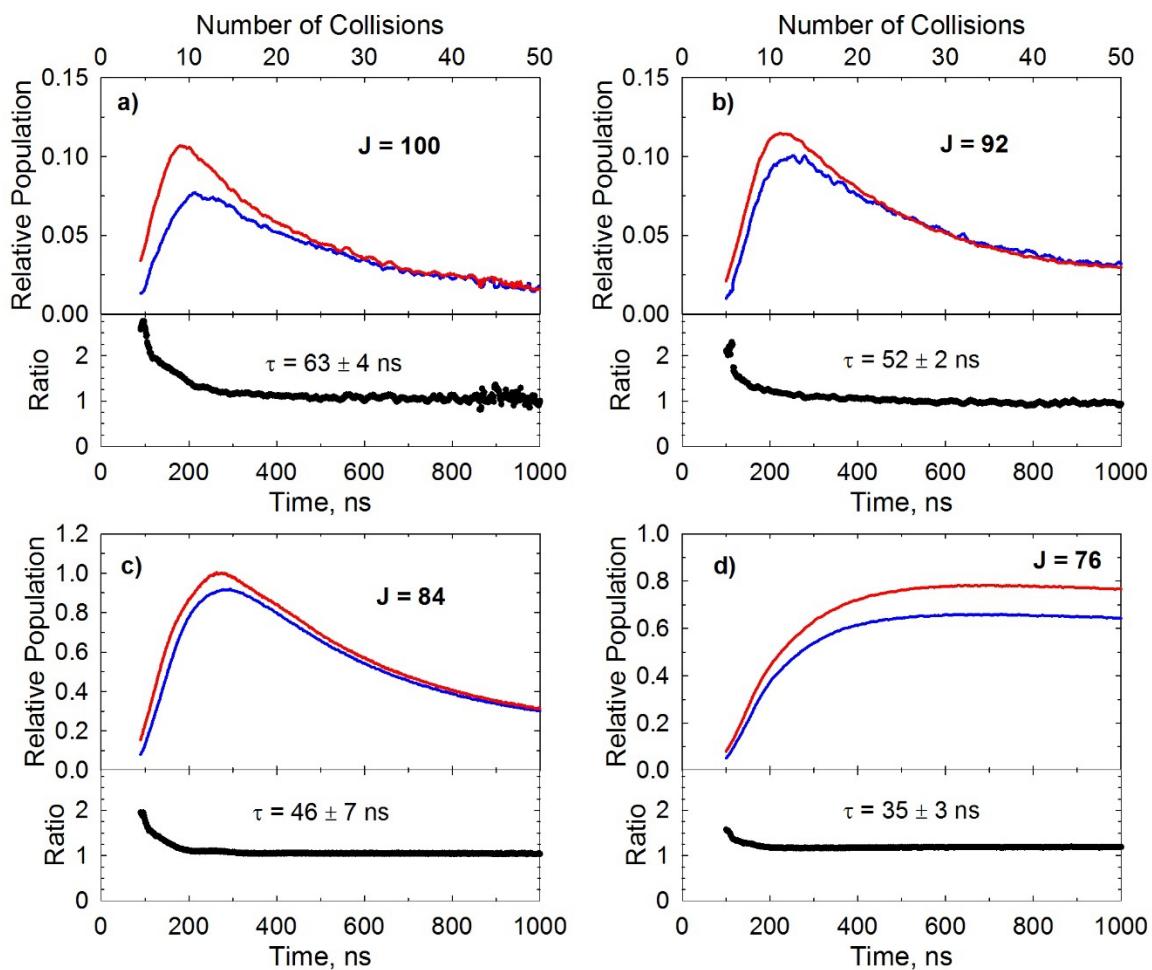
Figure 5.19 Polarization-dependent populations collected at 5 Torr with the multipass configuration for the CO_2 J = 100 (a), 92 (b), 84 (c), and 76 (d) states. The lower panel in each graph plots the time evolution of the parallel to perpendicular population ratio.

the molecules generated by the optical centrifuge. For each state, the decay of the ratio is fit to an exponential function and the resulting lifetimes are plotted as a function of J in Figure 5.20. The lifetime of the ratio of parallel to perpendicular populations increases with J.
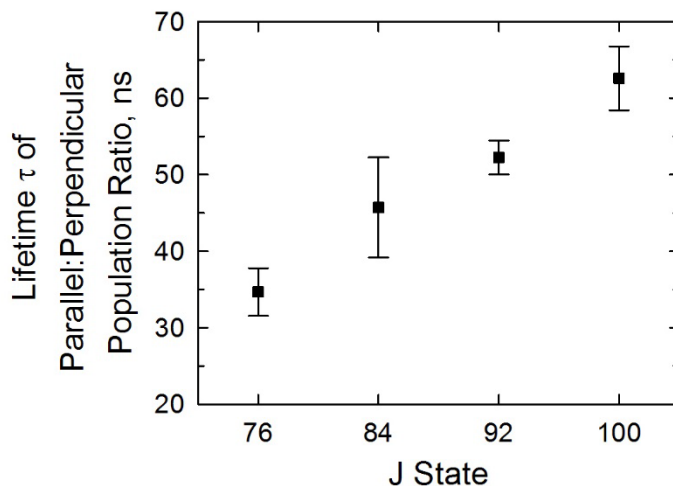
Figure 5.20 Exponential lifetime of the ratio of the parallel to perpendicular populations for the J = 76, 84, 92, and 100 states.

The fraction of in-plane rotors was calculated using equation 5.5 and plotted as a function of time as shown in Figure 5.21a. In each state, there is approximately 60% of the population rotating in the xy-plane at 100 ns (about 5 gas kinetic collisions). For each state, the decay of the fraction of in-plane rotors was fit to an exponential function. The resulting fits are shown in Figure 5.21a and the resulting lifetimes are plotted as a function of J in Figure 5.21b. In general, the lifetime of the orientational anisotropy increases with J.

The increased duration of the orientational anisotropy can be understood using a gyroscope model for the super rotor molecules. Collisions randomize molecular orientation. However, molecules with large amounts of angular momentum, like those created by the optical centrifuge, tend to retain their angular momentum orientation. An estimate of the maximum angle by which the angular momentum vector is perturbed during an orthogonal collision can be calculated using this gyroscope model and is shown on the upper x-axis in Figure 5.21b for each J state. The duration of the orientational anisotropy

126
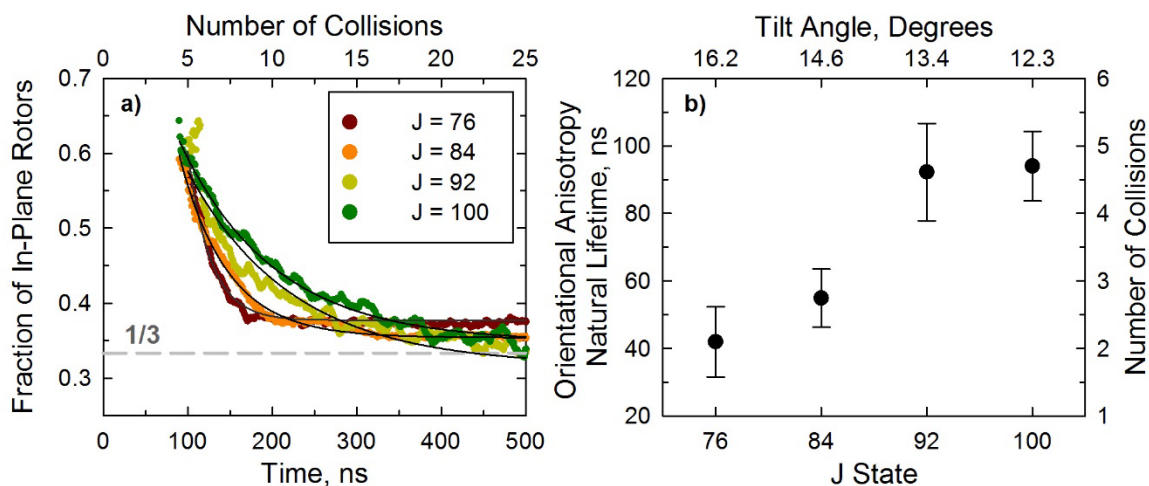
Figure 5.21 a) Fraction of in-plane rotors as a function of time measured at 5 Torr with the multipass configuration and with the high intensity OC. For each state, the decay of the fraction is fit to an exponential function and the fits are shown in black. b) The exponential lifetime of the decay in the fraction of in-plane rotors as a function of J. As a guide, the 300 K gas kinetic collision number is shown at the right.

increases with J state as expected by this model. The gyroscope is a classical model, which describes the behavior of molecules in the high energy, high J regime. Thus, we see a manifestation of the correspondence principle, wherein the quantum molecules behave classically at large energy.

The multipass measurements reported here investigated how orientational anisotropy is affected by the collisions of highly oriented rotors made in an optical centrifuge. Increases in signal-to-noise permit the study of super rotor dynamics in the single collision regime. Polarization-dependent Doppler profiles show an anistropic kinetic energy release from the oriented rotors. Populations measured with parallel and perpendicular probing reveal that the orientational anisotropy present has a longer duration in high J rotors. A correspondence between the quantum regime of molecular rotors and the classical gyroscope is observed and describes the behavior of the high energy rotors.

127

5.4 Conclusions

This work has investigated the collision dynamics of highly oriented rotors with an optical centrifuge. Polarization-sensitive measurements using high resolution transient IR absorption spectroscopy reveal detailed information about the time-dependent anisotropic release of translational energy and spatial orientation. Two IR beam configurations were used in this work. A single pass arrangement probes the most intense part of the optical centrifuge. Single pass studies explored how polarization-dependent dynamics vary with pressure, optical centrifuge intensity, and J state and identified the conditions under which the dynamics of super rotors could be studied in a regime with fewer collisions. Polarization-dependent line center transients revealed that the most significant differences are observed at the highest J states and lowest pressures. A more intense optical centrifuge likely produces a higher density of super rotors, leading to greater spatial anisotropies in translational energy profiles and populations.

The multipass IR configuration has increased signal-to-noise by a factor of 10 for some J states. This increase in signal permitted the study of orientation-dependent dynamics in the single collision regime. Transient absorption measurements at pressures from 2 Torr to 250 mTorr show inhibited rotational quenching of high J rotors at lower pressures. With the development of this new configuration, future studies will be able to probe higher J states that are closer to the initially prepared state.

One of the most significant results of this work is that within the first 200 ns (~20 collisions) molecules perpendicular to the initial plane of rotation gain more translational energy than do molecules detected parallel to the plane of rotation. This anisotropic kinetic

energy release indicates the types of rotational energy transfers that take place with the oriented super rotors   Polarization-dependent populations reveal how the orientational anisotropy of the rotors evolves with time and depends on J state. Single pass and multipass measurements show that the magnitude of the anisotropy is larger and the duration longer for high J rotors. The inhibited randomization of the spatial orientation of the rotors is a result of the large of the large amounts of angular momentum present in each molecule. The behavior of the super rotor molecules corresponds to the that of a classical gyroscopic. This work opens the door for new spatially dependent studies of super rotor molecules in a variety of experimental conditions.

Chapter 6: Rotational Quenching of CO_2 Super Rotor Molecules with Ar and He Buffer Gases

6.1 Introduction

The previous chapter showed that the optical centrifuge experiments can provide detailed information on the evolution of orientation, rotational relaxation, and translational energy of super rotor molecules. The results pose some interesting questions, such as how do super rotors interact with various types of collision partners? Different interaction potentials and masses could have significant effects on the behavior of energy evolution in a far-from-equilibrium regime. To begin investigating some of these questions, optical centrifuge experiments were conducted for two collision pairs: Ar-CO_2 and He-CO_2. To provide a theoretical framework with which to understand the results of the experiments, quantum scattering calculations were performed for these two collision systems The results of these calculations are presented in Chapter 7.

The work presented here used the same techniques outlined in Chapter 5 to investigate CO_2 super rotor collision dynamics. Here the dynamics were investigated as a function of collision partner, pressure, J state, and probe polarization. Line center transients were used to probe the overall effects of the varied experimental parameters. Polarization-dependent populations demonstrate the role the collision partner plays in rotational relaxation and spatial reorientation of CO_2 super rotors. Doppler-broadened line

profiles collected for both buffer gases show how the translational energy evolves for CO_2 rotors in the presence of a buffer gas.

6.2 Experimental Methods

The experimental set-up is described in Chapter 2 and details specifically relevant to polarization-dependent measurements are given in the Experimental Details section of Chapter 5. The measurements reported in this chapter used an optical centrifuge (OC) beam waist of 26 μm with a peak field intensity of 37 TW/cm^2. Based on the FWHM of the spectral chirp shown in Figure 2.5, the optical centrifuge rotational frequency was ~35 THz. For CO_2, this excitation corresponds to a rotational energy E_{rot} = 18,200 cm^{-1} and an angular momentum quantum number of J ~220. This work studied CO_2 super rotor collisions with argon and helium. Since an anisotropic polarizability is required for alignment with the OC field, the Ar and He atoms are not excited by the OC.

Collision-induced population changes of individual CO_2 rotational states were measured following the optical centrifuge pulse using high resolution transient IR absorption spectroscopy. A quantum cascade laser (QCL) operating between λ=4.2 and 4.5 μm was used to probe the J=76 and 100 states with the fundamental CO_2 $(00^00 \rightarrow 00^01)$ transition. Experiments reported in this chapter were made with the multipass IR configuration described in Section 2.2.2 and shown in Figure 2.12 and Figure 2.13. Section 5.3.2 describes how the multipass configuration improves the signal-to-noise levels and reduces the impact of molecular transport losses on transient signals. IR absorption measurements were collected at 5 Torr CO_2 and three different partial pressures of buffer gas: 0 Torr, 5 Torr, and 10 Torr.

An estimate of the collision rate in each buffer gas mixture can be made using the gas kinetic model. The rate of collisions per unit volume k is a product of the collision cross section σ and relative velocity v_{rel}

$$k = \sigma v_{rel}. \tag{6.1}$$

The hard sphere collision cross section is the area of a circle with a radius $r = r_A + r_B$, where r_A and r_B are the radii of each collision partner. Using a van der Waals radius of $r_{Ar} = 188$ pm for Ar and $r_{CO_2} = 205$ pm for CO_2, the hard sphere cross section for Ar-CO_2 is 0.48 nm^2 and using $r_{He} = 140$ pm for He, the cross section for He-CO_2 is 0.37 nm^2. At 300 K the relative velocity for Ar-CO_2 is $v_{rel} = 550$ m/s and for He-CO_2 is $v_{rel} = 1320$ m/s. Using equation 6.1, the collision rate for Ar-CO_2 is 2.6×10^{-10} cm^3/s and for He-CO_2 is 4.9×10^{-10} cm^3/s. Thus, the collision rate for He-CO_2 is about twice that for Ar-CO_2.

Polarization-dependent IR measurements of the line center transient absorption signal probed spatially-dependent differences in the dynamics for collisions with the two buffer gases. Transient Doppler-broadened line profiles were measured for both polarizations by collecting transient absorption signals at a series of closely-spaced IR frequency steps (~0.001 cm^{-1}) across individual ro-vibrational transitions. A detailed description of the spatial orientation of the molecules probed by two orthogonal polarizations of IR light is given in Section 5.2. To reiterate, the OC prepares super rotors that rotate in the xy-plane, as shown in Figure 5.1. IR light polarization that is parallel to the plane of OC rotation probes molecules whose angular momentum vector has a projection in the xz plane. IR light polarization that is perpendicular to the plane of OC rotation probes molecules whose angular momentum vector has a projection in the xy-

plane. The extent of orientational anisotropy was determined by polarization-sensitive measurements of $Ar-CO_2$ and $He-CO_2$ collisions.

6.3 Results and Discussion

6.3.1 Line Center Transients

The effects of argon and helium buffer gases on the line center transient dynamics were explored by making polarization-dependent measurements of the CO_2 J = 76 and J = 100 states. The results from each state were analyzed individually and then compared. Figure 6.1 shows the polarization-dependent line center transients for J = 76 at three partial pressures of buffer gas, where red indicates parallel probing and blue indicates perpendicular probing. Figure 6.1a-c show that increasing the pressure of Ar does not change the overall dynamics in the CO_2 J = 76 state as measured by the line center transient signal. The $Ar-CO_2$ signal magnitude decreases monotonically as the pressure of argon is increased. In contrast, Figure 6.1d-f show that increasing the pressure of He has the opposite effect on the transient signals. The signal magnitude increases by nearly a factor of 2 when adding 5 Torr of He to pure CO_2. In addition, the rates of the rise and decay of the signal increases as He pressure is increased. For J = 76, there is no detectable difference between signals collected with parallel and perpendicular IR polarizations, indicating little orientational anisotropy.

J = 76
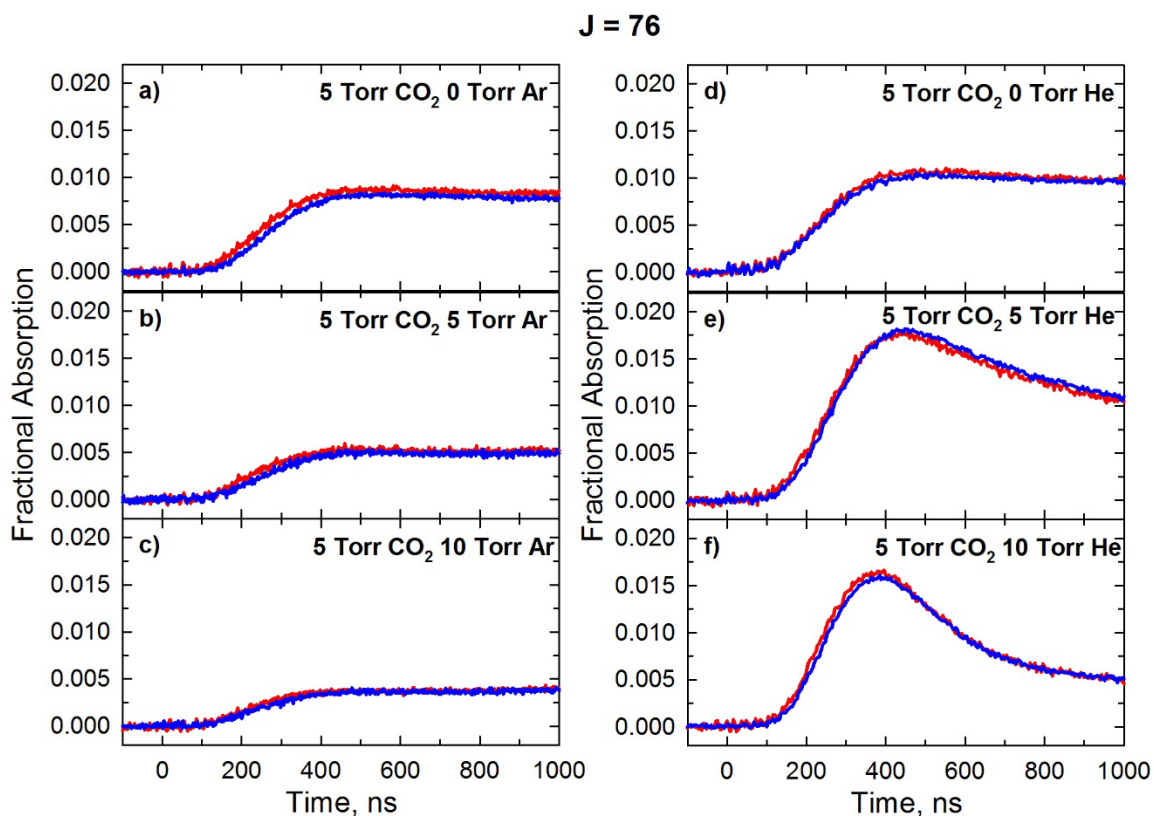
Figure 6.1 Polarization-dependent line center IR absorption measurements of CO_2 J = 76 collected with three partial pressures of Ar (a-c) and He (d-f). Parallel IR probing is shown in red and perpendicular IR probing is shown in blue.

To quantify the rate differences between the two buffer gases, the slopes of the parallel and perpendicular transient signals were fit to linear functions. The resulting fits for the parallel measurements with 5 and 10 Torr of buffer gas are shown in Figure 6.2a and Figure 6.2b, respectively. The slope of each linear fit represents an appearance rate for that transient absorption signal. The slopes are shown as a function of buffer gas pressure in Figure 6.2c. The data show that the rate of appearance decreases as pressure of Ar is increased. In contrast, the rate of appearance increases as pressure of He is increased. Figure 6.2c shows that at 10 Torr of buffer gas, the rate of appearance observed with He buffer gas is about 6 times greater than that observed with Ar buffer gas. This increase is

134
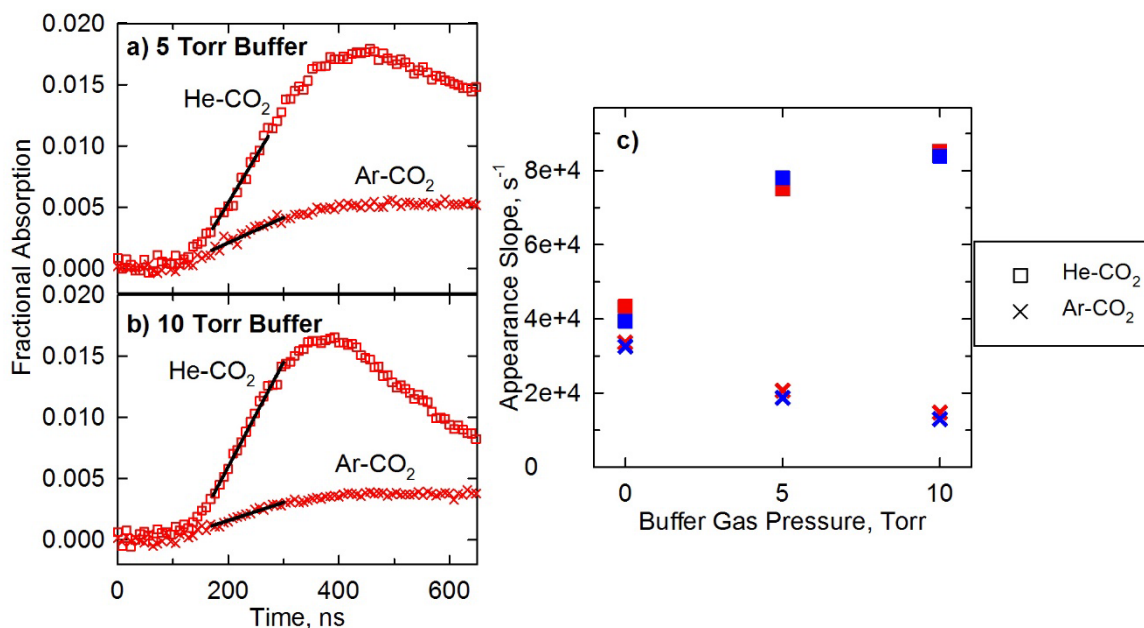
Figure 6.2 Parallel IR transient measurements of CO_2 J = 76 with 5 Torr (a) and 10 Torr (b) of buffer gas. The early time appearance is fit to linear functions and the fits are shown in black. c) Slopes of early time fits of polarization-dependent transients for He-CO_2 and Ar-CO_2. In all panels a He-CO_2 measurement is indicated by a square and Ar-CO_2 measurement by a "x".

greater than what would be expected from the increase in the collision rate described in Section 6.2, indicating that collisional quenching is more efficient in He-CO_2 than in Ar-CO_2.

Figure 6.3 shows the polarization-dependent line center transients for CO_2 J = 100 at three partial pressures of Ar or He buffer gas. In all measurements, the molecules probed with parallel IR light appear earlier than those probed with perpendicular IR light. The effect of changing the polarization is most pronounced with 10 Torr of He (Figure 6.3f) and least pronounced with 10 Torr of Ar (Figure 6.3c). To quantify differences between Ar and He in the signals for J = 100, the rises of the parallel and perpendicular transient signals were fit to linear functions. The resulting fits are shown in Figure 6.4a-d.
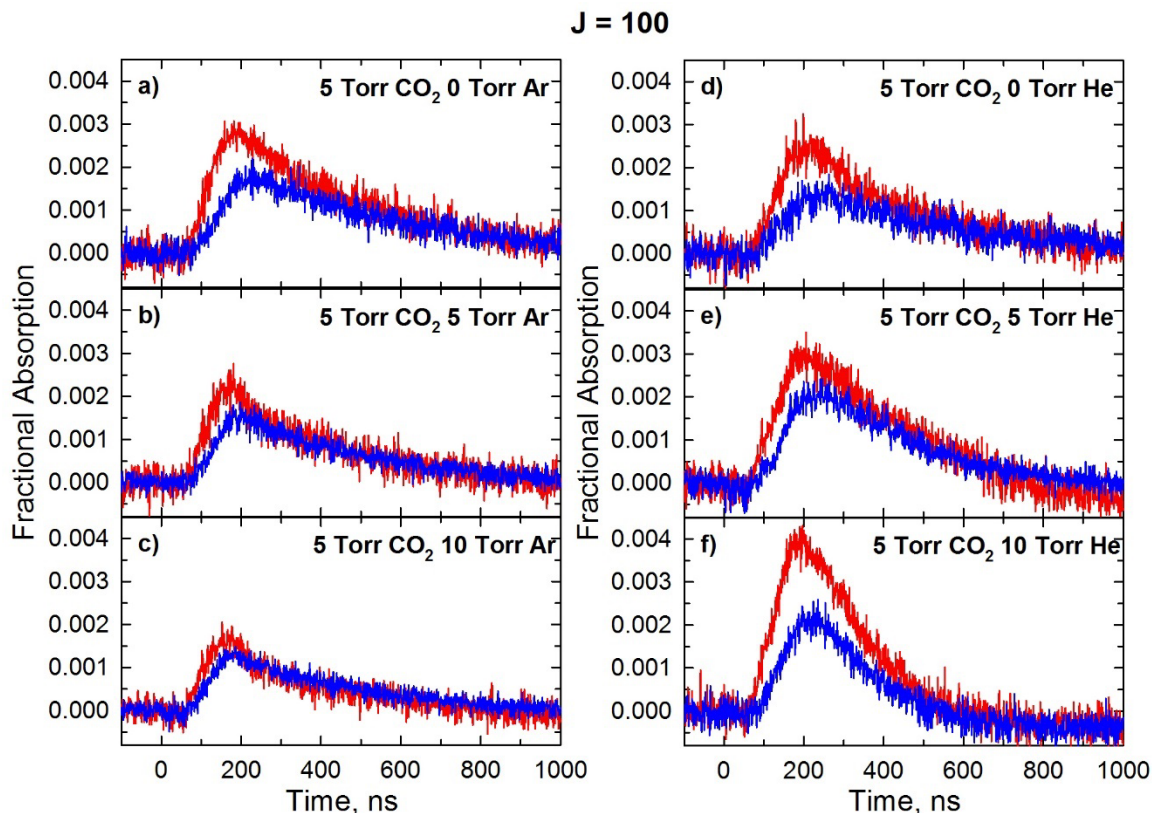
Figure 6.3 Polarization-dependent line center IR absorption measurements of CO_2 J = 100 collected with three partial pressures of Ar (a-c) and He (d-f). Parallel IR probing is shown in red and perpendicular IR probing is shown in blue.

The pressure dependence of the slopes from the linear fits for Ar-CO_2 is shown in Figure 6.4e. In each case, the rate observed with parallel probing is greater than that observed with perpendicular probing. However, the parallel probe rate decreases as pressure of Ar was increased. With 10 Torr of Ar, the orthogonally probed rates are nearly identical, showing there is little orientational anisotropy in the CO_2 rotors. The pressure dependence of the He-CO_2 slopes is shown in Figure 6.4f. At each pressure, the rate measured with parallel probing is greater than that measured with perpendicular probing. Both the parallel and perpendicular probe rates increase as the pressure of He increases.
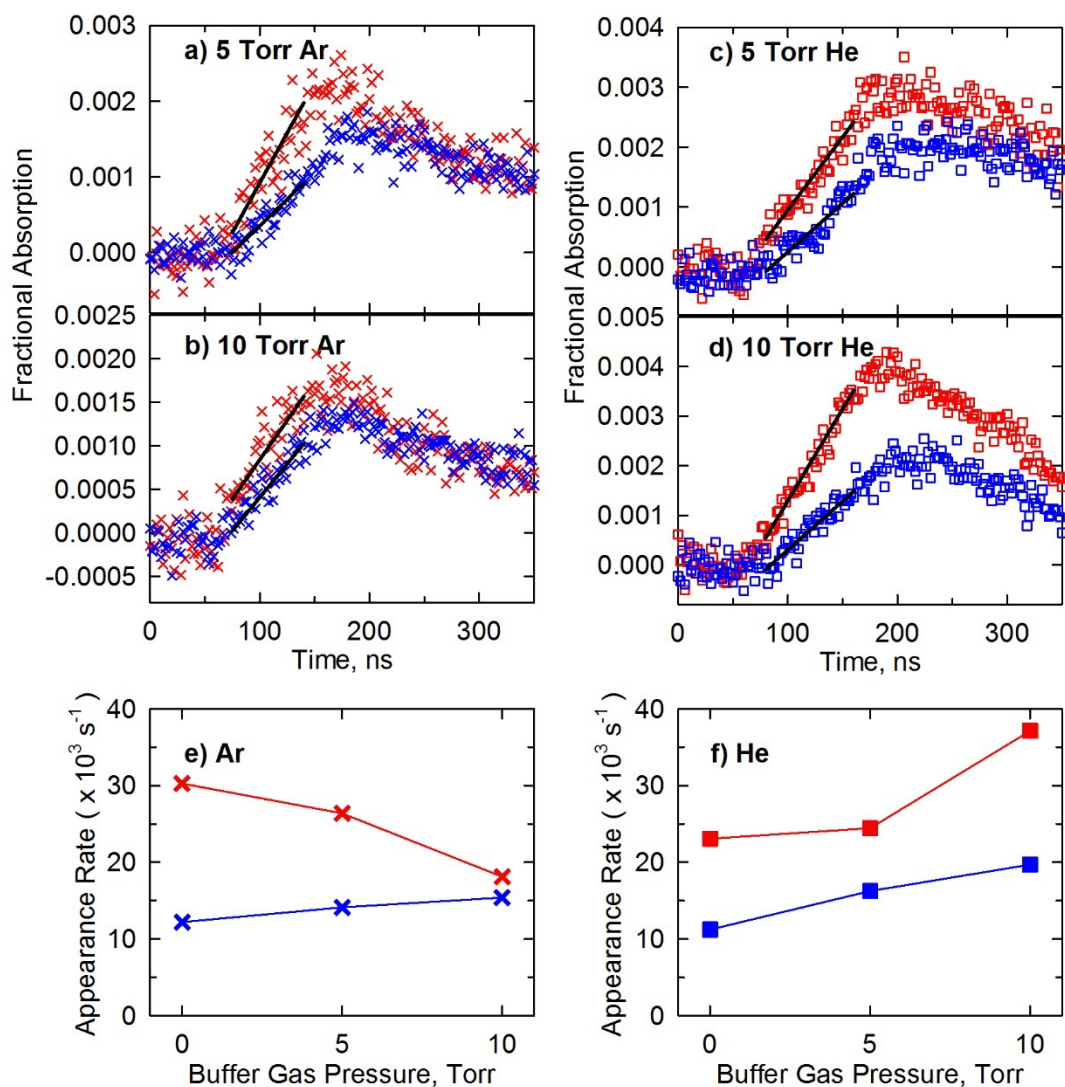
Figure 6.4 The polarization-dependent transient measurements of CO_2 J = 100 with Ar (a and b) and He (c and d) buffer gases. The pressure of CO_2 was 5 Torr in all measurements. The early-time linear fits are shown in black in each plot. The appearance rates as determined by the fits are shown for Ar (e) and He (f).

In the J = 76 and J = 100 states of CO_2, adding He increases the rate of appearance. Upon addition of Ar the rate decreases or remains unchanged. Differences between the appearance rates for Ar-CO_2 and He-CO_2 are more pronounced in the J = 76 state than in the J = 100 state. The differences between parallel and perpendicular probing of the J = 100 state are evidence of the orientational anisotropy generated by the optical centrifuge. As discussed in Chapter 5, evidence of the orientational anisotropy of CO_2 rotors is more

pronounced as J increases. Here, the line center data provide evidence that this trend is also observed in the presence of Ar and He buffer gases.

6.3.2 Evolution of Populations and Spatial Reorientation

The line center polarization-dependent measurements provide insights into the reorientation dynamics of CO_2 rotors with Ar and He collisions from a single Doppler slice. To get a full picture of the orientational anisotropy, spatially-dependent populations were determined by measuring polarization-dependent Doppler-broadened line profiles. Here, the focus is on the 10 Torr buffer gas data where the greatest effects were seen. Figure 6.5 shows the line profiles collected for the J = 76 and 100 states at 250 ns after the OC pulse and with 10 Torr of buffer gas. Measurements made with parallel IR probing are shown. Doppler-broadened line profiles were fit to Gaussian functions and the resulting fits were integrated to determine the time evolution of the relative population for each state. The translational temperatures were determined from the width of the profiles and are discussed in the next section. Here, the integrated populations are described.

Figure 6.6 shows the relative populations in the J =76 and J = 100 states with Ar and He buffer gases using parallel IR probing. Significant differences between the dynamics of the Ar-CO_2 and He-CO_2 data are observed. More population is seen with He collisions for both CO_2 states. The J = 76 state appears more quickly with He than with Ar and has faster decay back to equilibrium with He. For the J = 100 state, the rate of
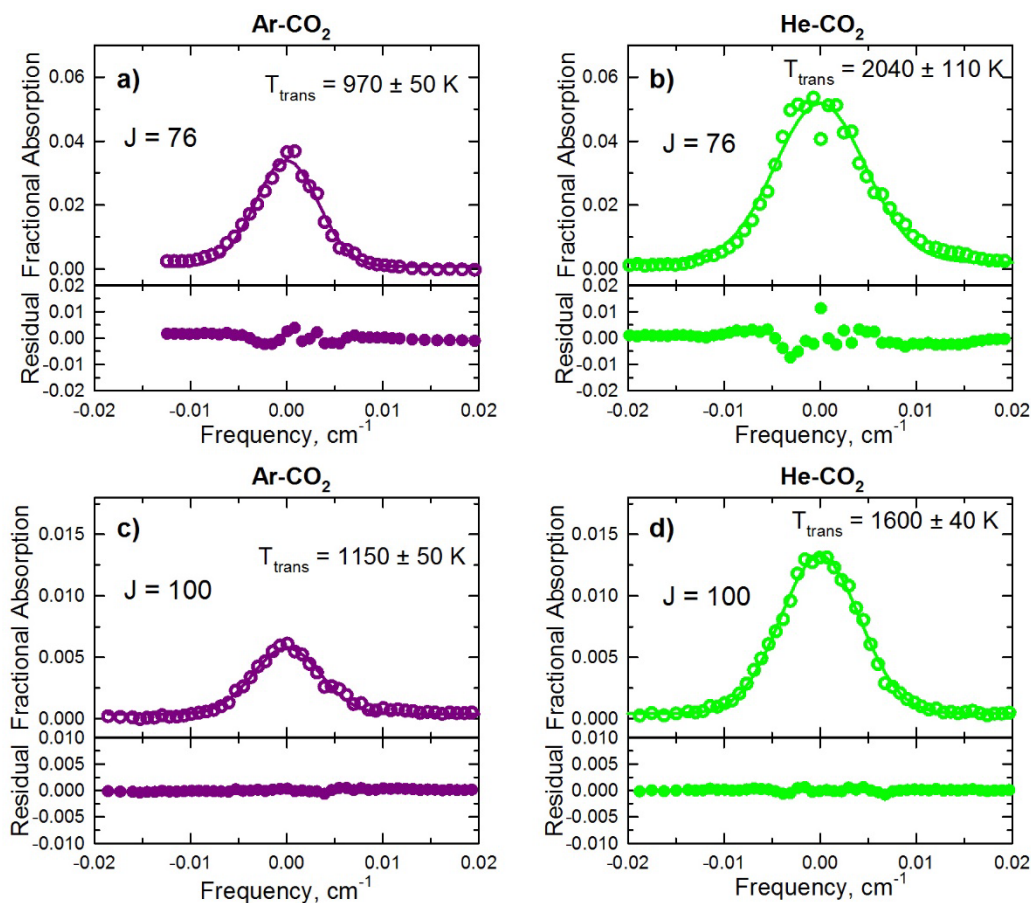
Figure 6.5 Doppler-broadened line profiles for the CO_2 J = 76 state (a and b) and the J = 100 state (c and d) collected with 10 Torr of Ar (left) and 10 Torr of He (right). 5 Torr of CO_2 was used in these measurements. The profiles displayed were measured with parallel IR polarization at 250 ns.

appearance is about the same, but the decay is faster with He. The data indicate that

rotational relaxation of CO_2 rotors occurs more quickly with He collisions.

The orientational anisotropy of the CO_2 molecules was investigated by measuring

the polarization-dependent relative populations of CO_2 with Ar and He buffer gases.

Figure 6.7 shows the polarization-dependent relative populations of the J = 76 and 100

states with 10 Torr of buffer gas. Measurements were collected in triplicate for each

experimental condition. Molecules trapped in the optical centrifuge initially are prepared
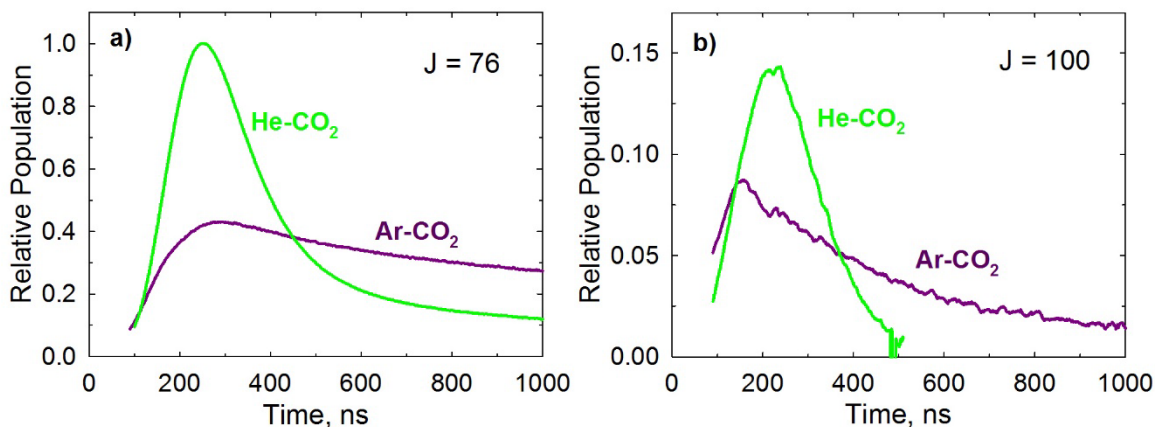
Figure 6.6 Time evolution of the relative population in the CO_2 J = 76 (a) and J = 100 (b) states with Ar (shown in purple) and He (shown in green) buffer gases. Experiments were collected with 10 Torr of buffer gas and with parallel IR polarization. For the J = 100 He measurement, transient signal approaches zero by 500 ns.

with their angular momentum projection along the z-axis. In Section 5.2 the molecules that have an angular momentum vector along the z-axis are termed in-plane rotors. The fraction of in-plane rotors f_z is determined from the polarization-dependent populations using the procedure outlined in Section 5.3.1 and the equation

$$f_z = \frac{p_z}{p_{tot}} = \frac{p_{\parallel} - \frac{1}{2}p_{\perp}}{p_{\parallel} + \frac{1}{2}p_{\perp}}, \tag{6.2}$$

where $p_{\parallel}$ is the population measured with parallel probing and $p_{\perp}$ is the population measured with perpendicular probing. The lower panel of each graph in Figure 6.7 shows the f_z fraction as a function of time, representing an average of three measurements.

The data in Figure 6.7 show that orientational anisotropy is detected at each state and with each buffer gas. At the earliest times, more than 50% of the molecules are

140
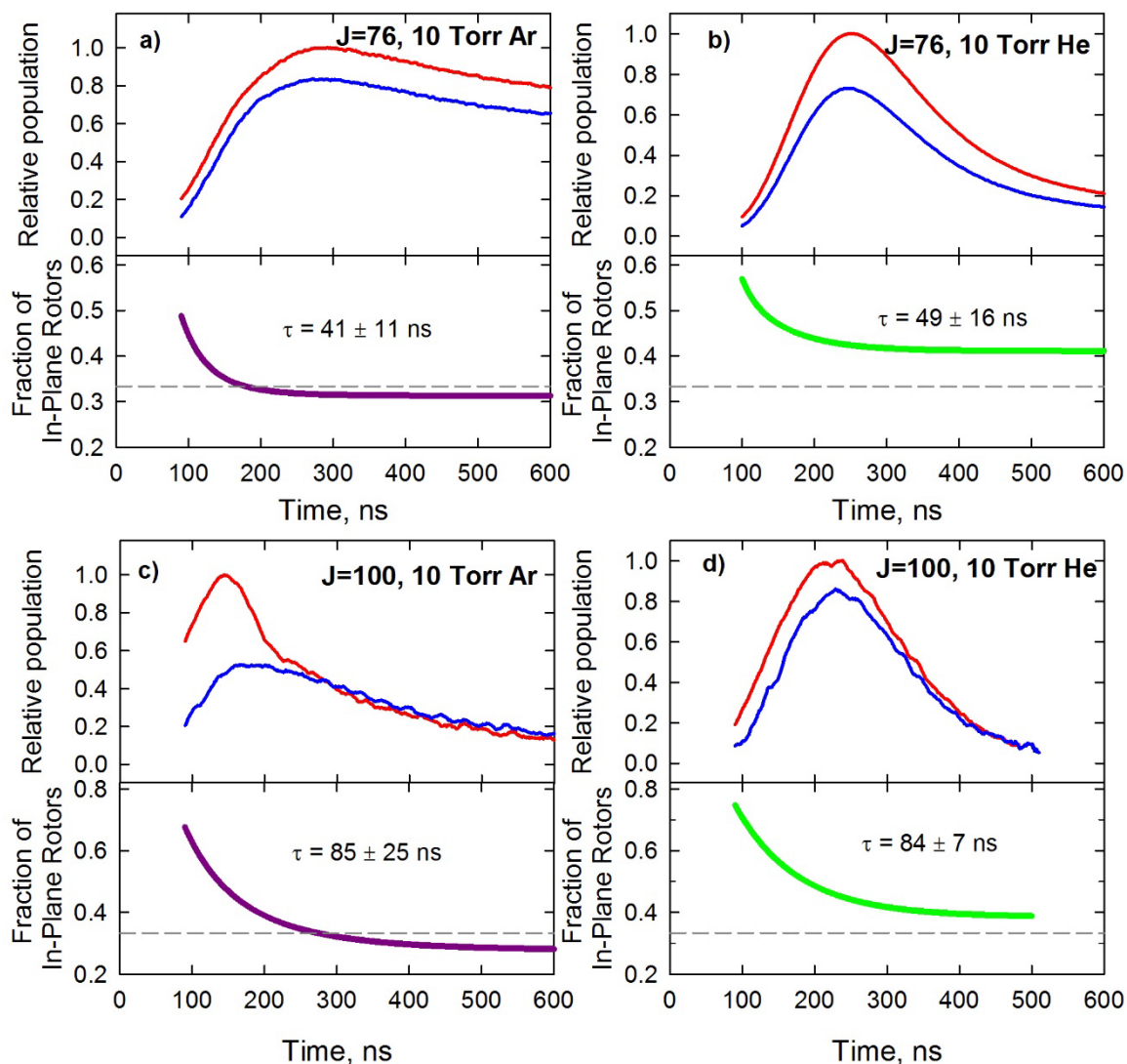
Figure 6.7 Time evolution of the polarization dependent populations for the $J = 76$ state (a and b) and $J = 100$ state (c and d). Measurements collected with 10 Torr of Ar are shown at the left and measurements collected with 10 Torr of He are shown at the right. The time evolution of the fraction of in-plane rotors is shown in the lower panel of each graph. The natural lifetime of the fraction is displayed on the plots.

observed to have their angular momentum along the z-axis. One important result is that the fraction of in-plane rotors for He-CO_2 is greater than that for Ar-CO_2 at all times. This finding means that super rotors retain more of their orientational anisotropy in collisions with He than with Ar. The evolution of each f_z fraction decays with an average natural lifetime shown in Figure 6.7. For each state, the natural lifetimes of the f_z fraction for Ar-

141

CO_2 and He-CO_2 are the same within the experimental uncertainty. However, since He-CO_2 collisions occur at twice the rate of Ar-CO_2 collisions, this result indicates that the orientation is retained through more collisions for He-CO_2.

The effect that the buffer gas has on reorientation can be understood in terms of the gyroscope model described in Section 4.3.3. This model considers collisions in which a 300 K particle collides with a super rotor with a velocity vector that is orthogonal to the plane of molecular rotation. In this type of collision, the incident particle induces a tilt in the classical angular momentum vector $\vec{L}$ of the rotor by an angle $d\varphi$ given by

$$d\varphi = \frac{r\mu \, dv}{|\vec{L}|},$$ (6.3)

where r is the distance from the center of mass of the rotor, μ is the reduced mass, and dv is the change in relative velocity. In the experiments presented in this chapter, the mass of the collision partner is varied. The model shows that a less massive particle causes less reorientation. An estimate of the maximum angle by which the angular momentum is perturbed during an orthogonal collision can be calculated using equation 6.3. For an Ar atom colliding with a CO_2 J = 220 super rotor, the maximum induced tilt angle in the rotor is 5.5°. For a He atom colliding with a CO_2 J = 220 super rotor, the maximum induced tilt angle is 2°. Therefore, the Ar atoms are more effective at randomizing the angular momentum of the CO_2 rotors when compared to He. In Chapters 4 and 5 the gyroscope model was used to explain the inhibited angular momentum reorientation as the angular momentum of the super rotor increased. The buffer gas results in this chapter provides further evidence that CO_2 super rotors are described by a classical gyroscope model.

142

6.3.2 Evolution of Translational Energy

Information about the evolution of translational energy for super rotor collisions is determined from the width of Doppler-broadened line profiles such as those shown in Figure 6.5. Polarization-dependent Doppler-broadened profiles for the J = 76 and 100 states were collected at 5 Torr and 10 Torr of Ar and He buffer gases. The data in Figure 6.8 shows the time evolution of the polarization-dependent translational temperatures of one representative data set for each experimental condition. Measurements with 5 Torr (Figure 6.8a and b) and 10 Torr (Figure 6.8c and d) of buffer gas show that all translational
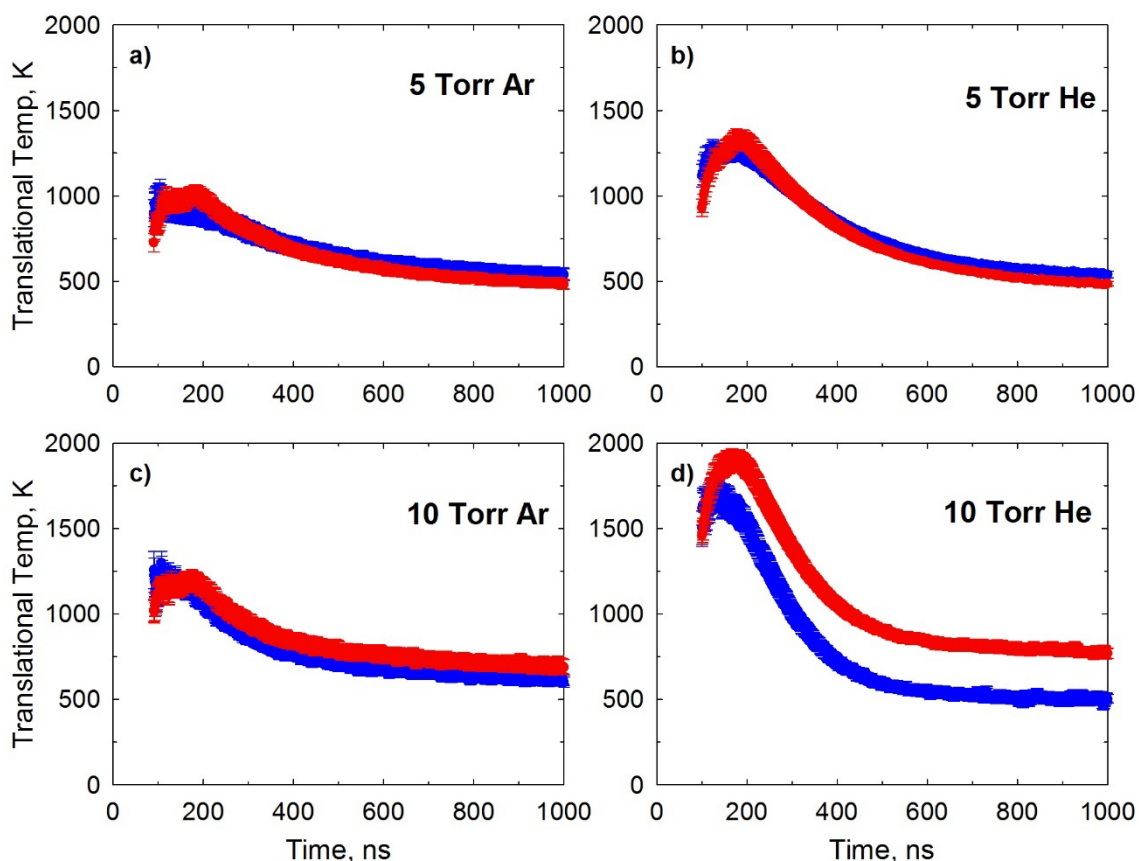
Figure 6.8 Time evolution of the polarization-dependent translational temperatures collected for the J = 76 state. Measurements were collected with 5 Torr of Ar (a), 5 Torr He (b), 10 Torr Ar (c) and 10 Torr He (d).

temperatures are initially well above 300 K. At early times, translational temperatures for Ar-CO_2 are less than those measured for He-CO_2.

Figure 6.9 shows the time evolution of the polarization-dependent translational temperatures for the J = 100 state. Figure 6.9 shows one representative set of three collected for each experimental condition. The translational temperatures initially increase then decrease as collisions occur. The data in Figure 6.9 show that translational temperatures measured with perpendicular polarization are initially greater than those measured with parallel polarization. This difference in translational temperature is also observed with pure CO_2 as described in Chapter 5. The polarization-dependent differences
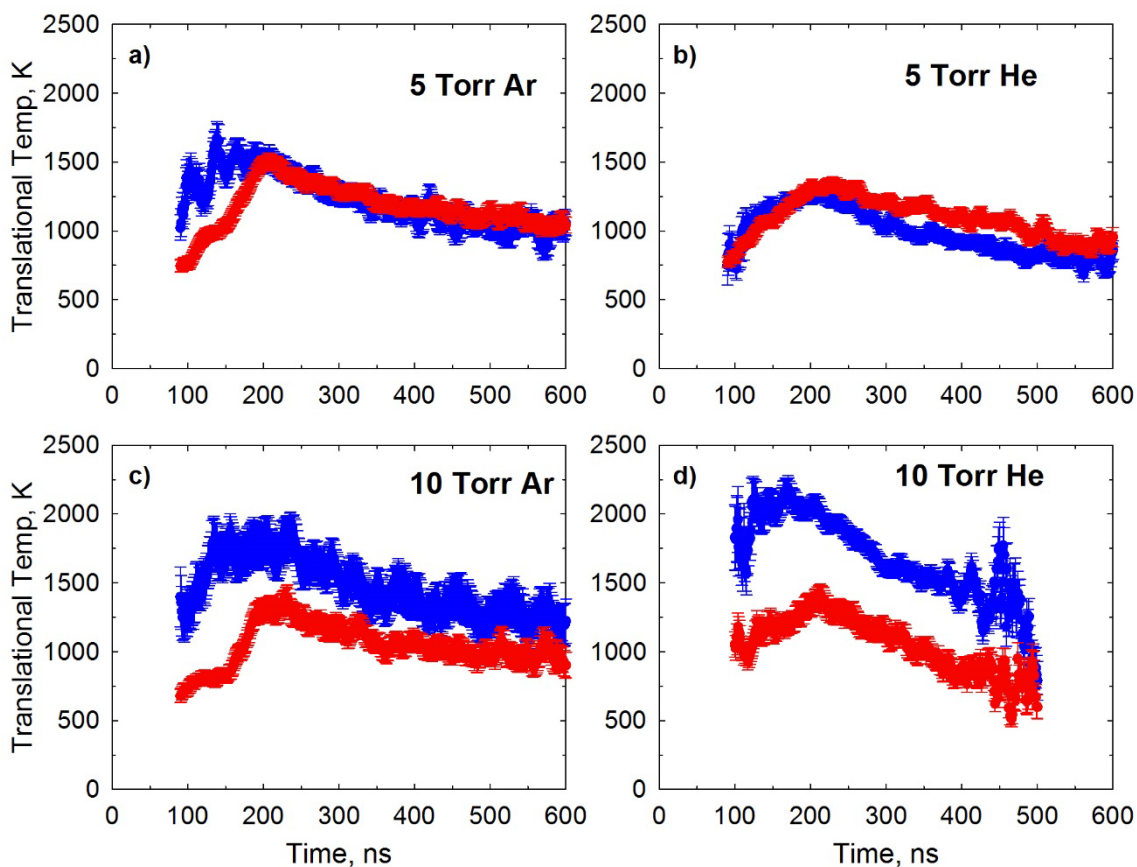
Figure 6.9 Time evolution of the polarization-dependent translational temperatures collected for the J = 100 state. Measurements were collected with 5 Torr of Ar (a), 5 Torr He (b), 10 Torr Ar (c) and 10 Torr He (d).

in translational energy are evidence of the oriented nature of the spinning molecules and are indicative of anisotropic kinetic energy release during collisions. Differences between the translational energies for Ar-CO$_2$ and He-CO$_2$ are less pronounced in the J = 100 state than in the J = 76 state.

To understand the larger amounts of translational energy gained by the CO$_2$ rotors for He-CO$_2$ collisions consider a collision between an atom A and a super rotor molecule SR. The total energy in the collision system E_{tot} is a sum of the translational energy E_{trans} and rotational energy E_{rot}. For this discussion, any changes in vibrational and electronic energy are ignored and the discussion is confined to the center of mass frame. The total energy in the collision system is conserved

$$\Delta E_{tot} = \Delta E_{trans} + \Delta E_{rot} = 0. \tag{6.4}$$

The atom has only translational energy, whereas the super rotor has translational and rotational energy. Therefore, equation 6.4 can be rewritten

$$\Delta E_{trans}(SR) + \Delta E_{rot}(SR) = -\Delta E_{trans}(A). \tag{6.5}$$

where $\Delta E_{trans}(A)$ has been moved to the other side of the equals sign. Conservation of linear momentum requires that

$$\Delta E_{trans}(A) = \left(\frac{m_{SR}}{m_A}\right)\Delta E_{trans}(SR), \tag{6.6}$$

where m_{SR} is the mass of the super rotor and m_A is the mass of the atom. Inserting equation 6.6 into equation 6.5

$$\Delta E_{trans}(SR) + \Delta E_{rot}(SR) = -\left(\frac{m_{SR}}{m_A}\right)\Delta E_{trans}(SR). \tag{6.7}$$

Rearranging

$$\Delta E_{rot}(SR) = -\left(1 + \frac{m_{SR}}{m_A}\right)\Delta E_{trans}(SR). \tag{6.8}$$

Translational energy gains correspond to a loss in rotational energy and are related by a factor proportional to the ratio of the super rotor and atom masses. For a given super rotor, a lighter mass atom will give a larger change in rotational energy. The data from the experiments show larger translational energy gains in CO_2 rotors for He-CO_2 than for Ar-CO_2. This result clearly show that the loss in rotational energy is greater for He collisions than with Ar collisions. Therefore, it appears that He collisions with CO_2 induce larger and more rapid changes in J than Ar collisions.

6.3.3 Rotational Adiabaticity in Super Rotor Collisions

Optical centrifuge experiments on Ar-CO_2 and He-CO_2 collisions show that super rotor relaxation occurs faster and involves transitions with larger ΔJs in the presence of He. Rotational and translational time scales affect collisional energy transfer. In the limit of high velocity particles, the collision is considered sudden, wherein the rotational motion is slow compared to the time of the collision. Rotation-to-translational energy transfer is efficient in the sudden limit. In the other extreme, when the time of collisions is long compared to the rotational period, rotational motion is faster than the relative velocity and the energy transfer is inefficient.

The duration of a collision t_{col} is defined as the interaction length ℓ divided by the relative velocity v_{rel}

$$t_{col} = \frac{\ell}{v_{rel}}. \tag{6.9}$$

146
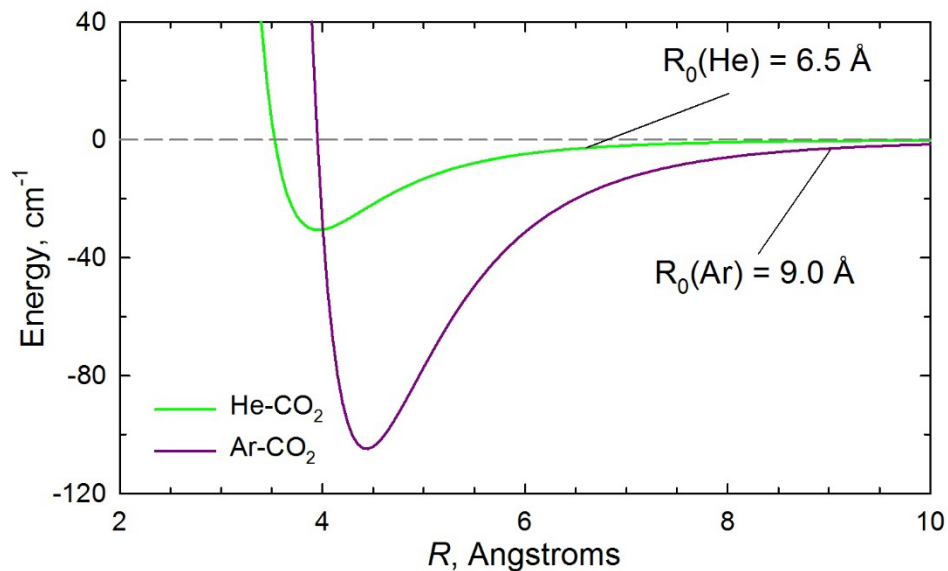
Figure 6.10 Lennard-Jones potential energy curves for Ar-CO$_2$ and He-CO$_2$.

The length of interaction is defined using the Lennard-Jones potentials for He-CO$_2$ and Ar-CO$_2$ systems (Figure 6.10). For this discussion, the interaction length ℓ is defined for 300 K collisions as the distance at which the potential is 1% of the thermal collision energy ($V(R_0) = 0.01E_{col} = 3$ cm^{-1}) to the start of the repulsive interaction at $R = \sigma$. For He-CO$_2$, $R_0 = 6.5$ Å, $\sigma = 3.5$ Å and $\ell = 3.0$ Å[96]. For Ar-CO$_2$, $R_0 = 9.0$ Å, $\sigma = 4.0$ Å and $\ell = 5.0$ Å[96]. The relative velocity at 300 K is $v_{rel} = 1320$ m/s for He-CO$_2$ and $v_{rel} = 550$ m/s for Ar-CO$_2$ collisions. Using equation 6.9 and the values for the interaction lengths and relative velocities, the collision time for He-CO$_2$ is $t_{col} = 0.23$ ps and for Ar-CO$_2$ is $t_{col} = 0.91$ ps.

The rotational period of a linear molecular is determined by its rotational quantum number and its moment of inertia I. Equating the classical rotational energy to the quantum energy

$$E_{rot} = \tfrac{1}{2}I\omega^2 = \frac{\hbar^2 J(J+1)}{2I} = BJ(J+1). \tag{6.10}$$

147

yields an expression for the angular velocity ω

$$\omega \approx \frac{\hbar J}{I} = \frac{2BJ}{\hbar}. \tag{6.11}$$

The rotational period is given by

$$t_{rot} = \frac{1}{\nu_{rot}} = \frac{2\pi}{\omega}. \tag{6.12}$$

Figure 6.11a shows t_{rot} vs J for CO_2 and compares the collision times for He and Ar collisions with CO_2.
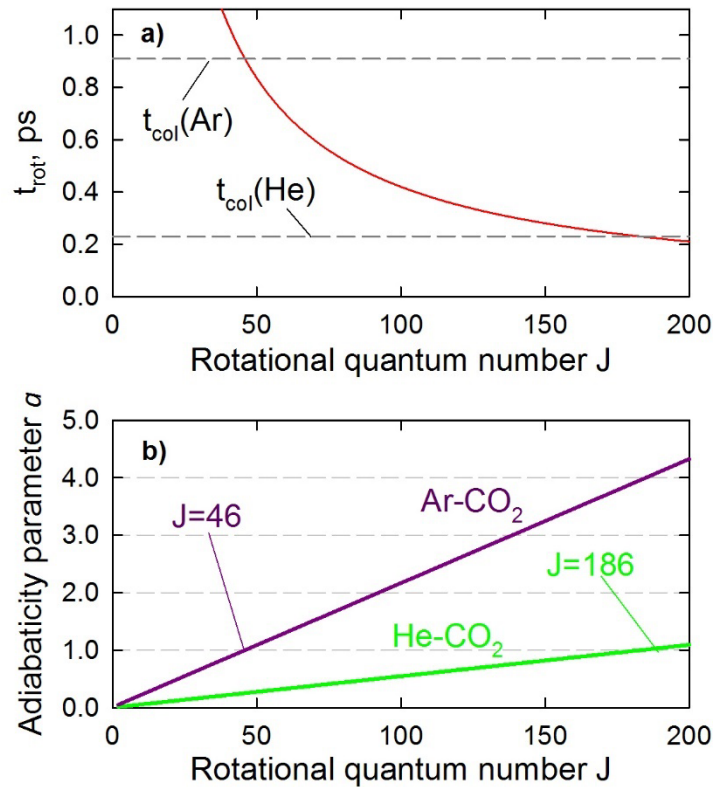
Figure 6.11 a) Rotational period of CO_2 as a function of J. Also shown on the plot are the collision durations for Ar-CO_2 and He-CO_2. b) Adiabaticity parameter for Ar-CO_2 and He-CO_2. The point where the collision system crosses into the adiabatic regime is labeled on the plot.

148

The adiabaticity parameter a is defined as[97]

$$a = \frac{t_{col}}{t_{rot}}.$$ (6.13)

The values of a are plotted in Figure 6.11b as a function of J for He-CO_2 and Ar-CO_2 collisions. He-CO_2 collisions are rotationally adiabatic above J = 186. For lower J states, the collisions are sudden and rotation-to-translation (R→T) energy transfer is efficient. In contrast, Ar-CO_2 collisions are in the rotationally adiabatic regime for J >46. In this case, R→T energy transfer is inefficient. The experimental results demonstrate the importance of rotational adiabaticity in super rotor relaxation.

6.4 Conclusions

This set of experiments investigated the effect of collision partner on CO_2 super rotor rotational dynamics. Two rare gas collision partners were used in this work: Ar and He. Rotational relaxation is much faster with He than with Ar. Polarization-dependent measurements indicate that CO_2 rotors have a greater amount of orientational anisotropy that remains through a greater number of He collisions than with Ar collisions. This result provides further evidence of the correspondence of CO_2 super rotors to the behavior described by a classical gyroscope. In addition, the larger amounts of translational energy gained by CO_2 rotors in collisions with He show that He induces larger changes in J. The results presented here demonstrate the importance of rotational adiabaticity to the rotational relaxation of super rotors.

Future experimental work would investigate the impact rotational adiabaticity of other collision partners, changing both the unexcited buffer gas and the optically

centrifuged super rotor. It would be interesting, for example, to investigate other rare gases such as neon and xenon. Changes in the interaction potential likely have important effects and other work would involve changing the super rotor to a molecule such as N_2O or CO, which would have more anisotropic potential energy surfaces. This work paves the way for studies using the orientation and rotational state generated by the optical centrifuge as a way to study spatially and energy dependent reactive and non-reactive collisions. To further investigate the rotational relaxation kinetics of the two collision systems studied here, close-coupled calculations were performed on $Ar-CO_2$ and $He-CO_2$. The results are presented in the next chapter.

Chapter 7: Comparing the Collision Dynamics of Ar-CO₂ and He-CO₂ Using the Results from Quantum Scattering Calculations

7.1 Introduction

Rotational energy dynamics is a complex process involving many molecular and intermolecular parameters[38, 39]. To describe state-to-state dynamics between rotational levels, many models based on the energy gap or angular momentum gap have been proposed, but no real consensus has been established for all molecules[40-47]. Additionally, most studies employing quantum scattering calculations have focused on the cross sections and rates for relatively low angular momentum states[98-102]. Here, quantum scattering calculations are presented on the Ar-CO_2 and He-CO_2 collision systems for a large range of rotational states to investigate the role of the collision partner on the rotational relaxation of CO_2 rotors and to compare with optical centrifuge studies of CO_2.

Close-coupled calculations performed on both collision systems determined the state-to-state inelastic scattering cross sections on a grid of five collision energies from 150 cm^{-1} to 1000 cm^{-1}. State-to-state rate constants calculated from the cross section data demonstrate the impact of the collision partner on transition rates. A master equation is used to describe rotational relaxation after a subset of the CO_2 population has been excited to a distribution of high rotational states. The solution to the master equation shows how differences between the rates of Ar-CO_2 and He-CO_2 relaxation manifest in the observed

dynamics of individual rotational states. The computational results are compared with optical centrifuge experiments.

7.2 Theory: Rotationally Inelastic Collisions

This section describes the theory used in this chapter to study rotationally inelastic collisions. An outline of this section is provided here. In Subsection 7.2.1, an explanation of the scattering cross section in classical and quantum terms is provided. Subsection 7.2.2 presents a derivation of the close-coupled equations, which model a quantum scattering system with internal degrees of freedom. Subsection 7.2.3 provides relevant details from quantum scattering theory to show how the state-to-state inelastic scattering cross sections of a rigid rotor are determined. Subsection 7.2.4 describes the algorithms used to solve the close-coupled equations and calculate the inelastic scattering cross sections. Subsection 7.2.5 describes how state-to-state rate constants are calculated from the inelastic scattering cross sections. Subsection 7.2.6 explains a master equation and shows how it can be solved analytically to find the time evolution of population in individual rotational states.

This section draws from several sources on quantum scattering theory and molecular collisions, but is largely based on lecture notes by Millard Alexander[103, 104]. The book *Quantum Mechanics in Chemistry* provides an accessible and clear introduction to quantum scattering theory[105]. The book *Introduction to the Theory of Atomic and Molecular Collisions,* provides details on elastic and inelastic quantum scattering theory and provides much of the notation used in this section[106]. The expression for the inelastic scattering cross section of a rigid rotor was first derived by Arthurs and Dalgarno in their

1960 paper[107]. The article by Secrest describes the close-coupled equations and gives details on the approaches by which the closed coupled equations are solved[108]. A thorough description of the analytic solution to the master equation is given in paper by Alexander *et. al*[109].

7.2.1 The Scattering Cross Section

Consider particles with flux I scattering off a spherically symmetric potential as shown in Figure 7.1. The impact parameter b is the perpendicular distance from the scattering center to the incident particle. The differential scattering cross section is defined as the ratio of the scattered flux per unit solid angle to the incident flux per unit area. Figure 7.1 shows the infinitesimal area dA is

$$dA = 2\pi b \, db \tag{7.1}$$

and the infinitesimal solid angle, $d\Omega$, is

$$d\Omega = 2\pi \sin \theta \, d\theta. \tag{7.2}$$

Therefore, the differential scattering cross section, $d\sigma/d\Omega$, is

$$\frac{d\sigma}{d\Omega} = \frac{I/d\Omega}{I/dA} = \left| \frac{b}{\sin \theta \, d\theta/db} \right|. \tag{7.3}$$
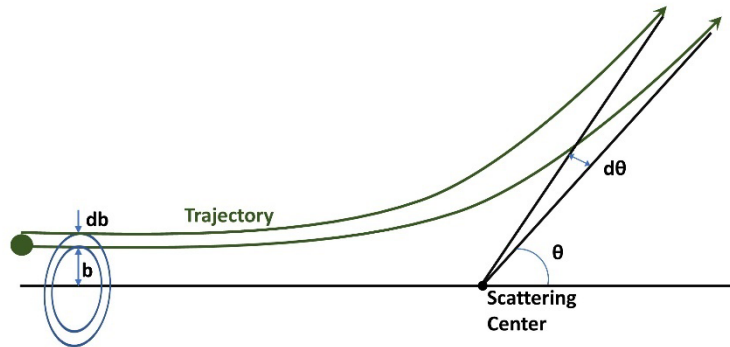
Figure 7.1 Particles with flux, I, scatter off a spherically symmetric potential. Parameters for the derivation of the cross-section are shown.

The differential scattering cross section has units of area and represents a probability of scattering at a particular solid angle. Integrating over all solid angles yields the integrated cross section:

$$\sigma = \int \left(\frac{d\sigma}{d\Omega}\right)(\theta,\phi)\, d\Omega. \tag{7.4}$$

The angle of deflection is a function of energy E, so the cross section is also a function of energy.

Scattering of a particle with a discrete set of states off a potential can result in a change of state of the particle. Similar to the classical definition, the state-to-state differential cross section is defined to be

$$\left(\frac{d\sigma}{d\Omega}\right)_{\text{if}} = \frac{\text{scattered flux in state f}}{d\Omega} \div \frac{\text{scattered flux in state i}}{dA}. \tag{7.5}$$

The integrated inelastic scattering cross section represents the total probability of transitioning from an initial state i to a final state f and is written as

$$\sigma_{\text{if}} = \int_0^\infty 2\pi b\, P_{\text{if}}(b)\, db, \tag{7.6}$$

where the integral is over all possible impact parameters and $P_{\text{if}}(b)$ is the probability of transitioning from state i to state f at a value of b. The total angular momentum of the system is $\vec{l} = \vec{b}\times\vec{p} = \mu v b$. Quantum mechanically, angular momentum is quantized as $\hbar\left(J+\frac{1}{2}\right)$. Therefore equation 7.6 becomes

$$\sigma_{\text{if}} = \frac{2\pi\hbar^2}{(\mu v)^2}\sum_{J=0}^\infty \left(J+\frac{1}{2}\right)P_{\text{if}}^J(v) = \frac{\pi}{k_i^2}\sum_{J=0}^\infty (2J+1)P_{\text{if}}^J(E), \tag{7.7}$$

154

where $k_i^2 = \frac{2\mu(E-\varepsilon_i)}{\hbar^2}$ is the wave vector in the initial state, E is the total energy of the

system, and ε_i is the internal energy of the initial state. In equation 7.6, the continuous

$P_{if}(b)$ has been replaced by the discrete $P_{if}^J(E)$ and the variable changed from velocity to

energy. The discrete probability of transitioning from state i to state f is found by solving

the Schrödinger equation for the collision system.

7.2.2 The Close-Coupled Equations

Consider a collision between an atom and a molecule. We will ignore the internal

structure of the atom for this discussion. The Hamiltonian $H(\vec{r}, q)$ describing the system,

which depends both on the separation between the atom and molecule $\vec{r}$ and the internal

coordinates of the molecule q is

$$H(\vec{r}, q) = -\frac{\hbar^2}{2\mu}\nabla^2(\vec{r}) + V(r, q) + H_{int}(q), \qquad (7.8)$$

The first term in equation 7.8 is the kinetic energy of the system, the second term is the

interaction potential, and the third is the Hamiltonian describing the internal structure of

the molecule. Note that the potential $V(r, q)$ is assumed to depend only on the magnitude

of $\vec{r}$, not its orientation Furthermore, at large separation

$$\lim_{r \to \infty} H(\vec{r}, q) = H_{int}(q). \qquad (7.9)$$

The time-independent Schrodinger equation of the collision system is

$$H \Psi(\vec{r}, q) = E \Psi(\vec{r}, q), \qquad (7.10)$$

where E is the total energy of the system. The total energy is equal to the collision energy,

E_C, plus the rigid rotor energy, $\varepsilon_j = Bj(j + 1)$, where B is the rotational constant. The

wavefunction, Ψ, is expanded in a complete orthogonal set of eigenfunctions with the angular and radial parts of the wavefunction separated. For the angular part, the eigenfunctions of the angular part of the kinetic energy operator are the spherical harmonics $Y_{lm}(\theta, \phi)$, where l is the orbital angular momentum of the collision system. The eigenfunctions of the rigid rotor are $Y_{jm_j}(\alpha, \beta)$, where j is the internal angular momentum of the rotor and α and β are internal coordinates. The radial part is an unknown function $G_{lj}(r)$, which is a function of the separation between the collision partners and depends on both the orbital angular momentum l of the system and internal angular momentum j of the rotor. Therefore, the wavefunction is written as

$$\Psi(\vec{r}, q) = \sum_{lm\,jm_j} Y_{lm}(\theta, \phi) Y_{jm_j}(\alpha, \beta) \left(\frac{G_{lj}(r)}{r} \right). \tag{7.11}$$

The angular momentum of the internal states couples with the angular momentum of the system in the usual way:

$$Y_{lj}^{JM} = \sum_{m\,m_j} C_{lmjm_j}^{JM} Y_{lm}(\theta, \phi) Y_{jm_j}(\alpha, \beta), \tag{7.12}$$

where $C_{lmjm_j}^{JM}$ are the Clebsch-Gordon coefficients. Therefore, the wavefunction is written in a new basis as

$$\Psi^{JM}(\vec{r}, q) = \frac{1}{r} \sum_{lj} Y_{lj}^{JM}(\theta, \phi, \alpha, \beta) G_{JMlj}(r). \tag{7.13}$$

In this basis, the total angular momentum, J, is conserved. By inserting equation 7.13 into the Schrödinger (equation 7.10), using the orthonormality of the spherical harmonics, and

integrating over all coordinates except for r, the Schrodinger equation becomes a set of coupled differential equations:

$$\left[-\frac{\partial^2}{\partial r^2} + \frac{l(l+1)}{r^2} - k_j^2\right] G_{JMlj}(r) = -\sum_{l'j'} V_{ljl'j'}^{JM} G_{JMl'j'}(r). \tag{7.14}$$

Equivalently, in matrix notation:

$$\left[\boldsymbol{I}\frac{\partial^2}{\partial r^2} + \boldsymbol{W}(r)\right]\boldsymbol{G}(r) = 0 \tag{7.15}$$

where $\boldsymbol{W}(r) = \boldsymbol{k}^2 - \boldsymbol{l}^2(r) - \boldsymbol{V}(r)$. Equation 7.14 is the close-coupled equation that defines a scattering system with internal degrees of freedom. The terms $\boldsymbol{k}^2$ and $\boldsymbol{l}^2$ are diagonal matrices defined by

$$(k^2)_{jj} = \frac{2\mu}{\hbar^2}(E - \varepsilon_j), \tag{7.16}$$

where ε_j is the internal energy in the jth channel and

$$(l^2)_{ll} = \frac{\hbar^2}{2\mu}\frac{l(l+1)}{r^2}, \tag{7.17}$$

where l is the orbital angular momentum in the lth channel. The potential can be written as an expansion of Legendre polynomials as

$$V(r) = \sum_{\lambda=0}^{\infty} K_\lambda(r)P_\lambda(\cos\gamma). \tag{7.18}$$

Therefore, the elements of the interaction matrix $\boldsymbol{V}(r)$ are given by

$$V_{ljl'j'}^{JM}(r) = \frac{2\mu}{\hbar^2}\sum_{\lambda=0}^{\infty} K_\lambda(r)\langle lj;J|P_\lambda(\cos\gamma)|l'j';J\rangle. \tag{7.19}$$

The expansion of the potential in terms of the Legendre polynomials is useful in solving the close-coupled equations.

157

7.2.3 The Scattering Matrix and the Scattering Amplitude

In general, the molecule does not need to be in just one $\psi_i(r,q)$ state, but rather can be in a linear combination of eigenstates:

$$\boldsymbol{\psi}(r,q) = \sum_i a_i \, \psi_i(r,q), \tag{7.20}$$

where $|a_i|^2$ represents the probability of finding the particle in state $\psi_i(r,q)$. The system can then be defined by the set of coefficients a_i, written as a vector:

$$\boldsymbol{A} = \begin{bmatrix} a_1 \\ \vdots \\ a_i \end{bmatrix}. \tag{7.21}$$

A matrix $\boldsymbol{S}$ can be defined to take the system from a set of initial states to a set of final states by

$$\boldsymbol{A}_{i'} = \boldsymbol{S}\boldsymbol{A}_i. \tag{7.22}$$

The $\boldsymbol{S}$ matrix must conserve probability and therefore must be unitary. The square modulus of the individual elements of the S-matrix, $\left|S^J_{ii'}\right|^2$ represent the probability that the scattered system makes a transition from state i to i'. It is important to note that the S-matrix is a function of energy and depends parametrically on the total angular momentum, J, of the collision system.

With this understanding of the S-matrix, we now write the asymptotic form of the solution to the close-coupled equations (i.e. the radial Schrödinger equation)

$$\boldsymbol{G}(r) \sim \boldsymbol{U}^- - \boldsymbol{S}\boldsymbol{U}^+, \tag{7.23}$$

where U^- and U^+ are the matrices of incoming and outgoing waves, respectively. Explicitly writing these matrices gives:

$$G_{ljl'j'}^J(r) \sim \delta_{jj'}\delta_{ll'}e^{-i(k_{jj}r - l\pi/2)} - S_{jlj'l'}^J \left(\frac{k_{jj}}{k_{j'j}}\right)^{1/2} e^{i\left(k_{j'j}r - l'\pi/2\right)}. \tag{7.24}$$

Inserting the asymptotic form of $G_{ljl'j'}^J(r)$ into equation 7.13 gives the asymptotic form of the total wavefunction in the J-conserved basis:

$$\lim_{r \to \infty} \Psi^{JM}(\vec{r}, q) = \frac{1}{r}\sum_{lj} Y_{lj}^{JM}(\theta, \phi, \alpha, \beta)$$

$$\times \left[\delta_{jj'}\delta_{ll'}e^{-i(k_{jj}r - l\pi/2)} - S_{jlj'l'}^J \left(\frac{k_{jj}}{k_{j'j}}\right)^{1/2} e^{i\left(k_{j'j}r - l'\pi/2\right)}\right]. \tag{7.25}$$

The asymptotic form of the *total* wavefunction in the Schrödinger equation (7.10) in the rigid rotor basis is written

$$\lim_{r \to \infty} \Psi(\vec{r}, q) \sim Y_{jm_j}(\alpha, \beta)e^{ik_{jj}r} + \sum_{j'} \frac{i}{k_{jj}}\left(\frac{k_{jj}}{k_{j'j}}\right)^{1/2} \frac{e^{ik_{j'j}r}}{r} \sum_{m_{j'}} f_{jj'}(\theta)Y_{j'm_{j'}}(\alpha, \beta). \tag{7.26}$$

Here, the first term in this equation represents the incoming plane wave of the molecule in state, $Y_{jm_j}(\alpha, \beta)$. The second term represents an outgoing spherical wave in state $Y_{j'm_{j'}}(\alpha, \beta)$ with a scattering amplitude $f_{jj'}(\theta)$ for each initial and final internal state. Note that because the potential only depends on the magnitude of the separation, r, the

scattering amplitude depends on the polar angle, θ, but not the azimuthal angle, ϕ. The differential scattering cross section is given by[*]

$$\left(\frac{d\sigma}{d\Omega}\right)_{jj'} = \left(\frac{k_{j'j}}{k_{jj}}\right)\left|f_{jj'}(\theta)\right|^2. \tag{7.27}$$

From here the integral cross sections can be calculated, which will give the state-to-state inelastic scattering cross sections:

$$\sigma_{jj'} = \iint \left(\frac{d\sigma}{d\Omega}\right)_{jj'} \sin\theta \; d\theta \; d\phi = 2\pi \int_0^\pi \left|f_{jj'}(\theta)\right|^2 \sin\theta \; d\theta. \tag{7.28}$$

The scattering amplitude can be expanded in terms of the spherical basis functions used above:

$$f_{jj'}(\theta) = \sum_{J=0}^\infty \sum_{M=-J}^{+J} \sum_{l=|J-j|}^{J+j} i^l\left(\pi(2l+1)\right)^{1/2} f_{jj'}^J \, Y_{lj}^{JM}(\vec{r}, q). \tag{7.29}$$

In addition, the incident plane wave in equation 7.25 is also written in the J conserved basis as

$$Y_{jm_j}(\alpha, \beta)e^{ik_{jj}r} = \frac{i\pi^{1/2}}{k_{jj}}\sum_{J=0}^\infty \sum_{M=-J}^{+J} \sum_{l=|J-j|}^{J+j} (2l+1)^{1/2}i^l C_{l0jm_j}^{JM} \, \Psi^{JM}(\vec{r}, q). \tag{7.30}$$

Equations 7.29 and 7.30 are inserted into equation 7.26. The result is equated to the asymptotic form given in 7.25 and the expression for the scattering amplitude in terms of the scattering matrix becomes:

---

[*] The expression of the differential cross section in terms of the scattering amplitude comes from the definition of the differential cross sections given in equation 6.5. Equation 6.27 can be obtained using the quantum mechanical flux, which is given by $I = Re[\Psi^*\hat{v}\Psi]$, where $\hat{v}$ is the velocity operator: $-\frac{i\hbar}{\mu}\nabla$.

$$f_{jj'}(\theta) = \sum_{JM \, ll' \, m'} i^{l-l'+1} \left(\frac{\pi(2l+1)}{k_{jj}k_{j'j}} \right)^{\frac{1}{2}} C^{JM}_{l0jm_j} C^{JM}_{l'm'j'm_{j'}} \atop \times \left[S^J_{jlj'l'} - \delta_{jj'}\delta_{ll'} \right] Y_{l'm'}(\theta,\phi) \qquad (7.31)$$

Note that $-\delta_{ij}$ in equation 7.31 represents unscattered waves that are necessarily elastic and therefore do not contribute to amplitude of the scattered waves. Using equation 7.28, the state-to-state inelastic scattering cross sections is

$$\sigma_{jj'} = \frac{\pi}{(2j+1)k_j^2} \sum_{J=0}^{\infty} \sum_{l} \sum_{l'} (2J+1) \left| S^J_{jlj'l'} - \delta_{jj'}\delta_{ll'} \right|^2 . \qquad (7.32)$$

Simplifying, equation 7.32 can be written as a sum of partial cross sections, $\sigma^J_{jj'}$, such that

$$\sigma_{jj'} = \sum_{J=0}^{\infty} (2J+1)\sigma^J_{jj'} . \qquad (7.33)$$

Comparing equation 7.32 with equation 7.7 we see that the probability of transitioning from state j to state j' is

$$P^J_{jj'} = \sum_{l} \sum_{l'} \left| S^J_{jlj'l'} - \delta_{jj'}\delta_{ll'} \right|^2 . \qquad (7.34)$$

Ultimately, the problem amounts to finding the elements of the S-matrix, from which the inelastic scattering cross sections can be determined.

Note that the S-matrix is symmetric, which is a consequence of the fact that the Schrödinger Equation is time reversible. As such, the transition probabilities satisfy microscopic reversibility, i.e.

$$P^J_{jj'}(E) = P^J_{j'j}(E) \qquad (7.35)$$

Since the above expression is written for probabilities at the same total energy, we have

161

$$(2j + 1)k_j^2\sigma_{jj'}^J = (2j' + 1)k_{j'}^2\sigma_{j'j}^J. \tag{7.36}$$

The explicit energy dependence is:

$$(2j + 1)(E - \varepsilon_j)\sigma_{jj'}^J(E) = (2j' + 1)(E - \varepsilon_{j'})\sigma_{j'j}^J(E). \tag{7.37}$$

The condition of microscopic reversibility is important in the understanding of the *rates* of inelastic transitions. However, first we describe the algorithms used to solve the close-coupled equations and find the elements of the S-matrix.

7.2.4 Solutions to the Close-Coupled Equations

There are typically two approaches to solving the close-coupled equations: *solution approximation* methods and *potential approximation* methods[108]. Solution approximation methods solve the close-coupled equations (Equation 7.15) numerically for a specified system. Potential approximation methods use a simplified interaction potential and solve the close-coupled equations exactly. Both approaches have merits based on the accuracy required, computing time allotted, and number of total energies at which a solution is needed. Solution approximation approaches have high accuracy with reasonable computing costs. Potential approximation methods can give acceptable accuracies with low computing costs as the simplified potential permits taking large integration step sizes.

In this work, we employ a hybrid approach as described by Alexander[110]. A solution approximation method is used at small distances from the scattering center, at which the potential rapidly changes. A potential approximation method is used at large distances, at which the potential is slowly varying. The technique used in the solution approximation region is a Log Derivative algorithm first developed by Johnson[111] and

162

later modified by Manolopoulos[112]. The technique used in the potential approximation region is an Airy Propagator algorithm developed by Alexander[110] and based on a technique by Gordon[113]. The hybrid algorithm is executed by the HIBRIDON scattering code developed by Alexander and Manolopoulos[86].

7.2.5 State-to-State Rate Constants

The rate of a collision-induced transition is equal to the flux times the cross section of the transition. From kinetic theory, as described in section 2.3, the flux is given by the particle density, ρ, multiplied by the relative velocity, v. Therefore,

$$\frac{dn_{i\rightarrow f}}{dt} = \rho v \sigma_{i\rightarrow f}(v) = \rho k_{i\rightarrow f}(v), \tag{7.38}$$

where $n_{i\rightarrow f}$ is the number of particles making a transition from state i to state f and $k_{i\rightarrow f}$ is the bimolecular rate constant and $k_{i\rightarrow f}(v) = v\sigma_{i\rightarrow f}(v)$. The thermal rate constant $k_{i\rightarrow f}(T)$ is given by an average over all possible collision velocities

$$k_{i\rightarrow f}(T) = \int k_{i\rightarrow f}(v)P(v)dv \tag{7.39}$$

where $P(v)$ is the Maxwell-Boltzmann velocity distribution given in equation 2.34. A change of variables converts the integration to be over collision energy, $E_C = \mu v^2/2$, rather than collision velocity:

$$k_{i\rightarrow f}(T) = \left[\frac{8}{\pi\mu(k_B T)^3}\right]^{\frac{1}{2}} \int_0^\infty \sigma_{i\rightarrow f}(E)E_C e^{-\left(\frac{E_C}{k_B T}\right)}dE_C. \tag{7.40}$$

Another change of variables converts this expression to integrate over total energy:

$$k_{i\rightarrow f}(T) = \left[\frac{8}{\pi\mu(k_B T)^3}\right]^{\frac{1}{2}} \int_{\varepsilon_i}^\infty \sigma_{i\rightarrow f}(E)(E - \varepsilon_i)e^{-\left(\frac{(E-\varepsilon_i)}{k_B T}\right)}dE. \tag{7.41}$$

The collision cross section vanishes for energies less than the energy of the initial state, ε_i. Therefore, the lower bound of the integral can be extended to 0 without any consequence:

$$k_{i \to f}(T) = \left[\frac{8}{\pi\mu(k_B T)^3}\right]^{\frac{1}{2}} e^{-\left(\frac{\varepsilon_i}{k_B T}\right)} \int_0^\infty \sigma_{i \to f}(E)(E - \varepsilon_i) e^{-\left(\frac{E}{k_B T}\right)} dE. \qquad (7.42)$$

Exchanging the indices and using the condition of microscopic reversibility given in equation 7.37, the thermal rate constant of the reverse process is

$$k_{f \to i}(T) = \left[\frac{8}{\pi\mu(k_B T)^3}\right]^{\frac{1}{2}} \left[\frac{2j_i + 1}{2j_f + 1}\right] e^{-\left(\frac{\varepsilon_f}{k_B T}\right)} \int_0^\infty \sigma_{i \to f}(E)(E - \varepsilon_i) e^{-\left(\frac{E}{k_B T}\right)} dE. \qquad (7.43)$$

Using equations 7.42 and 7.43 we arrive at the condition of detailed balance:

$$\frac{k_{f \to i}(T)}{k_{i \to f}(T)} = \left[\frac{2j_i + 1}{2j_f + 1}\right] e^{\left(\frac{\varepsilon_f - \varepsilon_i}{k_B T}\right)}. \qquad (7.44)$$

In summary, once the state-to-state inelastic cross sections are determined, an integration over energy yields the state-to-state rate constants. The calculation of a matrix of state-to-state rate constants can be simplified by using detailed balance to determine half of the values in the matrix.

7.2.6 The Master Equation

At equilibrium, the probability for population p_j of the rotational state j of a molecule is given by the Boltzmann distribution:

$$p_j = \frac{1}{Z} g_j e^{-\left(\frac{\varepsilon_j}{k_B T}\right)}, \qquad (7.45)$$

where g_j is the rotational degeneracy $(2j + 1)$ and Z is the rotational partition function

$$Z = \sum_j g_j e^{-\left(\frac{\varepsilon_j}{k_B T}\right)}. \qquad (7.46)$$

164

If the system is perturbed away from equilibrium and then allowed to return to equilibrium, the time evolution of the populations of all states will be governed by a set of differential equations called a master equation. For a system of rigid rotors with M rotational states, the time rate of change of the population of a state i is

$$\frac{dn_i}{dt} = \rho\left[-k_{ii}n_i + \sum_{f\neq i} k_{f\rightarrow i}n_f\right].$$ (7.47)

In the above expression, the depletion rate of a state k_{ii} is equal to the sum of the rate constants out of the state:

$$k_{ii} = \sum_{f\neq i} k_{i\rightarrow f}.$$ (7.48)

This equation is a result of requiring the total number of particles in the system to be constant. The set of coupled, first-order, linear differential equations in equation 7.47 can be written in matrix form as

$$\frac{d\boldsymbol{n}}{dt} = \rho\boldsymbol{Kn},$$ (7.49)

where $\boldsymbol{n}$ is a column vector of the populations of the M rotational states and $\boldsymbol{K}$ is the matrix of state-to-state rate constants. Note that the matrix $\boldsymbol{K}$ is not symmetric, but rather the off diagonal elements are related by the condition of detailed balance given in equation 7.44.

The master equation (7.49) can be solved analytically to find the time evolution of the M rotational states after the equilibrium populations have been altered. The solution proceeds as follows. The rate matrix is transformed via a similarity transformation to a basis in which the rate matrix is symmetric. The symmetric transformed matrix is diagonalized, which decouples the differential equations and thereby makes solving the

165

equations straightforward. The solutions are then transformed back into the original basis to find the evolution of the population distribution.

To begin, a diagonal matrix $\mathbf{\Pi}$ whose diagonal elements are the Boltzmann populations is constructed:

$$\Pi_{ij} = \delta_{ij} g_i \exp(-\varepsilon_i/k_B T)/Z. \tag{7.50}$$

The square root of this matrix, $\mathbf{\Pi}^{1/2}$, is also a diagonal matrix and has elements

$$\Pi_{ij}^{1/2} = \delta_{ij}[\Pi_{ii}]^{1/2}. \tag{7.51}$$

In addition, the inverse of the matrix exists, such that $\mathbf{\Pi}^{1/2}\left(\mathbf{\Pi}^{1/2}\right)^{-1} = \mathbf{1}$, the identity matrix. Inserting the identity in equation 7.49 gives

$$\frac{d\mathbf{n}}{dt} = \rho\mathbf{\Pi}^{1/2}\left[\left(\mathbf{\Pi}^{1/2}\right)^{-1}\mathbf{K}\mathbf{\Pi}^{1/2}\right]\left(\mathbf{\Pi}^{1/2}\right)^{-1}\mathbf{n}. \tag{7.52}$$

Multiplying both sides of equation 7.52 by $\left(\mathbf{\Pi}^{1/2}\right)^{-1}$ gives

$$\frac{d\tilde{\mathbf{n}}}{dt} = \rho\tilde{\mathbf{K}}\tilde{\mathbf{n}}, \tag{7.53}$$

where $\tilde{\mathbf{n}} = \left(\mathbf{\Pi}^{1/2}\right)^{-1}\mathbf{n}$ and $\tilde{\mathbf{K}} = \left(\mathbf{\Pi}^{1/2}\right)^{-1}\mathbf{K}\mathbf{\Pi}^{1/2}$. Using detailed balance, it can be shown that $\tilde{\mathbf{K}}$ is a symmetric matrix. Therefore, $\tilde{\mathbf{K}}$ can be diagonalized in the usual way

$$\mathbf{D}^T\tilde{\mathbf{K}}\mathbf{D} = \mathbf{\Lambda}, \tag{7.54}$$

where $\mathbf{D}$ is a matrix with columns that are the orthogonal eigenvectors of $\tilde{\mathbf{K}}$ and $\mathbf{\Lambda}$ is a diagonal matrix with the eigenvalues of $\tilde{\mathbf{K}}$, all of which are real. Note that

$$\mathbf{D}^T\mathbf{D} = \mathbf{D}\mathbf{D}^T = \mathbf{1}. \tag{7.55}$$

Therefore, equation 7.53 can be rewritten as

$$\frac{d\tilde{\mathbf{n}}}{dt} = \rho\mathbf{D}\mathbf{D}^T\tilde{\mathbf{K}}\mathbf{D}\mathbf{D}^T\tilde{\mathbf{n}} = \rho\mathbf{D}\mathbf{\Lambda}\mathbf{D}^T\tilde{\mathbf{n}}. \tag{7.56}$$

Multiplying by D^T gives

$$\frac{d\mathcal{N}}{dt} = \rho \Lambda \mathcal{N}, \tag{7.57}$$

where

$$\mathcal{N} = D^T \tilde{n} = D^T \left(\Pi^{1/2}\right)^{-1} n. \tag{7.58}$$

Equation 7.57 is now an uncoupled set of differential equations of which the solution is a simple exponential. Therefore, each component of the population vector $\mathcal{N}$ evolves as

$$\mathcal{N}_i(t) = \mathcal{N}_i(0)e^{\rho \Lambda_i t}. \tag{7.59}$$

The goal is to find the relaxation of populations of some initial state distribution given by n_0. The distribution is normalized such that $\sum_i (n_0)_i = 1$, which is done without any loss of generality. From equation 7.58, the distribution n_0 corresponds to $\mathcal{N}_0$, which evolves per equation 7.59. Transforming back into the n basis gives the time evolution of the populations in each state:

$$n(t) = \Pi^{1/2} D \mathcal{N}(t) = \Pi^{1/2} D \mathcal{N}_0 e^{\rho \Lambda t}. \tag{7.60}$$

There is always one eigenvalue of $\tilde{K}$ that is 0; all the rest are negative. The zero eigenvalue therefore is the only solution which survives at long time and corresponds to the Boltzmann distribution of populations. At long time, the system relaxes to the Boltzmann distribution.

7.3 Computational Methods

To study the rotational relaxation of CO_2 from collisions with argon and helium, inelastic scattering cross sections were calculated with the scattering code HIBRIDON[86]. Calculations assumed a rigid rotor model for the CO_2 molecule and that CO_2 is in the vibrational ground state. For the Ar-CO_2 system, the potential energy surface of Klos[85]

was used and for the He-CO_2 system the potential energy surface of Li and Le Roy[114] was used. The potentials are written as $V(r,\theta)$, where r is the distance from the CO_2 center of mass to the collision partner (Ar or He) and θ is the angle between r and the CO_2 molecular axis. Figure 7.2a and b show the potential energy surfaces used in the calculations described here.

The HIBRIDON scattering code solves the close-coupled equations with a hybrid approximate-solution/approximate-potential algorithm developed by Alexander and Manolopoulos, which numerically propagates the solution from the classically forbidden region at small r out to large r. In the calculations reported here, the solution was propagated out to $r = 80$ Å. Integrated cross sections are calculated from the S matrix according to equation 7.32. The state-to-state cross sections for each collision system were calculated at five collision energies: 150, 200, 310, 525, and 1000 cm^{-1}. At each energy, a sufficient number of total angular momentum J partial waves were used to ensure convergence of the inelastic cross sections. State-to-state inelastic cross sections were
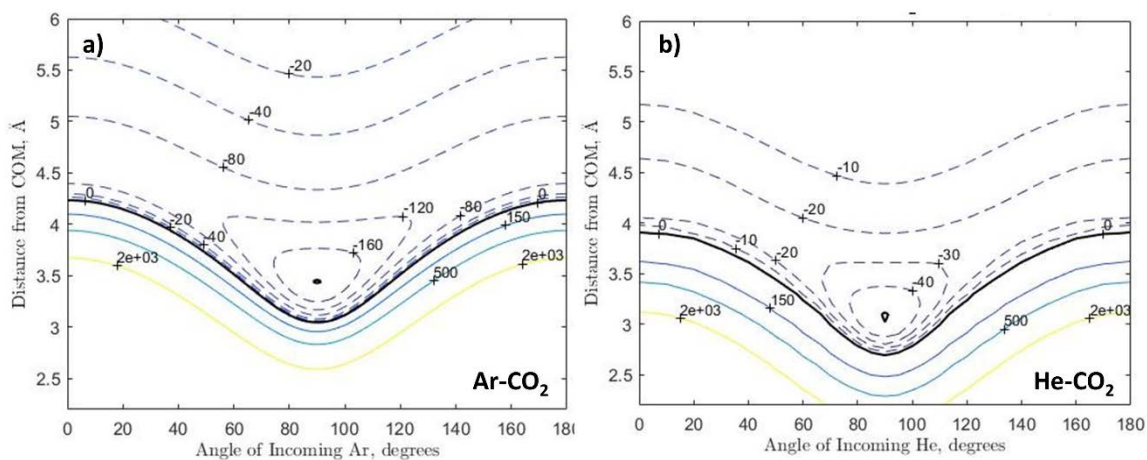
Figure 7.2 a) Potential energy surface by Klos[85] of Ar-CO_2 collision system. b) Potential energy surface by Li and Le Roy[114] of He-CO_2 collision system. Contours are in units of wavenumbers.

calculated for states with $j = 0$ to 72. Computation cost increases with j and cross sections for states with higher j became prohibitively expensive.

State-to-state rate constants involving transitions with $j = 0$ to 72 were determined from the cross section data. To integrate cross sections over a broad of a range of collision energies, it was assumed that the collision cross section at a collision energy of 0 cm^{-1} was 0 Å^2 for each transition. In addition, since the collision cross section is approximately independent of collision energy at high energies, it was assumed that the collision cross section at 2000 cm^{-1} was equal to that calculated at 1000 cm^{-1}. Using the two additional data points and the calculated cross sections, cross section data for each transition were interpolated between energies of 0 cm^{-1} and 2000 cm^{-1}. To calculate the 300 K state-to-state rate constants, the interpolated cross sections were averaged over a 300 K Boltzmann distribution of collision energies as described by equation 7.40. Note that the magnitude of the Boltzmann distribution is $\ll 1$ as the energy $E \rightarrow 0$ and $E \rightarrow \infty$, thereby suppressing the contribution from the data points at 0 cm^{-1} and 2000 cm^{-1}.

To investigate the rotational relaxation of CO_2 rotors from collisions with argon and helium, a master equation describing the state-specific population kinetics was solved analytically with a MATLAB script. The master equation is defined by a matrix of state-to-state rate constants from each collision system (see equation 7.49). Rate constants calculated from the inelastic cross sections were extrapolated to involve transitions up to $j = 110$. The resulting master equation is solved analytically as described in section 7.2.6.

7.4 Results and Discussion

Here, state-to-state integral cross sections for Ar-CO_2 and He-CO_2 are presented. A matrix of state-to-state rate constants is constructed to involve transitions with $j = 0$ to 72. The collision dynamics is investigated by solving a master equation using the rates from each collision system.

7.4.1 Inelastic Scattering Cross Sections

The 300 K Boltzmann distribution reaches a maximum at about 200 cm^{-1} and the characteristics of the cross section at a collision energy $E_C = 200$ cm^{-1} represents the most significant contribution to 300 K collision dynamics. Figure 7.3 shows the state-to-state inelastic scattering cross sections for Ar-CO_2 and He-CO_2 for transitions with an initial rotational quantum number $j_i = 0$ to 72 at a collision energy of 200 cm^{-1}. The elastic cross sections are not reported here. For CO_2 collisions with both rare gases, the largest cross sections for a given j_i occur for transitions with small changes in j. The results show that
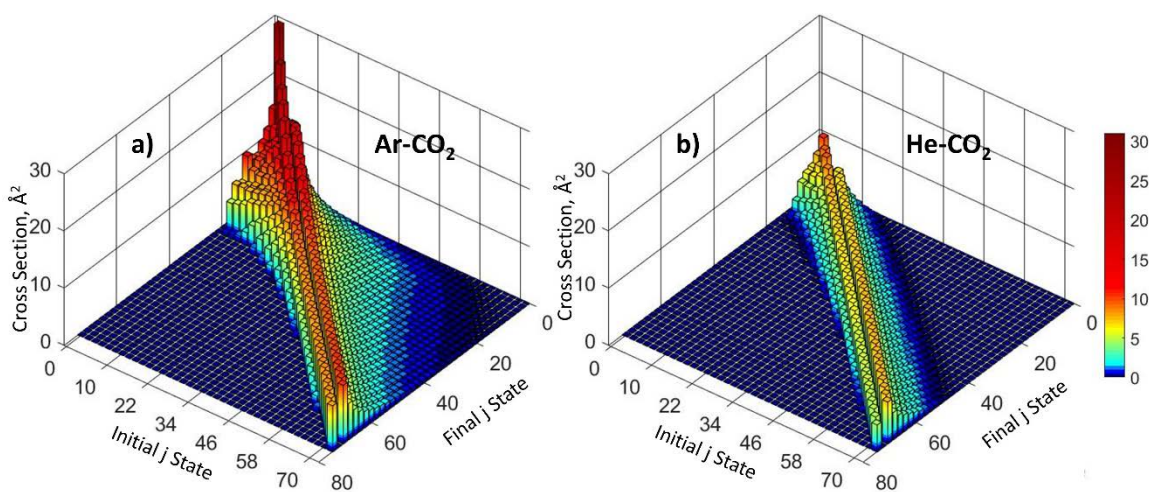
Figure 7.3 State-to-state integral cross sections of the Ar-CO_2 (a) and He-CO_2 (b) collision systems at a collision energy of 200 cm^{-1}.

for a given j_i, a broad range of final rotational quantum numbers j_f have non-zero cross sections. Cross sections are zero for up transitions ($j_f > j_i$) when the increase in rotational energy is greater than the available collision energy. In general, cross sections for CO_2 collisions with Ar are greater than cross sections for collisions with He.

Figure 7.4 shows a semi-log plot of the inelastic cross sections $\sigma_{j_i \to j_i + |\Delta j|}$ for transitions from j_i to $j_i + |\Delta j|$, where $\Delta j = j_f - j_i$. For Ar-CO_2 and He-CO_2, the cross sections decrease as $|\Delta j|$ increases. However, the He-CO_2 cross sections decrease faster than those for Ar-CO_2. The results presented in Figure 7.4 demonstrate the effect of the angular momentum gap on the behavior of the collision cross section for both collision systems. This effect is more pronounced for He-CO_2 than it is for Ar-CO_2. There is some asymmetry for up versus down collisions for a given $|\Delta j|$, but it is not significant on the semi-log plot.

Figure 7.5a and b show the inelastic cross section for $\Delta j = -2$ and $\Delta j = -4$ transitions as a function of initial state j_i. Cross sections for both Ar-CO_2 and He-CO_2 initially increase as j_i increases. Ar-CO_2 cross sections rise to a maximum around $j_i \cong$ 10, followed by a decrease at larger j_i. Cross sections for He-CO_2 quickly level off at $j_i \cong$ 6 and are approximately independent of j_i at larger j_i.

The total inelastic scattering cross section can be calculated by summing the state-to-state cross sections over all j_f given a particular j_i:

$$\sigma_{j_i} = \sum_{j_f \neq j_i} \sigma_{j_i \to j_f} . \tag{7.61}$$

171
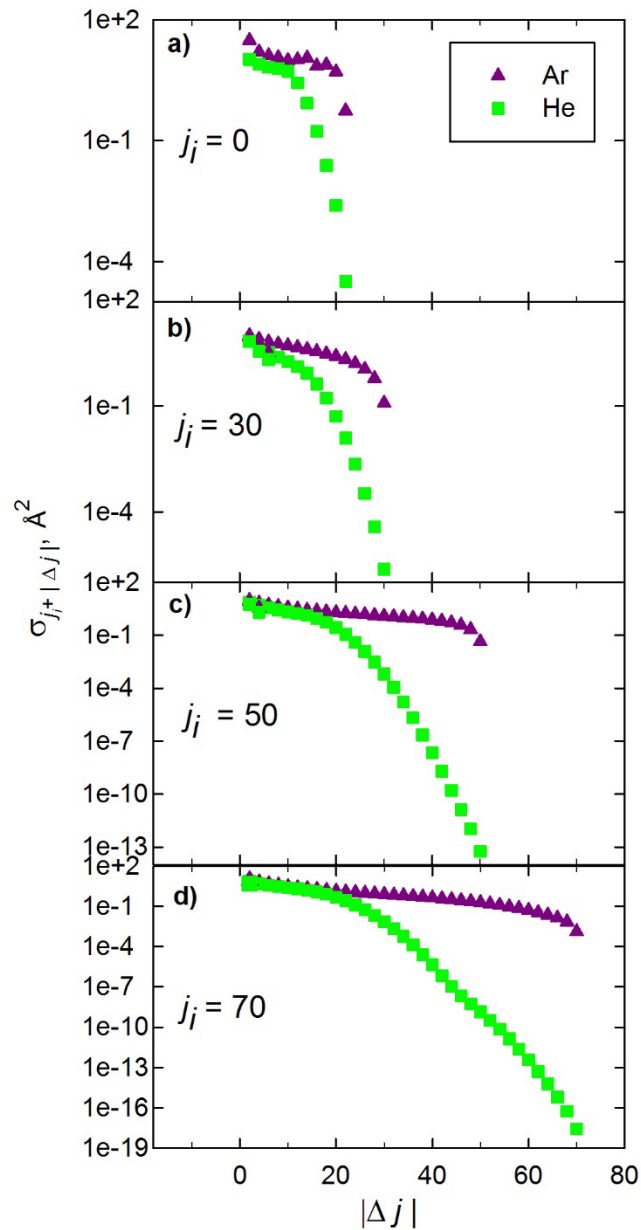
Figure 7.4 Inelastic cross sections $\sigma_{j_i \to j_i+|\Delta j|}$ for Ar-CO_2 and He-CO_2 as a function of $|\Delta j|$ for $j_i = 0$ (a), 30 (b), 50 (c), 70 (d).

Figure 7.5c shows the total inelastic cross section for Ar-CO_2 and He-CO_2 as a function of j_i. Inelastic cross sections for Ar-CO_2 are much larger than those for He-CO_2. Total inelastic cross sections for Ar-CO_2 decrease by a factor of 2 as j_i goes from 0 to 72. In contrast, the total inelastic cross sections for He-CO_2 are approximately constant with
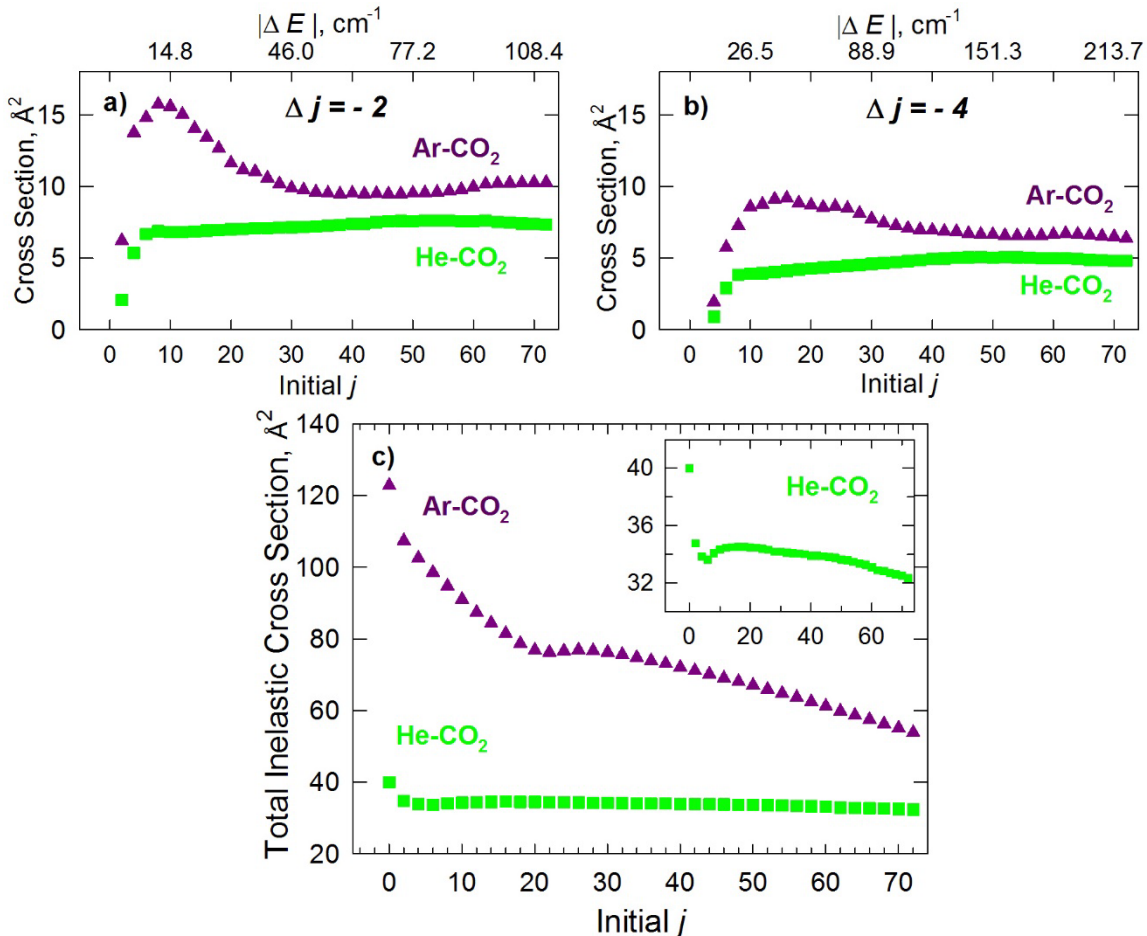
Figure 7.5 a) Ar-CO$_2$ and He-CO$_2$ cross sections for $\Delta j = -2$ transitions as a function of j_i. b) Ar-CO$_2$ and He-CO$_2$ cross sections for $\Delta j = -4$ transitions. c) The total inelastic cross sections for Ar-CO$_2$ and He-CO$_2$ as a function of j_i. The inset zooms in on the behavior of the He-CO$_2$ inelastic cross sections.

respect to j_i. The inset in Figure 7.5c shows that He-CO$_2$ cross sections display some dependence on j_i, but cross sections remain between 32 Å^2 and 34 Å^2 for all states between $j_i = 4$ and 72.

For a rigid rotor molecule, the energy gaps between states j_i and j_f, $\Delta E = E_f - E_i$, are linearly proportional to j_i. For example, for a $\Delta j = -2$ transition, $\Delta E = -B(4j_i - 2)$, where B is the rotational constant. The upper x-axis in Figure 7.5a and b is converted to $|\Delta E|$ and the plots show that the cross sections are approximately independent of $|\Delta E|$ at

large j_i. In conclusion, the fact that the He-CO_2 cross sections are largely independent of j_i is evidence that the angular momentum gap Δj, rather than the energy gap ΔE, has a larger effect on the behavior of the inelastic collision cross sections. In contrast, the dependence of the Ar-CO_2 cross sections shows that both Δj and ΔE have a significant effect.

Close-coupled calculations were also completed for Ar-CO_2 and He-CO_2 at collision energies of 150, 310, 525, and 1000 cm^{-1}. The plots showing the complete set of state-to-state cross sections for each collision system are shown in Figure A.1 through Figure A.4 in the Appendix. In general, the same trends observed in Figure 7.4 and Figure 7.5 were also seen at the other collision energies. However, as collision energy increases, the number of energetically allowed transitions increases, thereby spreading the distribution of cross sections across more states. Figure 7.6 shows the total inelastic cross sections at given j_i values for Ar-CO_2 and He-CO_2 as a function of collision energy. For both systems, the total inelastic cross section is largest at low collision energies. This result
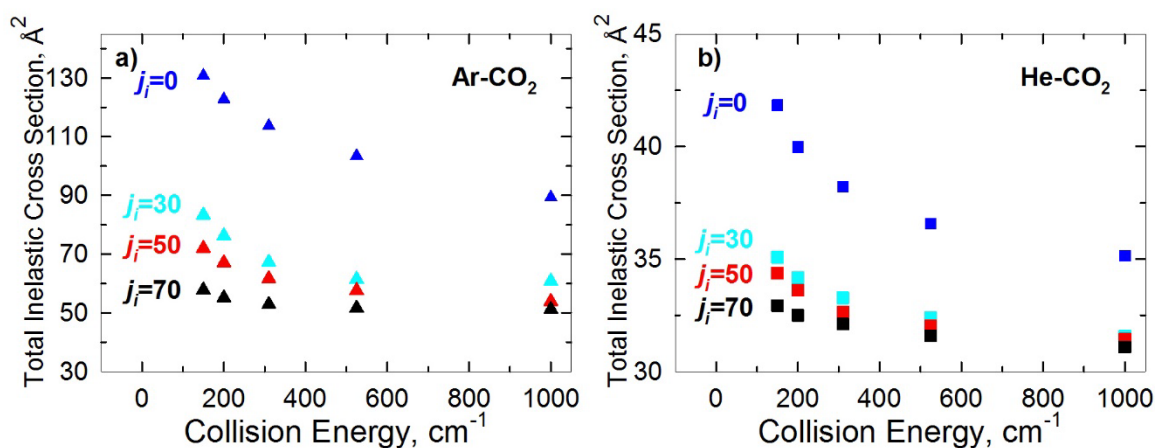
Figure 7.6 Total inelastic cross section as a function of collision energy for Ar-CO_2 (a) and He-CO_2 (b).
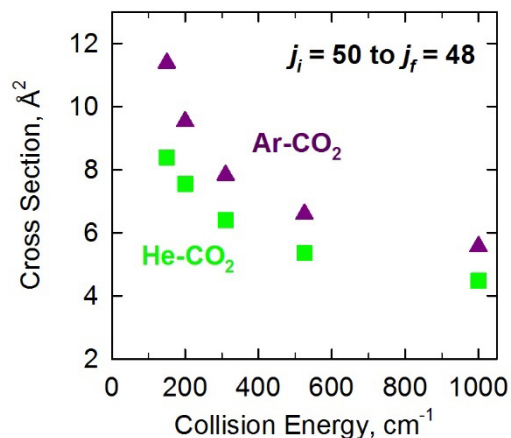
Figure 7.7 The state-to-state cross sections from $j_i = 50$ to $j_f = 48$ for Ar-CO$_2$ and He-CO$_2$ as a function of collision energy.

is consistent with the experiments described in Chapter 3, which revealed subthermal Doppler profiles for CO$_2$ $j = 0$ and 36, indicating that slow moving molecules are most likely to be scattered from these states.

As an example of the effect that collision energy has on the cross section for a single transition, Figure 7.7 shows the cross sections for transitions from $j_i = 50$ to $j_f = 48$ as a function of collision energy. For Ar-CO$_2$ and He-CO$_2$, as the collision energy is increased, the cross section for this transition decreases, in agreement with the trend observed for the total inelastic cross section. Individual state-to-state cross sections like the one shown in Figure 7.7 are averaged over a Boltzmann energy distribution to give the state-to-state rate constants.

7.4.2 State-to-State Rates

A set of 300 K state-to-state rate constants were calculated for Ar-CO$_2$ and He-CO$_2$ using the cross section results from the close-coupled calculations. Half of the rate constants were calculated from the cross section for transitions where $\Delta j < 0$. The other
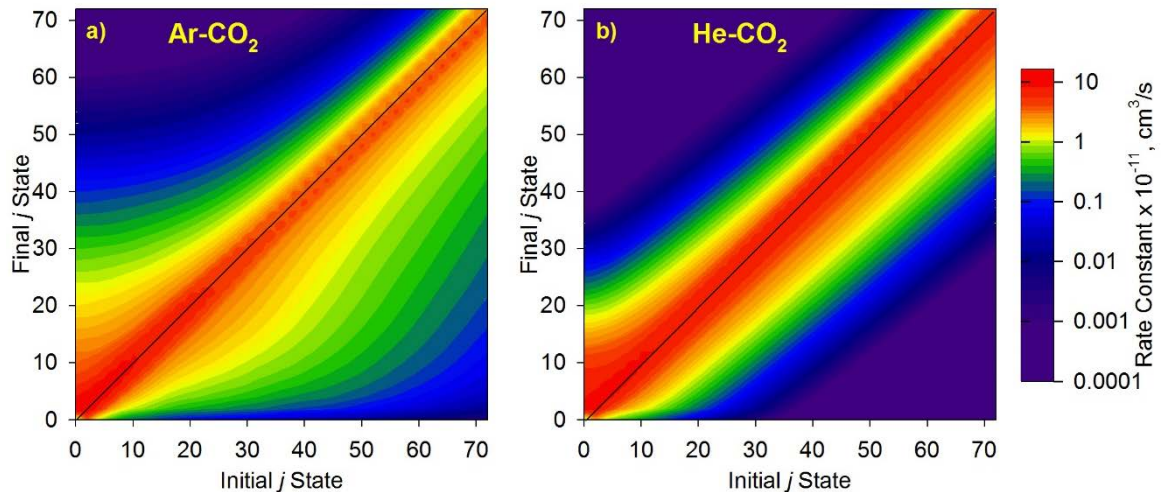
Figure 7.8 Contour plots showing the state-to-state rate constants for Ar-CO$_2$ (a) and He-CO$_2$ (b). The height of the contour represents the magnitude of the of the rate. The line $j_f = j_i$ is shown as black line in each plot. The elastic rates were not included in these plots.

half (with $\Delta j > 0$) of the rate constants were determined by the condition of detailed balance given in equation 7.44. Conservation of particles determines the elastic rate ($\Delta j = 0$) from equation 7.48. The result is a matrix of rate constants for all transitions from $j = 0$ to 72. Figure 7.8 shows contour plots of the state-to-state rate constants for Ar-CO$_2$ and He-CO$_2$. For Ar-CO$_2$ and He-CO$_2$, the largest rates occur for small changes in j. Rates for Ar-CO$_2$ are somewhat broadly distributed about the line $j_f = j_i$. In contrast, the largest He-CO$_2$ rates are more narrowly concentrated near the line $j_f = j_i$.

Figure 7.9 shows the Ar-CO$_2$ and He-CO$_2$ rate constants for $j_i = 50$. The plot illustrates that He-CO$_2$ rates are larger than Ar-CO$_2$ rates for transitions with small Δj. Plotting the rate constants another way, Figure 7.10 shows the Ar-CO$_2$ and He-CO$_2$ rates
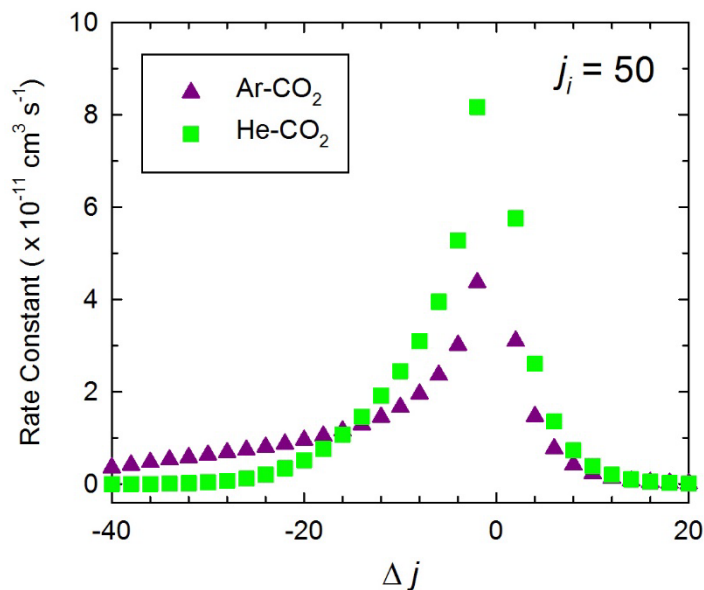
Figure 7.9 Ar-CO$_2$ and He-CO$_2$ rate constants for $j_i = 50$ as a function of Δj.

constants as a function of j_i for 5 values of Δj. At large j_i, the rates for He-CO$_2$ are about 2 times greater than those for Ar-CO$_2$.

The rate constant is a product of the relative velocity and the collision cross section: $k = \langle v_{rel}\sigma \rangle$. Since the Ar-CO$_2$ cross sections are larger than the He-CO$_2$ cross sections, the larger He-CO$_2$ rates illustrate the importance of the larger relative velocity of He-CO$_2$. He-CO$_2$ has relative velocity that is a factor of 2.4 larger than that for Ar-CO$_2$. As per the discussion in Section 6.3.3, He-CO$_2$, having a larger relative velocity, is less adiabatic than Ar-CO$_2$. The increased rates for He-CO$_2$ indicate the importance of rotational adiabaticity in CO$_2$ rotational relaxation.

7.4.3 Modeling Relaxation from High Rotational States

A master equation was used to investigate the effect of collision partner on the rotational relaxation dynamics of CO$_2$ and to compare with dynamics detected in optical
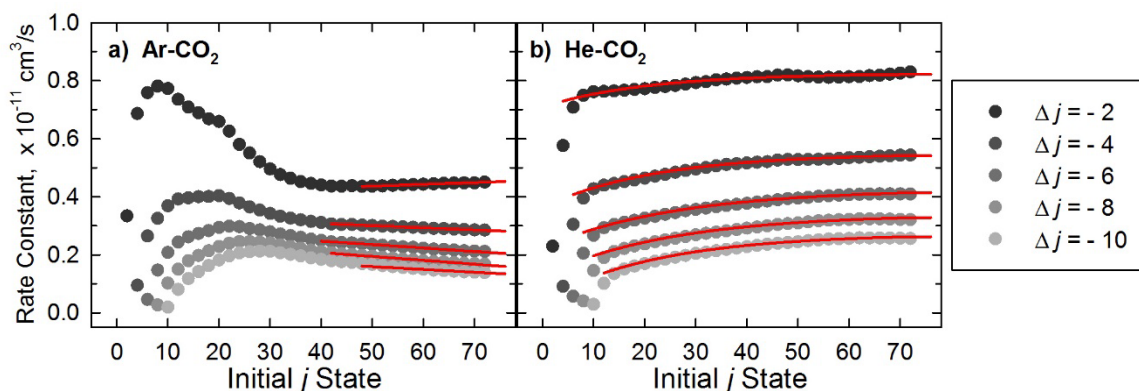
Figure 7.10 Rate constants for Ar-CO$_2$ (a) and He-CO$_2$ (b) as a function of j_i for transitions with $\Delta j = -2$, -4, -6, -8, and -10. To extrapolate the rates to higher states, the Ar-CO$_2$ rates are fit to a linear model at high j_i and the He-CO$_2$ rates are fit to an exponential rise to maximum. The fits used to extrapolate the rates for each value of Δj are shown in red in each plot.

centrifuge experiments. The time evolution of the population in individual rotational states of CO$_2$ was determined by solving the set of differential equations defined by the rate constants for Ar-CO$_2$ and He-CO$_2$. Comparisons are made with the optical centrifuge buffer gas experiments presented in Chapter 6.

Rates for Ar-CO$_2$ and He-CO$_2$ were calculated for all transitions involving states $j = 0$ to 72. In optical centrifuge experiments, a much larger number of states is involved in rotational dynamics because the optical centrifuge excites CO$_2$ molecules to super rotor states near $j = 220$. Close-coupled calculations beyond $j = 72$ were prohibitive. To more closely resemble the number of states involved in experimental super rotor relaxation, the rate constants were extrapolated beyond the calculated values to include states up to $j = 110$. The value of $j = 110$ was chosen as a balance between extending the rates to the highest possible state while remaining in a region where the observed trends continue.

The rates for Ar-CO$_2$ and He-CO$_2$ were extrapolated using a purely descriptive model of the behavior of the rates at large j_i. As seen in Figure 7.10a, the Ar-CO$_2$ rates for specific Δj transitions appear linear in j_i at large j_i. The corresponding linear fits for Ar-

CO_2 are shown in red in Figure 7.10a. The He-CO_2 rates for specific Δj transitions approach a maximum value at large j_i and so are fit to a model of the form:

$$y = a(1 - e^{-bx}),\qquad(7.62)$$

where a and b are adjustable parameters. The corresponding fits for He-CO_2 are shown in red in Figure 7.10b. Ar-CO_2 and He-CO_2 rate constants were extrapolated for values of $\Delta j = -2$ to -40. Rates of transitions with $|\Delta j| > 40$ are assumed to have a negligible contribution to the relaxation dynamics in states $j = 72$ to 110. The rates for transitions with $\Delta j > 0$ were determined by detailed balance.

Using the full rate matrix with both the calculated and extrapolated rates for each collision system, the master equation (equation 7.49) was solved as described in Section 7.2.6. To investigate the population dynamics in the two collision systems in a nonequilibrium environment that resembles the one produced by the optical centrifuge, a fraction of the 300 K population was removed from a Gaussian distribution ($\Delta j_{\text{FWHM}} \approx 6$) of states centered around $j = 16$ and placed in a narrower distribution ($\Delta j_{\text{FWHM}} \approx 2$) around $j = 100$. Experiments in Chapters 3 and 4 estimate the fraction of molecules excited by the optical centrifuge to be between 1% and 40%. For these calculations, 10% of the population was placed in the high rotational states and the pressure of the collision partner was set to 5 Torr. The same initial distribution of rotational states was used in the Ar-CO_2 and He-CO_2 calculations and is shown in Figure 7.11a and Figure 7.11e. The rest of the panels in Figure 7.11 show the time evolution of the distribution of populations for
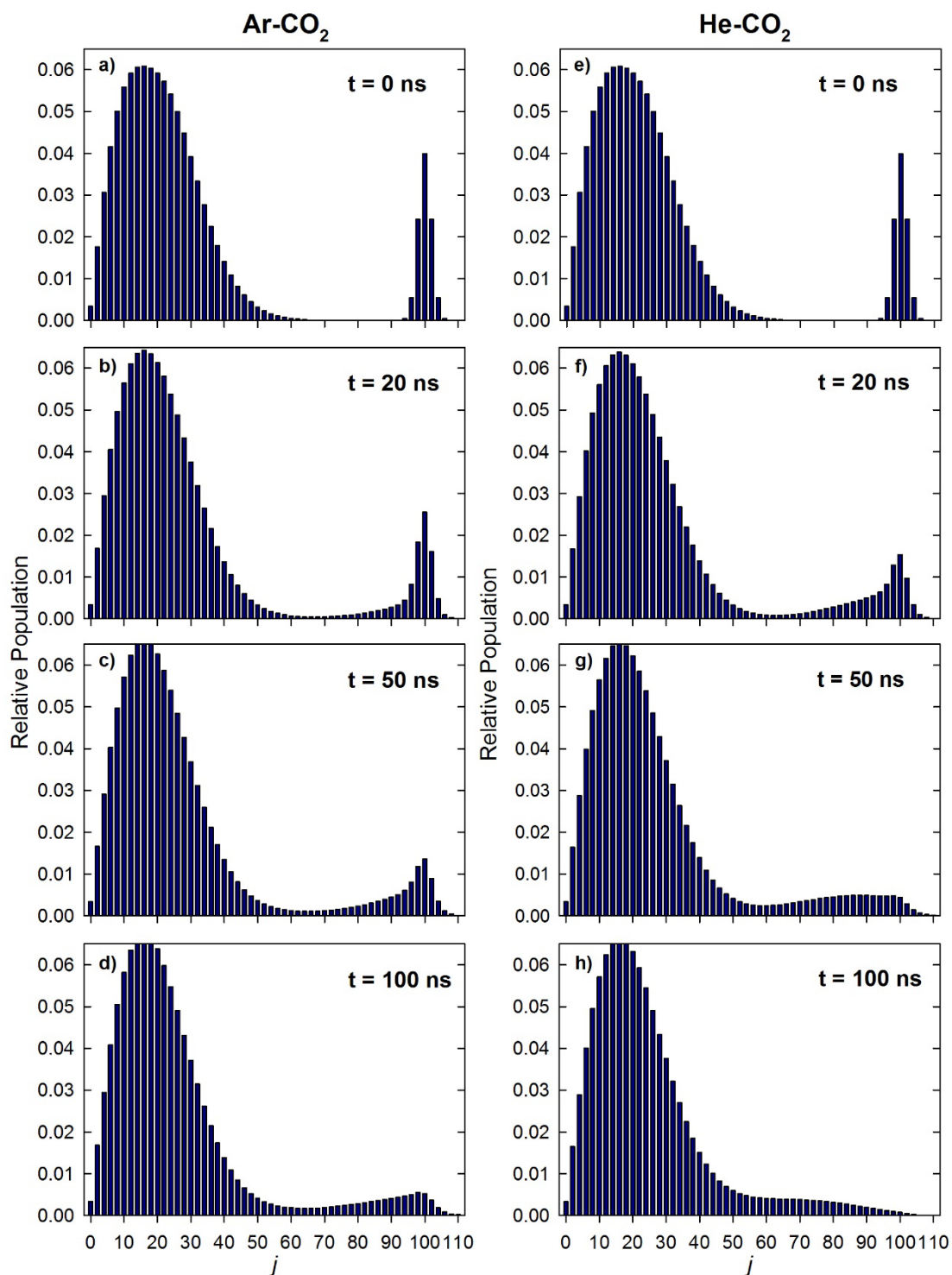
Figure 7.11 Time evolution of rotational state populations starting in the distribution shown at t = 0 (a and e) for Ar-CO_2 (a-d) and He-CO_2 (f-h). The pressure of the collision partner was set to 5 Torr.

180

Ar-CO$_2$ and He-CO$_2$ up to time t = 100 ns. Overall, rotational relaxation of CO$_2$ super rotors in He-CO$_2$ collisions occurs faster than it does for Ar-CO$_2$. Figure 7.12a shows the time evolution of the population in the $j = 76$ state for Ar-CO$_2$ and He-CO$_2$ from the master equation calculations. The master equation calculations show a significant difference between the kinetics for Ar-CO$_2$ relaxation and those for He-CO$_2$.

Comparisons are made to optical centrifuge experiments, which probed the dynamics of CO$_2$ $j = 76$ in a gas mixture with either Ar or He. Figure 7.12b shows the experimentally measured time evolution of the population in the CO$_2$ $j = 76$ state after optical centrifuge excitation. For these measurements, 5 Torr of CO$_2$ was used with 10 Torr of either Ar or He. Excellent qualitative agreement is observed when comparing the results of the master equation calculations in Figure 7.12a and the optical centrifuge experiments in Figure 7.12b. Calculations and experiments show that population enters the CO$_2$ $j = 76$ state more quickly with He-CO$_2$ collisions than it does with Ar-CO$_2$ collisions. Population also decays back toward equilibrium more quickly for the He-CO$_2$ conditions. This behavior is understood from the physical picture described by the rate constants shown in Figure 7.8. He-CO$_2$ undergoes more frequent changes in j than does Ar-CO$_2$, leading to a rapid increase and rapid decay of population in high rotational states. The experimentally observed dynamics provides evidence of the character of the rate constants shown in Figure 7.8.

The agreement between theory and experiment is encouraging. The key features of the transient population in an excited CO$_2$ state have been successfully simulated. Of course, there are several important differences between the conditions used in the
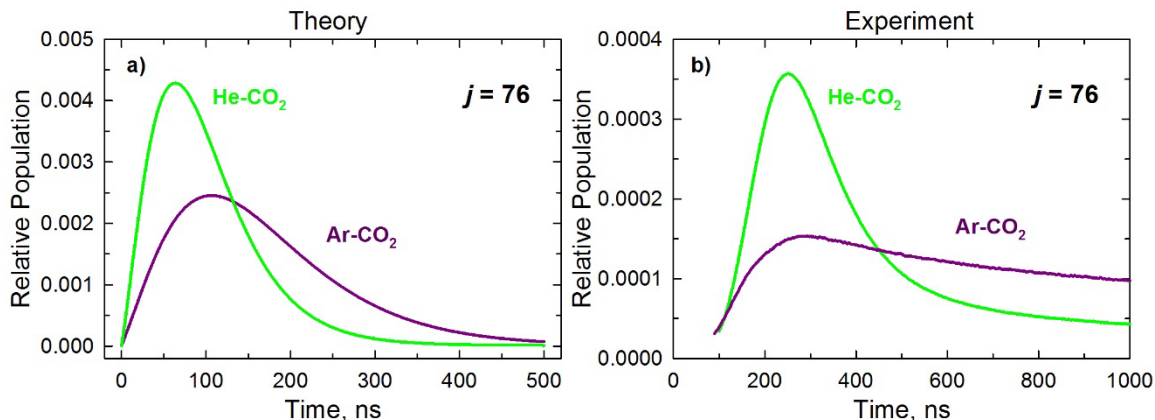
Figure 7.12 a) Master equation calculations showing the evolution of population in the $j = 76$ state for Ar-CO_2 and He-CO_2. For the results shown here, initially 10% of the population was placed in a distribution centered at $j = 100$ state and the pressure of the collision partner was set to 5 Torr. b) Experimental measurements of the CO_2 $j = 76$ state after a mixture of either CO_2 and Ar or CO_2 and He was excited by the optical centrifuge, presumably to a state near $j = 220$. The pressure of CO_2 was 5 Torr and the pressure of the rare gas was 10 Torr.

calculations and the conditions present in the experiments. The optical centrifuge excites molecules to much higher states than those used in the master equation calculations. There is also uncertainty in the fraction and distribution of the population excited by the optical centrifuge. Experiments measure translational temperatures that are far above 300 K for molecules in several rotational states. The rates calculation and subsequent master equation calculation were performed using a temperature of 300 K. In addition, the quantum scattering calculations only consider interactions between CO_2 and the rare gas collision partner. In the experiments, CO_2-CO_2 interactions also contribute to the measured dynamics. Such differences between the quantum scattering calculations and the experiments contribute to the observed differences between the timescales of the calculations and experiments. Future work in theory and experiments can improve upon the agreement by investigating the effect each difference has on the relaxation dynamics.

182

7.5 Conclusion

Close-coupled calculations were performed for Ar-CO_2 and He-CO_2 and state-to-state inelastic scattering cross sections were calculated at five collision energies for each collision system. For Ar-CO_2, both the angular momentum gap and the energy gap between states have a significant effect on the inelastic cross section. For He-CO_2, the angular momentum gap has a larger effect on the cross section. The 300 K state-to-state rate constants were calculated for each system and extrapolated up to $j = 110$. A master equation was solved to compare the time evolution of population in each state for Ar-CO_2 and He-CO_2. The smaller mass of He-CO_2 combined with the angular momentum gap dependence on the cross section yields larger rates for He-CO_2 than for Ar-CO_2. Excellent qualitative agreement was seen between the dynamics observed from the master equation calculations and the dynamics measured in optical centrifuge experiments. The result is that both theory and experiment reveal that rotational relaxation occurs faster for He-CO_2. This effect is attributed, in part, to the high relative velocity in He-CO_2 collisions.

This work provides additional insights into the relaxation of super rotor molecules. Future work could extend quantum scattering calculations to higher j states by implementing the coupled-states approximation. In addition, options should be explored for running similar calculations on CO_2-$CO_2(j)$ collisions. Further comparisons between quantum scattering calculations and optical centrifuge experiments paves the way for quantum-based models of rotational relaxation from super rotor states.

Chapter 8: Conclusions and Future Work

The optical centrifuge provides the opportunity to study a highly oriented ensemble of molecules in a far-from-equilibrium regime. High resolution transient IR absorption spectroscopy was used to investigate the collision dynamics of super rotor molecules prepared with oriented angular momentum by the optical centrifuge. The results provide new information about rotational relaxation and energy transfer from high rotational states.

In the investigations described in Chapters 3 and 4, Doppler-broadened line profiles show that molecular super rotors relax via a collisional cascade, whereby large amounts of translational energy are imparted to the molecules via impulsive collisions. The large translational temperatures indicate a propensity for small changes in rotational quantum number J. This finding is supported by quantum scattering calculations for Ar-CO_2 collisions. Sub-thermal Doppler profiles were measured for molecules leaving the CO_2 J = 0 and 36 states, indicating that the slow moving molecules are most likely to be scattered from these states. A polarization-dependent study of CO super rotors found anisotropic energy gains and more population in the initial plane of rotation.

Modifications made to the instrument and experimental procedures improved signal-to-noise levels and increased reproducibility, as described in Chapter 5. Polarization-sensitive measurements identified the conditions under which the dynamics of super rotors could be studied in a regime with fewer collisions. A new multipass IR detection scheme was implemented that increased signal-to-noise levels by a factor of 10.

The new experimental configuration permitted the study of CO_2 super rotors in the single collision regime. Polarization-dependent measurements show that molecules perpendicular to the plane of rotation initially have greater translational energy than do those parallel to the plane to rotation, demonstrating the orientational dependence of rotation-to-translational energy transfer processes.

Throughout this work, polarization-dependent populations indicate how the orientational anisotropy of the rotors evolves with time, J state, and molecular identity. The experiments reveal that the magnitude of the anisotropy is larger and the duration longer for molecules with large amounts of angular momentum. In this high-energy, high-J regime the oriented super rotor molecules behave as classical gyroscopes.

Further studies described in Chapter 6 used a pair of buffer gases to investigate the rotational dynamics of CO_2 super rotors with other collision partners. The results show that He-CO_2 collisions rotationally relax the excited CO_2 super rotors faster than do Ar-CO_2 collisions, demonstrating the importance of rotational adiabaticity in super rotor dynamics. Polarization-dependent measurements show that Ar-CO_2 collisions are more effective at randomizing the angular momentum of the CO_2 rotor, providing further correspondence to the classical gyroscope. In Chapter 7, quantum scattering calculations of the Ar-CO_2 and He-CO_2 collision systems were used to model the rotational relaxation in the presence of rare gas atoms. Excellent qualitative agreement was found between the computational and experimental work, indicating that further work on both theoretical and experimental fronts can provide additional insights into super rotor dynamics.

The results presented here indicate several avenues of future work with the optical centrifuge. The improvements made to the detection scheme permit the study of rotational states closer to the initially prepared states by the optical centrifuge. Measurements of higher states would test the gyroscopic behavior seen for the states measured in this thesis. At the same time, control of the initial states to which the optical centrifuge excites the molecules could be achieved by controlling the total bandwidth of the oppositely chirped pulses. Such measurements could probe the initial distribution of states generated in the optical centrifuge and provide a more precise determination of the fraction of molecules excited. The efficiency of the optical centrifuge trap might be improved by pre-aligning the molecules with a pulse of linearly polarized light prior to optical centrifuge excitation. Improved trapping would result in greater super rotor number densities and lead to even larger signal-to-noise levels.

The anisotropic kinetic energy release is an interesting result of the oriented nature of the molecules and suggests that future work could determine what types of collisions are most effective at transferring energy. Such anisotropic energy gains have been predicted to induce macroscopic gas vortices[35]. Measurements of Doppler-broadened line profiles that probe molecules at distinct locations from the center of the optical centrifuge pulse could test this prediction.

Concurrent experimental and computational work could test the effectiveness of theoretical rotational energy transfer models in the high J regime. Future computational work could also test different collision partners and compare with experimental results. In addition, computations could investigate the observed retention of angular momentum

orientation by looking at the evolution of the angular momentum projection number. The study of collisions with a highly energetic, highly oriented set of molecules provides insights into spatially dependent energy transfer in reactive and non-reactive collisions.

Appendix: State-to-State Cross Sections for Ar-CO_2 and He-CO_2

Additional plots of the state-to-state inelastic scattering cross sections calculated for Ar-CO2 and He-CO_2 are displayed here. In Chapter 6 the calculations performed at a collision energy of 200 cm-1 are given. Here, the cross sections at 150, 310, 525, and 1000 cm^{-1} are given.

Figure A.1 State-to-state integral cross sections of the Ar-CO_2 (a) and He-CO_2 (b) collision systems at a collision energy of 150 cm^{-1}.

Figure A.2 State-to-state integral cross sections of the Ar-CO_2 (a) and He-CO_2 (b) collision systems at a collision energy of 310 cm^{-1}.

Figure A.3 State-to-state integral cross sections of the Ar-CO$_2$ (a) and He-CO$_2$ (b) collision systems at a collision energy of 525 cm^{-1}.
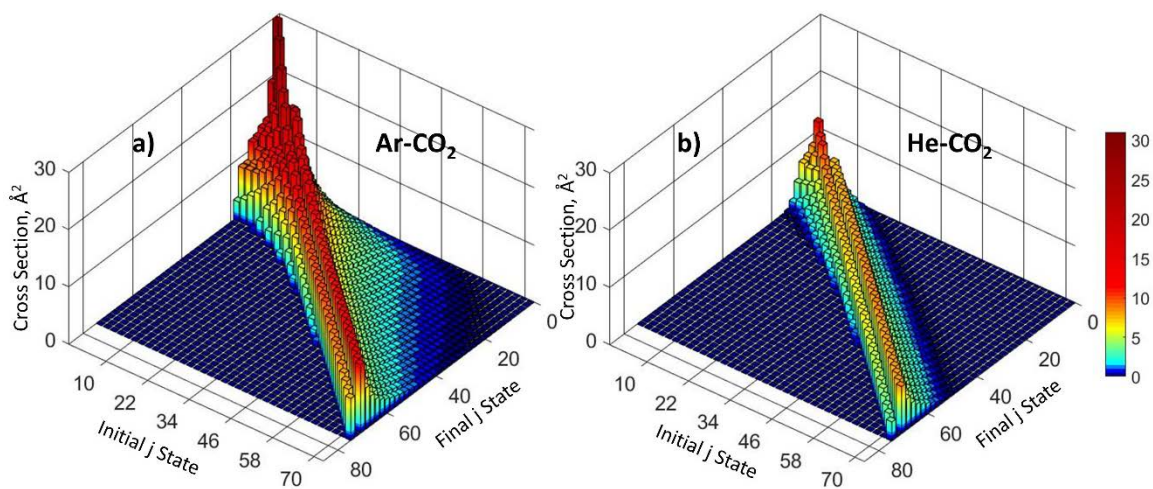

Figure A.4 State-to-state integral cross sections of the Ar-CO$_2$ (a) and He-CO$_2$ (b) collision systems at a collision energy of 1000 cm^{-1}.
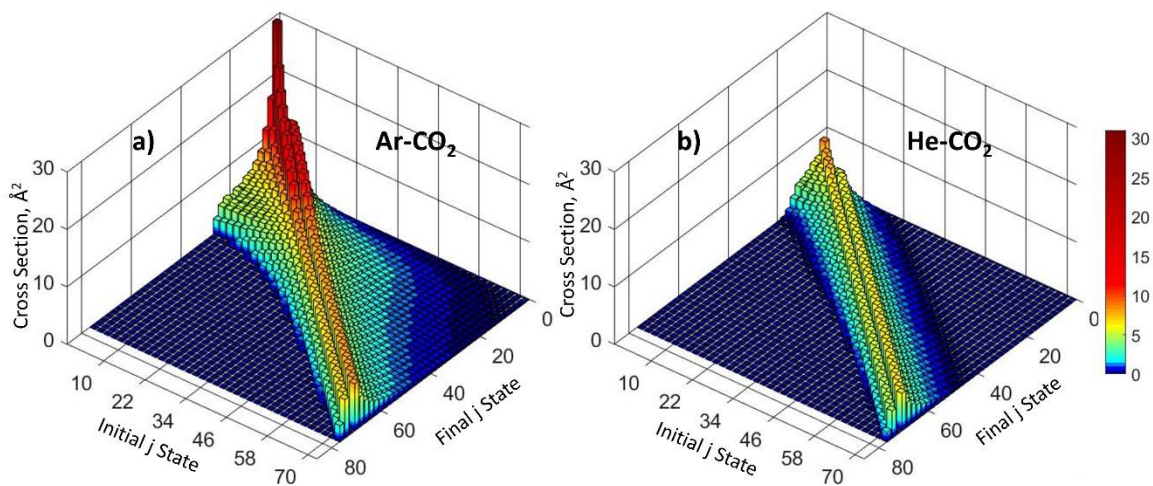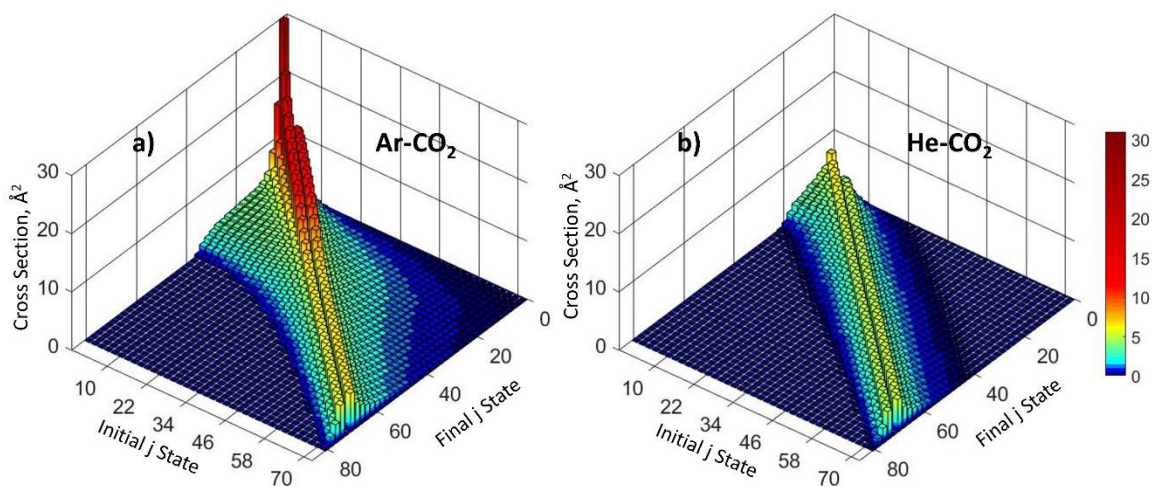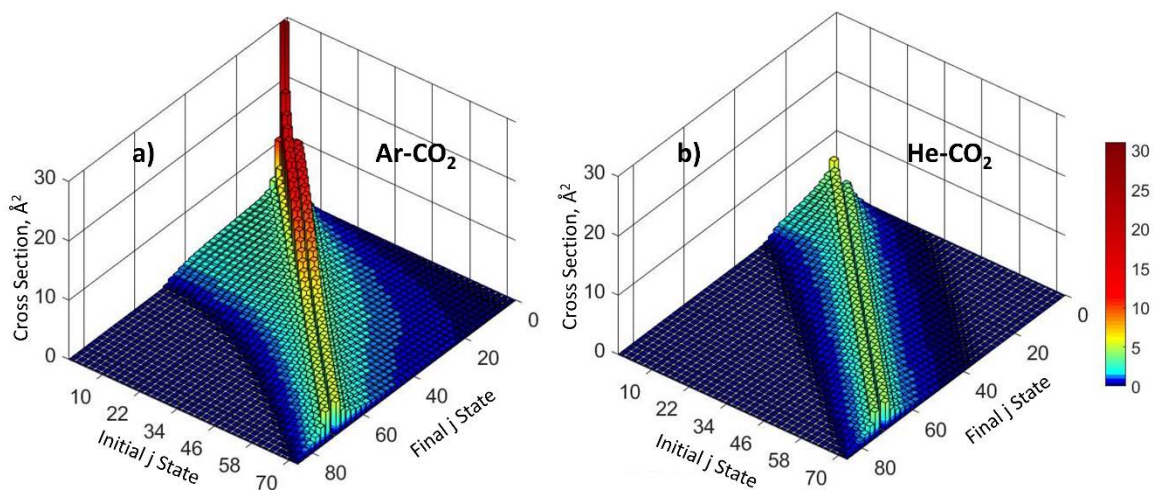
References

[1]   A. J. R. Heck, D. W. Chandler, Imaging Techniques for the Study of Chemical Reaction Dynamics. *Annu. Rev. Phys. Chem.* **1995**, *46*, 335-372.

[2]   F. F. Crim, Bond-Selected Chemistry: Vibrational State Control of Photodissociation and Bimolecular Reaction. *J. Phys. Chem.* **1996**, *100*, 12725-12734.

[3]   R. N. Zare, Laser Control of Chemical Reactions. *Science* **1998**, *279*, 1875-1879.

[4]   J. D. McDonald, Herschba.Dr, P. R. Lebreton, Y. T. Lee, Molecular Beam Kinetics - Reactions of Deuterium Atoms with Halogen Molecules. *J. Chem. Phys.* **1972**, *56*, 769-&.

[5]   R. N. Zare, R. B. Bernstein, State-to-State Reaction Dynamics. *Phys. Today* **1980**, *33*, 43-50.

[6]   H. Stapelfeldt, T. Seideman, Colloquium: Aligning Molecules with Strong Laser Pulses. *Rev. Mod. Phys.* **2003**, *75*, 543-557.

[7]   T. Seideman, E. Hamilton, P. R. Berman, C. C. Lin, in *Adv. At., Mol., Opt. Phys., Vol. Volume 52*, Academic Press, **2006**, pp. 289-329.

[8]   C. Vallance, Generation, Characterisation, and Applications of Atomic and Molecular Alignment and Orientation. *Phys. Chem. Chem. Phys.* **2011**, *13*, 14427-14441.

[9]   D. Herschbach, Chemical Stereodynamics: Retrospect and Prospect. *Eur. Phys. J. D* **2006**, *38*, 3-13.

[10]   J. Itatani, J. Levesque, D. Zeidler, H. Niikura, H. Pepin, J. C. Kieffer, P. B. Corkum, D. M. Villeneuve, Tomographic Imaging of Molecular Orbitals. *Nature* **2004**, *432*, 867-871.

[11]   T. Kanai, S. Minemoto, H. Sakai, Quantum Interference During High-Order Harmonic Generation from Aligned Molecules. *Nature* **2005**, *435*, 470-474.

[12]   B. K. Dey, M. Shapiro, P. Brumer, Coherently Controlled Nanoscale Molecular Deposition. *Phys. Rev. Lett.* **2000**, *85*, 3125-3128.

[13]   O. Gessner, A. M. D. Lee, J. P. Shaffer, H. Reisler, S. V. Levchenko, A. I. Krylov, J. G. Underwood, H. Shi, A. L. L. East, D. M. Wardlaw, E. t. H. Chrysostom, C. C. Hayden, A. Stolow, Femtosecond Multidimensional Imaging of a Molecular Dissociation. *Science* **2006**, *311*, 219-222.

[14]   J. Karczmarek, J. Wright, P. Corkum, M. Ivanov, Optical centrifuge for molecules. *Phys. Rev. Lett.* **1999**, *82*, 3420-3423.

[15]   J. Li, J. T. Bahns, W. C. Stwalley, Scheme for State-Selective Formation of Highly Rotationally Excited Diatomic Molecules. *J. Chem. Phys.* **2000**, *112*, 6255-6261.

[16]   K. Kitano, H. Hasegawa, Y. Ohshima, Ultrafast Angular Momentum Orientation by Linearly Polarized Laser Fields. *Phys. Rev. Lett.* **2009**, *103*.

[17]   A. D. Rudert, J. Martin, W. B. Gao, J. B. Halpern, H. Zacharias, Collisional Effects on Angular Momentum Orientation in Acetylene X Σ_g^+ ($\nu_2''=1$, j "). I.

Preparation, Detection and Conservation in Single Collisions. *J. Chem. Phys.* **1999**, *111*, 9549-9559.

[18]   G. Karras, M. Ndong, E. Hertz, D. Sugny, F. Billard, B. Lavorel, O. Faucher, Polarization Shaping for Unidirectional Rotational Motion of Molecules. *Phys. Rev. Lett.* **2015**, *114*, 103001.

[19]   Y. Ohshima, H. Hasegawa, Coherent Rotational Excitation by Intense Nonresonant Laser Fields. *Int. Rev. Phys. Chem.* **2010**, *29*, 619-663.

[20]   G. O. Sitz, R. L. Farrow, Preparation and Decay of Alignment in N_2 (v=1). *J. Chem. Phys.* **1994**, *101*, 4682-4687.

[21]   A. D. Rudert, J. Martin, W.-B. Gao, H. Zacharias, J. B. Halpern, Collisional Effects on Angular Momentum Orientation in Acetylene X Σ_g^+ (ν_2''=1, j ''). II. Disorientation by Rotationally Elastic and Multiple Inelastic Collisions. *J. Chem. Phys.* **2000**, *112*, 9749-9758.

[22]   T. A. Brunner, R. D. Driver, N. Smith, D. E. Pritchard, Rotational Energy-Transfer in $Na*_2$-Xe Collisions - Level to Level Dynamics. *J. Chem. Phys.* **1979**, *70*, 4155-4167.

[23]   O. Korech, U. Steinitz, R. J. Gordon, I. S. Averbukh, Y. Prior, Observing Molecular Spinning via the Rotational Doppler Effect. *Nat. Photon.* **2013**, *7*, 711-714.

[24]   C. Bloomquist, S. Zhdanovich, A. A. Milner, V. Milner, Directional Spinning of Molecules with Sequences of Femtosecond Pulses. *Phys. Rev. A* **2012**, *86*, 8.

[25]   M. Bitter, V. Milner, Rotational Excitation of Molecules with Long Sequences of Intense Femtosecond Pulses. *Phys. Rev. A* **2016**, *93*, 013420.

[26]   D. M. Villeneuve, S. A. Aseyev, P. Dietrich, M. Spanner, M. Y. Ivanov, P. B. Corkum, Forced molecular rotation in an optical centrifuge. *Phys. Rev. Lett.* **2000**, *85*, 542-545.

[27]   N. V. Vitanov, B. Girard, Adiabatic Excitation of Rotational Ladder by Chirped Laser Pulses. *Phys. Rev. A* **2004**, *69*, 033409.

[28]   T. Armon, L. Friedland, Capture into Resonance and Phase-Space Dynamics in an Optical Centrifuge. *Phys. Rev. A* **2016**, *93*, 043406.

[29]   L. W. Yuan, S. W. Teitelbaum, A. Robinson, A. S. Mullin, Dynamics of molecules in extreme rotational states. *Proc. Natl. Acad. Sci. U. S. A.* **2011**, *108*, 6872-6877.

[30]   C. Toro, Q. Liu, G. O. Echebiri, A. S. Mullin, Inhibited Rotational Quenching in Oriented Ultra-High Rotational States of CO_2. *Mol. Phys.* **2013**, *111*, 1892-1901.

[31]   A. Korobenko, A. A. Milner, V. Milner, Direct Observation, Study, and Control of Molecular Superrotors. *Phys. Rev. Lett.* **2014**, *112*, 5.

[32]   A. A. Milner, A. Korobenko, K. Rezaiezadeh, V. Milner, From Gyroscopic to Thermal Motion: A Crossover in the Dynamics of Molecular Superrotors. *Phys. Rev. X* **2015**, *5*, 031041.

[33]   J. L. Romero, A. B. Klimov, S. Wallentowitz, Semiclassical Dynamics of a Rigid Rotor: SO(3) Covariant Approach. *New J. Phys.* **2015**, *17*, 043015.

[34]   R. C. Forrey, Cooling and Trapping of Molecules in Highly Excited Rotational States. *Phys. Rev. A* **2001**, *63*, 051403.

[35]   U. Steinitz, Y. Prior, I. S. Averbukh, Laser-Induced Gas Vortices. *Phys. Rev. Lett.* **2012**, *109*, 5.

[36]   A. J. McCaffery, Vibration-Rotation Transfer in Molecular Super Rotors. *J. Chem. Phys.* **2000**, *113*, 10947-10951.

[37]   Y. Khodorkovsky, U. Steinitz, J.-M. Hartmann, I. S. Averbukh, Collisional Dynamics in a Gas of Molecular Super-Rotors. *Nat. Comm.* **2015**, *6*, 7791.

[38]   A. Schiffman, D. W. Chandler, Experimental Measurements of State-Resolved, Rotationally Inelastic Energy Transfer. *Int. Rev. Phys. Chem.* **1995**, *14*, 371-420.

[39]   A. J. McCaffery, M. J. Proctor, B. J. Whitaker, Rotational Energy-Transfer - Polarization and Scaling. *Annu. Rev. Phys. Chem.* **1986**, *37*, 223-244.

[40]   C. Ottinger, R. Velasco, R. N. Zare, Some Propensity Rules in Collision Induced Rotational Quantum Jumps. *J. Chem. Phys.* **1970**, *52*, 1636-1643.

[41]   T. A. Brunner, N. Smith, A. W. Karp, D. E. Pritchard, Rotational Energy-Transfer in Na*$_2$ (AΣ) Colliding with Xe, Kr, Ar, Ne, He, H$_2$, CH$_4$, and N$_2$: Experiment and Fitting Laws. *J. Chem. Phys.* **1981**, *74*, 3324-3341.

[42]   R. G. Gordon, P. E. Larson, C. H. Thomas, E. B. Wilson, Rotational Energy Transfer Rates in HCN by Microwave Double Resonance. *J. Chem. Phys.* **1969**, *50*, 1388-1393.

[43]   J. B. Cohen, E. B. Wilson, Rotational Energy Transfer in Pure HCN and in HCN-Rare Gas Mixtures by Microwave Double-Resonance and Pressure Broadening. *J. Chem. Phys.* **1973**, *58*, 442-455.

[44]   R. A. Copeland, F. F. Crim, Rotational Energy Transfer in HF (v=2): Double Resonance Measurments and Fitting Law Analysis. *J. Chem. Phys.* **1983**, *78*, 5551-5563.

[45]   J. D. Tobiason, A. L. Utz, F. F. Crim, State-to-State Rotational Energy Transfer in Highly Vibrationally Excited Acetylene. *J. Chem. Phys.* **1992**, *97*, 7437-7447.

[46]   H. K. Haugen, W. H. Pence, S. R. Leone, Infrared Double-Resonance Spectroscopy of V-T, R Relaxation of HF(v = 1) - Direct Measurement of the High-J Populations. *J. Chem. Phys.* **1984**, *80*, 1839-1852.

[47]   S. P. Phipps, T. C. Smith, G. D. Hager, M. C. Heaven, J. K. McIver, W. G. Rudolph, Investigation of the state-to-state rotational relaxation rate constants for carbon monoxide (CO) using infrared double resonance. *J. Chem. Phys.* **2002**, *116*, 9281-9292.

[48]   J. P. Looney, G. J. Rosasco, L. A. Rahn, W. S. Hurst, J. W. Hahn, Comparison of Rotational Relaxation Rate Laws to Characterize the Raman Q-Branch Spectrum of CO at 295 K. *Chem. Phys. Lett.* **1989**, *161*, 232-238.

[49]   G. O. Sitz, R. L. Farrow, Pump-Probe Measurements of State-to-State Rotational Energy Transfer Rates in N$_2$ (v=1). *J. Chem. Phys.* **1990**, *93*, 7883-7893.

[50]   S. Hay, F. Shokoohi, S. Callister, C. Wittig, Collisional Metastability of High Rotational States of CN(X $^2\Sigma^+$, v'' = 0). *Chem. Phys. Lett.* **1985**, *118*, 6-11.

[51]   L. W. Yuan, C. Toro, M. Bell, A. S. Mullin, Spectroscopy of Molecules in Very High Rotational States using an Optical Centrifuge. *Faraday Discuss.* **2011**, *150*, 101-111.

[52] A. A. Milner, A. Korobenko, J. W. Hepburn, V. Milner, Effects of Ultrafast Molecular Rotation on Collisional Decoherence. *Phys. Rev. Lett.* **2014**, *113*.

[53] A. A. Milner, A. Korobenko, V. Milner, Coherent Spin-Rotational Dynamics of Oxygen Superrotors. *New J. Phys.* **2014**, *16*, 9.

[54] A. Korobenko, A. A. Milner, J. W. Hepburn, V. Milner, Rotational Spectroscopy with an Optical Centrifuge. *Phys. Chem. Chem. Phys.* **2014**, *16*, 4071-4076.

[55] K. Aleksey, M. Valery, Dynamics of Molecular Superrotors in an External Magnetic Field. *J. Phys. B: At., Mol. Opt. Phys.* **2015**, *48*, 164004.

[56] A. A. Milner, A. Korobenko, J. Floβ, I. S. Averbukh, V. Milner, Magneto-Optical Properties of Paramagnetic Superrotors. *Phys. Rev. Lett.* **2015**, *115*, 033005.

[57] A. Korobenko, V. Milner, Adiabatic Field-Free Alignment of Asymmetric Top Molecules with an Optical Centrifuge. *Phys. Rev. Lett.* **2016**, *116*, 183001.

[58] A. Milner, A. Korobenko, V. Milner, Sound Emission from the Gas of Molecular Superrotors. *Opt. Express* **2015**, *23*, 8603-8608.

[59] R. C. Forrey, Prospects for Cooling and Trapping Rotationally Hot Molecules. *Phys. Rev. A* **2002**, *66*, 023411.

[60] K. Tilford, M. Hoster, P. M. Florian, R. C. Forrey, Cold Collisions Involving Rotationally Hot Oxygen Molecules. *Phys. Rev. A* **2004**, *69*, 052705.

[61] W. H. al-Qady, R. C. Forrey, B. H. Yang, P. C. Stancil, N. Balakrishnan, Cold Collisions of Highly Rotationally Excited CO_2 with He: The Prospects for Cold Chemistry with Super-Rotors. *Phys. Rev. A* **2011**, *84*, 054701.

[62] U. Steinitz, Y. Khodorkovsky, J.-M. Hartmann, I. S. Averbukh, Dynamics and Hydrodynamics of Molecular Superrotors. *ChemPhysChem* **2016**, 201600508.

[63] F. J. Lovas, J. S. Coursey, S. A. Kotochigova, J. Chang, K. Olsen, R. A. Dragoset, Molecular Parameters and Energy Level Formulation, *Triatomic Spectral Database* [Online] 2003, National Institute of Standards and Technology, Gaithersburg, MD
http://physics.nist.gov/PhysRefData/MolSpec/Triatomic/Html/sec2.html
(accessed April 4, 2017)

[64] Y. B. Band, *Light and Matter: Electromagnetism, Optics, Spectroscopy and Lasers*, John Wiley & Sons Ltd., West Sussex, England, **2006**.

[65] M. P. Bogaard, A. D. Buckingham, R. K. Pierens, A. H. White, Rayleigh-Scattering Depolarization Ratio and Molecular Polarizability Anisotropy for Gases. *J. Chem. Soc., Faraday Trans.* **1978**, *74*, 3008-3015.

[66] C. M. Dion, A. Keller, O. Atabek, A. D. Bandrauk, Laser-Induced Alignment Dynamics of HCN: Roles of the Permanent Dipole Moment and the Polarizability. *Phys. Rev. A* **1999**, *59*, 1382-1391.

[67] G. Maroulis, (Hyper)polarizability of Carbon Diselenide. *Mol. Phys.* **2008**, *106*, 1517-1524.

[68] *Micra Laser Operator's Manual*, Coherent, Inc., Santa Clara, CA, **2007**.

[69] *Legend-F Operator's Manual*, Coherent, Inc., Santa Clara, CA, **2006**.

[70] H. P. Weber, Method for Pulsewidth Measurement of Ultrashort Light Pulses Generated by Phase-Locked Lasers using Nonlinear Optics. *J. Appl. Phys.* **1967**, *38*, 2231-2234.

[71] E. P. Ippen, C. V. Shank, *Topics in Applied Physics, Vol. 18*, Springer-Verlag, New York, **1977**.

[72] *Synchronization and Delay Generator (SDG) Operator's Manual*, Coherent, Inc., Santa Clara, CA, **2005**.

[73] L. S. Rothman, I. E. Gordon, A. Barbe, D. C. Benner, P. E. Bernath, M. Birk, V. Boudon, L. R. Brown, A. Campargue, J. P. Champion, K. Chance, L. H. Coudert, V. Dana, V. M. Devi, S. Fally, J. M. Flaud, R. R. Gamache, A. Goldman, D. Jacquemart, I. Kleiner, N. Lacome, W. J. Lafferty, J. Y. Mandin, S. T. Massie, S. N. Mikhailenko, C. E. Miller, N. Moazzen-Ahmadi, O. V. Naumenko, A. V. Nikitin, J. Orphal, V. I. Perevalov, A. Perrin, A. Predoi-Cross, C. P. Rinsland, M. Rotger, M. Simeckova, M. A. H. Smith, K. Sung, S. A. Tashkun, J. Tennyson, R. A. Toth, A. C. Vandaele, J. Vander Auwera, The HITRAN 2008 Molecular Spectroscopic Database. *J. Quant. Spectrosc. Radiat. Transfer* **2009**, *110*, 533-572.

[74] H. H. Telle, A. G. Ureña, R. J. Donovan, *Laser Chemistry: Spectroscopy, Dynamics and Applications*, John Wiley & Sons Ltd., West Sussex, England, **2007**.

[75] D. Joyce, *An Introduction to Infrared Detectors*, Gemini Data Workshop, National Optical Astronomy Observatory, Tucson, AZ, **July 19-22, 2010**.

[76] *J10D Series InSb Detectors Operating Instructions*, Teledyne Judson Technologies, Montgomeryville, PA, **2000**.

[77] P. Atkins, J. De-Paula, *Physical Chemistry, Vol. 1*, 9th ed., W. H. Freeman and Company, New York, **2010**.

[78] R. Goldflam, S. Green, D. J. Kouri, Infinite-Order Sudden Approximation for Rotational Energy-Transfer in Gaseous Mixtures. *J. Chem. Phys.* **1977**, *67*, 4149-4161.

[79] E. R. Sirkin, G. C. Pimentel, HF Rotational Laser-Emission through Photoelimination from Vinyl Fluoride and 1,1-Difluoroethene. *J. Chem. Phys.* **1981**, *75*, 604-612.

[80] R. Eggers, M. N. Namboodiri, P. Gonthier, K. Geoffroy, J. B. Natowitz, Evidence for Large Rotational-Energy Contributions to Kinetic Energies of Products of Deep Inelastic Reactions. *Phys. Rev. Lett.* **1976**, *37*, 324-327.

[81] H. Chadwick, B. Nichols, S. D. S. Gordon, B. Hornung, E. Squires, M. Brouard, J. Klos, M. H. Alexander, F. J. Aoiz, S. Stolte, Inelastic Scattering of NO by Kr: Rotational Polarization over a Rainbow. *J. Phys. Chem. Lett.* **2014**, *5*, 3296-3301.

[82] M. D. Brynteson, L. J. Butler, Predicting the Effect of Angular Momentum on the Dissociation Dynamics of Highly Rotationally Excited Radical Intermediates. *J. Chem. Phys.* **2015**, *142*, 13.

[83] P. L. James, I. R. Sims, I. W. M. Smith, M. H. Alexander, M. B. Yang, A Combined Experimental and Theoretical Study of Rotational Energy Transfer in Collisions between NO(X $^2\Pi_{1/2}$, v=3,J) and He, Ar and N$_2$ at Temperatures Down to 7 K. *J. Chem. Phys.* **1998**, *109*, 3882-3897.

[84] M. H. Kabir, I. O. Antonov, M. C. Heaven, Probing Rotational Relaxation in HBr (v=1) using Double Resonance Spectroscopy. *J. Chem. Phys.* **2009**, *130*.

[85] J. Klos, University of Warsaw (Warsaw, Poland), **2001**.

[86] M. Alexander, D. Manolopoulos, H. Werner, B. Follmeg, P. Dagdigian, Q. Ma, HIBRIDON, a package of programs for the time-independent quantum treatment of inelastic collisions and photodissociation. *More information and/or a copy of the code can be obtained from the website* http://www2.chem.umd.edu/groups/alexander/hibridon.

[87] S. S. Viftrup, V. Kumarappan, S. Trippel, H. Stapelfeldt, E. Hamilton, T. Seideman, Holding and Spinning Molecules in Space. *Phys. Rev. Lett.* **2007**, *99*, 143602.

[88] Y. Kida, S. Zaitsu, T. Imasaka, Coherent Molecular Rotations Induced by a Femtosecond Pulse Consisting of Two Orthogonally Polarized Pulses. *Phys. Rev. A* **2009**, *80*, 021805.

[89] J. M. Hartmann, C. Boulet, Quantum and Classical Approaches for Rotational Relaxation and Nonresonant Laser Alignment of Linear Molecules: A comparison for CO_2 Gas in the Nonadiabatic Regime. *J. Chem. Phys.* **2012**, *136*, 184302.

[90] G. Karras, E. Hertz, F. Billard, B. Lavorel, J. M. Hartmann, O. Faucher, Using Molecular Alignment to Track Ultrafast Collisional Relaxation. *Phys. Rev. A* **2014**, *89*, 5.

[91] K. M. Evenson, H. P. Broida, Measurements of Collisional Energy Transfer between Rotational Energy Levels in CN. *J. Chem. Phys.* **1966**, *44*, 1637-1641.

[92] W. Swan, On the Prismatic Spectra of the Flames of Compounds of Carbon and Hydrogen. *Transactions of the Royal Society of Edinburg* **1857**, *21*, 411-430.

[93] W. L. Faust, L. S. Goldberg, B. B. Craig, R. G. Weiss, Time-Resolved C_2 Swan Emission from Short-Pulse UV Fragmentation of CO: Evidence for Two C_2 Formation Mechanisms. *Chem. Phys. Lett.* **1981**, *83*, 265-269.

[94] M. J. Murray, H. M. Ogden, C. Toro, Q. N. Liu, D. A. Burns, M. H. Alexander, A. S. Mullin, State-Specific Collision Dynamics of Molecular Super Rotors with Oriented Angular Momentum. *J. Phys. Chem. A* **2015**, *119*, 12471-12479.

[95] M. J. Murray, H. M. Ogden, C. Toro, Q. Liu, A. S. Mullin, Impulsive Collision Dynamics of CO Super Rotors from an Optical Centrifuge. *ChemPhysChem* **2016**, *17*, 3692-3700.

[96] D. A. McQuarrie, J. D. Simon, *Physical Chemistry: A Molecular Approach*, University Science Books, Sausalito, CA, **1997**.

[97] R. D. Levine, R. B. Bernstein, *Molecular Reaction Dynamics and Chemical Reactivity*, Oxford University Press, New York, **1987**.

[98] P. L. James, I. R. Sims, I. W. M. Smith, M. H. Alexander, M. B. Yang, A Combined Experimental and Theoretical Study of Rotational Energy Transfer in Collisions Between NO($X^2 \Pi_{1/2}$, v=3,J) and He, Ar and N_2 at Temperatures Down to 7 K. *J. Chem. Phys.* **1998**, *109*, 3882-3897.

[99] S. Antonova, A. Lin, A. P. Tsakotellis, G. C. McBane, State to State He-CO Rotationally Inelastic Scattering. *J. Chem. Phys.* **1999**, *110*, 2384-2390.

[100] B. Yang, P. C. Stancil, Rotational Quenching of CO_2 by Collision with He Atoms. *J. Chem. Phys.* **2009**, *130*, 134319.

[101] M. H. Alexander, Close Coupling Studies of the Orientation Dependence of Rotationally Inelastic Collisions. *J. Chem. Phys.* **1977**, *67*, 2703-2712.

[102] M. C. v. Beek, J. J. t. Meulen, M. H. Alexander, Rotationally Inelastic Collisions of OH+Ar. I. State-to-State Cross Sections. *J. Chem. Phys.* **2000**, *113*, 628-636.

[103] M. H. Alexander, *Quantum Molecular Collision Theory*, Lecture Notes, University of Maryland, **2014** http://www2.chem.umd.edu/groups/alexander/

[104] M. H. Alexander, *Cross Sections, Rate Constants, Microscopic Reversibility, Detailed Balance, and the Master Equation in Inelastic and Reactive Kinetics*, Lecture Notes, University of Maryland, **2010** http://www2.chem.umd.edu/groups/alexander/

[105] G. C. Schatz, M. A. Ratner, *Quantum Mechanics in Chemistry*, Dover Publications, Mineola, NY, **2002**.

[106] J. N. Murrell, S. D. Bosanac, *Introduction to the Theory of Atomic and Molecular Collisions*, John Wiley & Sons, New York, **1989**.

[107] A. M. Arthurs, A. Dalgarno, The Theory of Scattering by a Rigid Rotator. *Proceedings of the Royal Society of London Series a-Mathematical and Physical Sciences* **1960**, *256*, 540-551.

[108] D. Secrest, in *Atom-Molecule Collision Theory: A Guide for the Experimentalist* (Ed.: R. B. Bernstein), Plenum Press, New York, **1979**, p. 265.

[109] M. H. Alexander, G. E. Hall, P. J. Dagdigian, The Approach to Equilibrium: Detailed Balance and the Master Equation. *J. Chem. Educ.* **2011**, *88*, 1538-1543.

[110] M. H. Alexander, Hybrid Quantum Scattering Algorithms for Long-Range Potentials. *J. Chem. Phys.* **1984**, *81*, 4510-4516.

[111] B. R. Johnson, Multichannel Log-Derivative Method for Scattering Calculations. *J. Comput. Phys.* **1973**, *13*, 445-449.

[112] D. E. Manolopoulos, An Improved Log Derivative Method for Inelastic Scattering. *J. Chem. Phys.* **1986**, *85*, 6425-6429.

[113] R. G. Gordon, New Method for Constructing Wavefunctions for Bound States and Scattering. *J. Chem. Phys.* **1969**, *51*, 14-25.

[114] H. Li, R. J. Le Roy, Analytic Three-Dimensional 'MLR' Potential Energy Surface for CO_2-He, and its Predicted Microwave and Infrared Spectra. *Phys. Chem. Chem. Phys.* **2008**, *10*, 4128-4137.